

A Study of the Reaction  $K^- p \rightarrow \bar{K} N \pi$   
at Intermediate Energies

by Paul Newham

A thesis submitted for the degree of Doctor of Philosophy  
in the University of London

Department of Physics,  
Imperial College,  
London.

March 1977

To  
my Mother

### Abstract

This thesis describes a study carried out by the author on single pion production from  $K^-p$  reactions between 0.96 and 1.36 GeV/c incident beam momentum. Accurate values of the cross-sections for the three channels are presented. A Dalitz Plot analysis using three of the four independent variables is carried out on the data from these channels at each momentum setting using both non-interference and interference models. The extracted  $\bar{K}^*$  and  $\Lambda(1520)$  resonance contributions are then analysed in the fourth variable, production angle, to obtain a set of Legendre coefficients which describe the differential cross-section and differential density matrix elements at each momentum. A detailed partial wave analysis is carried out on the  $\bar{K}^*N$  system in both charge states, with additional data taken from the College de France - Rutherford - Saclay experiment and the Birmingham  $K^-d$  experiment. Information gained from a preliminary partial wave solution is used to set up barrier factors which are applied to the  $\bar{K}^*$ , and the Dalitz Plot is reanalysed to obtain accurate values of the  $\bar{K}^*N$  cross-sections.

Three similar solutions are obtained from the partial wave analysis, and evidence is presented for the existence of two new states. Amplitudes are also presented for several established and not so well established resonances. A rudimentary qualitative partial wave analysis of the  $\Lambda(1520)\pi$  system is also carried out.

An  $SU(6)_w \times O(3)$  model motivated by the Melosh transformation is used to try and explain the results of the  $\bar{K}^*N$  analysis for the case of some well established resonances. Some crucial relative amplitude signs are correctly predicted by the model, but other problems do arise. An attempt is also made to classify the new states within the  $SU(6)$  framework.

\* \* \* \* \*

Contents

	<u>Page</u>
Abstract	3
Contents	4
List of Tables	6
Figure Captions	8
<u>Chapter 1</u> The Experiment	11
1.1 Introduction	11
1.2 Exposure, scanning and measurements	13
1.3 Beam calibration and cross-section normalisation	14
<u>Chapter 2</u> $\bar{K}N\pi$ Cross-Sections	19
2.1 Introduction	19
2.2 Resolution of ambiguities	19
2.3 Scanning and throughput efficiencies	21
2.4 $K^- p \pi^0$ event weightings	22
2.5 $K^- n \pi^+$ event weightings	23
2.6 $\bar{K}^0 p \pi^-$ event weightings	24
2.7 Channel cross-sections	28
2.8 Estimation of the $\Lambda(1520)$ parameters	29
<u>Chapter 3</u> Dalitz Plot Analysis	39
3.1 Introduction	39
3.2 The non-interference model	40
3.3 The non-interference fits	44
3.4 Extension of the analysis	46
3.5 The interference model	47
3.6 The interference fits	51
3.7 Comments on the results of the fits	52
3.8 The $\phi$ distribution	53
<u>Chapter 4</u> Production Angular Dependence	77
4.1 Introduction	77
4.2 Method of analysis	78

4.3	The differential cross-sections	84
4.4	The $\phi$ distribution	86
<u>Chapter 5</u> The Partial Wave Analysis (Theory)		109
5.1	Introduction	109
5.2	The formalism	111
5.3	Application to the $\bar{K}^*N$ system	115
5.4	The program	118
<u>Chapter 6</u> The Partial Wave Analysis (Experiment)		122
6.1	Introduction	122
6.2	The preliminary solution	122
6.3	Refitting the Dalitz Plot	126
6.4	Integrated barrier factors	129
6.5	Incorporation of further data	130
6.6	Development of solution "A"	131
6.7	Solution "B"	136
6.8	Solution "C"	139
6.9	Discussion of the solutions	141
6.10	Qualitative partial wave analysis of the $\Lambda(1520)\pi$ system	142
<u>Chapter 7</u> The $SU(6)_w$ model		175
7.1	Introduction	175
7.2	Historical development	175
7.3	The Melosh approach	178
7.4	The model	179
7.5	Application to $\bar{K}^*N$ decays	183
7.6	Results and conclusions	184
7.7	Classification of the remaining resonances	186
Appendix		191
References		193
Acknowledgements		196

## List of Tables

### Chapter 1

- 1.1 Number of events of the main topologies after beam cuts.
- 1.2 Microbarn equivalents.

### Chapter 2

- 2.1 Throughput efficiencies used for the  $\bar{K}N\pi$  channels.
- 2.2 a) Scanning efficiencies for channel  $\bar{K}^- p \pi^0$  as a function of proton track length.
  - b)  $\bar{K}^- n \pi^+$  scanning efficiencies.
  - c)  $\bar{K}^0 p \pi^-$  scanning efficiencies.
- 2.3 Number of events per topology for channel  $\bar{K}^0 p \pi^-$ .
- 2.4  $\bar{K}N\pi$  channel cross-sections.

### Chapter 3

- 3.1 Results of the non-interference model for this experiment.
- 3.2 Results of the non-interference model for the CRS data.
- 3.3 Results of the interference model for this experiment.
- 3.4 Results of the interference model for the CRS data.

### Chapter 4

- 4.1 Legendre coefficients for the  $\bar{K}^{*0} n$  system.
- 4.2 Legendre coefficients for the  $K^{*-} p$  system.
- 4.3 Legendre coefficients for the  $K^{*-} p$  system for  $\bar{K}^- p \pi^0$  and  $\bar{K}^0 p \pi^-$  separately.
- 4.4 Legendre coefficients for the  $\Lambda(1520)\pi$  system (this experiment).

### Chapter 6

- 6.1 a) "Established" and "Probable" resonances in the energy region considered.
  - b) "Possible" resonances in the energy region considered.

- 6.2 Summary of the development of the preliminary solution.
- 6.3 a) Dominant partial waves for the preliminary solution.  
b) Intensity ratios for outgoing S, P and D waves.
- 6.4 Results of the Dalitz Plot analysis using interference and  $\bar{K}^*$  production barrier factor, including the final partial cross-sections for  $\bar{K}^*$  and  $\Lambda(1520)$ .
- 6.5 The Birmingham  $A_0$ 's.
- 6.6  $A_4$  and  $B_4$  Tripp coefficients for  $K^- p \rightarrow \bar{K}^* N$ .
- 6.7 Summary of the development of solution "A".
- 6.8 Summary of the development of solution "B".
- 6.9 Summary of the development of solution "C".
- 6.10 All three solutions with a common overall phase sign.
- 6.11 a)  $A_1$  and  $A_3$  Tripp coefficients for  $K^- p \rightarrow \Lambda(1520)\pi$ .  
b)  $C_2$  and  $C_4$  Tripp coefficients for  $K^- p \rightarrow \Lambda(1520)\pi$ .

#### Chapter 7

- 7.1 Results of the  $SU(6)_w$  fits to  $Np$  and  $N\bar{K}^*$  decays.

#### Appendix

- A.1 Comparison of solutions "A", "B" and "C" on using a refined set of  $\bar{K}^* N$  Legendre coefficients.

Figure Captions

Chapter 1

- 1.1 Beam momentum distribution from fitted  $\tau$  decays. The final intervals chosen are indicated by arrows on the axis and the central values by arrows above.

Chapter 2

- 2.1 Projected  $K^-$  decay length distribution -  $K^- p \pi^0$ .
- 2.2 Weighted number of events vs. minimum projected length cut-off -  $K^- p \pi^0$ .
- 2.3 Proper  $K^-$  lifetime distribution ( $c\tau$ ) -  $K^- n \pi^+$ .
- 2.4 Projected  $\bar{K}^0$  decay length distribution -  $\bar{K}^0 p \pi^-$ .
- 2.5 Weighted number of events vs. minimum projected length cut-off -  $K^0 p \pi^-$ .
- 2.6 Folded  $\cos\theta$  distribution for the decay- $\pi$  angle -  $\bar{K}^0 p \pi^-$ .
- 2.7  $\bar{K}^0$  decay plane azimuthal angle ( $\phi$ ) distribution -  $\bar{K}^0 p \pi^-$ .
- 2.8-10 Kinematic probability distributions for  $\bar{K}^0 p \pi^-$ ,  $K^- n \pi^+$  and  $K^- p \pi^0$  respectively.
- 2.11  $\bar{K}^0$  lab. momentum distribution for topologies 201/211 and 400/410 (shaded) -  $\bar{K}^0 p \pi^-$ .
- 2.12  $\bar{K}^0$  lab. momentum distribution for topologies 200/210 -  $\bar{K}^0 p \pi^-$ .
- 2.13 Channel Cross-Sections.
- 2.14 Fit to the  $\Lambda(1520)$  lineshape -  $K^- p \pi^0$ .

Chapter 3

- 3.1 Dalitz Plots at typical beam momenta for all three  $\bar{K}N\pi$  channels.
- 3.2 The helicity system.
- 3.3 Plot of  $\bar{K}^*$  Breit-Wigner function x barrier factor for several values of outgoing orbital angular momentum at 1850 MeV centre of mass energy.
- 3.4 Fits to all momenta above 1.045 GeV/c. The dashed curve is the result of the non-interference model. The solid curve is the result with  $\bar{K}^*$  - S-wave interference.

- 3.5 a) The asymmetry parameter across the  $\bar{K}^*$  band for all channels at 1.165 GeV/c.
- b) Sketches of the asymmetry parameter for limiting values of the interference parameters.
- 3.6 Fit to the  $\phi$  distributions at 1.355 GeV/c for  $\bar{K}^- n \pi^+$  as a result of the three-variable analysis.

#### Chapter 4

- 4.1 Definition of the production angle.
- 4.2 Typical  $K^{*-}$  p Legendre coefficients for  $\bar{K}^- p \pi^0$  and  $\bar{K}^0 p \pi^-$  plotted side by side.
- 4.3  $\chi^2$  vs. order of expansion for fits to the  $\bar{K}^{*0} n$  differential cross-sections of  $\bar{K}^- n \pi^+$ .
- 4.4 Typical differential cross-sections and fitted curves for  $K^{*-} n$ .
- 4.5 Possible t-channel exchanges for  $\bar{K}^- p \rightarrow \bar{K}^* N$ .
- 4.6 Fits to  $\phi$  and  $\cos \theta^*$  at 1.355 GeV/c for  $\bar{K}^- n \pi^+$ . The dashed curve is the result with angular dependence in the  $\bar{K}^*$  only. The solid curve is the result with angular dependence in all processes including background.

#### Chapter 6

- 6.1 Typical fits to the  $\bar{K}\pi$  system in all channels using a  $\bar{K}^*$  barrier factor. The dashed curve is the result of the fit from the interference model alone.
- 6.2 Typical fits to the  $\bar{K}^- p \pi^0$  channel below 1.125 GeV/c using a  $\bar{K}^*$  barrier factor.
- 6.3 Final partial cross-sections for the  $\bar{K}^*$  in all channels and for the  $\Lambda(1520)$ .
- 6.4 Plot of integrated and non-integrated background barrier factors for the  $\bar{K}^* N$  system as a function of centre of mass energy for several values of  $\ell$ .

- 6.5 The  $\bar{K}^* N$  Legendre coefficients with the fitted curve from one of the three partial wave solutions.
- 6.6 A selection of the Argand diagrams for the same solution.
- 6.7 A selection of the  $\Lambda(1520)$  Legendre coefficients.

#### Chapter 7

- 7.1 The SU(6)  $(70, 1^-)$  and  $(56, 2^+)$  multiplet structure showing the mixing possibilities.
- 7.2 Part of the spectrum of SU(6) multiplets as predicted by the harmonic oscillator quark model.

Chapter 1The Experiment1.1 Introduction

An experiment was carried out at CERN in 1970 by a collaboration between the Rutherford Laboratory and Imperial College, using the 2 metre hydrogen bubble chamber, to study the interactions of negative kaons ( $K^-$ ) on protons at beam momenta around 1 GeV/c (commonly referred to as the intermediate energy region). It was proposed as an extension to lower energies of the College de France - Rutherford - Saclay (CRS) experiment, which studied the centre of mass energy region between 1.915 and 2.170 GeV. The main aim of the present experiment was to study direct or S-channel resonance formation in the particularly prolific region between 1.77 and 1.96 GeV. It was intended that the data be of sufficiently high quantity that accurate determination of these resonance parameters could be made. Hence about half a million pictures were taken and about an equal number of interactions obtained. It was hoped that the information gained on these resonances would be a useful addition to the current tests of the SU(6) classification of the elementary particles.

Reactions in which a single pion is produced are perhaps the more interesting of the possible three body final states. They generally proceed via the production of a quasi two-body system in which one particle is a short lived resonance that decays strongly to the stable particles observed in the reaction. The dominant resonances in this so-called  $\bar{K}N\pi$  final state are the  $\bar{K}^*(890)$  in the  $(\bar{K}\pi)$  system and the  $\Lambda(1520)$  in the  $(\bar{K}p)$  system.

For the  $\bar{K}^*(890)$  the energy region of this experiment is particularly interesting since it lies in the threshold region for the production of the resonance. As such, the usual analysis in terms of the exchange or t-channel is less desirable than an S-channel analysis of the  $\bar{K}^*N$  system. A further encouragement for an S-channel analysis is the fact that no

previous analysis of that type has been carried out for the reaction  $\bar{K}^- p \rightarrow \bar{K}^* N$  in which two isospin states contribute, and so the very important information on the decay of S-channel resonances to the  $\bar{K}^* N$  - vector meson, nucleon - final state is missing. Data involving the decay to a vector meson is at present very scarce, the only information coming from the reactions  $\pi N \rightarrow \rho N$ , and so the application of the SU(6) models to these decays is very ill-understood. For this reason the aim of the study comprising this thesis is to obtain the information to as accurate a degree as possible.

When the author joined the Imperial College Bubble Chamber Group in October 1973, the data reduction process had already been completed and the two-body final states were well into the analysis stage. The author took part in some of the event weighting procedure for the  $\bar{K}N\pi$  final states, but was involved mainly in the analysis of these channels which is described in the ensuing chapters.

The thesis is organized as follows. The rest of this chapter briefly describes the experiment and the data reduction chain, together with the cross-section normalization. Chapter 2 describes how the kinematic ambiguities in the  $\bar{K}N\pi$  final states were resolved, and how the events were weighted to account for losses in the data reduction chain. The channel cross-sections are also presented in this chapter. Chapter 3 describes the Dalitz Plot analysis of the three  $\bar{K}N\pi$  channels in three variables in order to extract the partial cross-sections for the production of the quasi two-body resonances. Chapter 4 extends the analysis to the production angle variable, and the data for the S-channel partial wave analysis is extracted. Chapter 5 describes the theory behind the partial wave analysis and gives a description of the computer program used to carry it out. Chapter 6 gives a detailed account of the analysis of the  $\bar{K}^* N$  system, and also gives a qualitative analysis of

the  $\Lambda(1520)\pi$  system. Chapter 7 compares the results of the  $\bar{K}^*N$  analysis with the predictions of a current  $SU(6)_W \times O(3)$  model.

### 1.2 Exposure, scanning and measurements

Approximately 440,000 pictures were obtained in the CERN 2m. Hydrogen Bubble Chamber, exposed to a separated  $K^-$  beam tuned to eleven equally spaced momentum settings between 1.00 and 1.40 GeV/c at the chamber entrance (corresponding to 0.96 and 1.36 GeV/c at the centre of the chamber). The average number of beam tracks per picture varied from 6 at the lowest momentum to 15 at the highest. The momentum bite was typically  $\pm 1\%$ .

All frames were scanned for events of any topology except one prongs (predominantly beam decays) and zero prongs. A restricted fiducial volume was imposed for primary vertices in order to ensure a high scanning efficiency and to minimize reconstruction problems. Scanning efficiencies were determined by making a second independent scan on a quarter of the film. Discrepancies between the two scans were resolved by a third check scan. The scanning efficiencies were typically 96% for a single scan and greater than 99% for a double scan. Approximately 494,000 events were recorded and measured using the Rutherford Laboratory HPD flying spot digitiser. A condition was imposed that frames containing only one simple two-prong event were not measured at the same time as the rest of the film, in order to utilise the HPD to its maximum efficiency.

The events were processed through the Rutherford Laboratory geometry and kinematics programs. (1) The geometry program performs a spatial reconstruction of each event using the digitisings of the HPD and the optical constants of the bubble chamber. The results are used by the kinematics program to check the validity of several hypotheses. For each hypothesis a chi-squared fit is made using energy and momentum conservation as constraints. The quality of fit for each hypothesis is

expressed in terms of the chi-squared probability and a "helix fit" error for each track, which is essentially a measure of the scatter of the digitised points around the fitted helical track. Events which failed during the reconstruction were remeasured. If more than one hypothesis fitted a given event, the program JUDGE<sup>(2)</sup> was used to try and resolve the situation. The program uses information concerning each fit, together with the track ionizations measured by the HPD to identify the most likely hypothesis for the event. Events still unresolved were inspected at the scanning table, and truly ambiguous events were recorded as such.

Successful fits were summarised on a Data Summary Tape (DST). The number of events for each main topology on the DST's after beam cuts are given in table (1.1). (An event with I charged outgoing particles from the production vertex, J charged decays and K neutral decays is assigned the topology IJK).

### 1.3 Beam calibration and cross-section normalisation

The average beam momentum at each momentum setting was determined from four constraint (4C) kinematic fits to the  $\tau$  decays ( $K^- \rightarrow \pi^+ \pi^- \pi^-$ ). The beam momentum used for kinematic fitting was a weighted mean of this average momentum and the measured momentum for the event. Appropriate cuts were applied to the position and direction of the beam track for each event on the DST's, including  $\tau$  decays, to ensure a well defined beam at each momentum setting. Fig.(1.1) shows the beam momentum distribution at the primary vertex for  $\tau$  decays. It can be seen that there is a significant overlap between the momentum ranges spanned by adjacent momentum settings due to energy loss by ionization as the beam traverses the chamber. Thus data from different momentum settings were merged and binned according to the fitted beam momentum at the primary vertex. The momentum intervals for the  $\tau$  decays are shown as arrows in

fig.(1.1).

The definition of the cross-section for reaction R is given by:-

$$\sigma_R = \frac{N(R)}{L \left(\frac{A}{M}\right) \rho} \quad 1.1$$

where  $N(R)$  is the number of reactions R;  $L$  is the total pathlength of the incident particles;  $A$  is Avogadro's number =  $6.022 \times 10^{23} \text{ mole}^{-1}$ ;  $M$  is the atomic weight of hydrogen; and  $\rho$  is the density of the target.

The total pathlength for  $K^-$ 's can be determined by the number of decays into any one decay mode:-

$$N_D = \frac{L}{\tau c T} f \quad 1.2$$

where  $\tau = \frac{P_K}{m_K}$ ,  $T$  is the mean life and  $f$  the branching fraction of the  $K^-$  into that decay mode.

The pathlength was calculated from the number of successfully fitted  $\tau$  decays corrected for scanning and kinematical reconstruction losses. The density of hydrogen in the chamber,  $\rho$ , was taken as  $0.0620 \text{ g. cm.}^{-3}$  corresponding to the operating conditions of the chamber. Measurements of the range of a sample of 100 muons from stopping pions confirmed this result. With  $T$  taken as  $1.237 \times 10^{-8}$  sec. and  $f$  as  $0.0558^{(3)}$  the microbarn equivalent (events per microbarn) for each momentum interval is given by:-

$$\mu = (\text{number of } \tau \text{ decays}) \times P_K \times 5.024 \times 10^{-4} \quad 1.3$$

where  $P_K$  is the average  $K^-$  momentum in GeV/c for the interval. The values are given in table (1.2), together with the number of  $\tau$ 's before and after corrections.

This normalisation was checked by a measurement of the total beam track length at the first, sixth and eleventh momentum settings. The beam contamination was also determined at these settings from a delta ray count. The number of delta rays with a radius greater than that

possible from a given incident  $K^-$  momentum were counted. The contamination was found to vary from 8% at the highest momentum to 28% at the lowest. The small number of fits to the reaction  $\pi^- p \rightarrow K^+ \Sigma^-$  and the absence of fits to the reaction  $\pi^- p \rightarrow K^0 \Lambda$  indicated that the pion contribution was less than 2% at all momenta, decreasing to less than  $\frac{1}{2}$ % at the highest momentum. Hence, the contamination was predominantly muons.

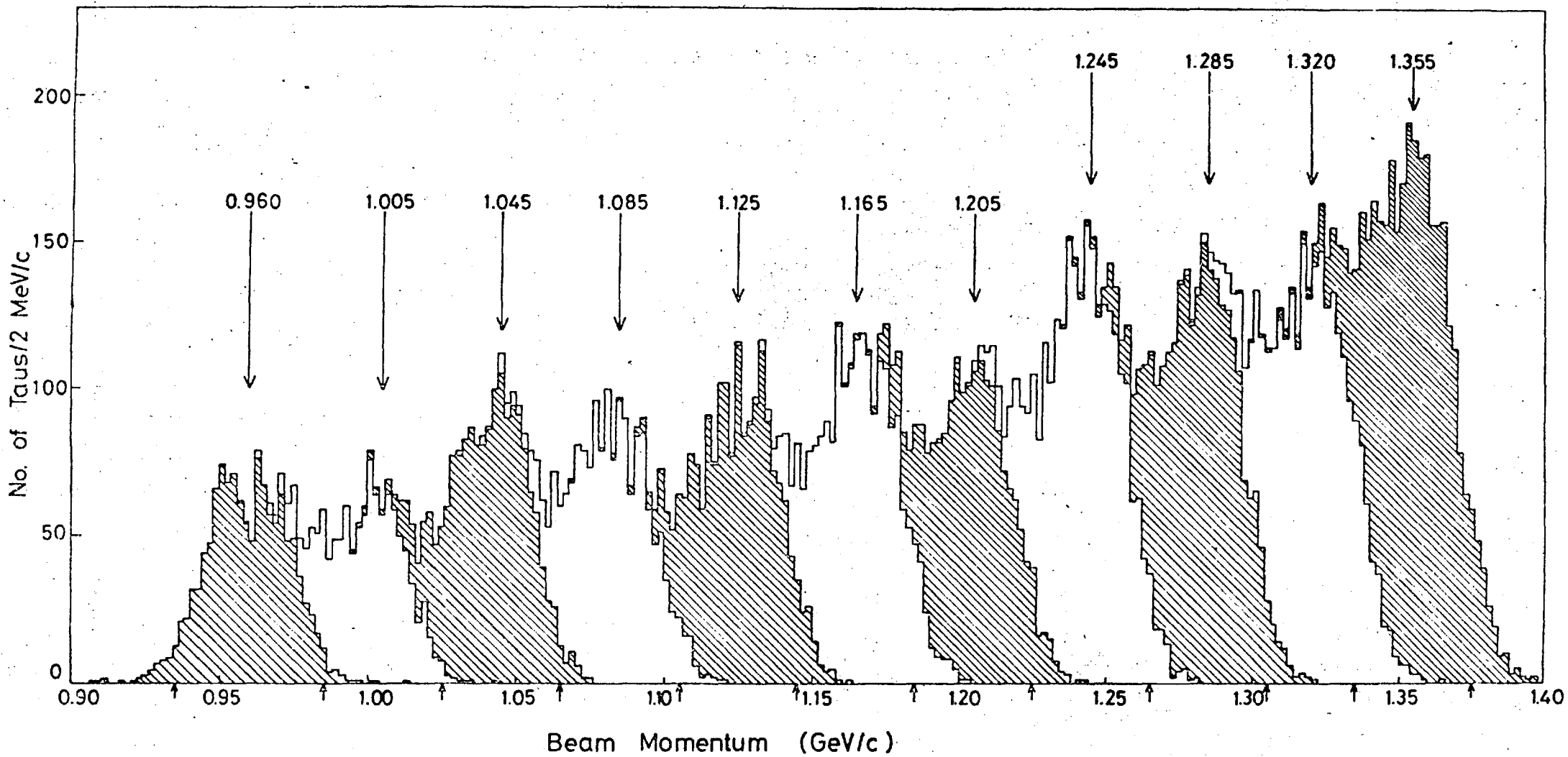
\* \* \* \* \*

Table(1.1)      Number of Events of the Main Topologies  
After Beam Cuts

Topology	Number of Events
001	56786
200	253477
210	58546
201	46750
300	22617

Table (1.2)      Microbarn Equivalents

Average Beam Momentum GeV/c	Centre of Mass Energy GeV	Number of Taus (after beam cuts)	Corrected Total Number of Taus	Number of Events / Microbarn
0.960	1.775	1340	1517 $\pm$ 45	0.732 $\pm$ 0.022
1.005	1.796	1134	1250 $\pm$ 39	0.631 $\pm$ 0.020
1.045	1.815	1617	1857 $\pm$ 50	0.975 $\pm$ 0.026
1.085	1.833	1525	1750 $\pm$ 49	0.954 $\pm$ 0.027
1.125	1.852	1702	1870 $\pm$ 48	1.057 $\pm$ 0.027
1.165	1.870	1970	2268 $\pm$ 56	1.327 $\pm$ 0.033
1.205	1.889	1952	2262 $\pm$ 56	1.369 $\pm$ 0.034
1.245	1.907	2483	2793 $\pm$ 60	1.747 $\pm$ 0.038
1.285	1.925	2306	2948 $\pm$ 63	1.903 $\pm$ 0.041
1.320	1.941	2088	2448 $\pm$ 58	1.624 $\pm$ 0.038
1.355	1.957	2974	3419 $\pm$ 69	2.328 $\pm$ 0.047



2.1 Introduction

To evaluate the cross-section for a particular final state such as the  $\bar{K}N\pi$  system, several weighting factors have to be applied to each event of the relevant hypothesis, to account for the corrections required at each stage of data reduction. These factors can be divided into two main classes. The first is for events missed at the scanning stage, or lost during the measuring procedure. The total effect before correction is to reduce the final accepted sample, and hence the cross-section. The second factor is concerned with the treatment of ambiguities between two or more hypotheses that fit the same event. Most ambiguities can be resolved by the JUDGE choicing program mentioned in the previous chapter, using the ionization information and helix fit errors of the particle tracks. The rest are treated external to the data reduction programs, and a brief description is given in this chapter.

With knowledge of the microbarn equivalent for the experiment at each energy, the final weighted sample of  $\bar{K}N\pi$  events can be converted into channel cross-sections for the three  $\bar{K}N\pi$  channels:-

$$K^-p \rightarrow K^-n\pi^+ \quad (1)$$

$$\bar{K}^0p\pi^- \quad (2) \quad 2.1$$

$$K^-p\pi^0 \quad (3)$$

The procedure taken to extract these cross-sections is described in this chapter, together with an estimation of the mass and width of the  $\Lambda(1520)$  resonance seen in the  $(K^-p)$  system of channel (3).

2.2 Resolution of Ambiguities

The procedure is fully described in ref.(4), and a brief description is given here for the main ambiguities.

In all three channels the multineutral hypotheses were not considered on the grounds that they were highly unlikely in the energy region of

this experiment.

a)  $K^- p \pi^0$

For topology 200, the vast majority of ambiguous events were with the  $\bar{K}^0 p \pi^-$  and  $\pi^- p \pi^0$  ( $\Sigma^+$  decaying in line to  $p \pi^0$ ) hypotheses. These events were about 2% of the total. From a study of the scatter plot for the  $\chi^2$  probabilities of two hypotheses, a decision was taken to prefer a fit if it had a probability greater than three times the other. For the rest of the events, both fits were taken with weights calculated from the ratio of the ambiguous events already assigned to the two hypotheses. These weights were:-  $K^- p \pi^0 / \bar{K}^0 p \pi^- = 0.70/0.30$  and  $K^- p \pi^0 / \pi^- p \pi^0 (\Sigma^+) = 0.19/0.81$ .

For topology 210, 2% of events were ambiguous with the  $\Sigma^- \pi^+ \pi^0$ ,  $K^- n \pi^+$  and  $\bar{K}^0 p \pi^-$  hypotheses. These events were rejected.

b)  $K^- n \pi^+$

For topology 200, 9% of events were ambiguous with other final states. Of these, 93% were ambiguous with  $\Lambda \pi^+ \pi^-$ . On making probability cuts as with  $K^- p \pi^0$ , the weights  $K^- n \pi^+ / \Lambda \pi^+ \pi^- = 0.73/0.27$  were assigned to these events.

For topology 210, the main ambiguity was with  $\Sigma^- \pi^0 \pi^+$ , being 20% of the total number of events. A decay time examination of the negative track suggested that all these events were  $\Sigma^-$ 's, and were subsequently rejected.

c)  $\bar{K}^0 p \pi^-$

For topology 200, 2% of events were ambiguous with mainly  $K^- p \pi^0$  and  $\pi^- p \pi^0$  ( $\pi$  incident). In the former case both fits were taken with the weights given in section (a). In the latter case the  $\pi$  incident fit was rejected.

The ambiguities within the 201 topology were completely negligible,

as expected for a 4-C fit at the production vertex.

For the 400 topology (short  $\bar{K}^0$  decay), 15% were ambiguous with  $\Lambda \pi^+ \pi^-$ . The ratio of  $\chi^2$  probabilities suggested that these were mainly  $\Lambda \pi^+ \pi^-$  events and they were subsequently rejected.

### 2.3 Scanning and Throughput efficiencies.

The scanner will miss valid events for various reasons on a first scan through the film. This will reduce the final accepted sample unless some weight is applied to account for this loss. The solution is to scan part of the film a second time, and the discrepancies between the two scans resolved by a third scan. This was carried out for about a quarter of the film. The rest were single scanned.

Consider a sub-sample of double-scanned events. Let  $n_1$  be the number found in scan 1 only,  $n_2$  for scan 2 only, and let  $n_{12}$  be the number of different events found in the two scans. From these, one gets the scanning efficiencies:-

$$\text{Double-Scan } \epsilon_D = \frac{n_{12} (n_1 + n_2 - n_{12})}{n_1 n_2}$$

2.2

$$\text{Scan 1 } \epsilon_1 = \frac{n_{12}}{n_2} \quad \text{Scan 2 } \epsilon_2 = \frac{n_{12}}{n_1}$$

So, in evaluating cross-sections, one has to split the contributing sample into two classes - one of events coming from the double scanned part of the film, and the second of events coming from the single scanned part of the film. The scanning efficiency weights for the two parts are respectively  $\frac{1}{\epsilon_D}$  and  $\frac{1}{\epsilon_1}$ . The scanning efficiencies were obtained separately for each topology and generally for each final state.

Not all events of a given topology found by the scanner get onto the DST. Some are unmeasurable (e.g. a scatter close to the vertex)

and others are lost during the measuring procedure, while others fail the geometry or kinematics programs. This loss is corrected by a throughput efficiency weight. The Master-List contains all events that were found in the scan, and the DST contains all events that passed successfully through the data processing. If  $N_T(1)$  is total number of events found in the single scanned part of the film, and  $N_T(2)$  that in the double scanned part, with  $N_D(1)$  and  $N_D(2)$  the corresponding numbers on the DST, then the throughput efficiencies are respectively  $N_D(1)/N_T(1)$  and  $N_D(2)/N_T(2)$ . The inverse of these numbers are the weights to be applied to the events.

The throughput efficiencies were obtained separately for each topology, and for elastic and inelastic events separately, and in the case of 210 type topologies, for  $\Sigma$  and non- $\Sigma$  type events separately. In the latter case this was due to the fact that  $\Sigma$  type events failed to give a successful kinematic fit more often than non- $\Sigma$  events during the first measure. For events with seen  $V^0$ 's, the  $\bar{K}^0$  and  $\Lambda$  events were also assigned separate throughput efficiencies. The throughput efficiencies used for the  $\bar{K}N\pi$  channels are given in table (2.1). The following sections deal with the corrections peculiar to each of the three  $\bar{K}N\pi$  channels.

#### 2.4 $\bar{K}^- p \pi^0$

It was thought that losses would occur in the 210 topology for short decays. This was checked by studying the distribution of projected decay length. As shown in fig.(2.1), there was found to be a negligible loss for short decays. This was confirmed by taking several cuts on the projected decay length and weighting each of the remaining 210 events by the factor  $e^{-l/l_1}$ , where  $l_1 = l_{min}^{proj}/\cos\lambda$ ,  $\lambda$  being the dip of the track with respect to the x-y plane of the bubble chamber, and  $l_{min}^{proj}$  the projected length cut-off.  $L = \frac{p}{m_k} c\tau$ , where  $\tau$  is the proper decay

time of the  $K^-$  (3) and  $P$  is its lab. momentum for the event. Fig.(2.2) shows a plot of weighted number of events versus projected length cut-off. It is seen that no dip occurs at short lengths. Thus no cut-off was taken in this channel. The slope seen in the plot is due to long decays being recorded as 200's rather than 210's and hence lost from the sample.

Scanning efficiency in this channel was assumed to be a function of the range of the proton. Short proton tracks were expected to be less easily seen than long ones. To determine the efficiency as a function of proton length would be impractical due to lack of good statistics in this channel. Thus the results of a similar determination in the elastic channel<sup>(5)</sup> were used and are shown in table (2.2a). They are independent of topology and beam momentum.

A throughput efficiency weight was applied separately for 200 and 210 topologies as mentioned in the previous section.

### 2.5 $K^- n \pi^+$

For the 210 topology, ionization information cannot cleanly separate the  $K^-$  decay events from the  $\Sigma^-$  decay events. As already mentioned, the ambiguous events were assigned the  $\Sigma^-$  hypothesis in preference to  $K^-$  from a study of the proper lifetime distribution. Thus losses in this distribution will be more severe than in the  $K^- p \pi^0$  case.

Fig.(2.3) shows the proper time distribution,  $c\tau$ , for topology 210 events. Between 6cm. and 30cm. the expected  $e^{-\frac{c\tau}{370.8}}$  distribution is seen. Above 30cm there is the usual loss due to long decays recorded as 200's rather than 210's. Below 6cm the distribution shows a steeper slope than that expected for  $K^-$  decays, well before losses due to short length decays occur. This is a clear indication of contamination from possible  $\Sigma^-$  events that have failed to fit as such, and have thus been classed as  $K^-$  events. The much shorter proper lifetime of  $\Sigma^-$ 's produces the

sharper slope in the proper time distribution. So events with  $c\tau < 6\text{cm}$  have been removed and the rest of the events in this channel (200's and 210's) weighted up by the factor  $e^{\frac{6.0}{370.8}} = 1.0163$ .

A cut in the proper time distribution is usually less desirable than a cut in the projected length, since the latter distribution itself records directly the scanning loss for short decays. In the case of this channel, however, the presence of  $\Sigma^-$  events can only be singled out in a proper time distribution, and so it is to be preferred. It must be noted, however, that the removal of  $K^-$ 's of short life will produce a loss of events not necessarily confined to the short decays, since high momentum  $K^-$ 's will sometimes have a short proper lifetime, but decay some distance from the production vertex.

No systematic dependence of the scanning efficiency on any single physical variable was observed in this channel. The overall efficiencies for 200's and 210's were calculated in the normal way and the weights are given in table (2.2b). The throughput efficiency was applied as for  $K^-p\pi^0$ .

## 2.6 $\bar{K}^0 p \pi^-$

The topologies listed in table (2.3) with the number of events involved, contribute to this channel. Two important results can be extracted from this channel with different event weightings for each.

### a) $K_S^0$ lifetime

This value can be obtained using the 201 and 211 samples of seen  $\bar{K}^0$ 's. For this purpose the following events were used.

i)  $\bar{K}^0 \rightarrow \pi^+ \pi^-$  i.e.  $K_S^0$  decays.

ii) Fig.(2.4) shows the distribution of projected decay length of the  $\bar{K}^0$ . A loss is observed for very short decays. The weighted total number of events as a function of projected length cut appears to

stabilize to a maximum at around 3.0mm. for the minimum projected length as shown in fig.(2.5) and around 8.0cm. for the maximum projected length. Events within these limits were used.

iii) Events with the  $V^0$  decay vertex within the decay volume defined by the limits  $-27.0 < x < 106.0$ ,  $-53.0 < y < -6.0$ ,  $-40.0 < z < -10.0$  for the  $x, y, z$  coordinates of the bubble chamber.

The  $K_S^0$  lifetime was determined by maximizing the likelihood function:-

$$h = \prod_{i=1}^N \frac{1}{\tau} \frac{e^{-\frac{[t(i) - t_c(i)]}{\tau}}}{1 - e^{-\frac{[\tau(i) - t_c(i)]}{\tau}}} \quad 2.3$$

where  $t_c(i)$  and  $\tau(i)$  are respectively the time limits corresponding to the minimum and maximum (or decay volume cut) projected length cuts for the  $i^{\text{th}}$  event. The function is simply  $e^{-\frac{t(i)}{\tau}}$  correctly normalized between these limits. The value of  $W = -\log h$  was a minimum when  $\tau = 0.891 \pm 0.017 \times 10^{-10}$  sec. This should be compared with the world average of  $0.893 \times 10^{-10}$  sec. (3)

b)  $K_E^0 \rightarrow \pi^+ \pi^-$  branching fraction

This value can be checked by using the samples of seen and unseen  $\bar{K}^0$ 's, after correction for losses and removal of any systematic biases have been made. These are described below.

1) Seen  $\bar{K}^0$ 's

Events with projected decay length smaller than 3.0mm. or greater than 8.0cm, or with the decay vertex outside the decay volume were removed, and the rest weighted up by:-

$$W_L^i = \frac{1}{e^{-\frac{l_0}{L}} - e^{-\frac{l_p}{L}}} \quad 2.4$$

where  $l_0$  and  $l_p$  are the true limits for event  $i$ , and  $L$  is its mean decay length in the lab.  $l_p$  was determined by the 8cm cut-off or the potential length to the edge of the decay volume, whichever was the shorter

for the event.

Fig.(2.6) shows the distribution of the cosine of the decay- $\pi$  angle with respect to the  $\bar{K}^0$  direction in the rest frame of the latter. It is expected to be uniform, but in fact shows a loss of events for  $|\cos \theta| \gg 0.96$ , corresponding to possible short decay tracks where the  $V^0$  would be missed by the scanner, and the event classed as a 200 topology rather than 201. Events in this region were assigned a weight so as to preserve uniformity in the  $\cos \theta$  distribution.

$V^0$ 's are systematically lost when the decay plane of the  $\bar{K}^0$  is in the line of sight of the cameras. Consider the following system of axes:-

$$\underline{z} = \hat{K}^0 \quad \underline{y} = \frac{\hat{z}' \times \hat{K}^0}{|\hat{z}' \times \hat{K}^0|} \quad \underline{x} = \frac{\underline{y} \times \hat{K}^0}{|\underline{y} \times \hat{K}^0|} \quad 2.5$$

where  $z'$  is the chamber z-axis.

The azimuthal angle  $\phi$  of the decay plane is then given by:-

$$\cos \phi = \hat{n} \cdot \underline{x} \quad \sin \phi = \hat{n} \cdot \underline{y} \quad 2.6$$

where  $\hat{n}$  is the normal to the decay plane.

Fig.(2.7) shows this  $\phi$  distribution, and a clear loss of events is seen around  $|\phi| = \frac{\pi}{2}$ . Events in the range  $0.4\pi \leq |\phi| \leq 0.6\pi$  have been weighted up to preserve uniformity in the distribution.

The throughput efficiencies of 201 events were calculated separately for  $\Lambda$  and  $\bar{K}^0$  final states. This was because the two values were found to differ to a large degree, and the fact that  $\Lambda$  events dominated over  $\bar{K}^0$  would mean that the  $\bar{K}^0$  throughput efficiency would tend to follow that of the  $\Lambda$ . The 211 sample was too small to make any difference and average values were used.

Scanning efficiencies were calculated for each of the two topologies and applied in the normal way. They are given in table (2.2c).

## ii) Unseen $\bar{K}^0$ 's

The probability distribution for the (1-C fit) topology 200 events

is shown in fig.(2.8) and is seen to be remarkably uniform except for a peak below 1%. Events with probability below 1% were removed and the remainder weighted up by the appropriate factor. This procedure was also carried out for the other two channels (see figs. (2.9) and (2.10)).

The missing mass-squared to the  $p\pi^-$  distribution was found to be Gaussian around the  $\bar{K}^0$  mass and no missing mass cut was thought to be necessary. This was also found to be true in the other two channels.

The inelastic 200 throughput efficiency was applied to the 200 topology, and the 210 (Non  $\Sigma$ ) efficiency applied to the 210's.

No systematic effects on the scanning efficiency as a function of any physical variable was found, and average values were calculated and applied to the two topologies. They are given in table (2.2c).

For the purpose of calculating the  $K_S^0 \rightarrow \pi^+\pi^-$  branching fraction, it was assumed that all scanning, maximum projected length cut,  $\cos \theta$  and  $\phi$  losses in the seen  $\bar{K}^0$  sample ended up in the unseen sample, and the latter was weighted down accordingly.

The branching fraction is calculated as follows:- If  $x$  is the final weighted seen  $\bar{K}^0$  sample (i.e. the total number of events where  $K_S^0 \rightarrow \pi^+\pi^-$ ) and  $y$  is the final weighted unseen  $K^0$  sample, then the total number of  $K_S^0$  events is  $\frac{x+y}{2}$  (the other half being  $K_L^0$ ). The branching fraction of  $K_S^0 \rightarrow \pi^+\pi^-$  is then  $\frac{2x}{x+y}$ . The final value obtained from all events combined was  $0.655 \pm 0.011$ , which should be compared with the world average of 0.687. (3)

### C) The Cross-Section

It is expected that the inclusion of topologies 400 and 410, where the  $V^0$  decay products appear to come from the primary vertex, should compensate for the loss of close  $V^0$ 's in the 201/211 sample mentioned above. To check this, the weighted total of 201/211 events with a minimum projected length cut of 3.0mm. was compared with the 201/211 sample with no length cut plus the 400/410 sample combined, with corrections

made for scanning and throughput losses. The numbers of events were 6001 and 6024 respectively, thus confirming the expectation.

The seen  $\bar{K}^0$  sample was found to have a clear depletion of low momentum  $\bar{K}^0$ 's ( $P_{\bar{K}^0} \lesssim 150$  MeV/c) which could not be compensated by applying the cuts described earlier and weighting appropriately. However, the 400/410  $\bar{K}^0$  momentum was found to be strongly biased towards the low momentum  $\bar{K}^0$ 's. With no minimum projected length cut and the 400/410 sample included, the  $\bar{K}^0$  momentum distribution was found to be consistent with that of the 200/210 sample. This procedure is illustrated in figs.(2.11) and (2.12).

For the above reasons the minimum projected length cut was not applied, and the 400/410 sample was included for cross-section and analysis purposes. The other cuts described earlier were also used, together with the relevant scanning and throughput efficiencies to obtain the final weighted sample of  $\bar{K}^0 p \pi^-$  events.

## 2.7 Channel Cross-Sections

Table (2.4) lists the total number of weighted events at each energy for the three channels. The errors on these values are purely statistical and are calculated from the formula:-

$$\Delta N = \sqrt{\sum_{i=1}^N W_i^2} \quad 2.7$$

where  $W_i$  is the weight assigned to the  $i^{\text{th}}$  event of the sample. To convert these numbers to cross-sections, the microbarn equivalent described in the previous chapter is used. The cross-section for a sample is then:-

$$\sigma = \frac{\sum_{i=1}^N W_i}{\mu} \quad 2.8$$

where  $\mu$  = events/microbarn

and the error is given by:-

$$\Delta \sigma = \frac{\sum W_i^2}{\mu^2} + \frac{(\sum W_i)^2 (\Delta \mu)^2}{\mu^4} \quad 2.9$$

where  $\Delta\mu$  is the error on the microbarn equivalent. The cross-sections for each channel and at each energy are listed in table (2.4) and plotted in fig.(2.13).

### 2.8 Estimation of the $\Lambda(1520)$ parameters

As described in the next chapter, the  $\Lambda(1520)$  resonance is produced very strongly in the  $(K^-p)$  system of the  $K^-p\pi^0$  channel. As such, an estimation of its mass and width is well worth carrying out with the abundant data of this channel. However, due to its narrow width, it is expected that the experimental resolution as a result of the errors on track variables, will broaden the experimentally observed width to some degree. Thus a resolution function should ideally be folded into the Breit-Wigner function describing the resonance shape when fitting the experimental distribution.

The data used in the fit was the effective mass region of the  $(K^-p)$  system between 1.470 and 1.570 GeV for all energies combined, i.e. about three full widths on either side of the resonance peak.

A function was set up in which a simple non-relativistic Breit-Wigner and a Gaussian resolution function were folded together numerically by computer, and to which was added a background term linear in effective mass, i.e.:-

$$F(m) = \left[ \int_0^\infty \frac{\Gamma_0/2\pi}{(m'-m_0)^2 + \Gamma_0^2/4} \times \frac{1}{\sqrt{2\pi}\sigma} e^{-\frac{(m'-m)^2}{2\sigma^2}} dm' \right] + a_0 + a_1 M \quad 2.10$$

where  $m_0, \Gamma_0$  are the  $\Lambda(1520)$  mass and width parameters,  $\sigma$  is the width of the resolution function,  $M = \frac{2(m-m_l)}{(m_u-m_l)} - 1$  where  $m_u$  and  $m_l$  are the upper and lower limits of the effective mass region, and  $a_0$  and  $a_1$  are the relative intensities of the background contribution for zeroth and linear orders in mass.

For numerical calculation the term in brackets was integrated between  $m_l$  and  $m_u$  using narrow bin widths. The theoretical number of

events in bin  $i$  is given by:-

$$N_i^{\text{theo}} = \frac{F(m_i) \times (\text{bin width})_i}{\sum_j F(m_j) \times (\text{bin width})_j} \times \text{Total Number of Events} \quad 2.11$$

An overall  $\chi^2$  was set up for 20 bins such that:-

$$\chi^2 = \sum_{i=1}^{20} \left( \frac{N_i^{\text{theo}} - N_i^{\text{expt}}}{\Delta N_i^{\text{expt}}} \right)^2 \quad 2.12$$

where  $\Delta N_i^{\text{expt}}$  is the statistical error on the number of experimental events in bin  $i$  and was made equal to  $\sqrt{N_i^{\text{expt}}}$  assuming Poissonian statistics were valid. This  $\chi^2$  was minimized by computer with respect to the parameters  $m_0, \Gamma_0, \sigma, a_0$  and  $a_1$ . The results of the fit are as follows:-

$$m_0 = 1517.4 \pm 0.8 \text{ MeV}$$

$$\Gamma_0 = 15.9 \pm 2.8 \text{ MeV}$$

$$\sigma = 2.2 \pm 0.5 \text{ MeV}$$

$$\chi_{\text{min}}^2 = 2.1 \text{ for 20 data points}$$

The  $\Lambda(1520)$  parameters are in excellent agreement with the world average values of  $1519 \pm 2$  MeV for mass and  $15 \pm 2$  MeV for width, (3) and the effective-mass resolution in the  $(K^-p)$  system appears to be 2 MeV. The fit to the data is shown in fig.(2.14).

\* \* \* \* \*

Table (2.1)

Throughput Efficiencies

Beam Momentum GeV/c	200 Inelastic		201 $\bar{K}^0$ 's		210 non $\Sigma$ 's		211		400		410	
	S	D	S	D	S	D	S	D	S	D	S	D
0.960	0.820	0.852	0.852	0.787	0.843	0.855	0.673	0.667	0.774	0.727	0.667	0.600
1.005	0.860	0.903	0.884	0.937	0.901	0.916	0.784	0.850	0.743	0.850	0.611	0.938
1.045	0.856	0.853	0.812	0.844	0.888	0.871	0.740	0.649	0.830	0.759	0.817	0.861
1.085	0.857	0.801	0.875	0.842	0.888	0.849	0.782	0.576	0.788	0.840	0.823	0.761
1.125	0.884	0.870	0.883	0.904	0.873	0.885	0.756	0.778	0.806	0.784	0.850	0.886
1.165	0.881	0.886	0.892	0.905	0.890	0.888	0.705	0.658	0.824	0.833	0.853	0.848
1.205	0.862	0.875	0.877	0.898	0.858	0.880	0.731	0.773	0.872	0.811	0.817	0.746
1.245	0.876	0.884	0.882	0.892	0.872	0.861	0.685	0.800	0.826	0.859	0.808	0.805
1.285	0.864	0.885	0.880	0.893	0.862	0.891	0.699	0.736	0.860	0.827	0.793	0.830
1.320	0.871	0.868	0.854	0.846	0.861	0.866	0.753	0.824	0.803	0.856	0.839	0.798
1.355	0.884	0.857	0.876	0.885	0.856	0.858	0.729	0.741	0.804	0.791	0.819	0.797

S = Single Scan

D = Double Scan

Table (2.2)

Scanning Efficienciesa)  $K^- p \pi^0$  Topologies 200/210

Range cm.	Double Scan Efficiency	Single Scan Efficiency
0.0 - 0.25	0.802	0.555
0.25 - 0.5	0.936	0.742
0.5 - 1.0	0.976	0.843
1.0 - 2.0	0.994	0.918
2.0 - 4.0	0.999	0.960
4.0 - 8.0	0.999	0.964
8.0 - 16.0	0.999	0.968
16.0 - 32.0	0.999	0.967
> 32.0	0.999	0.962

b)  $K^- n \pi^+$ 

Topology	Double Scan Efficiency	Single Scan Efficiency
200	0.998	0.956
210	0.999	0.961

c)  $\bar{K}^0 p \pi^-$ 

Topology	Double Scan Efficiency	Single Scan Efficiency
200	0.998	0.960
210	1.000	0.960
201	0.999	0.972
211	1.000	0.974
400	0.985	0.878
410	1.000	0.875

Table (2.3)

Topology	Number of Events (with ambiguity weights)
200	13220
210	263
201	5445
211	71
400	425
410	11

Table 2.4

Channel Cross-Sectionsa)  $\bar{K}^- p \pi^0$ 

Beam Momentum GeV/c	Unweighted Number	Final Weighted Number	Channel Cross-Section mb.
0.960	569	683 $\pm$ 29	0.933 $\pm$ 0.049
1.005	549	609 $\pm$ 27	0.965 $\pm$ 0.052
1.045	929	1080 $\pm$ 36	1.107 $\pm$ 0.047
1.085	879	1029 $\pm$ 35	1.078 $\pm$ 0.048
1.125	1201	1379 $\pm$ 40	1.304 $\pm$ 0.051
1.165	1509	1726 $\pm$ 45	1.301 $\pm$ 0.047
1.205	1552	1782 $\pm$ 46	1.302 $\pm$ 0.047
1.245	1977	2250 $\pm$ 51	1.288 $\pm$ 0.041
1.285	2207	2538 $\pm$ 55	1.334 $\pm$ 0.041
1.320	1689	1925 $\pm$ 48	1.185 $\pm$ 0.040
1.355	2875	3291 $\pm$ 62	1.414 $\pm$ 0.039

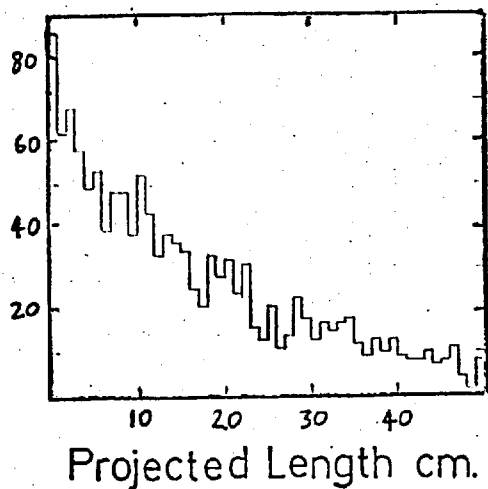
b)  $\bar{K}^- n \pi^+$ 

Beam Momentum GeV/c	Unweighted Number	Final Weighted Number	Channel Cross-Section mb.
0.960	314	372 $\pm$ 22	0.508 $\pm$ 0.033
1.005	363	399 $\pm$ 22	0.633 $\pm$ 0.040
1.045	697	804 $\pm$ 31	0.825 $\pm$ 0.039
1.085	837	981 $\pm$ 35	1.028 $\pm$ 0.047
1.125	1098	1253 $\pm$ 39	1.186 $\pm$ 0.048
1.165	1514	1737 $\pm$ 45	1.309 $\pm$ 0.047
1.205	1833	2106 $\pm$ 50	1.538 $\pm$ 0.053
1.245	2732	3141 $\pm$ 61	1.798 $\pm$ 0.052
1.285	3005	3484 $\pm$ 65	1.831 $\pm$ 0.052
1.320	2745	3182 $\pm$ 62	1.959 $\pm$ 0.060
1.355	4348	5027 $\pm$ 77	2.159 $\pm$ 0.055

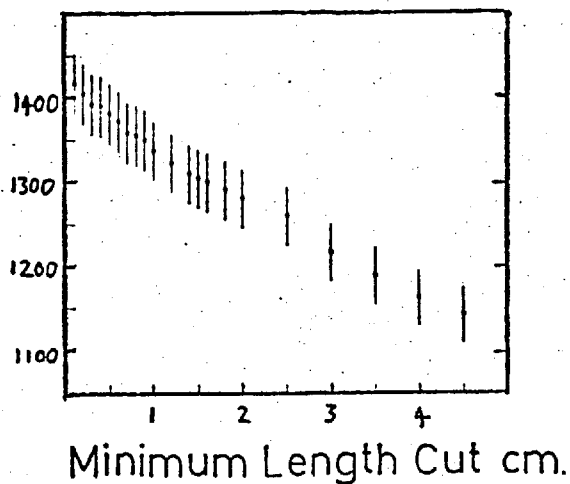
c)  $\bar{K}^0 p \pi^-$ 

Beam Momentum GeV/c	Unweighted Number	Final Weighted Number	Channel Cross-Section mb.
0.960	313	363 $\pm$ 21	0.496 $\pm$ 0.033
1.005	367	414 $\pm$ 22	0.656 $\pm$ 0.041
1.045	776	930 $\pm$ 34	0.954 $\pm$ 0.043
1.085	1019	1196 $\pm$ 39	1.254 $\pm$ 0.054
1.125	1525	1733 $\pm$ 46	1.640 $\pm$ 0.060
1.165	2076	2377 $\pm$ 53	1.791 $\pm$ 0.060
1.205	2152	2481 $\pm$ 55	1.812 $\pm$ 0.060
1.245	2771	3176 $\pm$ 62	1.818 $\pm$ 0.053
1.285	2829	3291 $\pm$ 64	1.729 $\pm$ 0.050
1.320	2319	2677 $\pm$ 58	1.648 $\pm$ 0.052
1.355	3555	4087 $\pm$ 71	1.756 $\pm$ 0.047

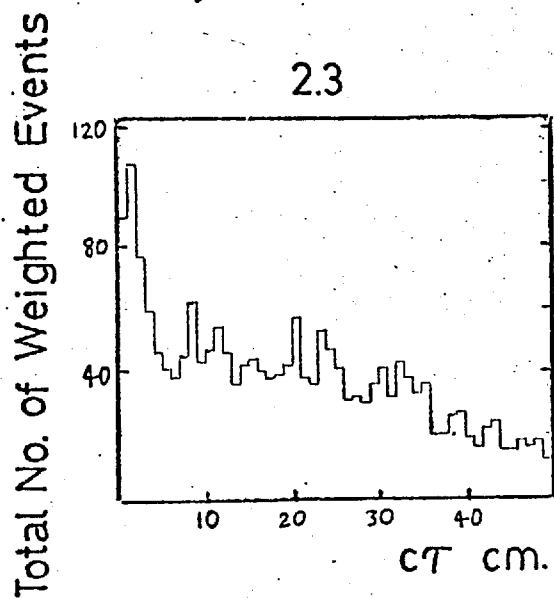
2.1



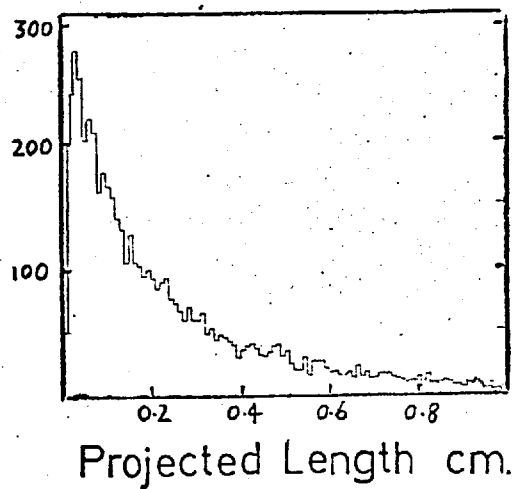
2.2



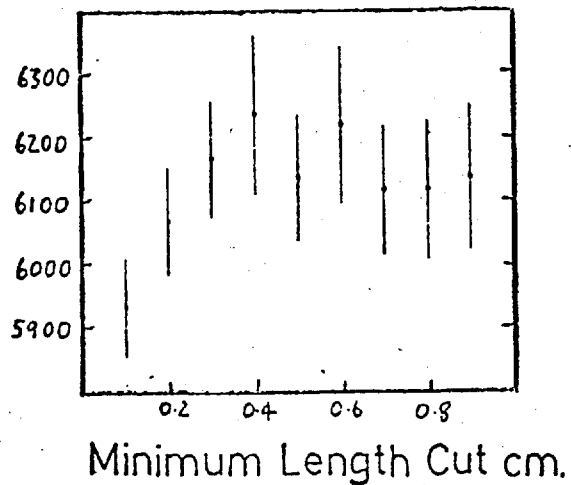
2.3



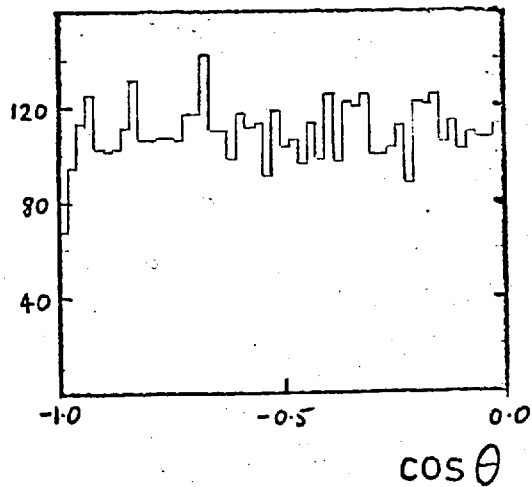
2.4



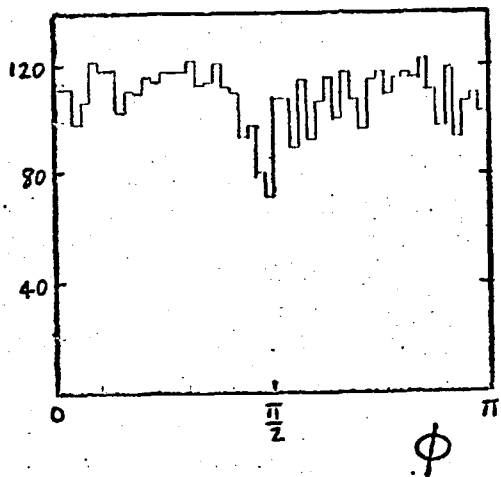
2.5



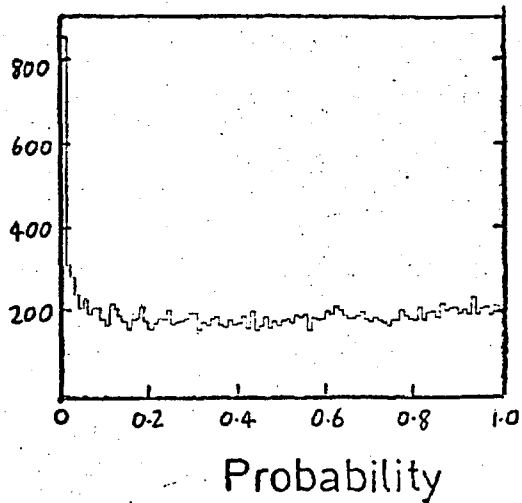
2.6



2.7

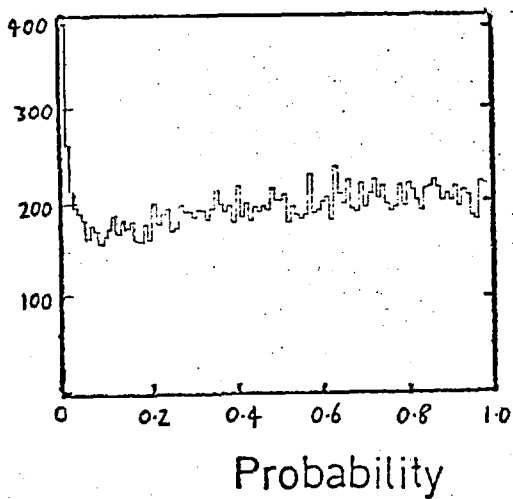


2.8

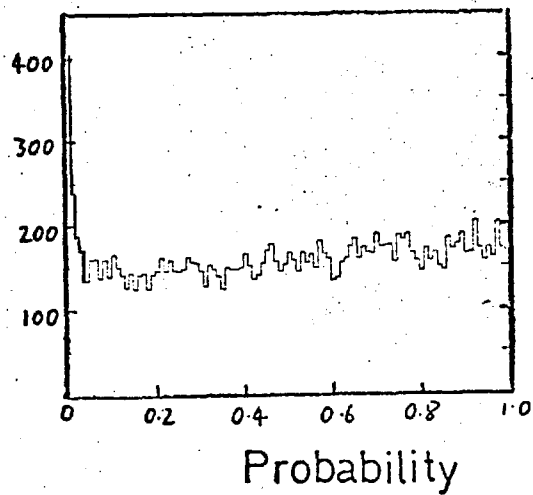


Total No. of Weighted Events

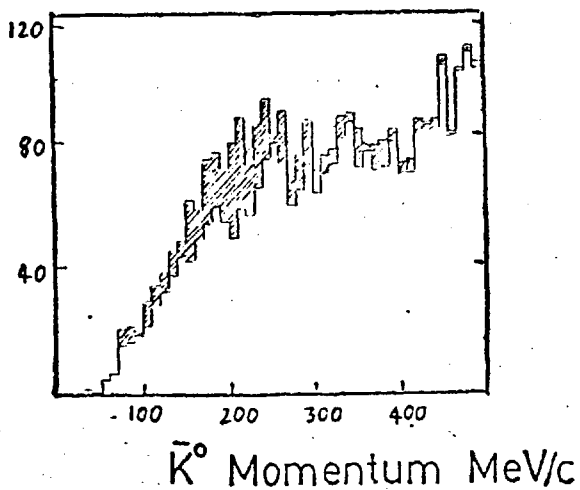
2.9



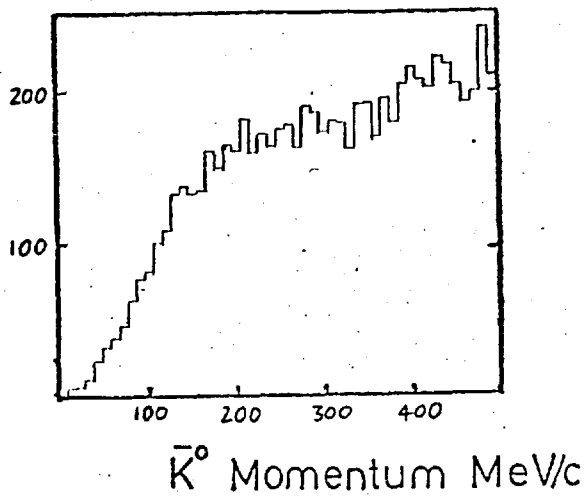
2.10

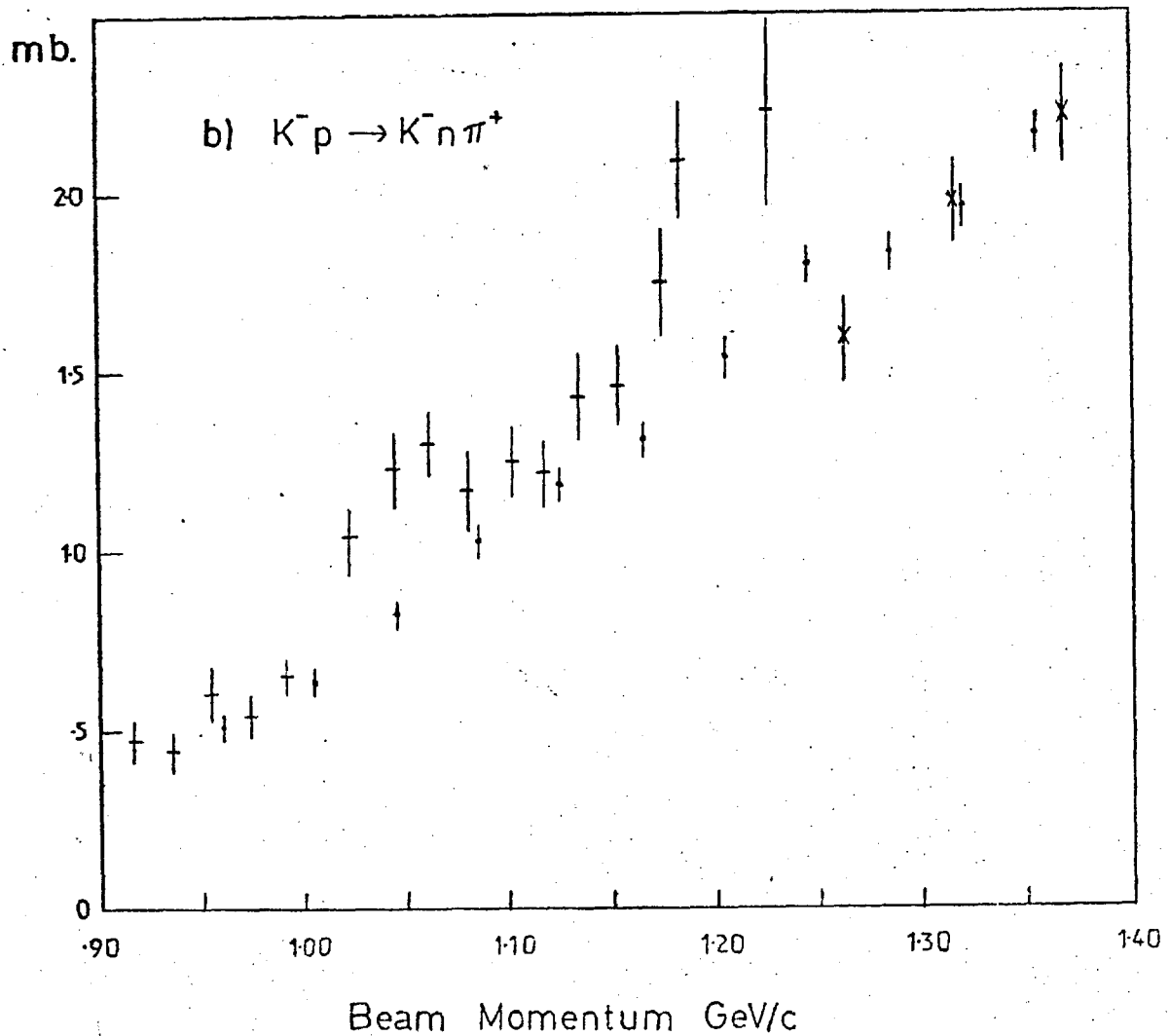
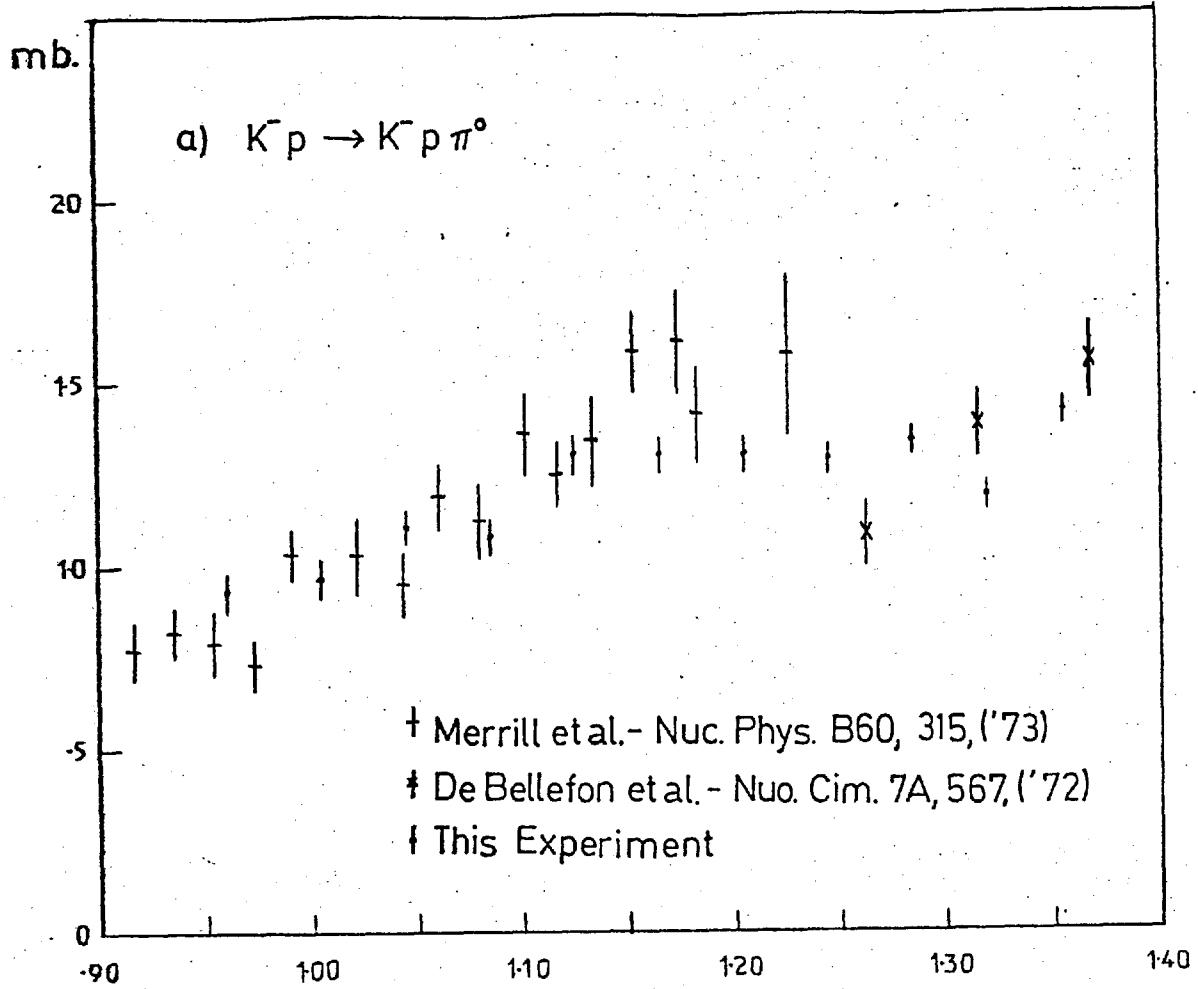


2.11

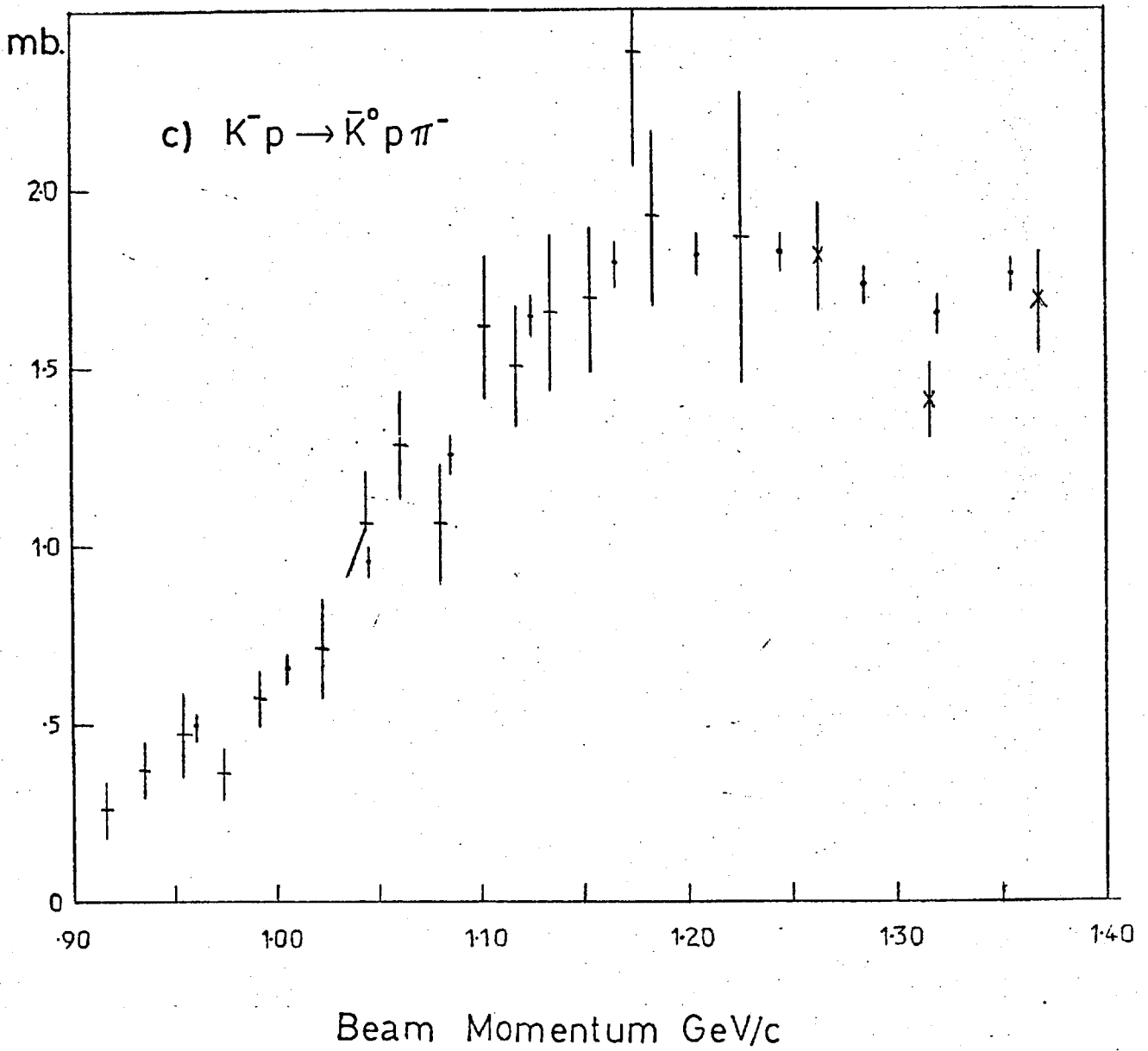


2.12

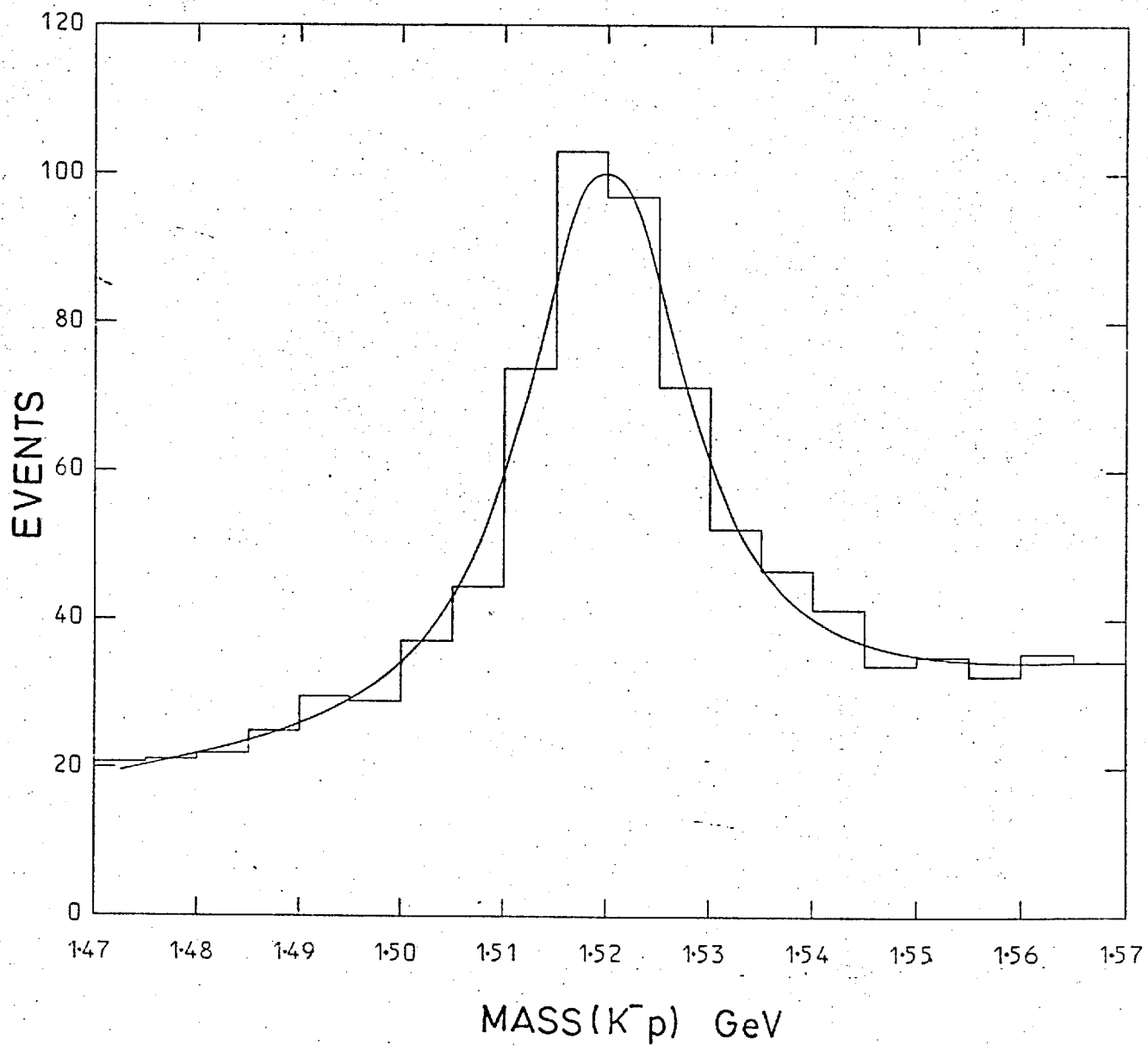




2.13

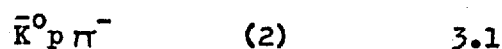
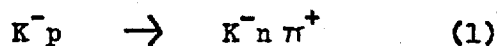


2.14



Chapter 3Dalitz Plot Analysis3.1 Introduction

Dalitz Plots are presented for typical beam momenta in figure (3.1) for the three channels:-



Clear evidence is seen for production of the  $\bar{K}^*(890)$  in the  $(\bar{K}\pi)$  system in all channels, except at the lowest energies which are below its threshold. Strong production of  $\Lambda(1520)$  is also seen in the  $(K^-p)$  system of channel (3). Less obvious is the presence of the  $\Delta(1236)$ , seen clearly only in channel (3). Clebsch-Gordan coefficients predict that the  $\Delta$  should be twice as intense in this channel as in each of the other two. For the  $\bar{K}^*(890)$  the prediction is that it is twice as intense in channel (2) as in channel (3), these being the two decay modes of  $K^{*-}$ . No other structure is visible from the Dalitz Plots except for the presence of an asymmetry along the  $\bar{K}^*$  band. This is most prominent around the threshold energies and is seen in all channels. It occurs around the cross-over region between the  $\bar{K}^*$  and  $\Delta$  and might be thought to be the result of an interference between these resonances. This possibility can, however, be discarded because the  $\Delta$  fraction is too small to produce such a large effect. Furthermore, the effect has also been seen at higher energies where it occurs outside the cross-over region.<sup>(6)</sup> This asymmetry has been attributed to an interference between the  $\bar{K}^*$  and a very wide S-wave  $\bar{K}\pi$  resonance. It is assumed that this is the effect that is being seen in this experiment, and is allowed for in a later stage of the analysis which is now described.

### 3.2 The non-interference model

The preliminary Dalitz Plot analysis used a model which assumed an incoherent mixture of background and resonant contributions. To describe completely a process of the type:-



the amplitude is generally a function of five variables. This number is reduced to four if the target proton is unpolarized as in this experiment. This is because the lack of fixed x,y coordinates for the reaction prevents any dependence upon the azimuthal angle of the final three body plane. Two of the four variables are chosen to be two Dalitz Plot coordinates,  $M_{K\pi}^2$  and  $M_{KN}^2$ . The third is the azimuthal decay angle  $\phi_1$  of the produced resonance,  $i$ , in its helicity frame, for each quasi two body process contributing to the final state. This angle, together with the helicity frame is defined in fig. (3.2). Only one of the three possible  $\phi$  angles is independent. The fourth variable is the production angle  $\theta^*$  of each resonance with respect to the incoming kaon in the centre of mass.

A basic assumption of the model was that the probability density for reaction (3.2) could be factorized into a production part and a decay part. The production part included all the dependence upon production angle, whereas the decay part gave the Dalitz Plot distribution together with the  $\phi$  dependence. This assumption is not strictly true as some correlation does occur and will be dealt with later. The reason for this assumption was to reduce the large number of parameters which would have to be fitted simultaneously if production angular dependence was included in the analysis. The basic Dalitz Plot analysis was therefore an analysis in three variables, the dependence on the fourth being ignored. On extracting each resonance contribution, the production angular dependence could be studied separately for each resonance.

To carry out a fit to the data at each energy and for each channel, the method of maximum likelihood was employed. The probability of a given event,  $l$ , occurring was given by:-

$$P_l(M_{KN}^2, M_{KN}^2, \phi) = \frac{1}{N} \left[ \alpha_{ps}^2 + \sum_i \alpha_i^2 |BW_i(m)|^2 W_i(\cos \theta_i, \phi_i) \right] \quad 3.3$$

where the sum is over all contributing resonances in all three two-body systems.

$\alpha_{ps}$  is the amplitude of the non resonant part of the distribution - background which consists of a phase space contribution plus possibly unresolved resonances.

$\alpha_i$  is the production amplitude of resonance  $i$

$N$  is a normalization factor

$BW_i$  is the Breit-Wigner amplitude of resonance  $i$

$W_i$  is the decay distribution of resonance  $i$  in terms of the helicity decay angles.

The Breit-Wigner function used was the relativistic form given by Jackson:- (7)

$$|BW(m)|^2 = \frac{m_0 \Gamma(m)}{(m_0^2 - m^2)^2 + m_0^2 \Gamma^2(m)} \quad 3.4$$

where  $m_0$  is the mass of the resonance, and  $\Gamma(m)$  is the mass-dependent full width of the form:-

$$\Gamma(m) = \Gamma_0 \left( \frac{q}{q_0} \right)^{2l+1} \frac{\rho(m)}{\rho(m_0)} \quad 3.5$$

where  $\Gamma_0$  is the natural full width;  $q$  is the momentum of the decay particles in the two-body rest frame;  $q_0$  is  $q$  at the resonance mass;

$l$  is the relative orbital angular momentum between the decay particles;

$\rho(m)$  is a slowly varying factor whose form was taken from Jackson. (7)

For the  $\bar{K}^*$  the form  $m^{-1}$  was used. For baryon resonances  $m^{-1}(X^2 + q^2)^{-l}$  was used with  $X=350$  MeV/c.

The decay distributions for the dominant resonances were those given by Deen. (8) For the  $\bar{K}^*$ , the form relevant for a vector meson was used:-

$$W(\cos \theta, \phi) = \frac{3}{4\pi} \left[ \frac{1}{2} \sin^2 \theta - \frac{1}{2} (1 - 3 \cos^2 \theta) \rho_{00} - \sqrt{2} \operatorname{Re} \rho_{10} \sin 2\theta \cos \phi - \rho_{11} \sin^2 \theta \cos 2\phi \right] \quad 3.6$$

For the  $\Delta(1236)$  and  $\Lambda(1520)$ , both spin  $\frac{3}{2}$  particles, the form

$$\begin{aligned} W(\cos \theta, \phi) = & \frac{3}{4\pi} \left[ \frac{1}{2} \left( \frac{1}{3} + \cos^2 \theta \right) + 2 \left( \frac{1}{3} - \cos^2 \theta \right) \rho_{\frac{3}{2}\frac{3}{2}} \right. \\ & \left. - \frac{2}{3} \operatorname{Re} \rho_{\frac{3}{2}\frac{1}{2}} \sin 2\theta \cos \phi - \frac{2}{3} \operatorname{Re} \rho_{\frac{3}{2}-\frac{1}{2}} \sin^2 \theta \cos 2\phi \right] \quad 3.7 \end{aligned}$$

where  $\theta$  is the polar helicity decay angle and is related to the mass-squared variables of the other two-body systems.<sup>(9)</sup> The  $\rho$ 's are the spin density matrix elements which contribute to the decay distribution. They are functions of production angle, but were taken as constants in the following analysis. Their angular dependence was determined later.

For small resonance contributions which were usually required in addition to the above three to fit the data, a decay term of the form:-

$$W(\cos \theta) = \frac{3}{8\pi} \left[ (1 - \beta) + (3\beta - 1) \cos^2 \theta \right] \quad 3.8$$

was used, with  $\beta$  a parameter varying between 0 and 1, determining the shape of the decay distribution.

For the fitting procedure a method had to be devised to impose the positivity conditions<sup>(10)</sup> on the density matrix elements, so as to keep the probability function positive. This was achieved by parameterising the density matrix elements according to the following prescription:-<sup>(11)</sup>

For the  $\bar{K}^*$ :-

$$\begin{aligned} \rho_{00} &= \sin^2 \gamma \\ \rho_{11} &= \frac{1}{2} (1 - \rho_{00}) \cos 2\delta & 0 \leq \delta \leq \frac{\pi}{2} \\ \operatorname{Re} \rho_{10} &= \left[ \frac{1}{2} \rho_{00} (1 - \rho_{00}) \right]^{\frac{1}{2}} \sin \delta \cos \epsilon & 0 \leq \epsilon \leq \pi \end{aligned} \quad 3.9$$

For the  $\Delta$  and  $\Lambda(1520)$ :-

$$\begin{aligned} \rho_{\frac{3}{2}\frac{3}{2}} &= \gamma \cos^2 \delta & 0 \leq \delta \leq \frac{1}{2} \\ \operatorname{Re} \rho_{\frac{3}{2}\frac{1}{2}} &= \frac{1}{2} \gamma \sin 2\delta \cos \epsilon & 0 \leq \delta \leq \frac{\pi}{2} \\ \operatorname{Re} \rho_{\frac{3}{2}-\frac{1}{2}} &= \frac{1}{2} \gamma \sin 2\delta \sin \epsilon & 0 \leq \epsilon \leq 2\pi \end{aligned} \quad 3.10$$

Thus  $\gamma, \delta$  and  $\epsilon$  were the parameters that were fitted, rather than the density matrix elements.

The normalization factor  $N$  in eqn. (3.3) is the integral of the bracketed term over all the three variable space. For the  $\phi$  variable the integral is a trivial matter. To calculate the integral over the Dalitz Plot a numerical computation was employed for each separate, parameter-independent term. This consisted of dividing the rectangle defined by the boundary limits of the Dalitz Plot into a 50 x 50 grid of rectangular elements. This was done at the central value of each of a set of narrow bins spread out over the finite centre of mass energy region of the data in question. For each centre of mass energy point, the area of each element within the Dalitz Plot boundary was weighted by the value of each separate term at the centre of that element. Those elements overlapping the boundary curve were divided into yet smaller elements with those outside the curve being discarded. For each separate term, therefore, a sum over all elements was made with the relevant weight, and at each centre of mass energy point, to obtain the numerical value of the integral of that term for each energy bin. Thus each event had a normalization factor calculated very near its own centre of mass energy.

A negative log-likelihood was then set up defined by:-

$$L = - \sum_i^n w_i \log_e p_i \quad \text{where } w_i \text{ is the weight assigned to the } i^{\text{th}} \text{ event.} \quad 3.11$$

It was this  $L$  that was minimized with respect to the following parameters: i) the production amplitudes of each contribution, including background,  $\alpha$  ; ii) the density matrix element parameters,  $\gamma, \delta$  and  $\epsilon$  ; iii) the decay parameters for small resonance contributions,  $\beta$  . The CERN minimizing program MINUIT<sup>(12)</sup> was used for this purpose.

### 3.3 The non-interference fits

The channel  $K^- n \pi^+$  was analysed first, being a simple channel with strong  $\bar{K}^*$  production, and minimal  $\Delta$  production. Initial runs were made at the highest energy containing about 4000 events. Nominal values of mass and width for the  $\bar{K}^*$  and  $\Delta$  were used, (3) and no other contribution was included at first. The result was a very bad fit to the  $\bar{K}^*$  where the experimental mass appeared to lie much lower than the input value of 896 MeV. On repeating the run at lower energies the same effect occurred. The  $\bar{K}^*$  peak was fitted well, but the wings of the resonance showed a skew towards the lower mass end of the distribution. Thus an asymmetric resonant shape was present. Several other workers (13) have seen this effect for resonances near threshold and have attributed the effect to production angular momentum barrier factors between the resonance and the third particle. (See figure (3.3)). This has the effect of suppressing the decay amplitude at small centre of mass momentum to a degree depending upon the relative orbital angular momentum,  $l$ , of the system. Bland et al. assume P-wave dominance and use, for  $\bar{K}^*$  production, the Blatt and Weisskopf (14) form for the barrier factor:-

$$\frac{q^2}{q^2 + \frac{1}{2} m_\omega^2} \quad 3.12$$

where  $m_\omega$  is the mass of the  $\omega$  meson, thought to dominate the t-channel exchange in their reaction;  $q$  is the centre of mass momentum of the  $\bar{K}^* N$  system. However it is undesirable in a formation study to assume a single dominant outgoing  $l$  value when several may be present; a more correct form being a sum of terms for each  $l$  value with amplitudes proportional to the relative intensities of these waves. Since a partial wave analysis of the  $\bar{K}^* N$  system had not yet been carried out, these relative intensities were not known.

The solution adopted, therefore, was to reduce the mass of the  $\bar{K}^*$  at each energy until the best fit to the asymmetric Breit-Wigner was obtained. Since the barrier effect is most severe near threshold, this mass depression was larger at the lower energies. Reasonable fits to the  $\bar{K}^*$  were then obtained. The  $\bar{K}^*$  mass values used are listed in table (3.1).

An excess of events was seen at the high end of the  $K^-n$  effective mass distribution. Being a wide effect it was attributed to the  $\Sigma(1765)$ , subsequent inclusion of which improved the fit.

The asymmetric band of the  $\bar{K}^*$  was also seen producing an enhancement at the high end of the  $K^-n$  effective mass and a depletion at the lower end. This appeared in the  $n\pi$  system as an effective shift of the  $\Delta$  mass to lower energies. In neither case could the effect be accounted for with the present model. At the higher energies the  $K^-n$  problem could be accounted for by including the narrow  $\Sigma(1670)$  in the model. However as the energy decreased the enhancement moved further and further away from 1670 MeV until the resonance could not fit it at all. Furthermore, the effect in the  $n\pi$  system was increasing as the energy decreased. Assuming that the  $\bar{K}^*$  decay asymmetry was due to an interference effect, and because the model currently in use was a non-interfering model, the solution to this problem was to invoke pseudo-effects to account for the asymmetry. In the  $n\pi$  system the  $\Delta$  mass was reduced at each energy to give the best fit, whereas in the  $K^-n$  system pseudo-resonances were invoked with variable mass to fit the enhancement. The  $\Sigma(1670)$  was therefore a manifestation of this effect at the higher energies. Below 1.285 GeV/c this mass was changed to 1640 MeV, and at 1.205 GeV/c a mass of 1580 MeV gave the best fit. The  $\Delta$  mass was varied from its nominal mass of 1232 MeV at 1.355 GeV/c to 1200 MeV at the lower energies. Improved fits at all energies were now

obtained except below the  $\bar{K}^*$  threshold where the severe  $\bar{K}^*$  mass asymmetry could not be accounted for by mass depression. This region comprised the first four energy points where only test runs were made. The results from 1.125 GeV/c upwards are given in table (3.1).

A similar analysis was carried out on the other two channels,  $\bar{K}^0 p \pi^-$  and  $K^- p \pi^0$ , from 1.125 GeV/c upward. For the latter channel the  $\Lambda$  (1520) production was also included. Both channels showed signs of the  $\bar{K}^*$  decay asymmetry which was accounted for in the same way as in the  $K^- n \pi^+$  channel.

Although the above method is far from satisfactory, the  $\bar{K}^*$  parameters extracted at different stages of the analysis were found to be consistent with each other, showing that the  $\bar{K}^*$  was being extracted fairly clearly from the background. The  $\Delta$  extraction, however, was very much more uncertain due to its large width, and its fitted parameters were found to be unstable during the above procedure.

#### 3.4 Extension of the analysis

Because of the subsequent  $\bar{K}^* N$  partial wave analysis it was necessary to extend the energy region towards the higher energies. This was achieved by including in the analysis the  $\bar{K} N \pi$  data of the CRS collaboration. (15) Because of systematic errors in the  $\bar{K}^0 p \pi^-$  channel, (16) however, this channel was unavailable for analysis. The other channels were analysed in an identical way to those of the present experiment, although fewer events at each energy caused large fluctuations in fitted resonance parameters across the energy region. Nominal values of  $\bar{K}^*$  mass and width fitted the data adequately, since the effect of barrier factors is less severe in this region. For the  $K^- n \pi^+$  channel the  $\bar{K}^*$  decay asymmetry was still present, and it was found necessary to vary the

mass of the  $\Sigma(1765)$  to fit the enhancement. The  $\Delta$  fraction was very small and in most cases was omitted from the fit. For the  $K^-p\pi^0$  channel the inclusion of  $\Sigma(1765)$  was unable to fit a wide enhancement in the  $K^-p$  system. Litchfield,<sup>(17)</sup> in his analysis of this data ascribed this enhancement to the  $\Lambda(1815)$ . On replacing the  $\Sigma(1765)$  by this resonance the fit improved dramatically. Reasonably good fits were therefore obtained in both channels and the results are listed in table (3.2).

The quality of all fits are expressed as a  $\frac{\chi^2}{NDF}$  averaged over all three Dalitz Plot projections. The number of degrees of freedom (NDF) is defined as the total number of bins minus the total number of variable parameters contributing to the Dalitz Plot projections. The fits to the data of this experiment are shown as dashed curves in figure (3.4).

### 3.5 The interference model

The problems in fitting the data using the non-interference model stem basically from the fact that the  $\bar{K}^*$  band has an asymmetric distribution, which cannot be fitted properly using simple incoherent processes. An attempt was now made to explain this asymmetry by a simple interference effect between the P-wave  $\bar{K}^*$  and an S-wave resonance, assumed to be very wide. An S-wave was chosen because of the following fact:- If the  $\bar{K}^*$  decays predominantly via  $l_2=0$  into two spinless mesons, a decay amplitude of the form "cos  $\theta$ " occurs in the helicity  $\theta$  angle. Putting the dependence on all other variables into one function "A", then the coherent combination of  $\bar{K}^*$  and a constant S-wave amplitude gives an intensity distribution of the form:-

$$I = |A_S + A_{K^*} \cos \theta|^2 = |A_S|^2 + |A_{K^*}|^2 \cos^2 \theta + 2 \operatorname{Re}(A_S A_{K^*}^*) \cos \theta \quad 3.15$$

where the interference term contributes an asymmetric cos  $\theta$  form to the decay distribution. This term becomes the basis for a more rigorous expression which will now be developed.

Consider the following set of reactions:-



where all resonances  $c_k$  have a common decay channel:-



The generalized form of the angular distribution of "e" in the helicity frame of "c" is given by:-<sup>(18)</sup>

$$I(\theta, \phi) = \frac{1}{N} \sum_{\lambda_e \lambda_f} \sqrt{\frac{2J+1}{4\pi}} M_{\lambda_e \lambda_f}^J D_{m\Lambda}^{*J}(\phi, \theta, 0) \rho_{mm'} \sqrt{\frac{2J'+1}{4\pi}} M_{\lambda_e \lambda_f}^{*J'} D_{m'\Lambda}^{J'}(\phi, \theta, 0) \quad 3.16$$

where the summation is over all  $J, J'$  the spin of "c";  $m, m'$ , the spin projection on the z-axis;  $\lambda_e, \lambda_f$  the helicities of the final state particles with  $\Lambda = \lambda_e - \lambda_f$ . The D's are rotation matrices for the angles  $\theta, \phi$  of the helicity system.  $N$  is a normalization factor.  $\rho$  is the density matrix of "c".  $M_{\lambda_e \lambda_f}^J$  represents the combined mass dependent part of the helicity amplitude for the decay of a "c" state, together with its production amplitude.

It is assumed that the only contributions to "c" are spins 1 and 0, corresponding to the  $\bar{K}^*$  and S-wave. Furthermore, on dealing with the  $\bar{K}\pi$  system the helicities  $\lambda_e, \lambda_f$  and  $\Lambda$  are all zero and their summation is dropped. Thus only two helicity amplitudes exist - one for the  $\bar{K}^*$  and one for the S-wave. Expanding eqn.(3.16) over  $J$  and  $J'$  with the above conditions:-

$$I(\theta, \phi) = \frac{1}{N} \left[ \frac{1}{4\pi} |M^0|^2 + \frac{3}{4\pi} |M^1|^2 \sum_{m,m'} D_{m0}^{*1}(\phi, \theta, 0) \rho_{mm'} D_{m0}^1(\phi, \theta, 0) \right. \\ \left. + \frac{\sqrt{3}}{4\pi} \sum_m (M^1 M^{0*} D_{m0}^{*1}(\phi, \theta, 0) \rho_{m0}^{int} + M^{1*} M^0 D_{m0}^1(\phi, \theta, 0) \rho_{0m}^{int}) \right] \quad 3.17$$

The first two terms represent the normal incoherent decay distributions of  $\bar{K}^*$  and the S-wave - the second being the form of Jacob and Wick<sup>(19)</sup> and reducing to eqn.(3.6). The third term is the interference between the two states with  $\rho_{m0}^{int}$  being the interference density matrix elements of "c".

Assuming that the complete density matrix  $\rho$  is hermitian, using the property that  $\rho_{m_0}^{int} = \rho_{0m}^{int}$ , the interference term simplifies to:-

$$\frac{\sqrt{3}}{4\pi} 2 \operatorname{Re} \left[ M^1 M^{0*} \sum_m D_m^{*1}(\phi, \theta, 0) \rho_{m_0}^{int} \right] \quad 3.18$$

The M amplitudes can be represented as follows:-

$$\text{For the } \bar{K}^*: M^1 = A_{K^*} e^{i\phi_{K^*}} BW_{K^*} \quad 3.19$$

where A is the  $\bar{K}^*$  production amplitude;  $BW_{K^*}$  is the  $\bar{K}^*$  Breit-Wigner amplitude;  $\phi_{K^*}$  is an arbitrary phase.

For the S-wave it is assumed that, being slowly varying over the narrow width of the  $\bar{K}^*$ , the contribution beneath the  $\bar{K}^*$  is approximately of constant amplitude and phase

$$\text{and } M^0 = A_s e^{i\phi_s} \quad 3.20$$

where "S" means S-wave.

Now interference can only occur if the  $\bar{K}^*$  and S-wave are produced from the same S-channel partial wave. As it is highly unlikely for this to occur in all waves, the final interference between both contributions on the Dalitz Plot will only be partial. On including a coherence factor  $A_{int}$  into eqn. (3.18) together with eqns. (3.19) and (3.20) where  $0 \leq A_{int} \leq 1$ , the interference term becomes:-

$$\frac{1}{\sqrt{4\pi}} 2 A_{int} A_{K^*} A_s \operatorname{Re} \left\{ [Y_1^{1*} \rho_{10}^{int} + Y_1^{0*} \rho_{00}^{int} + Y_1^{-1*} \rho_{-10}^{int}] BW_{K^*} e^{i\psi} \right\} \quad 3.21$$

where  $\psi$  is the relative phase between S-wave and P-wave at the  $\bar{K}^*$  peak, and the Y's are spherical harmonics.

Assuming no polarization of the incident particles, a generalized parity condition:- (18)

$$\rho_{mm'} = \eta \eta' (-1)^{J-J'} (-1)^{m-m'} \rho_{-m-m'} \quad 3.22$$

where  $\eta$  is the intrinsic parity of the J state

can be applied to the density matrix in the case of parity conservation for the production reaction. Eqn. (3.22) is true only for spin reference frames with the y-axis normal to the production plane, such

as the helicity and Jackson frames.

For the case in question  $J=1$ ,  $\eta = -1$ ,  $J'=0$ ,  $\eta' = +1$  and  $m'=0$

$$\text{and } \rho_{10}^{\text{int}} = -\rho_{-10}^{\text{int}} \quad 3.23$$

Thus one interference density matrix element is redundant. On expanding eqn. (3.21) using condition (3.23) the interference term

becomes:-

$$\frac{1}{\sqrt{4\pi}} \sqrt{\frac{3}{8\pi}} 2 A_{\text{int}} A_{K^*} A_s [\sqrt{2} \cos \theta \{ (\text{Re}(BW) \cos \psi - \text{Im}(BW) \sin \psi) \text{Re} \rho_{00}^{\text{int}} - (\text{Im}(BW) \cos \psi + \text{Re}(BW) \sin \psi) \text{Im} \rho_{00}^{\text{int}} \} - 2 \sin \theta \cos \phi \{ (\text{Re}(BW) \cos \psi - \text{Im}(BW) \sin \psi) \text{Re} \rho_{10}^{\text{int}} - (\text{Im}(BW) \cos \psi + \text{Re}(BW) \sin \psi) \text{Im} \rho_{10}^{\text{int}} \} ] \quad 3.24$$

This is the final form of the term and contains four extra parameters.

There are two angular terms;  $\cos \theta$  and  $\sin \theta \cos \phi$ . Only the  $\cos \theta$  term shows itself on the Dalitz Plot, and is indeed the rigorous expression based upon eqn. (3.13) which introduces an asymmetry to the  $\bar{K}^*$  decay distribution. Furthermore the whole term integrates to zero over  $\cos \theta$  as expected, since interference does not add or subtract intensity but redistributes it. The term is similar to that given by Lyons and McCubbin<sup>(20)</sup> who explain the asymmetry in their data with the same hypothesis.

For fitting purposes it is evident that two of the parameters in eqn. (3.24) are redundant since each separate term consists of a multiple of three parameters. Thus  $A_{\text{int}}$  and  $\psi$  are absorbed into the density matrix elements, and after rearrangement, the final form for the interference term becomes:-

$$A_{K^*} A_{\rho_s} [ (\text{Re}(BW) \rho_a - \text{Im}(BW) \rho_b) \cos \theta - \sqrt{2} (\text{Re}(BW) \rho_c - \text{Im}(BW) \rho_d) \sin \theta \cos \phi ] \quad 3.25$$

where  $\rho_a, \rho_b, \rho_c, \rho_d$  are free parameters of the model, but were generally allowed to vary between  $\pm 1$ .

The parameters absorb the constants outside the brackets in eqn. (3.24). They also absorb the fraction of background which is S-wave, so that  $A_s$  is replaced by  $A_{\rho_s}$ , the phase space amplitude. This is a reasonable assumption if the S-wave contribution beneath the  $\bar{K}^*$

is of a constant amplitude because it then simulates a fraction of phase space. Eqn. (3.25) was the interference term used in the fitting program and was added onto eqn. (3.3), contributing a maximum of four extra parameters. No other interference between contributing processes on the Dalitz Plot was assumed in any channel (although the  $K^- p \pi^0$  channel did show some small signs of this at the  $\Lambda(1520) - \Delta$  overlap region).

### 3.6 The interference fits

For Dalitz Plot fitting purposes only the first term in eqn. (3.25) was necessary, the second being independent of position on the plot. Thus for best  $\chi^2$  values only two parameters were necessary, whereas for the best likelihood value the second term was included. On removing the pseudo-effects from the non-interference fits and inserting the first term of eqn. (3.25) the fits at almost every energy showed dramatic improvements, with the  $\bar{K}^*$  asymmetric effect in decay being fitted correctly now by the  $\cos \theta$  term. The improvement was most impressive around the  $\bar{K}^* N$  threshold region, i.e. around 1.165 GeV/c, and especially so in the  $K^- p \pi^0$  channel where the asymmetry was most severe. On inclusion of the second interference term the negative log-likelihood dropped considerably at almost all energies showing that the  $\phi$  distribution in the  $\bar{K}^*$  region was also being fitted better. The  $\chi^2$  values for the fit to the Dalitz Plot variables remained unchanged, as expected. The fits to the data of this experiment are shown as solid curves in figure (3.4).

It was noticed that the fitted  $\bar{K}^*$  parameters, that is the cross-section and density matrix elements, were essentially unchanged between the interference and non-interference models. This indicated that the  $\bar{K}^*$  extraction was not very sensitive to the choice of model used. The fitted quantities for all resonance contributions in all channels are

given in table (3.3) for this experiment, and in table (3.4) for the CRS data. They should be compared with the results of the non-interference model in tables (3.1) and (3.2), especially for the likelihood values. The large values of  $\frac{\chi^2}{\text{NDF}}$  originate mainly from the inability of the  $\bar{K}^*$  mass depression technique to fit the asymmetric mass distribution resulting from production barrier factors. It is for this reason that final determinations of the  $\bar{K}^*N$  partial cross sections for this experiment are deferred until chapter 6, where a better technique is described. The errors on the partial cross-sections for this experiment are compounded from statistical errors and empirical fit errors obtained by estimating from the mass plots the fraction of each resonance which could be mistaken for background. For the CRS data, where no event weights were available from the DST, the errors on the partial cross-sections were taken from ref. (21).

### 3.7 Comments on the results of the fits

The results show a smooth energy dependence for the  $\bar{K}^*$  and  $\Lambda(1520)$  parameters. For the  $\Delta$ , however, its large width and small cross-section in the  $K^-n\pi^+$  and  $\bar{K}^0p\pi^-$  channels make it difficult to be distinguished from background. Consequently, its fitted parameters are seen to fluctuate somewhat wildly with energy for these two channels. A constant feature, though, is that the  $\rho_{ii}$  density matrix element of the  $\Delta$  is near to its upper limit of 0.5 in all channels. This has the effect of producing a  $\sin^2\theta$  form to the  $\Delta$  decay band, and so effectively concentrating the  $\Delta$  contribution in the middle of its band. This effect has been observed several times before, (22) including the  $\Delta$  contribution to the reaction  $\pi N \rightarrow \pi\pi N$ , (23) where duality models have been invoked to explain it. (24)

The four interference parameters of eqn. (3.25) are also found to fluctuate somewhat wildly with energy. This may be the result of

statistical fluctuations in the data reproducing structure which requires one parameter of a pair to be larger or smaller than usual.

It is of interest to compare the interference term with typical  $\bar{K}^*$  decay asymmetries in the data. This is achieved by introducing an asymmetry parameter  $\alpha$  defined by:-

$$\alpha = \frac{F - B}{F + B} \quad 3.26$$

where  $F(B)$  is the number of events with  $\cos \theta$  greater (smaller) than zero.  $\alpha$  is a function of the  $\bar{K}\pi$  effective mass-squared. It is sketched for the two contributions of the first term of eqn. (3.25), and plotted at a typical energy for all three channels in figure (3.5). It can be seen that the data requires a combination of the two shapes from the interference term, and this is confirmed in the fitted values for the parameters of this term.

A further problem lies in the ratio of the  $K^{*-}$  p partial cross-sections from the channels  $\bar{K}^0 p \pi^-$  and  $K^- p \pi^0$ . These being the two decay modes of the  $K^{*-}$ , the Clebsch-Gordan coefficients predict a ratio of 2:1 for the partial cross-sections. As seen in table (3.3) this ratio is consistently smaller than 2:1 by more than one standard deviation. At this stage a possible reason for the effect is the peak mass depression of the  $\bar{K}^*$  which allows for production barrier effects. Since there is a much larger amount of background beneath the  $\bar{K}^*$  in the  $K^- p \pi^0$  channel, the inability of this technique to fit the  $\bar{K}^*$  at a distance from the peak may cause some of this background to be classed as resonance, and hence increase the cross-section. In the  $\bar{K}^0 p \pi^-$  channel, the lack of a large background will prevent this from happening to any serious extent.

### 3.3 The $\phi$ distribution

So far, no mention has been made of the quality of fit to the helicity azimuthal angle  $\phi$ , all emphasis having been placed on the



momentum spread and shape similar to that of the data. FOWL automatically generates events with a true phase-space distribution by weighting the events appropriately. Thus all that was necessary was to include an extra weight for each event corresponding to the fitted density function at that point, and histogramming these weighted events in all the variables. About 50,000 events were found to be required to produce reasonably smooth histograms, which were then converted to curves, smoothed out further by the computer, normalized to the total number of events in the dataset and projected onto histograms of the actual data.

The results showed good fits to the mass distributions as expected, and also to the  $\cos \theta$  distributions. However the fit to the  $\theta$ 's of the  $(n\pi)$  and  $(\bar{K}n)$  systems were extremely bad, whereas for the  $(K\pi)$  system the fit was very good. This result confirmed the necessity of a  $\bar{K}^*$  production angular distribution, and the lack of any appreciable angular structure in the other two-body systems. The  $\bar{K}^*$  structure was therefore expected to reproduce the  $\theta$  structure in the  $(n\pi)$  and  $(\bar{K}n)$  systems. These fits to  $\theta$  are shown in figure (3.6). The production angle projections were, of course, flat and bore no resemblance to the highly structured data. It is for these reasons that the  $\theta$  distributions were not used to determine the quality of fit to the Dalitz Plot analysis.

Despite the bad fits to  $\theta$ , the validity of the analysis can still be believed for the following reason. By dealing with a density function in three variables, the resonant processes are kept distinct from each other, and are defined in terms of the variables of their own systems. Thus the contribution of a resonance to its own  $\theta$  variable can be fitted independently of the reflections of other processes into this variable, so long as the processes do not overlap to an appreciable degree. It is therefore the likelihood which determines the quality of fit (in conjunction with the effective mass projections), and the overall  $\theta$

distributions are ignored. In this experiment, overlap between processes on the Dalitz Plot has been seen to be small, and so the three-variable analysis can be thought of as being a valid analysis in this case. To confirm this hypothesis, structure in the  $\bar{K}^*$  production angle should be included in the FOWL plots to see whether the  $(n\pi)$  and  $(\bar{K}n) \emptyset$  distributions are fitted properly. This procedure is described in the next chapter where the  $\bar{K}^*$  production angular structure is extracted.

\* \* \* \* \*

Table (3.1)

## Results of the Non-Interference Model for this Experiment

a)  $K^- p \pi^+$ 

Beam Momentum GeV/c	$\frac{\chi^2}{NDF}$	L	Mass used for $K^*$ MeV	Mass used for $\Delta$ MeV	$\sigma_{K^*}$ mb.	$\sigma_{\Delta}$ mb.	$\sigma_{\Sigma(1765)}$ mb.	Pseudo-Resonances $\Gamma =$ Width
1.125	1.07	150	884	1200	$0.498 \pm 0.035$	$0.219 \pm 0.040$	-	-
1.165	1.46	380	888	1213	$0.668 \pm 0.037$	$0.118 \pm 0.024$	-	$\Sigma(1640) \Gamma=35$
1.205	1.10	776	890	1213	$0.786 \pm 0.044$	$0.164 \pm 0.025$	-	$\Sigma(1580) \Gamma=30$
1.245	1.40	1474	890	1213	$1.044 \pm 0.052$	$0.174 \pm 0.027$	$0.042 \pm 0.014$	$\Sigma(1640) \Gamma=35$
1.285	1.58	1956	892	1220	$1.138 \pm 0.057$	$0.194 \pm 0.029$	$0.072 \pm 0.024$	$\Sigma(1670) \Gamma=50$
1.320	1.36	2040	892	1232	$1.313 \pm 0.065$	$0.142 \pm 0.021$	$0.108 \pm 0.036$	$\Sigma(1670) \Gamma=50$
1.355	1.75	3549	892	1232	$1.494 \pm 0.071$	$0.122 \pm 0.018$	$0.195 \pm 0.065$	$\Sigma(1670) \Gamma=50$

b)  $\bar{K}^0 p \pi^-$ 

1.125	1.68	26	886	1213	$0.880 \pm 0.056$	$0.209 \pm 0.043$	-	$\Sigma(1550) \Gamma=15$
1.165	1.51	396	886	1213	$1.067 \pm 0.065$	$0.162 \pm 0.033$	-	-
1.205	1.41	749	888	1232	$1.099 \pm 0.055$	$0.166 \pm 0.026$	-	-
1.245	1.51	1422	888	1232	$1.127 \pm 0.056$	$0.192 \pm 0.029$	$0.018 \pm 0.009$	-
1.285	1.26	1835	888	1232	$1.106 \pm 0.055$	$0.162 \pm 0.025$	-	-
1.320	1.43	1779	890	1232	$1.045 \pm 0.053$	$0.222 \pm 0.034$	$0.043 \pm 0.020$	$\Sigma(1670) \Gamma=50$
1.355	1.11	3155	890	1232	$1.119 \pm 0.057$	$0.179 \pm 0.027$	$0.054 \pm 0.025$	$\Sigma(1670) \Gamma=50$

c)  $K^- p \pi^0$ 

								$\sigma_{\Lambda(1520)}$ mb.
1.125	1.97	141	886	1200	$0.449 \pm 0.038$	$0.326 \pm 0.067$	$0.021 \pm 0.010$	$0.305 \pm 0.019$
1.165	1.83	406	886	1200	$0.560 \pm 0.036$	$0.392 \pm 0.061$	$0.061 \pm 0.030$	$0.263 \pm 0.018$
1.205	1.39	740	890	1213	$0.610 \pm 0.035$	$0.306 \pm 0.048$	$0.104 \pm 0.050$	$0.186 \pm 0.012$
1.245	1.44	1269	890	1220	$0.602 \pm 0.032$	$0.321 \pm 0.035$	$0.086 \pm 0.030$	$0.164 \pm 0.010$
1.285	1.23	1714	892	1232	$0.640 \pm 0.033$	$0.342 \pm 0.036$	$0.124 \pm 0.025$	$0.214 \pm 0.013$
1.320	1.09	1526	892	1232	$0.541 \pm 0.030$	$0.282 \pm 0.030$	$0.162 \pm 0.026$	$0.195 \pm 0.013$
1.355	1.08	2907	892	1232	$0.618 \pm 0.031$	$0.285 \pm 0.030$	$0.216 \pm 0.023$	$0.237 \pm 0.013$

Table (3.2)

Results of the Non-Interference Model for the CRS Dataa)  $K^- n \pi^+$ 

Beam Momentum GeV/c	$\frac{\chi^2}{\text{NDF}}$	L	$\sigma_{K^*}$ mb.	$\sigma_{\Delta}$ mb.	$\sigma_{\Sigma(1765)}$ mb.	Pseudo- Resonances $\Gamma = \text{Width}$
1.271	1.20	163	$0.892 \pm 0.140$	-	-	
1.321	1.10	375	$1.165 \pm 0.170$	-	$0.079 \pm 0.040$	
1.370	1.63	343	$1.506 \pm 0.190$	$0.348 \pm 0.150$	$0.135 \pm 0.060$	
1.419	1.13	397	$1.667 \pm 0.180$	$0.088 \pm 0.050$	$0.250 \pm 0.100$	
1.464	1.59	429	$1.742 \pm 0.200$	$0.085 \pm 0.050$	$0.282 \pm 0.100$	
1.512	1.25	467	$1.571 \pm 0.140$	-	$0.311 \pm 0.100$	
1.546	1.45	910	$1.751 \pm 0.140$	-	-	$\Sigma(1780) \Gamma=140$
1.606	1.18	895	$2.143 \pm 0.160$	-	-	$\Sigma(1820) \Gamma=140$
1.652	1.10	995	$1.717 \pm 0.150$	-	-	$\Sigma(1800) \Gamma=120$
1.706	1.24	1024	$1.950 \pm 0.190$	-	-	
1.741	1.32	1373	$1.813 \pm 0.190$	-	-	
1.800	1.03	988	$1.795 \pm 0.160$	$0.280 \pm 0.150$	-	
1.841	1.08	901	$1.300 \pm 0.130$	-	-	

b)  $K^- p \pi^0$

Beam Momentum GeV/c	$\frac{\chi^2}{\text{NDF}}$	L	$\sigma_{\bar{K}^*}$ mb.	$\sigma_{\Delta}$ mb.	$\sigma_{\Sigma(1765)/\Lambda(1815)}$ mb.	$\sigma_{\Lambda(1520)}$ mb.
1.271	1.16	145	$0.454 \pm 0.070$	$0.158 \pm 0.190$	$0.169 \pm 0.080$	$0.106 \pm 0.050$
1.321	1.44	329	$0.626 \pm 0.130$	$0.199 \pm 0.190$	$0.263 \pm 0.080$	$0.174 \pm 0.050$
1.370	0.91	315	$0.632 \pm 0.160$	$0.227 \pm 0.160$	$\uparrow_{\Sigma} 0.251 \pm 0.080$	$0.256 \pm 0.060$
1.419	1.16	304	$0.613 \pm 0.130$	$0.398 \pm 0.160$	$\downarrow_{\Lambda} 0.121 \pm 0.050$	$0.160 \pm 0.060$
1.464	1.07	361	$0.554 \pm 0.140$	$0.329 \pm 0.190$	$\downarrow 0.287 \pm 0.070$	$0.219 \pm 0.060$
1.512	1.14	493	$0.643 \pm 0.120$	$0.277 \pm 0.220$	$0.191 \pm 0.055$	$0.138 \pm 0.040$
1.546	0.93	780	$0.635 \pm 0.110$	$0.372 \pm 0.270$	$0.270 \pm 0.060$	$0.233 \pm 0.060$
1.606	1.62	758	$0.768 \pm 0.170$	$0.153 \pm 0.230$	$0.227 \pm 0.070$	$0.168 \pm 0.050$
1.652	1.37	832	$0.652 \pm 0.090$	$0.202 \pm 0.130$	$0.278 \pm 0.070$	$0.122 \pm 0.040$
1.706	1.39	713	$0.625 \pm 0.110$	$0.351 \pm 0.140$	$0.305 \pm 0.080$	$0.157 \pm 0.050$
1.741	1.15	970	$0.806 \pm 0.130$	$0.440 \pm 0.120$	$0.128 \pm 0.065$	$0.155 \pm 0.050$
1.800	1.33	670	$0.780 \pm 0.100$	$0.413 \pm 0.140$	$0.142 \pm 0.070$	$0.138 \pm 0.050$
1.841	1.05	772	$0.569 \pm 0.100$	$0.256 \pm 0.140$	$0.097 \pm 0.040$	$0.122 \pm 0.040$

Table (3.3)

## Results of the Interference Model for the Present Experiment

a)  $K^- n \pi^+$ 

Beam Momentum GeV/c	$\frac{\chi^2}{\text{NDF}}$	L	$\sigma_{K^*}$ mb.	$\rho_{00}$	$\rho_a$	$\rho_b$	$\rho_c$	$\rho_d$	$\sigma_{\Delta}$ mb.	$\rho_{\frac{3}{2} \frac{3}{2}}$	$\sigma_{\Sigma(1765)}$ mb.	$\Sigma(1765)^{\beta}$
1.125	1.06	147	0.493 $\pm 0.035$	0.35	0.20	0.01	0.12	-0.03	0.182 $\pm 0.040$	0.33	-	-
1.165	1.30	358	0.664 $\pm 0.037$	0.41	0.04	0.24	0.16	-0.05	0.095 $\pm 0.024$	0.47	-	-
1.205	1.13	771	0.790 $\pm 0.044$	0.41	0.09	0.16	0.07	-0.02	0.092 $\pm 0.020$	0.46	-	-
1.245	1.31	1463	1.043 $\pm 0.052$	0.47	0.05	0.19	0.09	-0.08	0.068 $\pm 0.010$	0.50	0.017 $\pm 0.010$	0.00
1.285	1.56	1946	1.136 $\pm 0.057$	0.54	0.10	0.06	0.13	-0.10	0.129 $\pm 0.020$	0.50	0.062 $\pm 0.020$	0.44
1.320	1.32	2016	1.304 $\pm 0.065$	0.51	0.12	0.04	0.13	-0.16	0.106 $\pm 0.020$	0.50	0.082 $\pm 0.030$	0.27
1.355	1.71	3522	1.475 $\pm 0.071$	0.49	0.12	0.08	0.16	-0.07	0.088 $\pm 0.015$	0.50	0.158 $\pm 0.060$	0.31

b)  $\bar{K}^0 p \pi^-$ 

1.125	1.50	19	0.881 $\pm 0.056$	0.46	0.08	0.14	-0.02	-0.14	0.217 $\pm 0.043$	0.49	-	-
1.165	1.36	381	1.056 $\pm 0.065$	0.44	-0.06	0.13	-0.03	-0.09	0.182 $\pm 0.033$	0.49	-	-
1.205	1.33	723	1.100 $\pm 0.055$	0.43	-0.10	0.17	-0.01	-0.18	0.177 $\pm 0.026$	0.46	-	-
1.245	1.47	1401	1.119 $\pm 0.056$	0.46	-0.02	0.12	-0.01	-0.16	0.172 $\pm 0.029$	0.48	-	-
1.285	1.25	1808	1.107 $\pm 0.055$	0.44	-0.02	0.05	0.04	-0.19	0.179 $\pm 0.025$	0.46	-	-
1.320	1.38	1751	1.037 $\pm 0.053$	0.47	0.06	0.13	0.03	-0.25	0.230 $\pm 0.034$	0.49	0.027 $\pm 0.010$	0.33
1.355	1.07	3099	1.106 $\pm 0.057$	0.46	0.07	0.06	0.16	-0.21	0.197 $\pm 0.027$	0.48	0.035 $\pm 0.020$	0.00

c)  $K^- p \pi^0$

Beam Momentum GeV/c	$\frac{\chi^2}{\text{NDF}}$	L	$\sigma_{K^*}$ mb.	$\rho_{00}$	$\rho_a$	$\rho_b$	$\rho_c$	$\rho_d$	$\sigma_\Delta$ mb.	$\rho_{\frac{3}{2} \frac{3}{2}}$	$\sigma_{\Sigma(1765)}$ mb.	$\sigma_{\Lambda(1520)}$ mb.	$\rho_{\frac{3}{2} \frac{3}{2}}$	$\frac{\sigma_{K^*}^{K^0 p \pi^-}}{\sigma_{K^*}^{K^- p \pi^0}}$
1.125	1.25	122	0.459 $\pm 0.038$	0.53	0.24	0.55	0.07	0.05	0.232 $\pm 0.050$	0.47	-	0.256 $\pm 0.015$	0.14	1.92 $\pm 0.21$
1.165	1.10	379	0.574 $\pm 0.036$	0.49	0.13	0.92	0.25	-0.14	0.321 $\pm 0.055$	0.49	0.064 $\pm 0.030$	0.222 $\pm 0.015$	0.10	1.84 $\pm 0.15$
1.205	1.35	723	0.608 $\pm 0.035$	0.37	-0.06	0.46	0.30	-0.21	0.242 $\pm 0.040$	0.48	0.104 $\pm 0.050$	0.174 $\pm 0.012$	0.32	1.81 $\pm 0.14$
1.245	1.50	1257	0.594 $\pm 0.032$	0.43	0.20	0.25	0.17	-0.24	0.275 $\pm 0.030$	0.46	0.071 $\pm 0.030$	0.169 $\pm 0.010$	0.28	1.88 $\pm 0.14$
1.285	1.19	1705	0.650 $\pm 0.033$	0.44	0.30	0.22	0.26	-0.40	0.324 $\pm 0.035$	0.46	0.127 $\pm 0.025$	0.208 $\pm 0.013$	0.13	1.70 $\pm 0.12$
1.320	1.07	1514	0.537 $\pm 0.030$	0.40	0.34	0.32	0.50	-0.14	0.267 $\pm 0.030$	0.49	0.152 $\pm 0.026$	0.203 $\pm 0.013$	0.17	1.93 $\pm 0.15$
1.355	1.00	2873	0.605 $\pm 0.031$	0.52	0.30	-0.26	0.79	-0.52	0.314 $\pm 0.030$	0.47	0.211 $\pm 0.023$	0.252 $\pm 0.013$	0.22	1.83 $\pm 0.13$

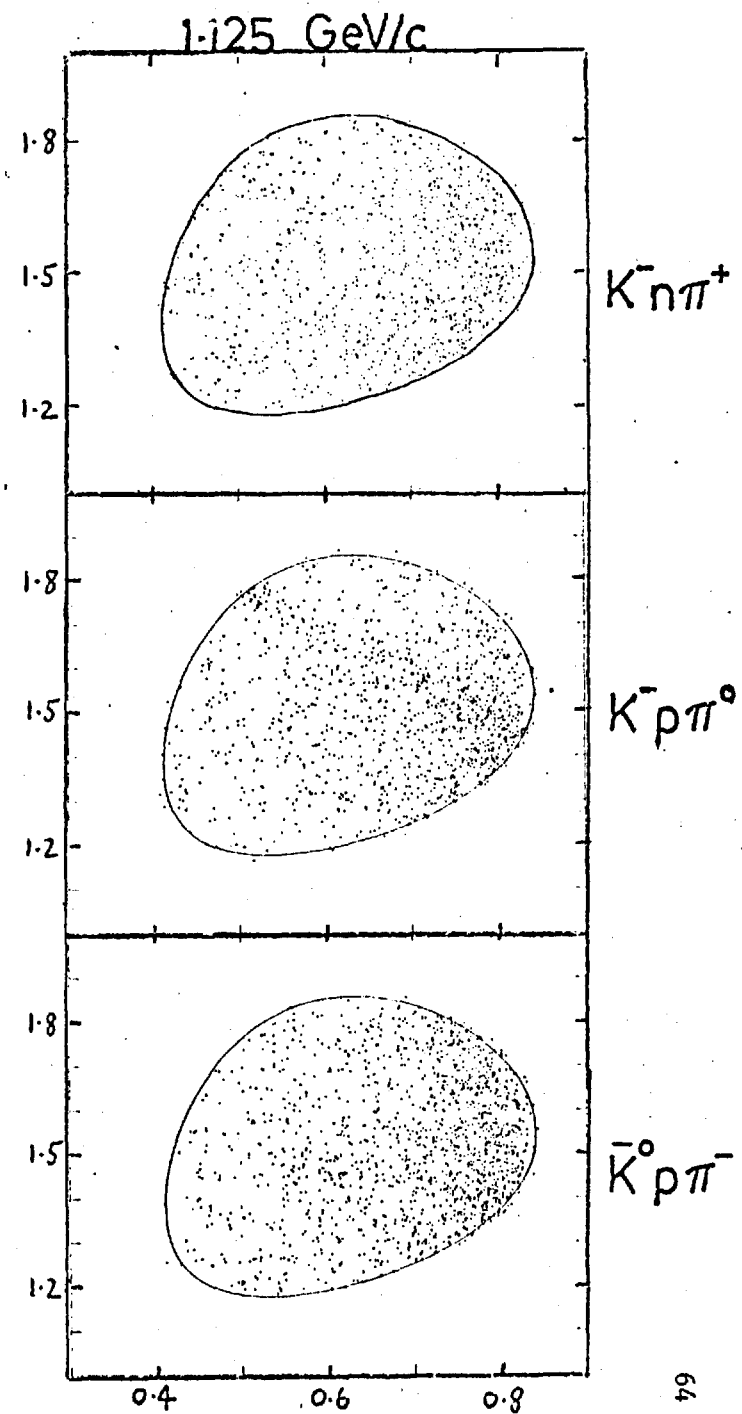
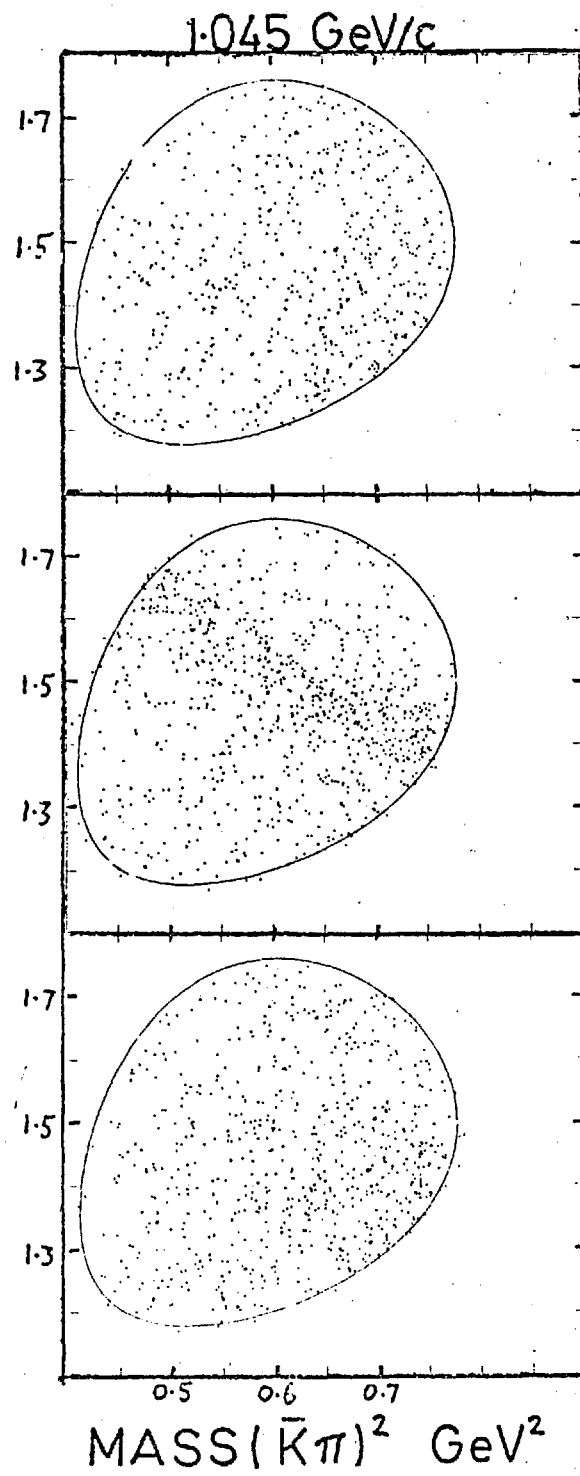
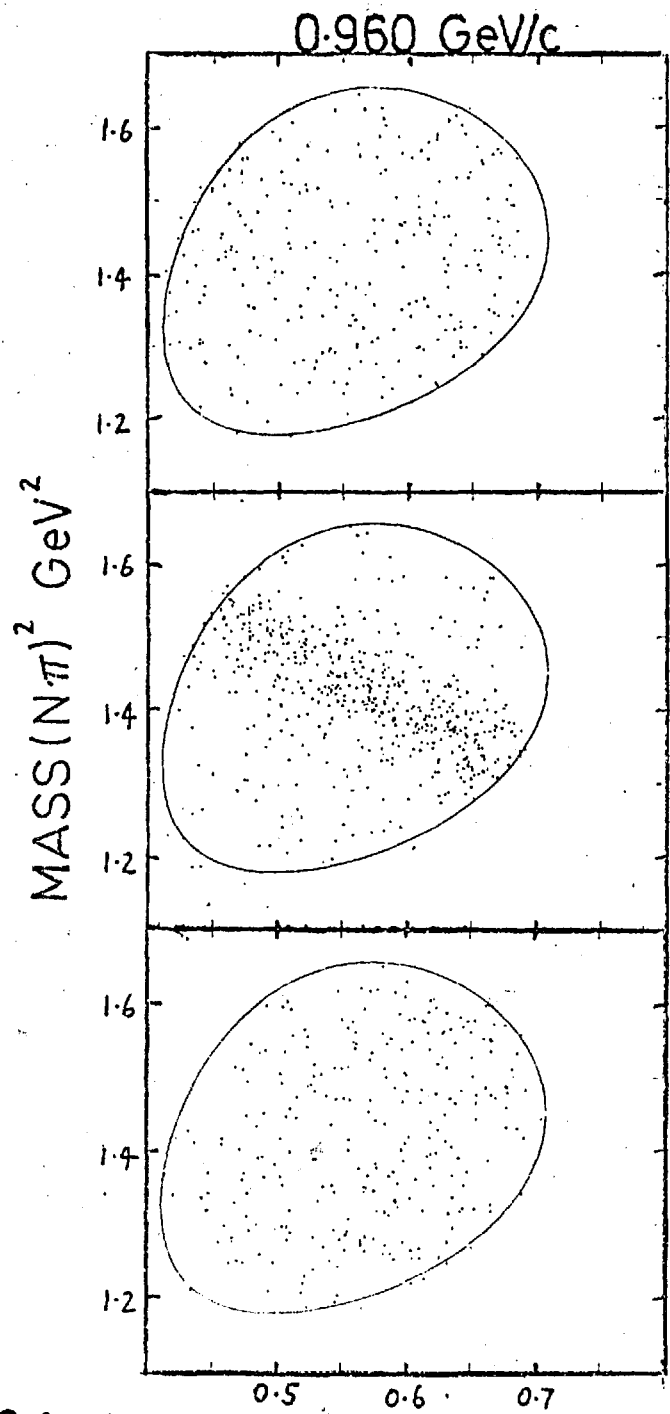
Table (3.4)

Results of Interference Model for the CRS Dataa)  $K^- n \pi^+$ 

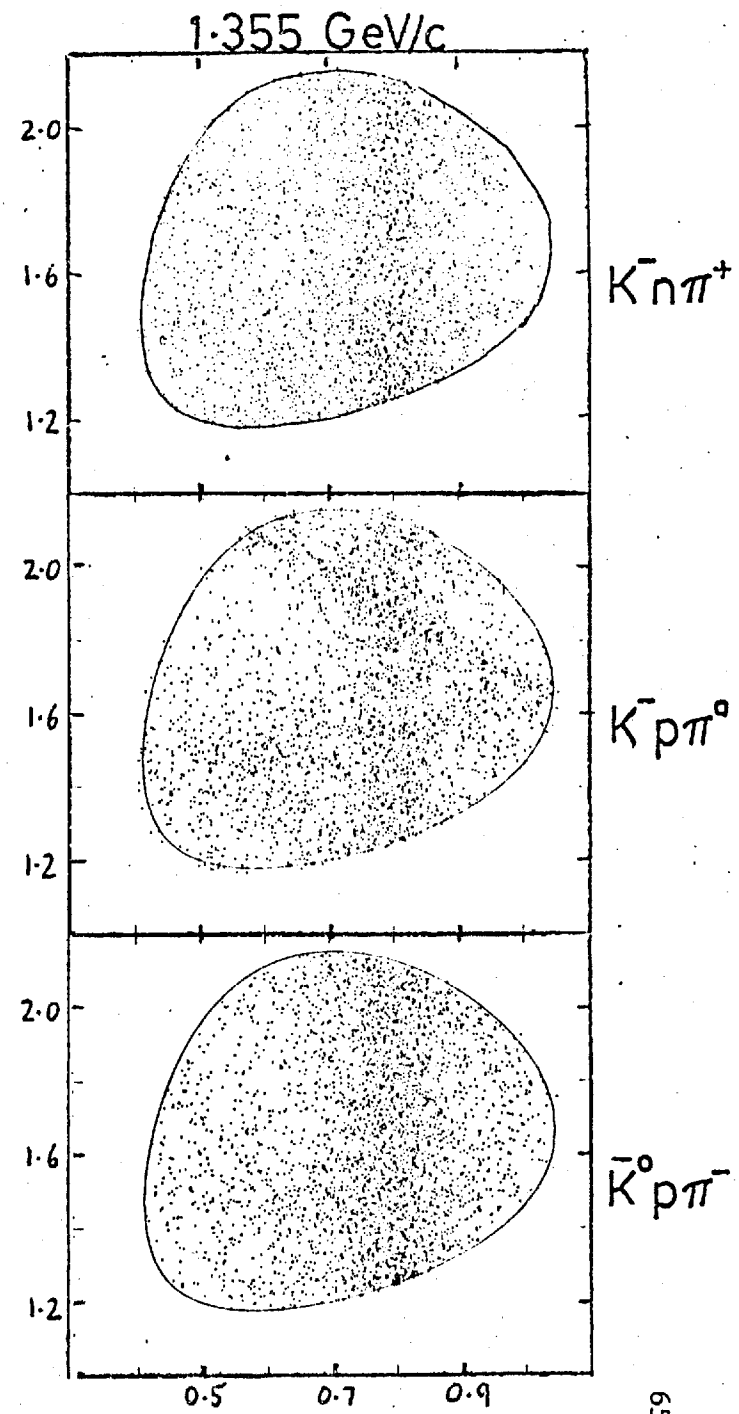
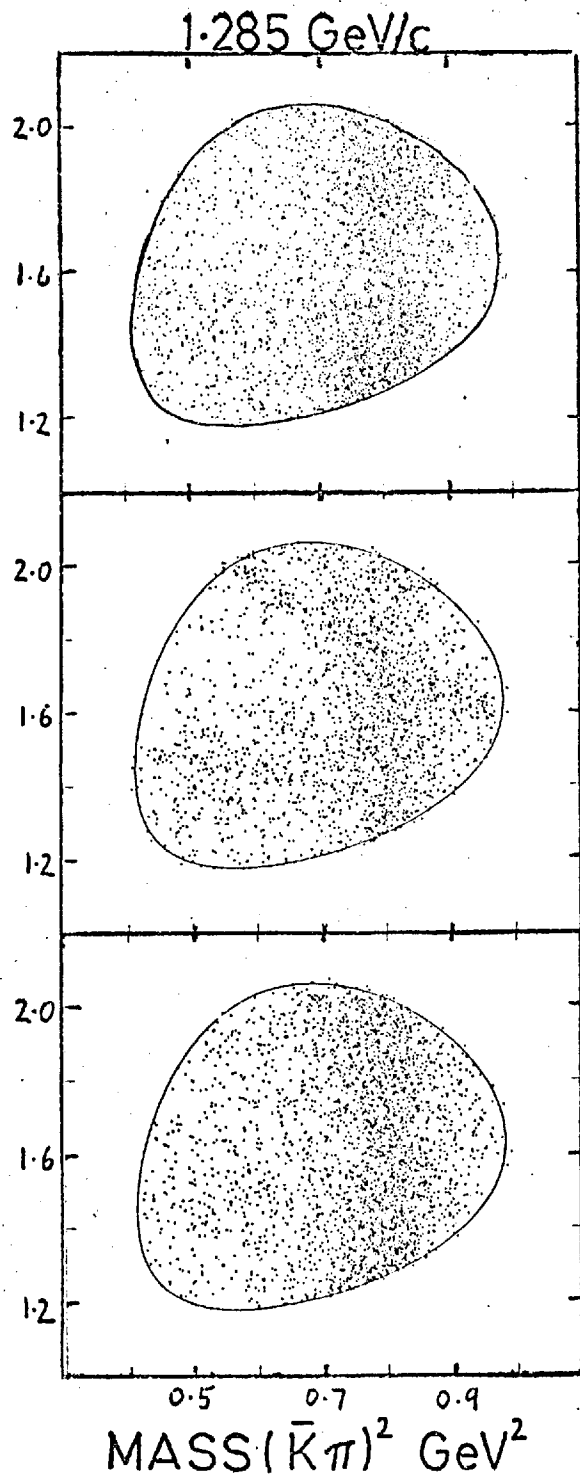
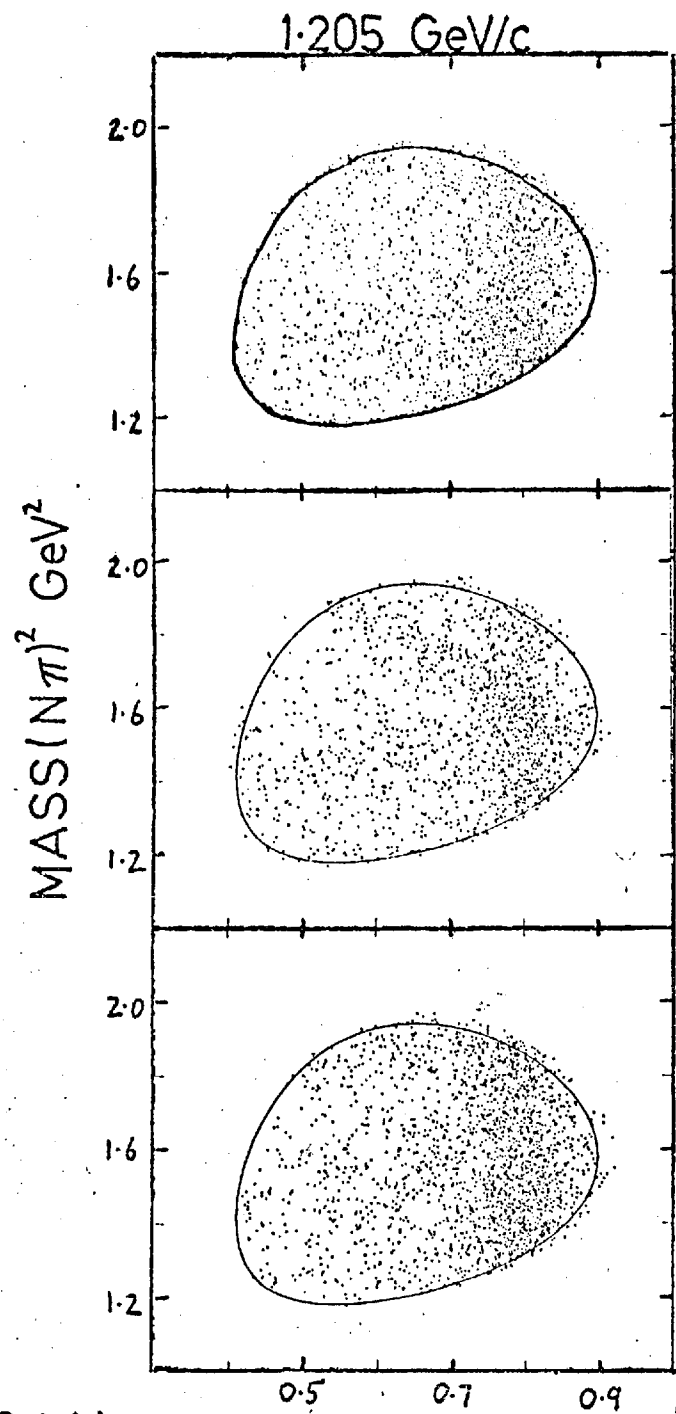
Beam Momentum GeV/c	$\frac{\chi^2}{\text{NDF}}$	L	$\sigma_{K^*}^*$ mb.	$\sigma_{\Delta/\Sigma(1765)}$ mb.	$\rho_a$	$\rho_b$	$\rho_c$	$\rho_d$
1.271	1.00	163	$0.884 \pm 0.140$	-	-0.01	-0.01	0.05	-0.03
1.321	1.00	374	$1.159 \pm 0.170$	$0.426 \pm 0.100$ †	0.15	0.08	0.10	-0.10
1.370	1.65	339	$1.509 \pm 0.190$	$0.189 \pm 0.090$ Δ	0.20	-0.06	0.22	-0.05
1.419	1.05	389	$1.684 \pm 0.180$	$0.259 \pm 0.050$ Σ	0.33	0.16	0.12	-0.16
1.464	1.47	421	$1.780 \pm 0.200$	$0.351 \pm 0.070$ †	-0.08	-0.09	0.22	-0.35
1.512	1.17	457	$1.549 \pm 0.140$	$0.234 \pm 0.050$	0.34	0.37	0.23	-0.25
1.546	1.16	903	$1.747 \pm 0.140$	$0.201 \pm 0.040$	0.17	0.29	0.09	0.04
1.606	1.46	898	$2.097 \pm 0.160$	$0.246 \pm 0.050$	0.25	0.06	0.12	0.02
1.652	1.17	992	$1.729 \pm 0.150$	$0.352 \pm 0.070$	0.21	0.10	0.10	-0.04
1.706	1.15	1010	$1.906 \pm 0.190$	$0.182 \pm 0.035$	0.19	-0.06	0.09	-0.24
1.741	1.32	1373	$1.760 \pm 0.190$	$0.214 \pm 0.040$	0.14	0.08	0.09	-0.03
1.800	1.08	981	$1.796 \pm 0.160$	$0.266 \pm 0.050$	0.19	0.15	0.16	-0.11
1.841	1.10	893	$1.323 \pm 0.130$	$0.190 \pm 0.040$	0.28	0.03	0.10	-0.07

b)  $K^- p \pi^0$

Beam Momentum GeV/c	$\frac{\chi^2}{\text{NDF}}$	L	$\sigma_{K^*}^*$ mb.	$\sigma_{\Delta}$ mb.	$\sigma_{\Lambda(1520)}$ mb.	$\sigma_{\Sigma(1765)/\Lambda(1815)}$ mb.	$\rho_a$	$\rho_b$	$\rho_c$	$\rho_d$
1.271										
1.321			UNRELIABLE							
1.370	0.91	308	$0.603 \pm 0.160$	$0.265 \pm 0.160$	$0.256 \pm 0.040$	$\Sigma$ $0.207 \pm 0.080$	0.32	-0.21	0.30	-0.12
1.419	1.16	301	$0.577 \pm 0.130$	$0.412 \pm 0.160$	$0.169 \pm 0.030$	$\Lambda$ $0.112 \pm 0.050$	0.22	-0.20	0.32	-0.13
1.464	0.98	355	$0.548 \pm 0.140$	$0.297 \pm 0.190$	$0.229 \pm 0.040$	$\dagger$ $0.261 \pm 0.070$	0.15	0.31	0.34	-0.24
1.512	1.14	487	$0.654 \pm 0.120$	$0.282 \pm 0.220$	$0.139 \pm 0.020$	$0.168 \pm 0.055$	0.32	0.04	0.29	-0.02
1.546	0.93	779	$0.625 \pm 0.110$	$0.426 \pm 0.270$	$0.230 \pm 0.040$	$0.284 \pm 0.060$	0.03	-0.45	0.01	-0.07
1.606	1.65	752	$0.755 \pm 0.170$	$0.197 \pm 0.230$	$0.157 \pm 0.030$	$0.227 \pm 0.070$	0.00	-0.15	0.19	-0.08
1.652	1.37	829	$0.655 \pm 0.090$	$0.168 \pm 0.130$	$0.135 \pm 0.020$	$0.245 \pm 0.070$	0.03	0.22	0.12	0.08
1.706	1.39	705	$0.649 \pm 0.110$	$0.373 \pm 0.140$	$0.157 \pm 0.030$	$0.313 \pm 0.080$	0.22	-0.17	0.20	-0.02
1.741	1.15	966	$0.806 \pm 0.130$	$0.396 \pm 0.120$	$0.158 \pm 0.030$	$0.141 \pm 0.065$	-0.12	0.00	-0.02	0.10
1.800	1.23	666	$0.753 \pm 0.100$	$0.454 \pm 0.140$	$0.124 \pm 0.020$	$0.165 \pm 0.070$	0.25	-0.43	0.13	-0.02
1.841	1.04	770	$0.577 \pm 0.100$	$0.252 \pm 0.140$	$0.126 \pm 0.020$	$0.097 \pm 0.040$	0.08	0.11	0.08	-0.01

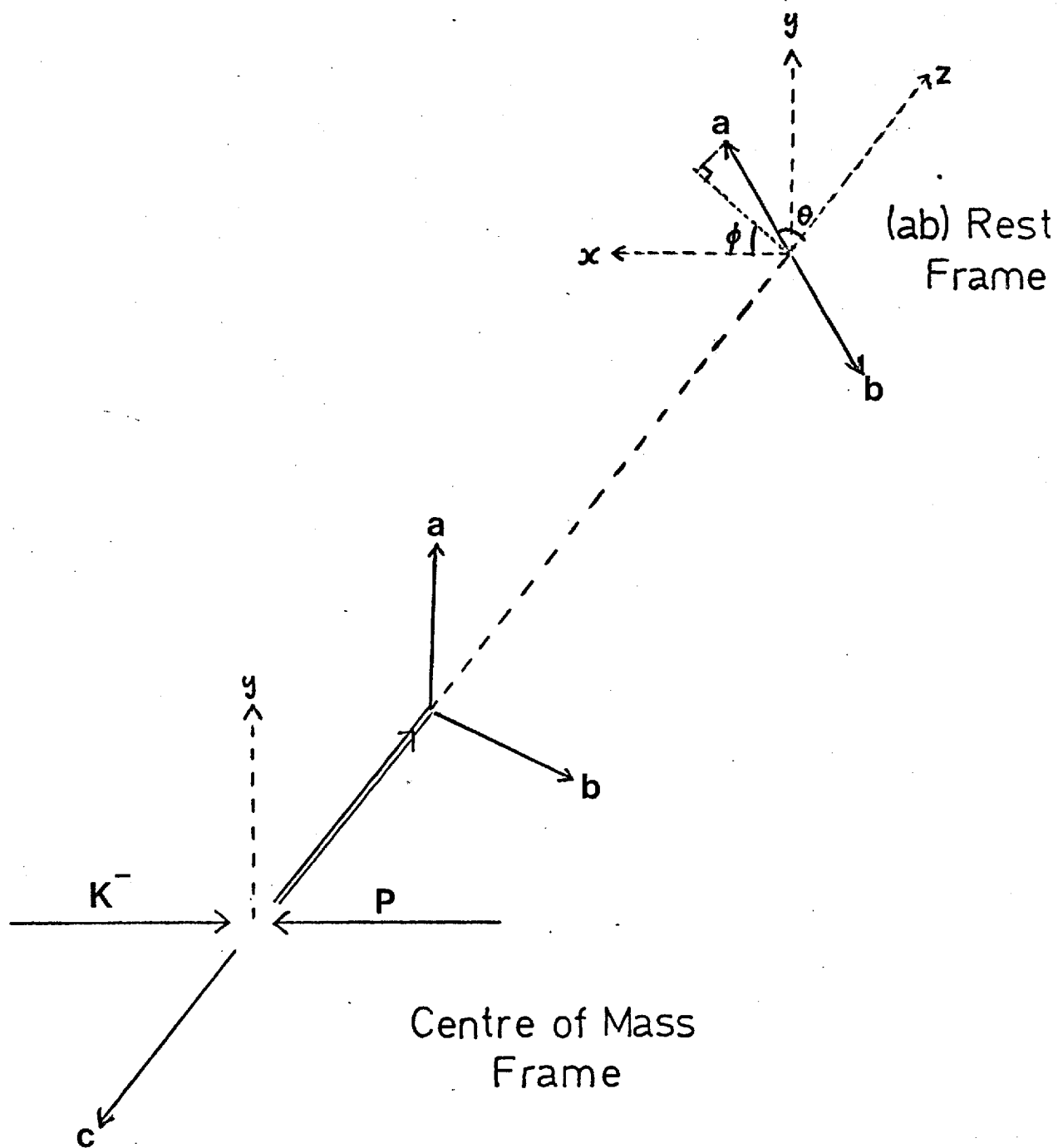


3.1 a)



3.1 b)

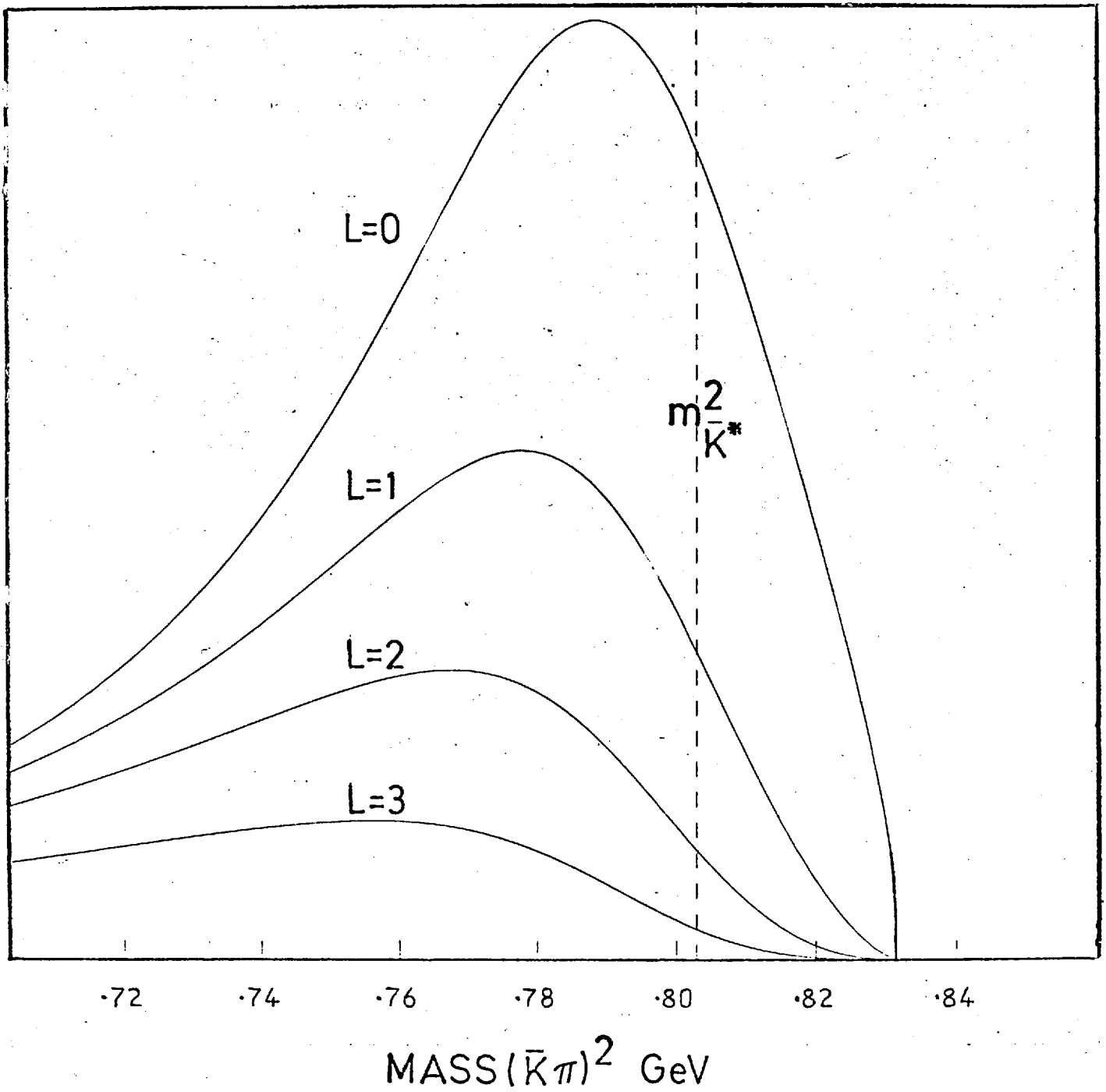
### 3.2 The Helicity System

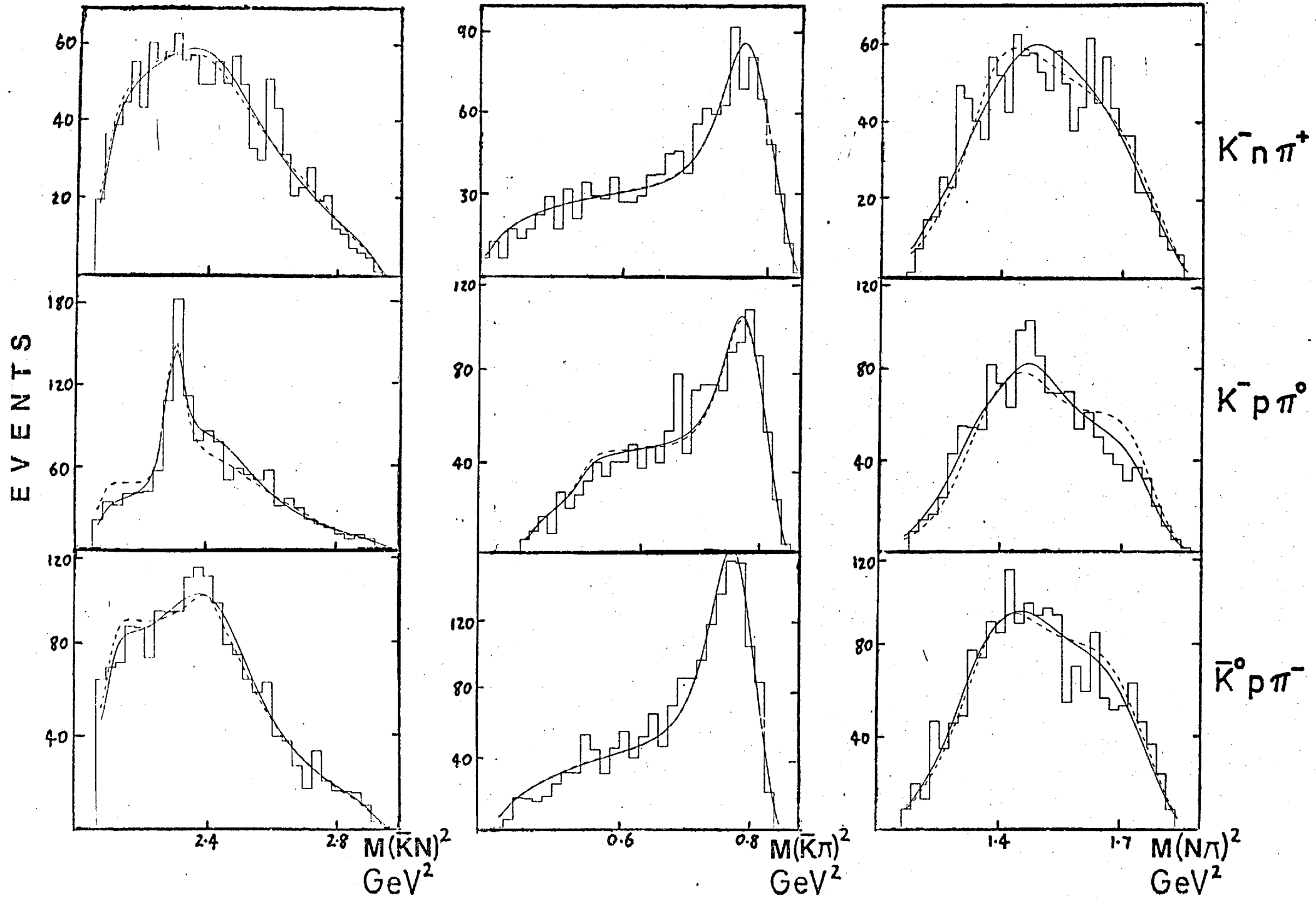


$$K^- p \rightarrow a+b+c$$

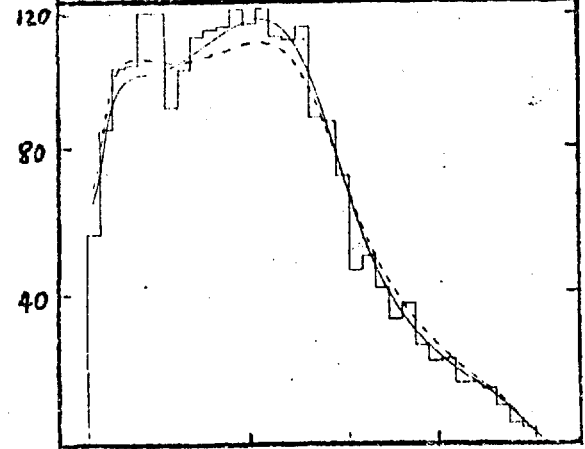
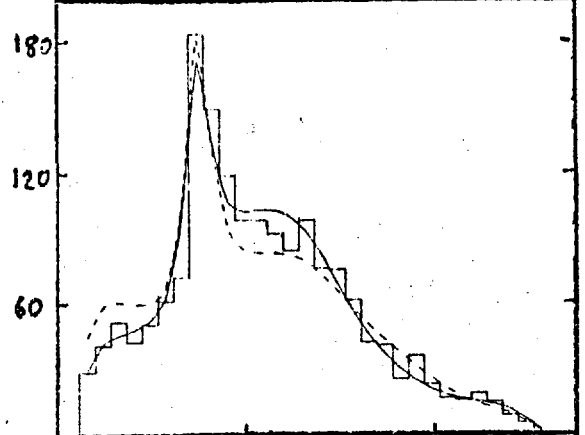
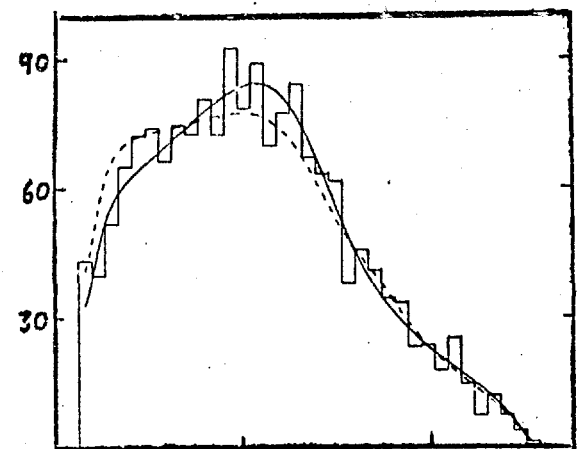
3.3

$$BW_{\bar{K}^*} \times p^{2L+1}$$

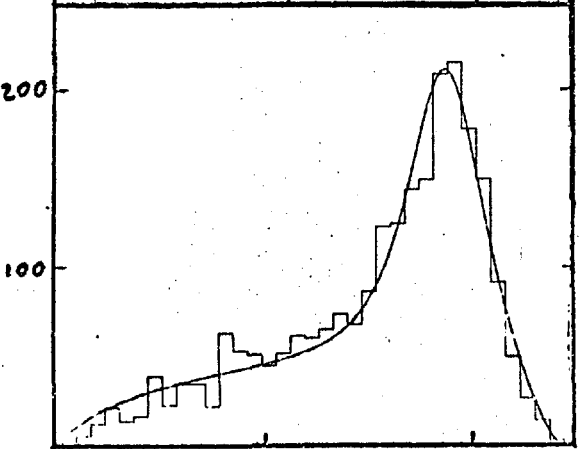
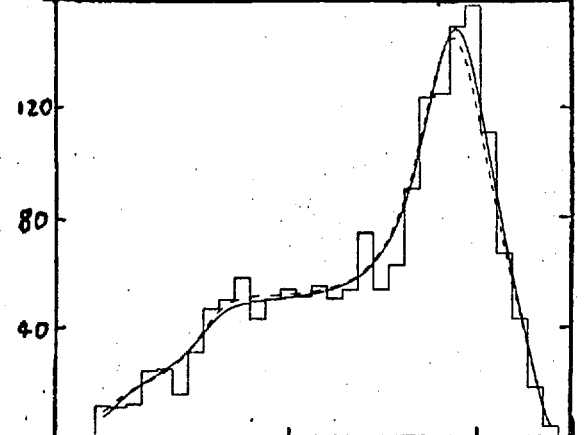
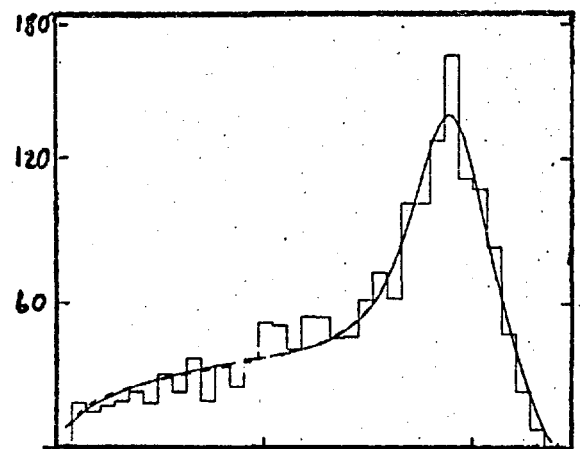




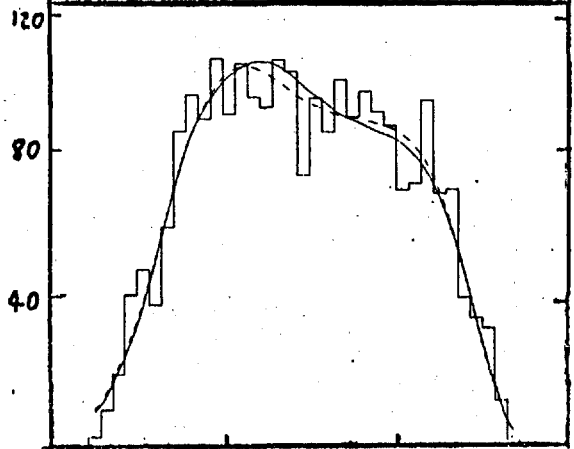
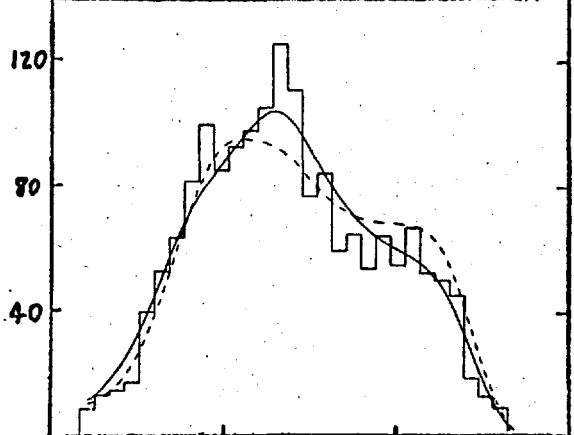
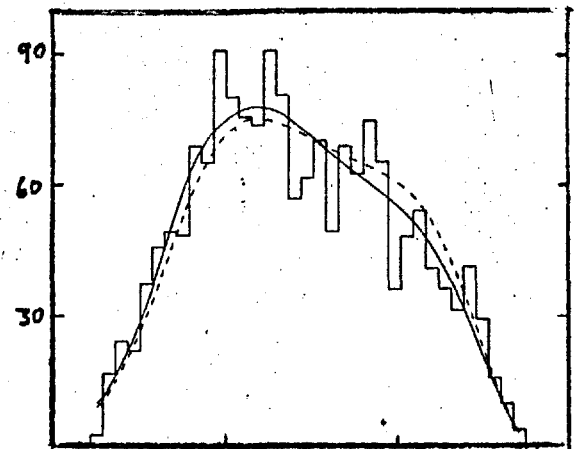
3.4  
 d) 1.125 GeV/c



$M(\bar{K}N)^2$   
GeV<sup>2</sup>



$M(\bar{K}\pi)^2$   
GeV<sup>2</sup>

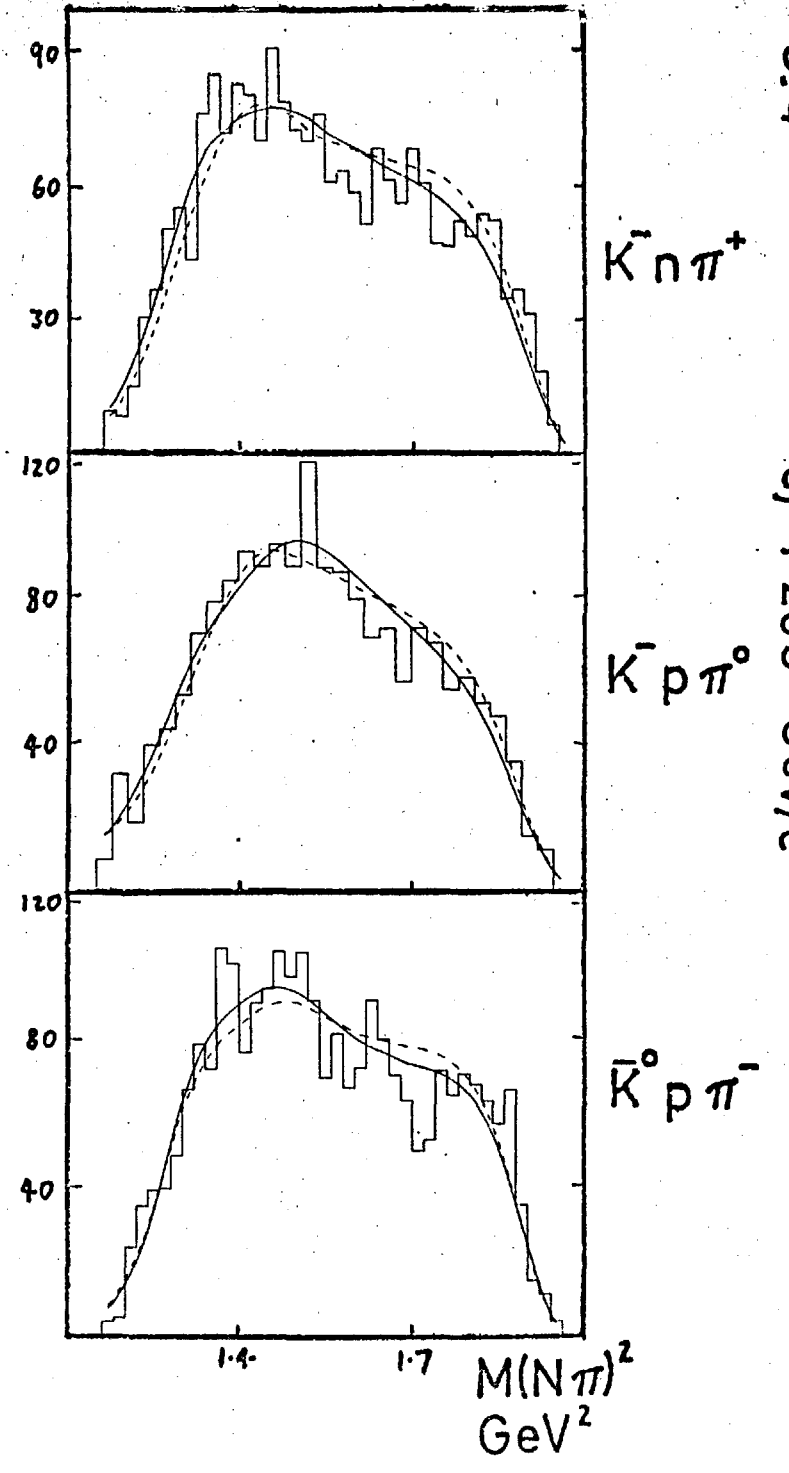
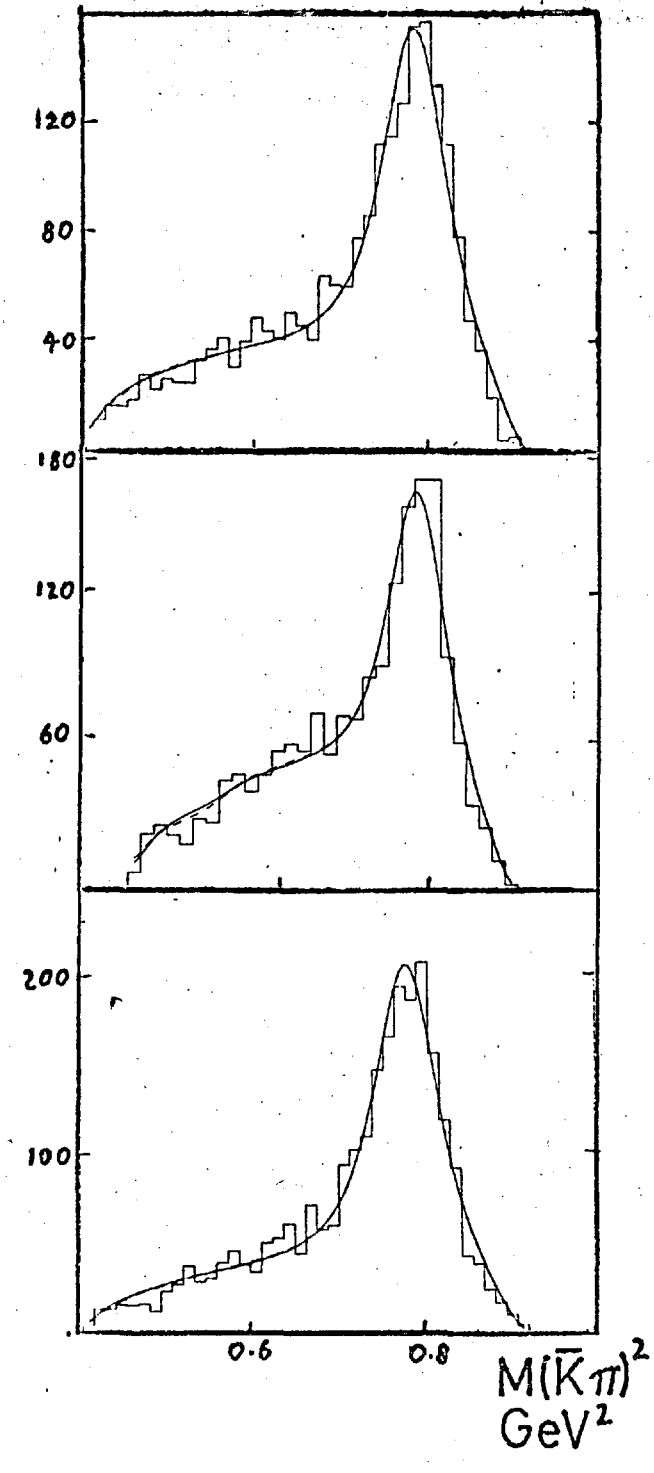
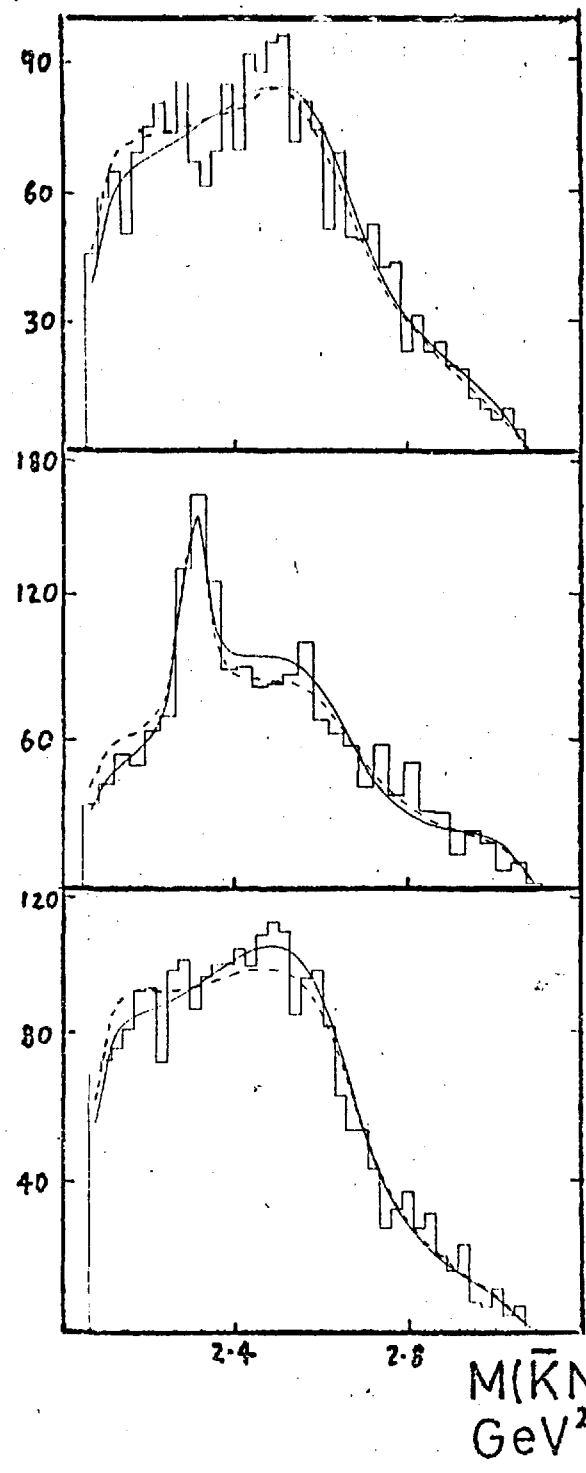


$M(N\pi)^2$   
GeV<sup>2</sup>

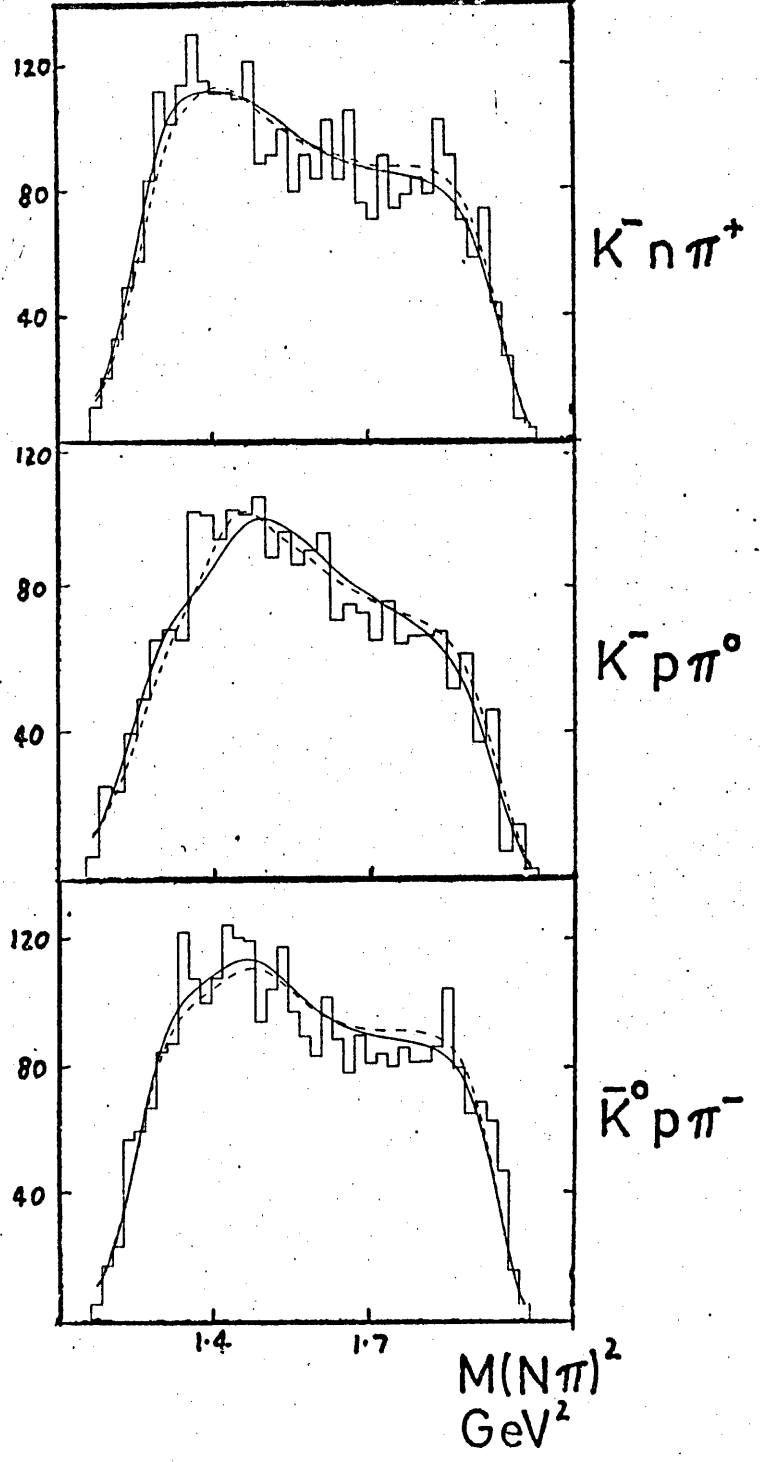
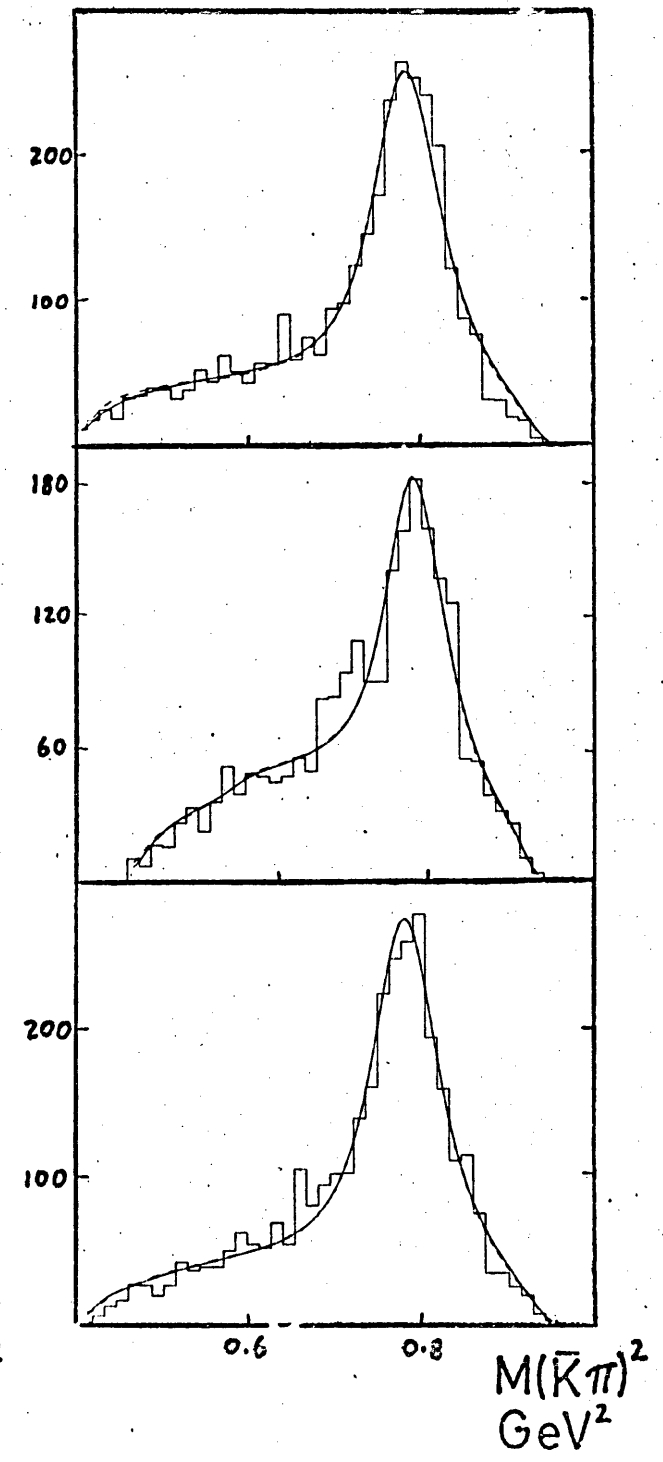
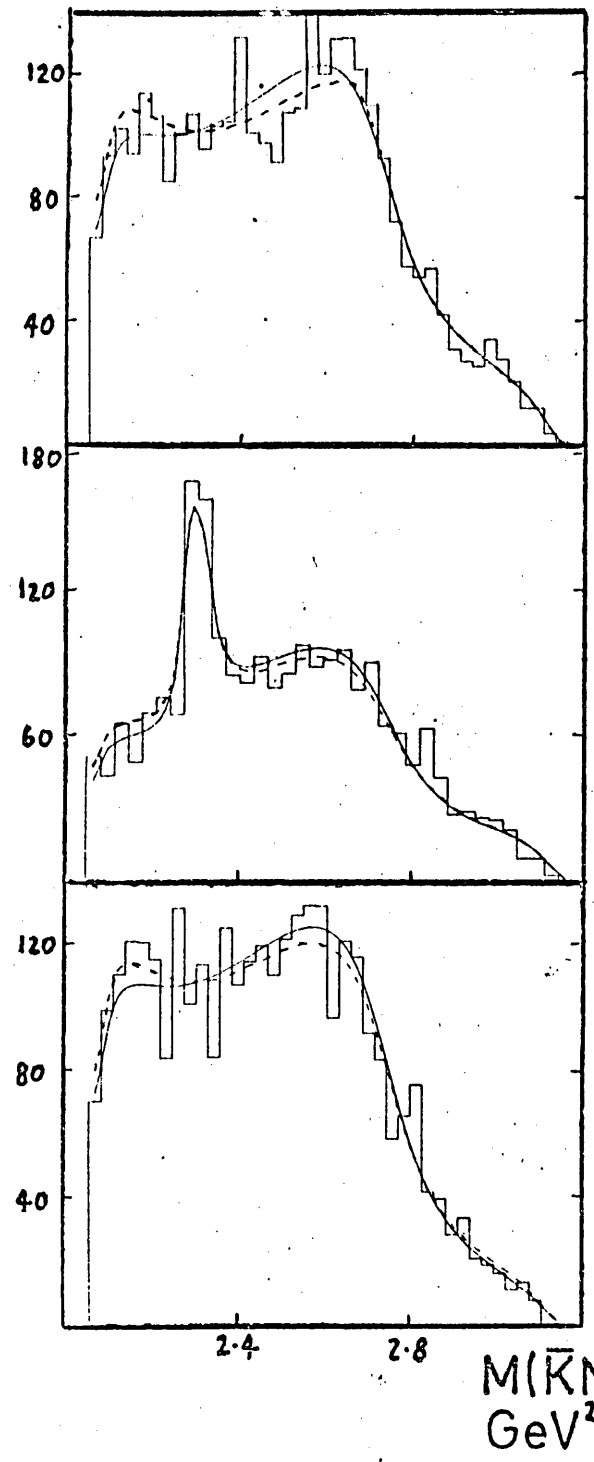
$K^-p\pi^+$

$K^-p\pi^0$

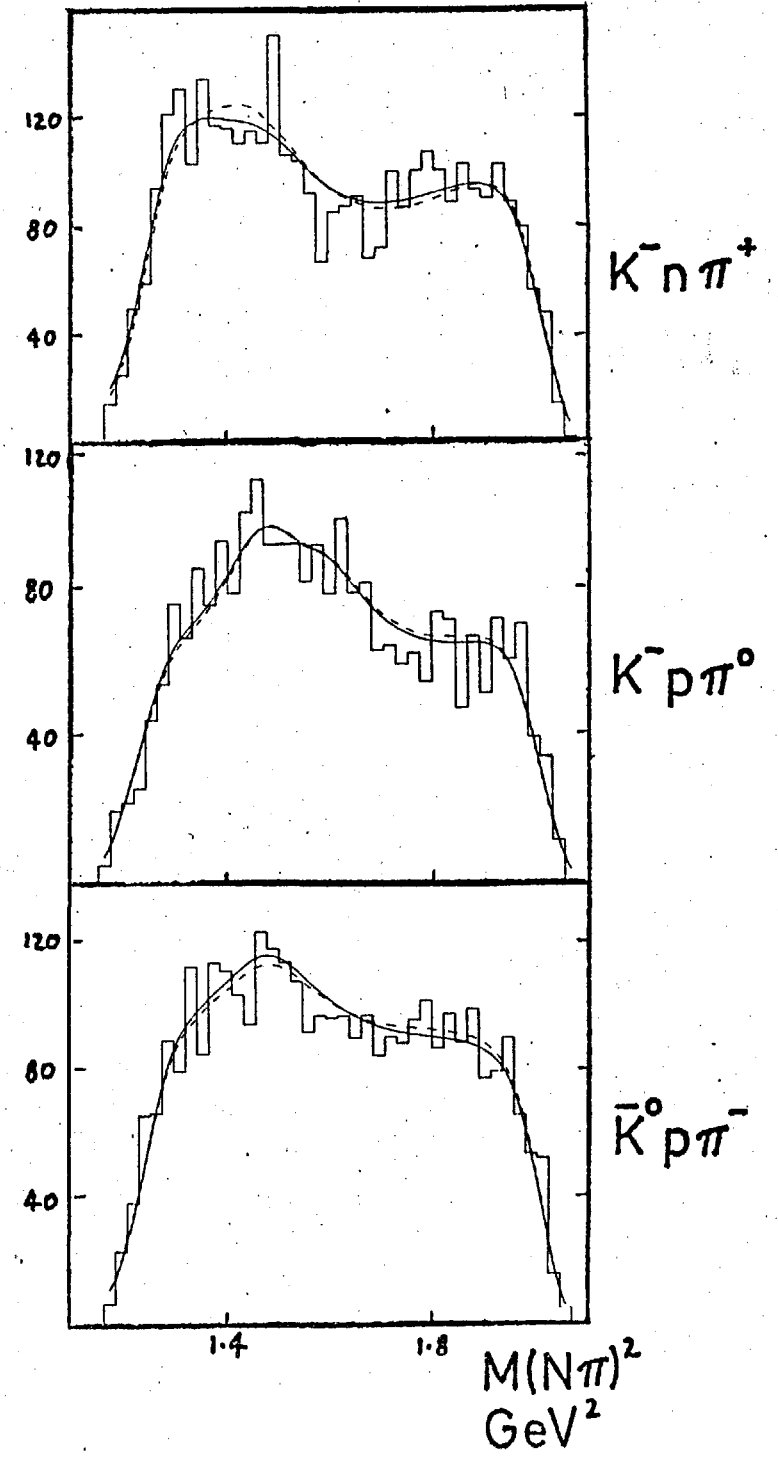
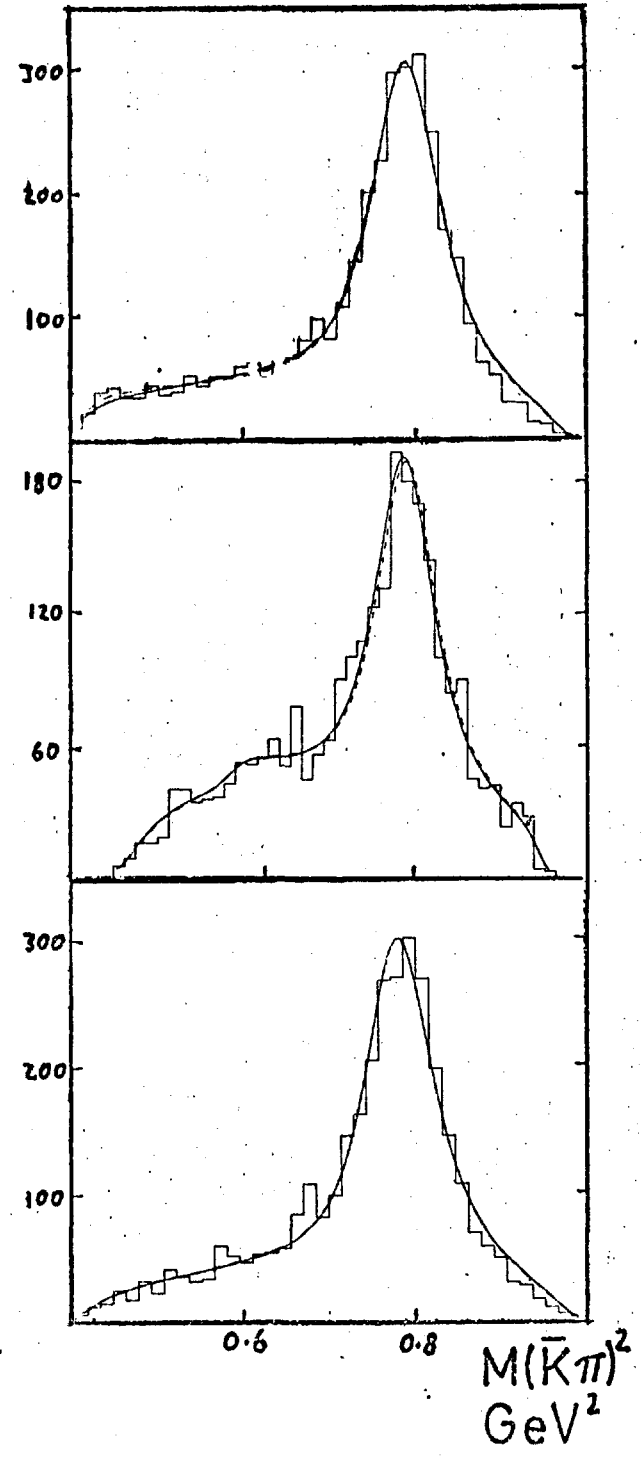
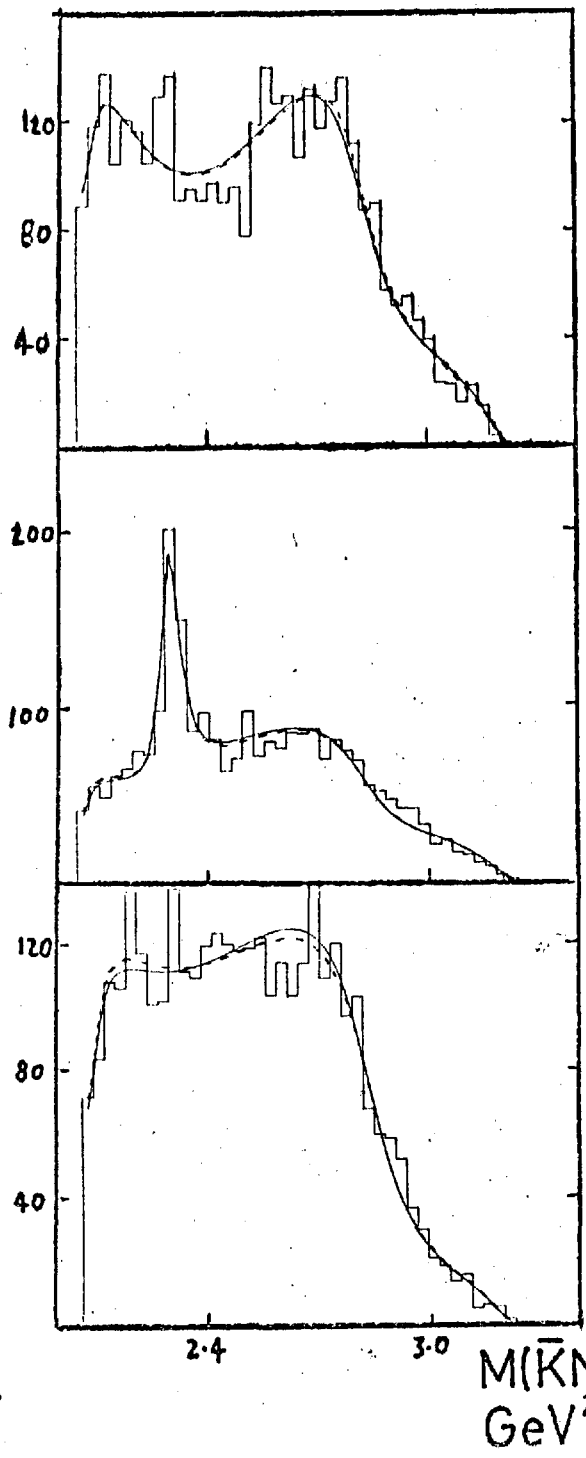
$\bar{K}^0p\pi^-$

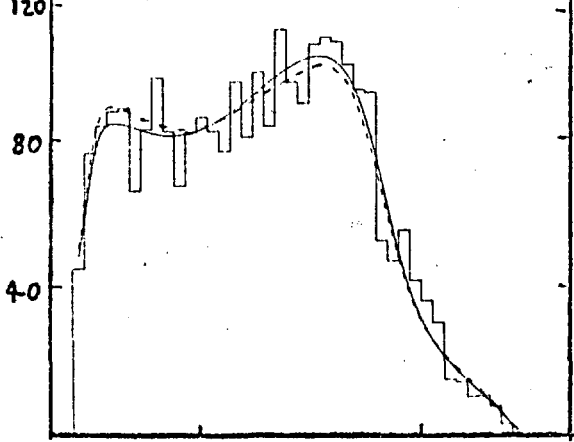
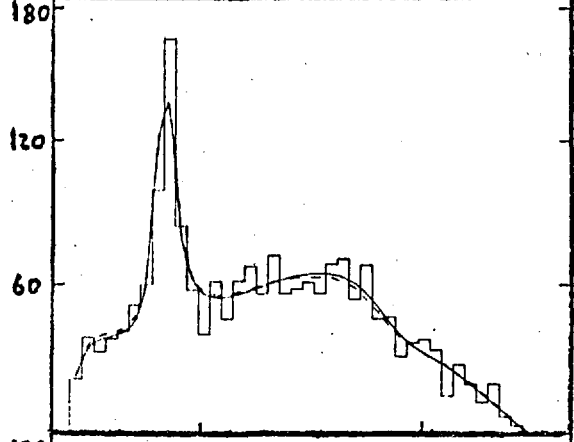
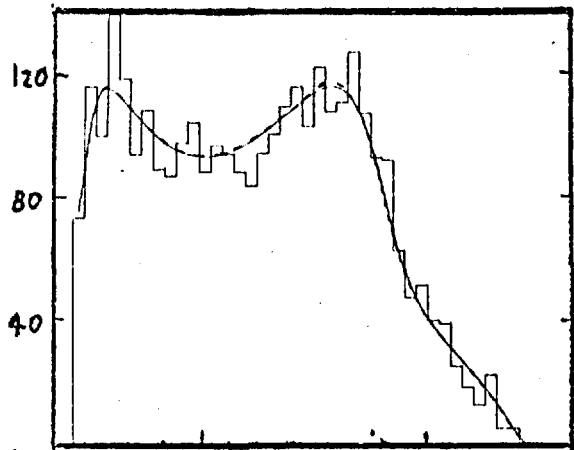


EVENTS

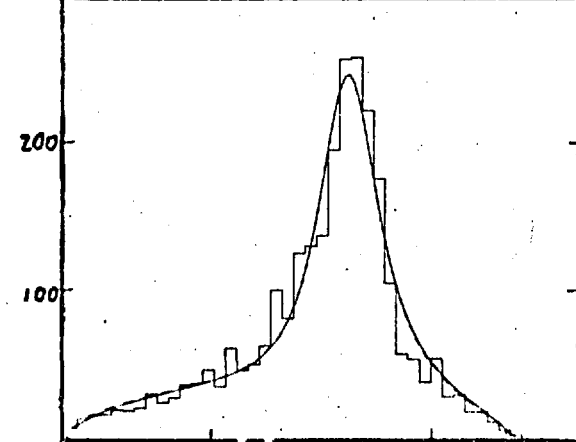
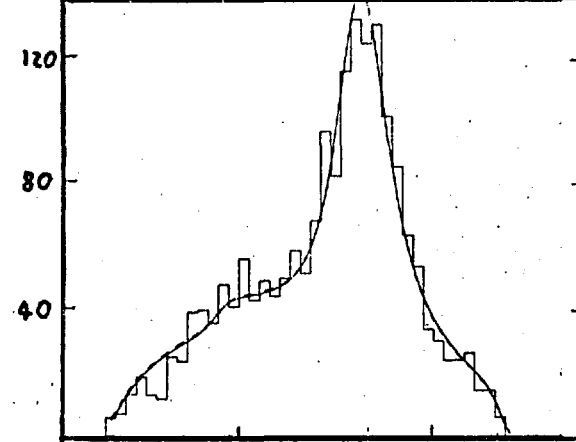
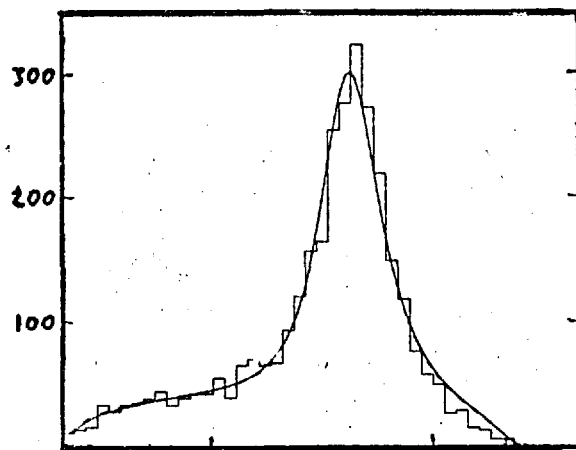


EVENTS

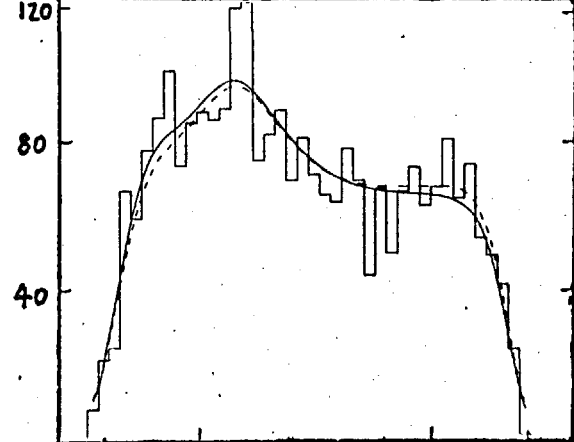
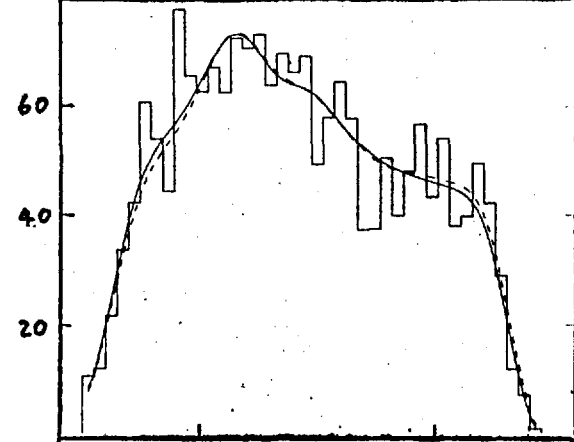




$M(\bar{K}N)^2$   
GeV<sup>2</sup>



$M(\bar{K}\pi)^2$   
GeV<sup>2</sup>

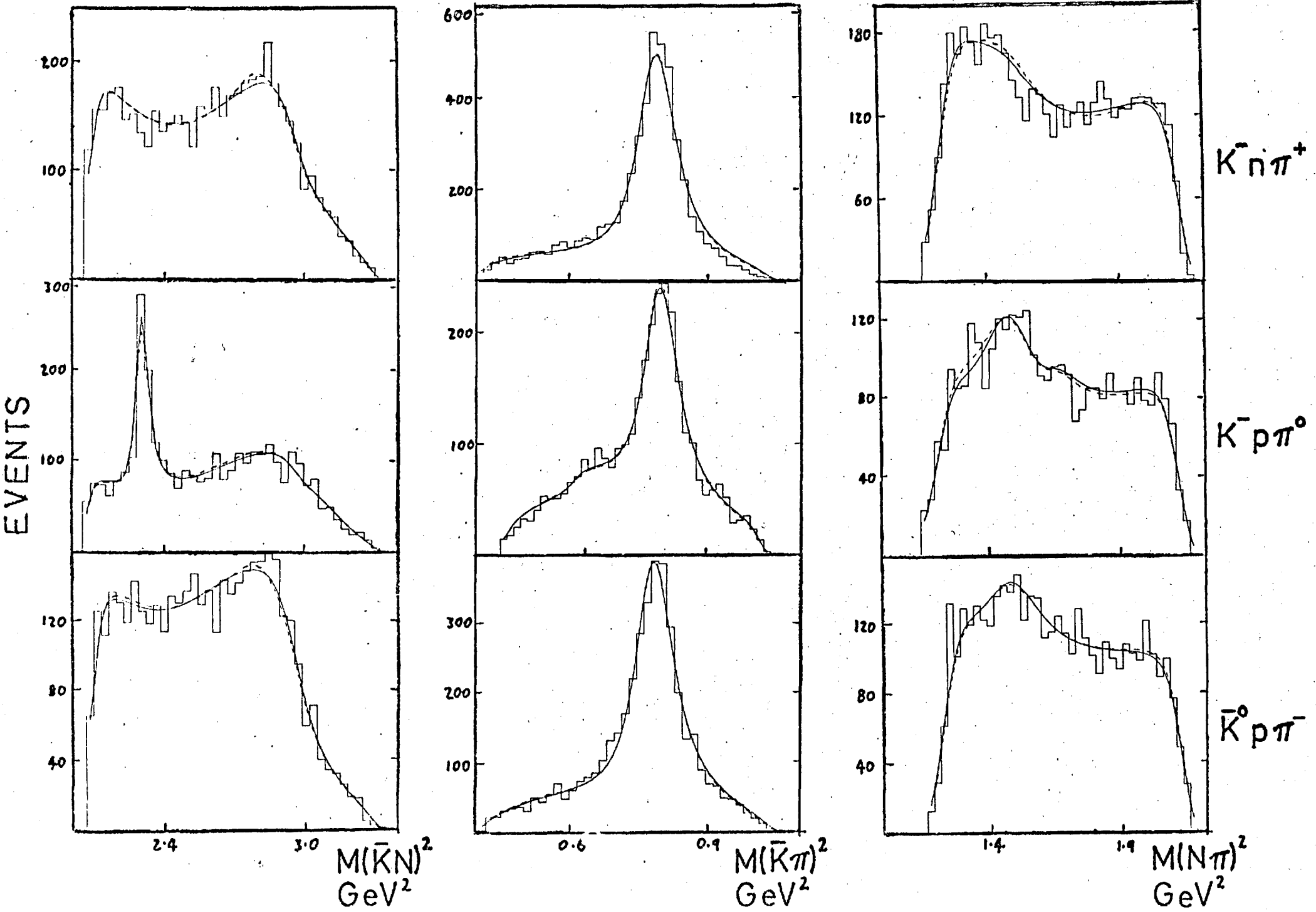


$M(N\pi)^2$   
GeV<sup>2</sup>

$K^- n \pi^+$

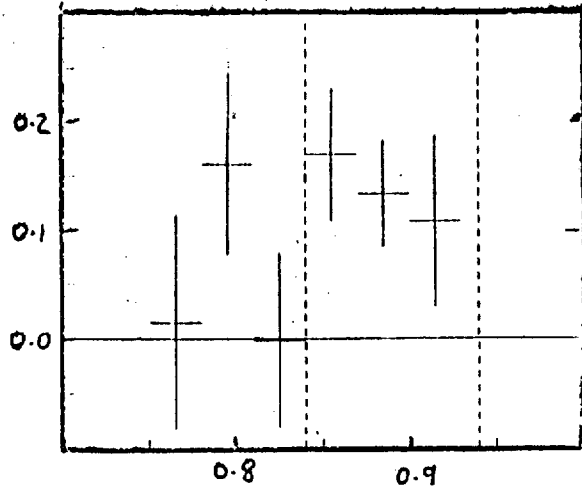
$K^- p \pi^0$

$\bar{K}^0 p \pi^-$

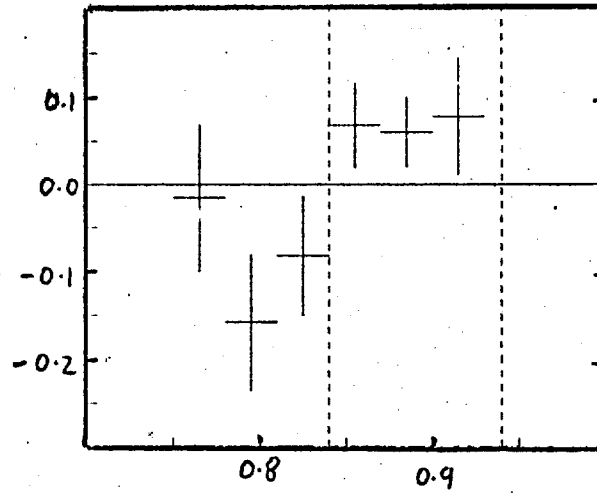


3.5 a)

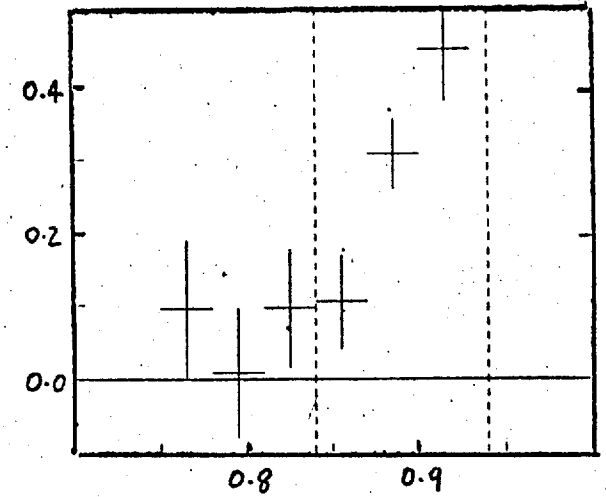
$K^- n \pi^+$



$\bar{K}^0 p \pi^-$

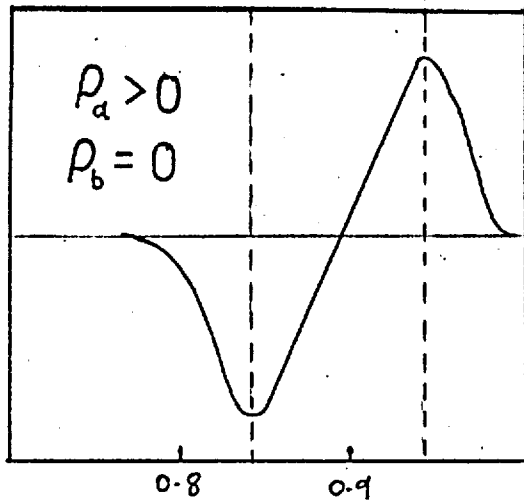


$K^- p \pi^0$

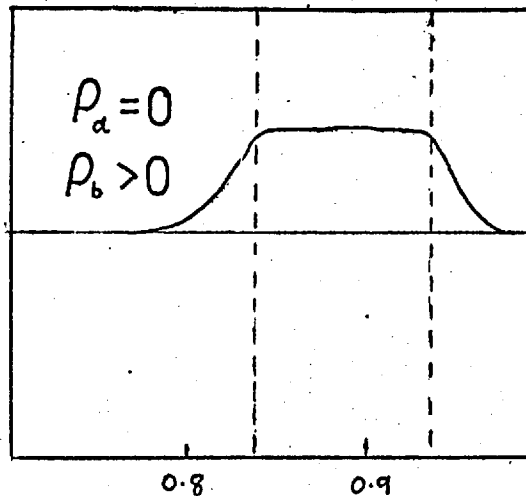


3.5 b)

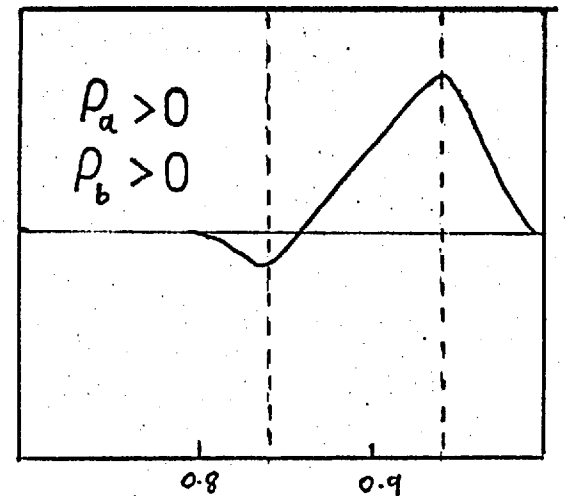
$\rho_a > 0$   
 $\rho_b = 0$



$\rho_a = 0$   
 $\rho_b > 0$

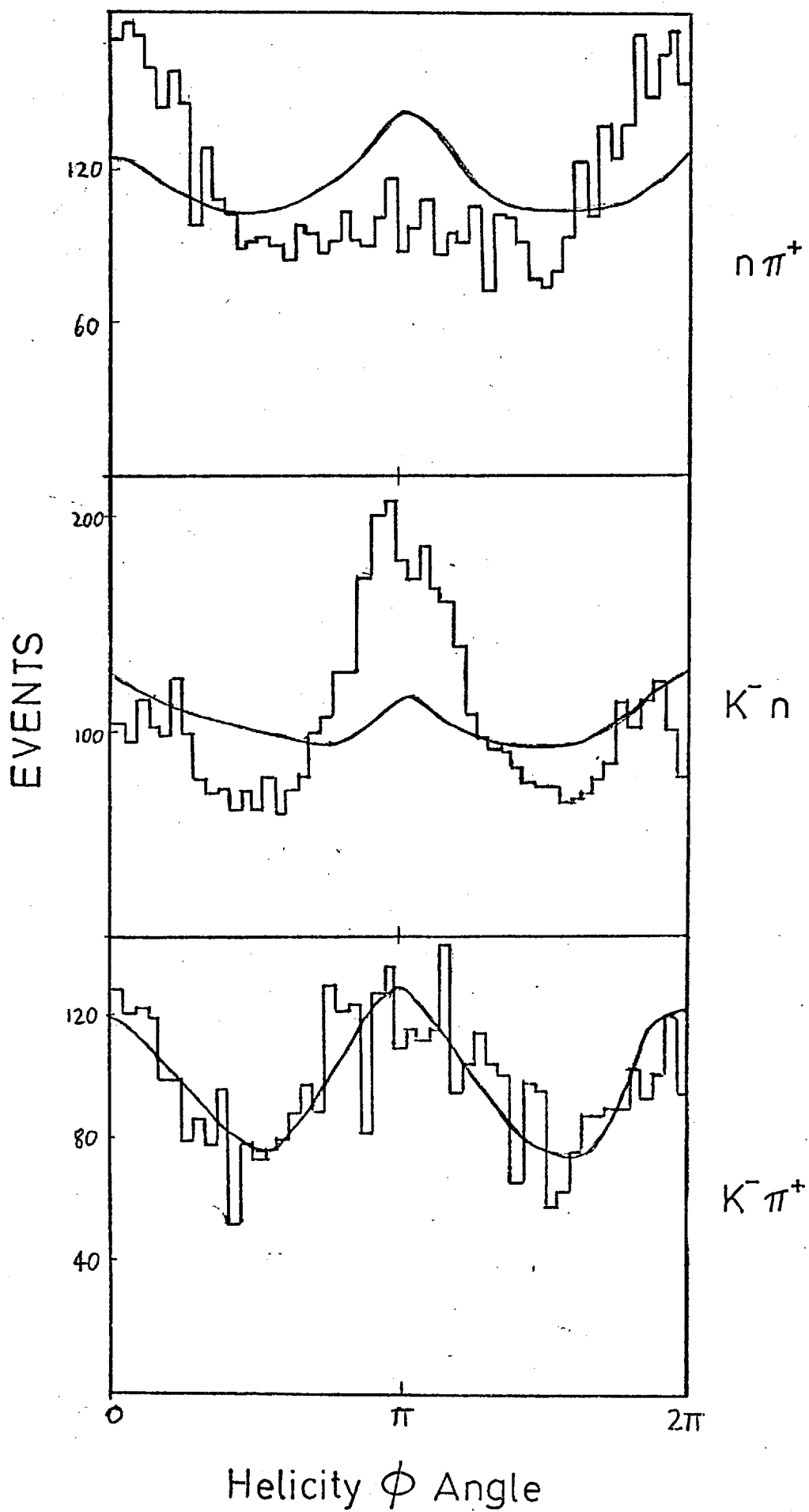


$\rho_a > 0$   
 $\rho_b > 0$



MASS( $\bar{K}\pi$ ) GeV

## 3.6



### 4.1 Introduction

In the analysis of the previous chapter, production angular dependence was ignored, with the result that average values of the density matrix elements were obtained. In reality these are all dependent upon production angle. The differential cross section,  $\frac{d\sigma}{d\cos\theta^*}$ , was also not considered, on the assumption that production effects could be factorized out from the overall density function. This is not strictly true, because in the physical world there are correlations between the distributions in the four independent variables. For instance, the relative intensities of the partial waves which form the production angle distributions vary across a resonance shape due to the effect of production angular momentum barrier factors. This results in a slightly different angular distribution on either side of the resonance band.

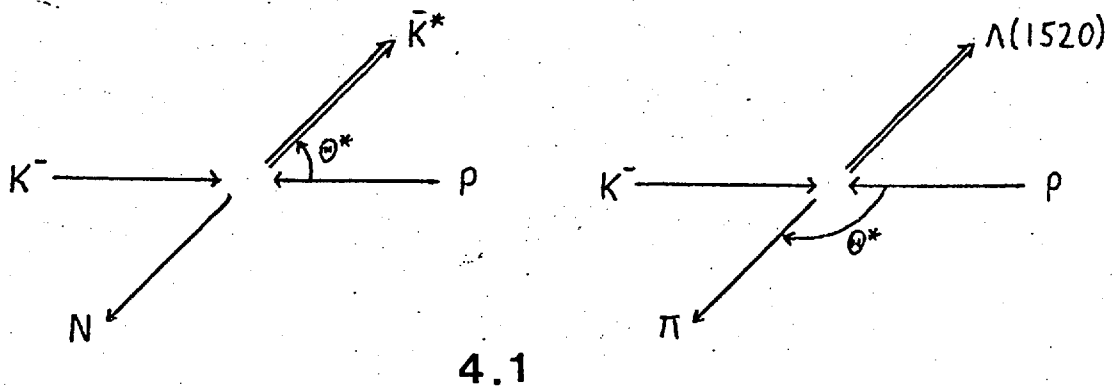
Further, the crossing resonance bands on the Dalitz Plot cannot be cleanly separated, and as mentioned in the previous chapter, the production angular structure of one resonance will reflect into the  $\phi$  distribution of the other. Both of these systematic effects have been considered unimportant compared with statistical fluctuations, and complete factorization has been assumed.

The result of the previous analysis was to assign to each event of each dataset a series of weights corresponding to the fractional contribution of each resonance and background such that  $\sum_i W_i = 1$ . By assigning the relevant weight to each event for all events in the dataset, a particular resonance contribution could be extracted, and its production angular dependence studied independent of the other contributions. This has been carried out for the  $\bar{K}^*$  and  $\Lambda(1520)$ . The  $\Delta$  has not been analysed in this variable due to the uncertainty in its extraction.

The object of the analysis described in this chapter is to use the angular dependence to study the production of  $\bar{K}^* N$  and  $\Lambda(1520)\pi$  via an S-channel partial wave analysis. A detailed analysis of the  $\bar{K}^* N$  channel is described in chapter 6. A rough qualitative analysis for the  $\Lambda(1520)\pi$  channel is also given in that chapter.

#### 4.2 Method of Analysis

The definition of production angle,  $\theta^*$ , is a matter of convention. It can be defined as the scattering angle from either the meson or baryon line of flight in the centre of mass. To keep to the general convention of "baryon goes to baryon",  $\theta^*$  is defined for  $\bar{K}^*$  and  $\Lambda(1520)$  in fig. (4.1).



The definition of the y-axis in the helicity system (see fig. (3.2)) is then  $(\underline{K}_{in}^- \times \underline{meson}_{out}) / |\underline{K}_{in}^-| \times |\underline{meson}_{out}|$ .

On inserting the  $\theta^*$  dependence into the probability density of the  $\bar{K}^*$  and  $\Lambda(1520)$  the following modifications to eqns. (3.6) and (3.7) are obtained;

For the  $\bar{K}^*$  :-

$$W(\cos \theta^*, \cos \theta, \phi) = \frac{3}{4\pi} \left[ \frac{1}{2} \sin^2 \theta - \frac{1}{2} (1 - 3 \cos^2 \theta) \rho_{00}(\cos \theta^*) - \sqrt{2} \operatorname{Re} \rho_{10}(\cos \theta^*) \sin 2\theta \cos \phi - \rho_{11}(\cos \theta^*) \sin^2 \theta \cos 2\phi \right] \frac{d\sigma}{d \cos \theta^*} \quad 4.1$$

For the  $\Lambda(1520)$  :-

$$W(\cos \theta^*, \cos \theta, \phi) = \frac{3}{4\pi} \left[ \frac{1}{2} \left( \frac{1}{3} + \cos^2 \theta \right) + 2 \left( \frac{1}{3} - \cos^2 \theta \right) \rho_{\frac{3}{2}, \frac{3}{2}}(\cos \theta^*) - \frac{2}{\sqrt{3}} \operatorname{Re} \rho_{\frac{3}{2}, \frac{1}{2}}(\cos \theta^*) \sin 2\theta \cos \phi - \frac{2}{\sqrt{3}} \operatorname{Re} \rho_{\frac{1}{2}, \frac{1}{2}}(\cos \theta^*) \sin^2 \theta \cos 2\phi \right] \frac{d\sigma}{d \cos \theta^*} \quad 4.2$$

where the Breit-Wigner functions have been removed, since we are dealing with angular effects only. To investigate the form and energy dependence of the  $\theta^*$  dependent terms, they are expanded in terms of the orthogonal Legendre polynomial series. (8) The expansion for the  $\bar{K}^*$  is given, and the  $\Lambda(1520)$  form is similar. A factor of  $2\pi$  is included to take account of the implied integration over  $\phi$ , the centre of mass azimuthal angle:-

$$\frac{d\sigma}{d\cos\theta^*} = 2\pi\lambda^2 \sum_l A_l P_l^0(\cos\theta^*) \quad 1.$$

$$P_{00} \frac{d\sigma}{d\cos\theta^*} = 2\pi\lambda^2 \sum_l B_l P_l^0(\cos\theta^*) \quad 2.$$

$$\text{Re } P_{10} \frac{d\sigma}{d\cos\theta^*} = 2\pi\lambda^2 \sum_l C_l P_l^1(\cos\theta^*) \quad 3. \quad 4.3$$

$$P_{11} \frac{d\sigma}{d\cos\theta^*} = 2\pi\lambda^2 \sum_l D_l P_l^2(\cos\theta^*) \quad 4.$$

where  $\lambda^2$  is proportional to the inverse square of the incident centre of mass momentum, and is a kinematic factor in units of cross-section.

The reason for this expansion is two-fold. In the first place the coefficients of the expansion become simply related to the series of binomial combinations of partial waves which will be developed later. Secondly, the orthogonality of the polynomials means that the  $n^{\text{th}}$  term of the expansion will theoretically give the best fit to  $n^{\text{th}}$  order structure in  $\cos\theta^*$ , so that increasing the order of expansion should increase the accuracy of the fit without changing the values of the lower order coefficients.

To extract these coefficients the method of moments was employed. Taking the simplest case of eqn. (4.3.1), and considering the coefficient  $A_n$ , the moment formula gives:-

$$\begin{aligned} \langle P_n^0 \rangle &= \frac{\sum_{i=1}^N P_n^0(\cos \theta_i^*) \times \omega_i}{\sum_{i=1}^N \omega_i} = \frac{\iiint W \times P_n^0 d\cos\theta^* d\cos\theta d\phi}{\iiint W d\cos\theta^* d\cos\theta d\phi} \\ &= \frac{\int P_n^0 \frac{d\sigma}{d\cos\theta^*} d\cos\theta^*}{\int \frac{d\sigma}{d\cos\theta^*} d\cos\theta^*} = \frac{\int P_n^0 \sum_L A_L P_L^0 d\cos\theta^*}{\int \sum_L A_L P_L^0 d\cos\theta^*} = \frac{1}{2n+1} \frac{A_n}{A_0} \end{aligned} \quad 4.4$$

where the integrals are over all physical space, and the orthonormality relation:-

$$\int_{-1}^1 P_n P_L d\cos\theta^* = \frac{2}{2n+1} \delta_{nL} \quad 4.5$$

has been employed.  $\omega_i$  is the weight of event  $i$ , consisting of the scanning weight and the resonance fraction for that event. The moment is summed over all events,  $N$ , of the dataset. Thus the moment of the  $n^{\text{th}}$  Legendre polynomial is proportional to its coefficient, provided the sample of events is large and unbiased. Applying this method with slight modifications to the other coefficients of eqn. (4.3), the following equalities are obtained:- (8)

$$\begin{aligned} A_L/A_0 &= (2L+1) \langle P_L^0(\cos\theta^*) \rangle \\ B_L/A_0 &= \frac{1}{2}(2L+1) \langle (5\cos^2\theta-1) P_L^0(\cos\theta^*) \rangle \\ C_L/A_0 &= \frac{-5(2L+1)}{4\sqrt{2}L(L+1)} \langle \sin 2\theta \cos\phi P_L^1(\cos\theta^*) \rangle \\ D_L/A_0 &= \frac{-(2L+1)(L-2)!}{(L+2)!} \langle \cos 2\phi P_L^2(\cos\theta^*) \rangle \end{aligned} \quad 4.6$$

for the  $\bar{K}^*$  coefficients, and :-

$$\begin{aligned} A_L/A_0 &= (2L+1) \langle P_L^0(\cos\theta^*) \rangle \\ B_L/A_0 &= \frac{1}{8}(2L+1) \langle (7-15\cos^2\theta) P_L^0(\cos\theta^*) \rangle \\ C_L/A_0 &= \frac{-5\sqrt{3}(2L+1)}{8L(L+1)} \langle \sin 2\theta \cos\phi P_L^1(\cos\theta^*) \rangle \\ D_L/A_0 &= \frac{-\sqrt{3}(2L+1)(L-2)!}{2(L+2)!} \langle \cos 2\phi P_L^2(\cos\theta^*) \rangle \end{aligned} \quad 4.7$$

for the  $\Lambda(1520)$  coefficients.

The error on  $\langle X \rangle$  is given by:-

$$\Delta \langle X \rangle = \left( \frac{\langle X^2 \rangle - \langle X \rangle^2}{N} \right)^{\frac{1}{2}} \quad 4.8$$

where  $X$  incorporates the constants given in eqns. (4.6) and (4.7).

The values extracted using this method are the normalized "shape"

coefficients of the distributions. They are independent of the partial cross-section and therefore do not incorporate an error due to the resonance extraction process. They are therefore to be preferred to the absolute values of the coefficients in any partial wave analysis. The value of  $A_0$  is obtained by integrating eqn. (4.3.1) over  $\cos \theta^*$ . Then:-

$$A_0 = \frac{\sigma}{4\pi \chi^2} \quad 4.9$$

where  $\sigma$  is the partial cross-section for that resonance production.

There are two methods by which the maximum order of expansion can be determined. In the first case this applies only to the  $A_L$ 's and involves setting up a fitted curve  $f(\cos \theta^*)$  where:-

$$f(\cos \theta^*) = \frac{N}{2} \sum_{L=0}^n \frac{A_L}{A_0} P_L^0(\cos \theta^*) \quad 4.10$$

where  $n$  is the maximum order under test,  $N$  is the total number of events. This curve is then compared with the data using the  $\chi^2$  formula:-

$$\chi^2 = \sum_{i=1}^M \frac{[N_i - f(\cos \theta^*) \Delta(\cos \theta^*)]^2}{\Delta N_i} \quad 4.11$$

where the sum is over  $M$  bins of width  $\Delta(\cos \theta^*)$  and content  $N_i$  for the  $i^{\text{th}}$  bin.  $\Delta N_i$  is the Poissonian error for the weighted  $N_i$  events, assuming  $N_i$  is large enough to justify its use. With bin widths of about 0.05,  $N_i$  is large enough for the data of this experiment.

This is repeated for increasing values of  $n$  where it is seen that the  $\chi^2$  drops rapidly with increasing order until it starts to level off at the ideal maximum order. However, because of statistical fluctuations in the data, and various effects in the S-channel, this maximum order varies with energy. To carry out a partial wave analysis, a maximum order must be decided upon for the whole of the energy range, because some higher order coefficients may be zero in one region and large in another. To do this, a second method has been used, which is

to plot each coefficient as a function of energy up to an arbitrary order, and decide empirically at which order the coefficients are consistent with zero. This method can be used for  $A_L$ 's to  $D_L$ 's, whereas the first method is limited to  $A_L$ 's only, since the differential cross-section is the only available experimental distribution in  $\cos \theta^*$ . As a check, the first method was also applied to the  $A_L$ 's in the  $K^- n \pi^+$  channel.

Normalized coefficients were extracted using the above method of moments for the  $\bar{K}^*$  contribution from all three channels for both the non-interference and interference models from 1.125 GeV/c upwards. Very little difference was observed between the two sets of coefficients within their errors, thus confirming the statement made in the previous chapter that the  $\bar{K}^*$  was extracted rather cleanly from the background. The coefficients were also obtained for the two channels analysed from the CRS data. Again there was little difference between the two models. The coefficients from the interference model were those used for further analysis. These are presented in table (4.1) for both experiments for the  $\bar{K}^* n$  channel.

The normalized coefficients for the  $K^{*-} p$  system are expected to be identical in the  $\bar{K}^0 p \pi^-$  and  $K^- p \pi^0$  channels. Experimentally, large differences were seen to occur in some coefficients, especially at 1.125 GeV/c. This was attributed to the more difficult extraction of the  $\bar{K}^*$  from the large background in the  $K^- p \pi^0$  channel. As a result, the coefficients at 1.125 GeV/c in the  $K^- p \pi^0$  channel were ignored. The coefficients for the  $K^{*-} p$  channel are presented separately for the  $\bar{K}^0 p \pi^-$  and  $K^- p \pi^0$  channels in table (4.3), and plotted side by side for some sample coefficients in figure (4.2). It can be seen that the only seriously affected coefficient is  $A_3/A_0$ . Since only one coefficient was affected, it was decided to combine the two channels and extract coefficients from the total  $K^{*-} p$  contribution for all

momenta above 1.125 GeV/c. These are presented together with those obtained from the  $\bar{K}^- p \pi^0$  channel of the CRS data in table (4.2).

It must be emphasized that  $\bar{K}^*$  extraction below 1.125 GeV/c was too unreliable to be used in the partial wave analysis, and so no coefficients were extracted for this region.

The normalized coefficients for the  $\Lambda(1520)\pi$  channel were obtained for the whole energy region of the present experiment. Below 1.125 GeV/c the coefficients were obtained from fits to the data described in chapter 6, where production barrier factors were applied to the  $\bar{K}^*$ . These are presented in table (4.4).

The  $A_0$ 's were all calculated using eqn. (4.9) and multiplied by an appropriate Clebsch-Gordan factor to allow for the missing decay mode of that particular charge state of the  $\bar{K}^*$ . For the  $\bar{K}^- n \pi^+$  channel this factor was  $\frac{3}{2}$  to allow for the missing  $\bar{K}^0 n \pi^0$ . For the CRS  $\bar{K}^- p \pi^0$  channel this factor was 3 to allow for the missing  $\bar{K}^0 p \pi^-$ . Because of the discrepancy between the  $\bar{K}^{*-} p$  cross-sections from the  $\bar{K}^0 p \pi^-$  and  $\bar{K}^- p \pi^0$  channels and the predicted 2:1 ratio mentioned in the last chapter, the  $A_0$ 's were taken from the former channel only, as the more reliable of the two. They were multiplied by  $\frac{3}{2}$  to give the values for the total  $\bar{K}^{*-} p$  channel.

All coefficients of the  $\bar{K}^* N$  system up to the highest order fitted in the partial wave analysis are plotted in chapter 6 as a function of centre of mass energy, together with the final fitted curves. A sample of the important coefficients of the  $\Lambda(1520)\pi$  channel are also plotted. It can be seen for the  $\bar{K}^* N$  case that the energy dependence of the higher order coefficients is highly structured, indicating a number of resonances present in the direct or S-channel. For the  $\bar{K}^{*0} n$  channel structure is seen as far as  $A_7$ ,  $B_7$ ,  $C_6$  and  $D_6$ , with higher order coefficients seen in table (4.1) to be consistent with zero across the whole energy range. For the  $\bar{K}^{*-} p$  channel statistical fluctuations appear to be more severe, and it is difficult to see

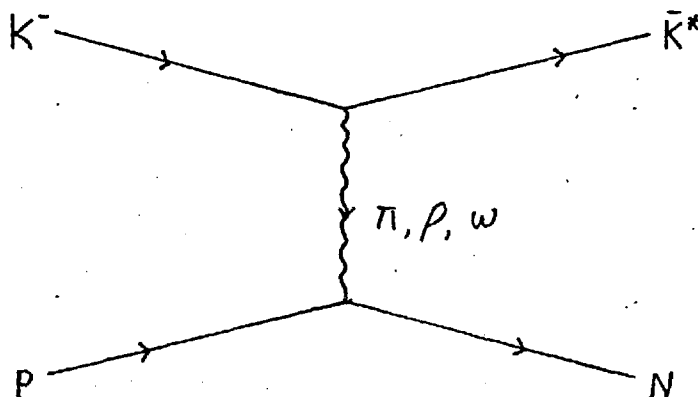
structure above  $A_6$ ,  $B_6$ ,  $C_5$  and  $D_4$ .

Fig. (4.3) plots  $\chi^2$  against increasing order of expansion for the fits to the differential cross-sections of the  $\bar{K}^{*0}n$  channel for the present experiment. The ideal maximum order is indicated by an arrow. This order is, on average, equal to 4, which should be compared with 7 for the whole energy range. The discrepancy is due to the higher order structure in the CRS energy region which is negligible at the lower energies due to the vicinity of the  $\bar{K}^*N$  threshold. Thus the inclusion of higher order coefficients in the lower energy region of the present experiment, which are in fact consistent with zero, acts as a constraint on the structure during the partial wave analysis. This is more desirable than omitting these coefficients completely.

In the  $\Lambda(1520)\pi$  system less structure is evident and appears to be present up to fourth order only.

#### 4.3 The Differential Cross Sections

The extracted  $\bar{K}^*N$  differential cross-sections are presented for some typical energies in fig. (4.4). Superimposed on these histograms are the fitted curves calculated using eqn. (4.10) up to the highest meaningful coefficient. It can be seen that in all three channels there is a prominent forward peaking of the distribution which increases in importance with increasing energy. This peaking is typical of peripheral reactions which are usually explained in terms of the exchange of certain virtual particles in the t-channel, (see fig. (4.5)).



4.5

Field theory predicts the differential cross-section in the  $t$ -variable for the exchange of a virtual particle of mass  $m_0$  to be proportional to:-

$$\frac{t}{(t - m_0^2)^2} \quad 4.12$$

where  $t$  is the exchanged four-momentum-squared of the system, defined as:-

$$t = (P_1 - P_3)^2 \quad \text{for } 1 + 2 \rightarrow 3 + 4 \quad 4.13$$

and  $P$  is a 4-momentum.

$t$  can be shown to be a function of production angle, and so peaking in the latter can be explained by a sum of terms such as eqn. (4.12) for all possible exchanges in the  $t$ -channel, which obey the selection rules for the conservation of the quantum numbers at each vertex. For the  $K^- p \rightarrow \bar{K}^* N$  system possible exchange particles are the  $\pi$ ,  $\rho$  and  $\omega$ , the latter possible for  $K^- \rightarrow K^{*-}$  only, since it has isospin zero.

The data of fig. (4.4) show, however, that this simple picture of  $t$ -channel exchange is inadequate to explain the structure beneath the forward peak where rapid variation with energy is seen, especially in the Legendre coefficients which parametrize this structure. Thus an  $S$ -channel approach is more desirable at these low energies where the energy variation can be more readily explained. At higher energies where resonant structure disappears, or more correctly blurs into a continuum, the forward peaking in  $\cos \theta^*$  becomes far the most dominant effect, and here a  $t$ -channel analysis is more appropriate. An interesting point which can be made here is that, whereas an  $S$ -channel analysis demands a maximum order of expansion in terms of Legendre polynomials, thus biasing the analysis somewhat due to the omission of high spin contributions, a  $t$ -channel study automatically takes these effects into account, since it parametrizes the forward peak in a different way. Thus an ideal analysis would be to carry out an  $S$ -channel partial wave

analysis in which some form of t-channel exchange contributes a high spin background. In this experiment however, for the sake of simplicity, this was not carried out and a pure S-channel partial wave analysis was undertaken.

#### 4.4 The $\varnothing$ distribution

As mentioned in section (3.8) of the previous chapter, the three-variable Dalitz Plot analysis was unable to fit the helicity  $\varnothing$  distributions. This was attributed to structure in production angle,  $\cos \vartheta^*$ , reflecting into these distributions. A test was now made to see whether this was indeed the case. At 1.355 GeV/c in the  $\bar{K}^- n \pi^+$  channel the complete production angular dependence of the  $\bar{K}^*$  was applied to the density function eqn. (3.3) in differential cross-section and the differential density matrix elements. The resulting four-variable function was then superimposed on the data using the FOWL technique described in section (3.8). As expected there was no change to the mass squared and helicity  $\cos \vartheta$  projections. A large improvement, though, was seen in the  $\varnothing$  projections in the  $n\pi$  and  $\bar{K}n$  systems, thus confirming what was expected. The structure in  $\cos \vartheta^*$  for the  $\bar{K}\pi$  and  $\bar{K}n$  projections was well fitted, except that the forward  $\bar{K}\pi$  peak could not be fully reproduced. The  $n\pi$  projection was badly fitted. To improve on this, required structure much larger than the  $\Delta$  or  $\Sigma(1765)$  could suffice. This pointed to the background having some form of angular distribution in the  $n\pi$  system. Legendre coefficients were extracted using the method of moments from the differential cross-section of the background contribution in the  $n\pi$  system. For completeness this was also carried out for the  $\Delta$  and  $\Sigma(1765)$  in their respective systems. Expansions were taken up to the seventh order in all cases. The total angular dependence was then applied to FOWL. The result showed a much improved fit to  $\cos \vartheta^*$  in the  $n\pi$

system. However a decrease in quality of the  $\emptyset$  fit in the  $\bar{K}\pi$  system was also noted. Furthermore the fit to  $\cos \theta^*$  in the  $\bar{K}\pi$  system could still not reproduce the full forward peak. To account for the latter, the Legendre coefficients were calculated for the background contribution in the  $\bar{K}\pi$  system, and the total angular dependence was assumed to be a combination of structure in both the  $n\pi$  and  $\bar{K}\pi$  systems:-

$$\text{i.e. } \frac{d\sigma}{d\cos\theta_{K\pi}^* d\cos\theta_{n\pi}^*} \propto \left( \sum_L A_L P_L^0(\cos\theta_{K\pi}^*) \right) \left( \sum_L A'_L P_L^0(\cos\theta_{n\pi}^*) \right) \quad 4.14$$

The results from FOWL showed an improvement in the fit to  $\cos \theta^*$  in the  $\bar{K}\pi$  system, but still gave a bad fit to  $\emptyset$  in this system. Fig. (4.6) shows two fits to the  $\emptyset$  and  $\cos \theta^*$  distributions. The dashed curve is the result with angular dependence in the  $\bar{K}^*$  only. The solid curve is the result of angular dependence in all processes including the two contributions to background.

A possible explanation for the bad fit to  $\emptyset$  in the  $\bar{K}\pi$  system is that the angular dependence of the background in the  $n\pi$  system has been double-counted. That is, the angular dependence in the  $n\pi$  system has been assumed to originate within that system, whereas there is a possibility of structure in, say, the  $\bar{K}\pi$  system also reflecting into it. In this case,  $\bar{K}\pi$  structure in  $\cos \theta^*$  which does not reflect into its own  $\emptyset$  system, will do so if it is classed as  $n\pi$  structure, thus producing a bad fit to the data in this projection. Since it is impossible to tell where angular structure originates in background, the structure from the  $n\pi$  and  $\bar{K}\pi$  systems cannot be uniquely determined, and hence there is no easy way out of this problem.

It is of interest to consider why background has been assigned a large  $\cos \theta^*$  dependence. If a strong resonance such as the  $\bar{K}^*$  is present above background, then events within the resonance band will have a certain probability of being either  $\bar{K}^*$  or background. On

extracting the background contribution by applying the relevant weight to each event, a certain proportion of the sample will always be pure  $\bar{K}^*$  events, since resonance and background events are indistinguishable within the resonance band. Thus the background contribution will simulate in  $\cos \theta^*$ , to some extent, the structure of the  $\bar{K}^*$ . It is for this reason that the above fits were unable to reproduce the full forward peak in  $\cos \theta^*$  of the  $\bar{K} \pi$  system when background was not given an angular distribution in this variable.

Conversely, the fact that background is assigned an angular structure similar to that of the  $\bar{K}^*$  means that this structure is being taken from the  $\bar{K}^*$  and is being replaced by a uniform phase-space - like distribution. The result is that the extracted  $\bar{K}^* N$  normalized Legendre coefficients will be slightly smaller than the true values. This feature is unique to a three variable analysis, since no uniformity in production angle can be imposed on the background. Thus a possible systematic effect may occur in the following partial wave analysis, which is hoped to be small compared with the errors in the coefficients.

As regards a four variable analysis, where production angular dependence is included, the above discussion shows that a uniform  $\cos \theta^*$  distribution must be imposed on background, just as in the other three variables. If it is attempted to fit possible background structure in  $\cos \theta^*$ , a certain amount of structure will be taken from the resonance as well. Analysis is at present continuing using a four variable approach.

\* \* \* \* \*

Table (4.1)

 $\bar{K}^{*0}_n$  Legendre Coefficients

a)

BEAM MOMENTUM (GEV/C)	$A_0$	$A_1/A_0$	$A_2/A_0$	$A_3/A_0$	$A_4/A_0$	$A_5/A_0$	$A_6/A_0$	$A_7/A_0$
1.125	± 0.056 0.005	0.067 0.076	0.008 0.097	0.103 0.113	-0.075 0.131	0.038 0.145	-0.162 0.154	-0.019 0.164
1.165	± 0.073 0.004	0.264 0.060	0.225 0.079	0.464 0.093	0.149 0.105	0.092 0.116	0.084 0.125	-0.173 0.133
1.205	± 0.090 0.004	0.448 0.055	0.413 0.073	0.529 0.086	0.261 0.099	0.110 0.110	0.096 0.119	0.088 0.128
1.245	± 0.122 0.004	0.422 0.044	0.558 0.056	0.531 0.067	0.230 0.077	0.002 0.085	0.107 0.091	0.030 0.097
1.285	± 0.138 0.004	0.576 0.041	0.757 0.052	0.592 0.062	0.246 0.071	-0.038 0.078	-0.100 0.085	0.017 0.091
1.320	± 0.164 0.005	0.682 0.041	0.868 0.051	0.629 0.061	0.005 0.072	-0.219 0.079	-0.210 0.084	-0.182 0.091
1.355	± 0.192 0.005	0.742 0.032	0.944 0.040	0.418 0.049	-0.038 0.056	-0.239 0.062	-0.095 0.068	-0.002 0.073
1.370	± 0.198 0.025	0.779 0.108	1.043 0.127	0.716 0.164	-0.270 0.193	0.225 0.219	0.198 0.237	0.191 0.260
1.419	± 0.232 0.025	0.771 0.101	0.926 0.124	0.294 0.159	-0.111 0.183	-0.082 0.197	0.096 0.212	0.122 0.235
1.464	± 0.256 0.029	1.036 0.099	1.151 0.124	0.665 0.160	-0.087 0.183	-0.166 0.200	-0.026 0.221	-0.295 0.236
1.512	± 0.232 0.021	0.935 0.090	0.923 0.115	0.262 0.146	-0.178 0.163	0.073 0.172	-0.018 0.190	0.171 0.208
1.546	± 0.271 0.022	1.068 0.074	1.208 0.095	0.535 0.127	0.118 0.143	0.030 0.156	0.318 0.168	0.302 0.184
1.606	± 0.342 0.026	1.182 0.075	1.174 0.102	0.236 0.138	0.235 0.155	0.334 0.169	0.525 0.183	0.361 0.196
1.652	± 0.292 0.025	1.136 0.080	1.242 0.106	0.567 0.139	0.341 0.156	0.540 0.170	0.231 0.186	0.253 0.201
1.706	± 0.336 0.033	1.202 0.086	1.410 0.112	0.562 0.153	0.371 0.174	0.313 0.194	0.292 0.211	0.363 0.229
1.741	± 0.318 0.034	1.169 0.075	1.253 0.104	0.813 0.136	0.588 0.157	0.738 0.169	0.575 0.186	0.341 0.202
1.800	± 0.339 0.030	1.334 0.088	1.461 0.125	0.869 0.163	0.756 0.187	0.520 0.211	0.211 0.229	-0.289 0.252
1.841	± 0.257 0.025	1.175 0.102	1.318 0.144	1.012 0.185	0.844 0.217	0.548 0.244	0.591 0.266	0.317 0.284

b)

BEAM MOMENTUM (GEV/C)	$B_0/A_0$	$B_1/A_0$	$B_2/A_0$	$B_3/A_0$	$B_4/A_0$	$B_5/A_0$	$B_6/A_0$	$B_7/A_0$
1.125	$\pm$ 0.352 0.032	0.022 0.061	-0.096 0.086	0.083 0.094	0.375 0.109	0.140 0.118	-0.208 0.130	-0.040 0.140
1.165	$\pm$ 0.406 0.026	0.192 0.053	0.117 0.076	0.494 0.086	0.504 0.093	0.190 0.106	0.118 0.115	-0.071 0.124
1.205	$\pm$ 0.412 0.024	0.203 0.050	0.174 0.070	0.570 0.079	0.542 0.089	-0.009 0.099	0.011 0.108	0.119 0.117
1.245	$\pm$ 0.467 0.018	0.244 0.040	0.259 0.056	0.331 0.065	0.552 0.072	-0.045 0.079	0.170 0.083	0.046 0.090
1.285	$\pm$ 0.537 0.017	0.388 0.040	0.439 0.053	0.414 0.061	0.434 0.068	-0.042 0.075	-0.057 0.082	-0.052 0.089
1.320	$\pm$ 0.515 0.017	0.454 0.040	0.511 0.051	0.430 0.059	0.128 0.069	-0.223 0.075	-0.137 0.080	-0.096 0.087
1.355	$\pm$ 0.492 0.013	0.412 0.032	0.514 0.041	0.374 0.049	0.225 0.055	-0.054 0.061	0.197 0.066	0.114 0.070
1.370	$\pm$ 0.563 0.041	0.427 0.102	0.564 0.124	0.602 0.145	0.001 0.178	-0.061 0.205	-0.093 0.210	-0.157 0.231
1.419	$\pm$ 0.423 0.042	0.218 0.095	0.306 0.117	0.213 0.142	0.087 0.161	0.247 0.172	0.289 0.182	0.025 0.208
1.464	$\pm$ 0.441 0.042	0.516 0.099	0.554 0.125	0.325 0.154	0.222 0.175	0.118 0.182	0.322 0.201	0.099 0.221
1.512	$\pm$ 0.488 0.040	0.435 0.091	0.424 0.121	0.258 0.145	0.378 0.155	0.464 0.159	0.242 0.180	0.098 0.192
1.546	$\pm$ 0.368 0.030	0.431 0.069	0.571 0.089	0.276 0.112	0.381 0.124	0.283 0.135	0.392 0.143	0.303 0.159
1.606	$\pm$ 0.483 0.034	0.654 0.077	0.608 0.104	0.331 0.131	0.518 0.145	0.544 0.153	0.464 0.167	0.318 0.180
1.652	$\pm$ 0.457 0.034	0.569 0.080	0.612 0.107	0.323 0.133	0.482 0.149	0.670 0.155	0.417 0.169	0.227 0.189
1.706	$\pm$ 0.447 0.036	0.526 0.087	0.564 0.114	0.296 0.140	0.404 0.157	0.444 0.171	0.365 0.186	0.329 0.208
1.741	$\pm$ 0.467 0.033	0.590 0.076	0.566 0.105	0.471 0.132	0.516 0.149	0.720 0.164	0.652 0.180	0.484 0.192
1.800	$\pm$ 0.492 0.037	0.735 0.092	0.765 0.128	0.581 0.154	0.683 0.173	0.572 0.193	0.336 0.208	-0.066 0.223
1.841	$\pm$ 0.435 0.044	0.517 0.102	0.561 0.147	0.592 0.176	0.893 0.195	0.879 0.213	0.636 0.232	0.198 0.246

c)

BEAM MOMENTUM (GEV/C)	$C_0/A_0$	$C_1/A_0$	$C_2/A_0$	$C_3/A_0$	$C_4/A_0$	$C_5/A_0$	$C_6/A_0$	$C_7/A_0$
1.125	± 0.0	0.056 0.028	-0.017 0.020	0.005 0.017	0.082 0.014	-0.002 0.013	-0.002 0.012	-0.008 0.012
1.165	± 0.0	0.025 0.020	0.010 0.016	0.059 0.013	0.088 0.012	0.016 0.011	0.017 0.010	0.019 0.009
1.205	± 0.0	0.043 0.018	-0.018 0.014	0.045 0.012	0.059 0.010	0.012 0.010	0.010 0.009	0.006 0.008
1.245	± 0.0	-0.018 0.014	-0.008 0.011	0.026 0.009	0.050 0.008	-0.001 0.008	0.004 0.007	-0.002 0.007
1.285	± 0.0	0.070 0.012	0.023 0.010	0.048 0.009	0.067 0.008	0.005 0.007	0.013 0.006	-0.009 0.006
1.320	± 0.0	0.060 0.012	0.012 0.011	0.030 0.009	0.042 0.008	0.000 0.007	0.007 0.007	0.007 0.006
1.355	± 0.0	0.054 0.009	0.027 0.008	0.053 0.007	0.056 0.006	0.012 0.006	0.008 0.005	-0.001 0.005
1.370	± 0.0	0.084 0.032	0.051 0.029	0.095 0.024	0.102 0.021	0.025 0.020	0.030 0.018	0.018 0.017
1.419	± 0.0	0.043 0.030	0.009 0.025	0.049 0.021	0.042 0.018	0.008 0.017	0.027 0.016	0.020 0.015
1.464	± 0.0	0.045 0.029	0.041 0.027	0.057 0.022	0.031 0.020	0.021 0.019	0.022 0.017	-0.004 0.016
1.512	± 0.0	0.081 0.027	0.033 0.024	0.060 0.020	0.066 0.017	0.026 0.016	0.048 0.014	0.006 0.013
1.546	± 0.0	0.073 0.021	0.046 0.020	0.056 0.017	0.060 0.016	0.049 0.014	0.032 0.013	0.019 0.012
1.606	± 0.0	0.066 0.023	0.084 0.020	0.066 0.017	0.072 0.016	0.054 0.015	0.045 0.014	0.032 0.013
1.652	± 0.0	0.106 0.022	0.075 0.020	0.074 0.018	0.064 0.017	0.031 0.016	0.031 0.014	0.012 0.013
1.706	± 0.0	0.082 0.024	0.061 0.022	0.049 0.020	0.038 0.018	0.062 0.016	0.030 0.015	0.019 0.014
1.741	± 0.0	0.085 0.022	0.077 0.020	0.076 0.017	0.072 0.016	0.070 0.015	0.058 0.014	0.049 0.013
1.800	± 0.0	0.101 0.026	0.095 0.023	0.077 0.022	0.095 0.019	0.080 0.018	0.041 0.017	0.013 0.016
1.841	± 0.0	0.111 0.028	0.076 0.025	0.079 0.023	0.091 0.021	0.060 0.020	0.051 0.019	0.012 0.018

d)

BEAM MOMENTUM (GEV/C)	$D_0/A_0$	$D_1/A_0$	$D_2/A_0$	$D_3/A_0$	$D_4/A_0$	$D_5/A_0$	$D_6/A_0$	$D_7/A_0$
1.125	$\pm$ 0.0	0.0	-0.109 0.012	0.012 0.007	-0.014 0.005	-0.003 0.003	-0.002 0.003	0.002 0.002
1.165	$\pm$ 0.0	0.0	-0.086 0.010	-0.008 0.005	-0.022 0.004	-0.006 0.003	-0.002 0.002	-0.003 0.002
1.205	$\pm$ 0.0	0.0	-0.094 0.009	-0.013 0.005	-0.015 0.003	-0.005 0.002	-0.003 0.002	-0.003 0.002
1.245	$\pm$ 0.0	0.0	-0.056 0.007	-0.004 0.004	-0.010 0.003	-0.001 0.002	0.000 0.002	-0.001 0.001
1.285	$\pm$ 0.0	0.0	-0.034 0.006	-0.006 0.004	-0.013 0.002	-0.003 0.002	-0.002 0.001	-0.001 0.001
1.320	$\pm$ 0.0	0.0	-0.049 0.006	-0.002 0.004	-0.014 0.002	-0.008 0.002	-0.004 0.001	-0.001 0.001
1.355	$\pm$ 0.0	0.0	-0.054 0.005	-0.019 0.003	-0.016 0.002	-0.008 0.002	-0.004 0.001	0.0 0.001
1.370	$\pm$ 0.0	0.0	-0.022 0.015	-0.002 0.010	-0.009 0.007	-0.009 0.005	0.001 0.004	-0.001 0.003
1.419	$\pm$ 0.0	0.0	-0.053 0.014	-0.007 0.009	-0.012 0.006	-0.008 0.005	-0.005 0.004	-0.003 0.003
1.464	$\pm$ 0.0	0.0	-0.071 0.014	-0.022 0.009	-0.018 0.006	-0.006 0.005	-0.003 0.004	-0.002 0.003
1.512	$\pm$ 0.0	0.0	-0.041 0.013	-0.019 0.009	-0.012 0.006	-0.006 0.004	-0.001 0.003	0.003 0.003
1.546	$\pm$ 0.0	0.0	-0.054 0.010	-0.019 0.007	-0.014 0.005	-0.008 0.004	-0.003 0.003	-0.002 0.002
1.606	$\pm$ 0.0	0.0	-0.072 0.011	-0.039 0.007	-0.018 0.005	-0.004 0.004	-0.002 0.003	-0.001 0.002
1.652	$\pm$ 0.0	0.0	-0.032 0.011	-0.010 0.007	-0.012 0.005	-0.006 0.004	-0.000 0.003	-0.002 0.002
1.706	$\pm$ 0.0	0.0	-0.039 0.012	-0.019 0.008	-0.019 0.005	-0.010 0.004	-0.005 0.003	0.000 0.003
1.741	$\pm$ 0.0	0.0	-0.042 0.011	-0.014 0.007	-0.014 0.005	-0.010 0.003	-0.006 0.003	-0.007 0.002
1.800	$\pm$ 0.0	0.0	-0.023 0.012	-0.021 0.008	-0.004 0.006	-0.010 0.004	-0.006 0.003	-0.002 0.003
1.841	$\pm$ 0.0	0.0	-0.046 0.015	-0.027 0.009	-0.011 0.006	-0.007 0.005	-0.007 0.004	-0.007 0.003

Table (4.2)

 $K^*_{-p}$  Legendre Coefficients

a)

BEAM MOMENTUM (GEV/C)	$A_0$	$A_1/A_0$	$A_2/A_0$	$A_3/A_0$	$A_4/A_0$	$A_5/A_0$	$A_6/A_0$	$A_7/A_0$
1.125	0.100 ± 0.009	0.066 0.056	-0.104 0.071	0.308 0.083	-0.076 0.095	-0.018 0.104	-0.144 0.115	-0.048 0.105
1.165	0.118 ± 0.006	0.022 0.036	-0.087 0.047	0.134 0.056	0.013 0.063	0.029 0.069	-0.093 0.075	0.064 0.081
1.205	0.127 ± 0.005	0.008 0.036	-0.026 0.046	0.182 0.055	-0.065 0.062	0.003 0.070	0.101 0.075	0.004 0.080
1.245	0.132 ± 0.004	0.036 0.032	0.133 0.042	0.197 0.049	0.047 0.056	-0.074 0.061	0.044 0.067	0.060 0.073
1.285	0.135 ± 0.004	0.123 0.032	0.356 0.040	0.238 0.047	-0.064 0.054	-0.141 0.060	-0.036 0.065	-0.055 0.070
1.320	0.129 ± 0.004	0.138 0.037	0.428 0.046	0.241 0.054	-0.070 0.062	-0.093 0.068	-0.070 0.074	-0.103 0.078
1.355	0.141 ± 0.004	0.195 0.030	0.489 0.036	0.200 0.044	-0.150 0.050	-0.126 0.055	-0.006 0.060	0.093 0.064
1.370	0.158 ± 0.042	0.145 0.173	0.622 0.207	0.164 0.254	-0.138 0.273	-0.040 0.315	0.027 0.331	0.228 0.352
1.419	0.159 ± 0.036	0.367 0.179	0.778 0.215	0.200 0.262	-0.029 0.293	0.286 0.316	-0.120 0.346	-0.251 0.372
1.464	0.158 ± 0.040	0.285 0.189	0.634 0.221	0.134 0.265	-0.316 0.304	-0.665 0.343	-0.330 0.389	-0.151 0.397
1.512	0.196 ± 0.036	0.539 0.136	0.431 0.174	0.014 0.211	-0.124 0.241	0.084 0.252	0.091 0.279	-0.331 0.311
1.546	0.194 ± 0.034	0.408 0.128	0.655 0.155	0.108 0.186	-0.142 0.209	-0.262 0.230	-0.252 0.248	0.004 0.269
1.606	0.246 ± 0.055	0.429 0.131	0.538 0.160	-0.327 0.190	-0.217 0.217	-0.187 0.243	-0.200 0.267	-0.295 0.291
1.652	0.221 ± 0.030	0.505 0.134	0.672 0.165	0.128 0.201	-0.080 0.231	0.169 0.261	-0.051 0.284	-0.322 0.290
1.706	0.229 ± 0.039	0.634 0.142	0.409 0.182	-0.126 0.225	-0.225 0.256	-0.214 0.275	0.199 0.305	-0.357 0.318
1.741	0.292 ± 0.047	0.789 0.116	0.706 0.148	0.095 0.181	-0.156 0.209	-0.172 0.225	-0.149 0.248	0.257 0.271
1.800	0.284 ± 0.038	0.616 0.148	0.831 0.186	0.395 0.221	0.152 0.249	0.024 0.283	-0.320 0.315	0.017 0.340
1.841	0.224 ± 0.039	0.643 0.156	0.694 0.197	0.136 0.239	-0.024 0.258	-0.354 0.290	-0.101 0.317	-0.478 0.344

b)

BEAM MOMENTUM (GEV/C)	$B_0/A_0$	$B_1/A_0$	$B_2/A_0$	$B_3/A_0$	$B_4/A_0$	$B_5/A_0$	$B_6/A_0$	$B_7/A_0$
1.125	± 0.468 0.026	-0.081 0.049	-0.184 0.068	0.225 0.078	0.246 0.091	0.170 0.100	0.032 0.108	0.035 0.103
1.165	± 0.454 0.016	-0.083 0.032	-0.074 0.044	0.204 0.051	0.188 0.056	-0.034 0.061	0.047 0.066	0.034 0.071
1.205	± 0.405 0.016	-0.047 0.031	-0.094 0.041	0.049 0.048	0.147 0.054	-0.099 0.061	0.056 0.065	0.001 0.070
1.245	± 0.444 0.014	-0.028 0.028	-0.020 0.038	0.154 0.045	0.231 0.051	-0.092 0.058	0.071 0.063	0.036 0.066
1.285	± 0.439 0.014	0.059 0.028	0.068 0.037	0.117 0.042	0.177 0.048	-0.189 0.054	-0.150 0.058	0.033 0.062
1.320	± 0.444 0.015	0.073 0.033	0.163 0.043	0.112 0.050	0.136 0.056	-0.201 0.062	0.020 0.067	-0.154 0.071
1.355	± 0.478 0.012	0.092 0.027	0.202 0.035	0.119 0.041	0.142 0.046	-0.201 0.051	-0.005 0.056	0.043 0.060
1.370	± 0.633 0.071	0.230 0.189	0.785 0.234	0.384 0.275	0.328 0.292	0.277 0.341	-0.191 0.366	0.493 0.395
1.419	± 0.537 0.068	0.189 0.164	0.232 0.215	0.338 0.256	0.145 0.272	0.161 0.271	0.116 0.322	-0.291 0.308
1.464	± 0.527 0.079	-0.103 0.178	0.209 0.208	0.181 0.233	-0.097 0.242	-0.499 0.318	-0.279 0.357	0.316 0.363
1.512	± 0.286 0.054	0.309 0.111	0.254 0.153	0.244 0.172	0.451 0.181	0.382 0.197	-0.170 0.218	-0.354 0.227
1.546	± 0.457 0.053	-0.068 0.116	0.129 0.154	0.059 0.178	0.215 0.200	-0.214 0.223	0.011 0.236	0.339 0.268
1.606	± 0.382 0.052	-0.006 0.118	0.284 0.155	-0.279 0.175	0.283 0.199	-0.187 0.221	-0.129 0.247	-0.487 0.252
1.652	± 0.389 0.053	0.129 0.117	0.255 0.160	0.066 0.193	0.453 0.214	0.330 0.238	0.237 0.267	-0.075 0.274
1.706	± 0.359 0.060	0.151 0.123	0.243 0.158	-0.096 0.203	0.206 0.220	0.093 0.237	0.397 0.270	-0.071 0.274
1.741	± 0.505 0.049	0.325 0.110	0.225 0.138	0.049 0.163	-0.152 0.183	-0.192 0.207	0.018 0.222	-0.081 0.252
1.800	± 0.399 0.059	0.311 0.129	0.263 0.177	0.153 0.212	0.512 0.242	0.379 0.268	0.287 0.295	0.458 0.329
1.841	± 0.493 0.064	0.403 0.140	0.231 0.189	-0.175 0.215	0.143 0.234	0.096 0.273	-0.196 0.293	-0.567 0.328

c)

BEAM MOMENTUM (GEV/C)	$C_0/A_0$	$C_1/A_0$	$C_2/A_0$	$C_3/A_0$	$C_4/A_0$	$C_5/A_0$	$C_6/A_0$	$C_7/A_0$
1.125	± 0.0	-0.058 0.020	-0.001 0.015	0.003 0.012	0.011 0.011	0.001 0.010	0.011 0.009	0.003 0.007
1.165	± 0.0	-0.062 0.013	-0.014 0.010	0.008 0.008	0.038 0.007	0.006 0.006	0.001 0.006	-0.005 0.005
1.205	± 0.0	-0.053 0.012	-0.005 0.009	-0.016 0.007	0.035 0.006	0.005 0.006	-0.008 0.005	0.000 0.005
1.245	± 0.0	-0.057 0.011	-0.026 0.008	-0.010 0.007	0.043 0.006	-0.010 0.005	0.008 0.005	-0.001 0.005
1.285	± 0.0	-0.034 0.010	-0.018 0.008	-0.022 0.006	0.039 0.006	-0.016 0.005	0.002 0.005	-0.014 0.004
1.320	± 0.0	-0.018 0.011	-0.018 0.009	-0.020 0.008	0.033 0.007	-0.023 0.006	-0.004 0.006	-0.008 0.005
1.355	± 0.0	-0.018 0.009	-0.010 0.007	-0.012 0.006	0.029 0.005	-0.005 0.005	0.009 0.004	0.003 0.004
1.370	± 0.0	0.030 0.049	0.035 0.042	-0.021 0.036	0.049 0.032	-0.016 0.029	-0.032 0.027	-0.005 0.025
1.419	± 0.0	0.021 0.053	0.045 0.043	-0.017 0.037	-0.002 0.032	0.007 0.029	0.022 0.027	0.022 0.025
1.464	± 0.0	0.006 0.053	0.037 0.045	0.017 0.038	0.035 0.032	-0.002 0.029	-0.005 0.026	-0.022 0.026
1.512	± 0.0	0.058 0.039	-0.001 0.034	-0.019 0.028	0.015 0.025	-0.011 0.023	0.025 0.021	-0.010 0.019
1.546	± 0.0	0.133 0.034	0.064 0.029	0.042 0.025	0.047 0.021	0.008 0.019	0.012 0.017	-0.003 0.016
1.606	± 0.0	-0.030 0.040	0.028 0.032	-0.018 0.027	0.030 0.023	0.027 0.020	0.009 0.018	0.016 0.017
1.652	± 0.0	0.067 0.035	0.011 0.029	0.043 0.025	0.007 0.023	0.028 0.020	0.007 0.019	-0.014 0.018
1.706	± 0.0	0.030 0.042	0.027 0.035	0.066 0.029	0.040 0.025	0.007 0.024	-0.003 0.022	0.002 0.021
1.741	± 0.0	0.110 0.035	0.043 0.030	0.013 0.025	0.012 0.021	0.008 0.020	0.023 0.018	-0.004 0.016
1.800	± 0.0	0.132 0.037	0.026 0.032	0.057 0.028	0.037 0.026	0.064 0.023	0.003 0.021	0.022 0.020
1.841	± 0.0	-0.009 0.045	0.003 0.038	0.023 0.033	0.078 0.029	0.011 0.025	0.036 0.023	0.027 0.020

d)

BEAM MOMENTUM (GEV/C)	$D_0/A_0$	$D_1/A_0$	$D_2/A_0$	$D_3/A_0$	$D_4/A_0$	$D_5/A_0$	$D_6/A_0$	$D_7/A_0$
1.125	± 0.0	0.0	-0.062 0.011	0.002 0.006	-0.019 0.004	-0.003 0.003	-0.003 0.002	0.003 0.001
1.165	± 0.0	0.0	-0.039 0.007	0.007 0.004	-0.005 0.002	0.002 0.002	-0.000 0.001	0.001 0.001
1.205	± 0.0	0.0	-0.024 0.007	0.012 0.004	-0.012 0.002	0.000 0.002	0.001 0.001	0.000 0.001
1.245	± 0.0	0.0	-0.033 0.006	0.020 0.003	-0.006 0.002	0.001 0.002	-0.000 0.001	0.001 0.001
1.285	± 0.0	0.0	-0.029 0.005	0.024 0.003	-0.007 0.002	0.002 0.002	-0.001 0.001	-0.002 0.001
1.320	± 0.0	0.0	-0.024 0.006	0.021 0.003	-0.010 0.002	0.001 0.002	-0.003 0.001	-0.001 0.001
1.355	± 0.0	0.0	-0.036 0.005	0.022 0.003	-0.014 0.002	0.001 0.001	-0.002 0.001	-0.001 0.001
1.370	± 0.0	0.0	-0.004 0.026	0.004 0.015	-0.010 0.010	-0.009 0.008	-0.004 0.006	-0.010 0.005
1.419	± 0.0	0.0	-0.013 0.026	-0.005 0.015	0.002 0.011	0.001 0.008	-0.001 0.006	0.003 0.005
1.464	± 0.0	0.0	-0.039 0.029	0.005 0.018	-0.024 0.012	-0.004 0.009	-0.005 0.007	-0.006 0.005
1.512	± 0.0	0.0	-0.011 0.023	-0.012 0.013	-0.021 0.008	0.007 0.006	0.009 0.005	0.005 0.004
1.546	± 0.0	0.0	0.030 0.019	-0.009 0.011	-0.000 0.008	-0.003 0.006	0.000 0.005	0.001 0.004
1.606	± 0.0	0.0	-0.010 0.020	0.002 0.012	0.005 0.008	-0.002 0.006	-0.002 0.005	0.001 0.004
1.652	± 0.0	0.0	0.034 0.021	0.006 0.012	0.009 0.008	0.010 0.006	0.003 0.005	0.001 0.004
1.706	± 0.0	0.0	0.031 0.025	0.019 0.014	-0.006 0.009	-0.009 0.006	-0.002 0.005	-0.005 0.004
1.741	± 0.0	0.0	-0.006 0.019	0.001 0.011	0.001 0.008	0.006 0.005	0.003 0.004	-0.001 0.004
1.800	± 0.0	0.0	0.041 0.021	0.013 0.013	0.005 0.009	0.008 0.007	0.005 0.005	0.001 0.004
1.841	± 0.0	0.0	0.014 0.025	0.016 0.015	0.008 0.010	0.008 0.008	0.001 0.006	-0.005 0.005

Table (4.3) i)  $K^{*-}p$  Legendre Coefficients from Channel  $K^-p\pi^0$

a)

BEAM MOMENTUM (GEV/C)	$A_0$	$A_1/A_0$	$A_2/A_0$	$A_3/A_0$	$A_4/A_0$	$A_5/A_0$	$A_6/A_0$	$A_7/A_0$
1.125	$\pm$ 0.103 0.009	0.115 0.079	0.046 0.106	0.139 0.126	0.318 0.140	-0.159 0.158	0.143 0.175	-0.081 0.191
1.165	$\pm$ 0.127 0.007	0.025 0.062	-0.085 0.080	-0.115 0.094	-0.005 0.105	0.067 0.116	-0.058 0.125	0.059 0.136
1.205	$\pm$ 0.143 0.008	0.051 0.059	-0.089 0.075	0.023 0.091	-0.106 0.103	-0.005 0.116	0.094 0.123	-0.159 0.132
1.245	$\pm$ 0.141 0.006	0.073 0.055	0.135 0.071	0.040 0.086	0.077 0.096	-0.012 0.105	0.164 0.113	0.092 0.124
1.285	$\pm$ 0.158 0.006	0.086 0.052	0.300 0.067	0.080 0.079	0.093 0.090	-0.148 0.100	0.044 0.108	-0.099 0.113
1.320	$\pm$ 0.135 0.005	0.055 0.062	0.319 0.079	0.143 0.094	0.056 0.107	0.117 0.117	-0.004 0.127	-0.117 0.132
1.355	$\pm$ 0.156 0.005	0.123 0.049	0.386 0.062	0.162 0.074	-0.012 0.084	-0.056 0.093	0.028 0.101	0.078 0.107

b)

BEAM MOMENTUM (GEV/C)	$B_0/A_0$	$B_1/A_0$	$B_2/A_0$	$B_3/A_0$	$B_4/A_0$	$B_5/A_0$	$B_6/A_0$	$B_7/A_0$
1.125	$\pm$ 0.517 0.036	0.049 0.080	0.208 0.112	0.373 0.132	0.545 0.147	0.108 0.167	0.311 0.184	-0.026 0.202
1.165	$\pm$ 0.483 0.028	-0.116 0.057	0.006 0.078	0.035 0.089	0.187 0.096	-0.075 0.100	-0.091 0.111	0.045 0.120
1.205	$\pm$ 0.366 0.027	-0.072 0.049	-0.151 0.065	-0.043 0.076	0.081 0.088	-0.110 0.101	0.010 0.107	-0.260 0.114
1.245	$\pm$ 0.426 0.023	-0.033 0.050	0.122 0.068	0.201 0.081	0.353 0.092	0.010 0.103	0.103 0.109	-0.036 0.117
1.285	$\pm$ 0.449 0.022	0.023 0.047	0.133 0.063	0.117 0.072	0.215 0.083	-0.129 0.092	-0.154 0.099	-0.050 0.102
1.320	$\pm$ 0.401 0.026	0.076 0.054	0.110 0.074	0.120 0.086	0.276 0.096	0.004 0.103	0.031 0.111	-0.217 0.114
1.355	$\pm$ 0.516 0.021	0.036 0.047	0.222 0.062	0.161 0.073	0.190 0.081	-0.045 0.090	0.089 0.100	0.116 0.106

c)

BEAM MOMENTUM (GEV/C)	$C_0/A_0$	$C_1/A_0$	$C_2/A_0$	$C_3/A_0$	$C_4/A_0$	$C_5/A_0$	$C_6/A_0$	$C_7/A_0$
1.125	$\pm$ 0.0	0.030 0.027	-0.004 0.020	0.037 0.017	0.017 0.015	0.016 0.013	0.011 0.012	-0.005 0.012
1.165	$\pm$ 0.0	-0.064 0.022	-0.019 0.016	0.018 0.013	0.042 0.012	0.018 0.010	-0.005 0.009	-0.022 0.008
1.205	$\pm$ 0.0	-0.065 0.020	-0.001 0.015	-0.007 0.012	0.027 0.010	0.007 0.009	-0.018 0.009	-0.001 0.008
1.245	$\pm$ 0.0	-0.066 0.018	-0.010 0.014	-0.018 0.011	0.042 0.010	-0.005 0.009	0.006 0.008	0.001 0.007
1.285	$\pm$ 0.0	-0.014 0.016	-0.024 0.013	-0.022 0.010	0.040 0.009	-0.005 0.009	-0.001 0.008	-0.017 0.007
1.320	$\pm$ 0.0	0.016 0.019	-0.006 0.015	-0.023 0.013	0.026 0.011	-0.003 0.010	-0.007 0.009	-0.001 0.009
1.355	$\pm$ 0.0	-0.007 0.015	-0.007 0.012	-0.010 0.010	0.017 0.009	-0.004 0.008	0.011 0.008	-0.007 0.007

d)

BEAM MOMENTUM (GEV/C)	$D_0/A_0$	$D_1/A_0$	$D_2/A_0$	$D_3/A_0$	$D_4/A_0$	$D_5/A_0$	$D_6/A_0$	$D_7/A_0$
1.125	$\pm$ 0.0	0.0	-0.082 0.014	0.004 0.008	-0.013 0.005	-0.004 0.004	-0.001 0.003	0.005 0.002
1.165	$\pm$ 0.0	0.0	-0.049 0.012	0.001 0.006	-0.002 0.004	0.001 0.003	0.003 0.002	0.000 0.002
1.205	$\pm$ 0.0	0.0	-0.019 0.011	-0.001 0.006	-0.014 0.004	-0.001 0.003	0.003 0.002	-0.000 0.002
1.245	$\pm$ 0.0	0.0	-0.020 0.010	0.010 0.005	-0.010 0.003	0.001 0.002	0.002 0.002	0.000 0.002
1.285	$\pm$ 0.0	0.0	-0.037 0.009	0.013 0.005	-0.005 0.003	-0.002 0.002	0.002 0.002	-0.003 0.002
1.320	$\pm$ 0.0	0.0	-0.017 0.010	0.018 0.006	-0.005 0.004	0.004 0.003	-0.004 0.002	-0.002 0.002
1.355	$\pm$ 0.0	0.0	-0.045 0.008	0.015 0.005	-0.012 0.003	0.0 0.002	-0.003 0.002	-0.001 0.001

ii)  $K^{*-}$  Legendre Coefficients from Channel  $K^0 p \pi^-$

a)

BEAM MOMENTUM (GEV/C)	$A_0$	$A_1/A_0$	$A_2/A_0$	$A_3/A_0$	$A_4/A_0$	$A_5/A_0$	$A_6/A_0$	$A_7/A_0$
1.125	$\pm$ 0.100 0.009	0.066 0.056	-0.104 0.071	0.308 0.083	-0.076 0.095	-0.018 0.104	-0.144 0.115	-0.031 0.124
1.165	$\pm$ 0.118 0.006	0.020 0.045	-0.088 0.059	0.270 0.069	0.023 0.078	0.008 0.085	-0.113 0.094	0.066 0.101
1.205	$\pm$ 0.127 0.005	-0.016 0.045	0.009 0.057	0.270 0.068	-0.043 0.078	0.007 0.087	0.105 0.095	0.094 0.100
1.245	$\pm$ 0.132 0.004	0.015 0.040	0.132 0.052	0.280 0.061	0.031 0.069	-0.108 0.076	-0.020 0.083	0.044 0.090
1.285	$\pm$ 0.135 0.004	0.144 0.040	0.389 0.050	0.330 0.059	-0.156 0.067	-0.137 0.075	-0.083 0.082	-0.029 0.088
1.320	$\pm$ 0.129 0.004	0.181 0.046	0.485 0.056	0.292 0.067	-0.135 0.076	-0.202 0.083	-0.104 0.091	-0.096 0.097
1.355	$\pm$ 0.141 0.004	0.234 0.037	0.545 0.045	0.221 0.054	-0.227 0.062	-0.165 0.068	-0.025 0.075	0.101 0.081

b)

BEAM MOMENTUM (GEV/C)	$B_0/A_0$	$B_1/A_0$	$B_2/A_0$	$B_3/A_0$	$B_4/A_0$	$B_5/A_0$	$B_6/A_0$	$B_7/A_0$
1.125	$\pm$ 0.468 0.026	-0.081 0.049	-0.184 0.068	0.225 0.078	0.246 0.091	0.170 0.100	0.032 0.108	0.067 0.116
1.165	$\pm$ 0.438 0.020	-0.064 0.039	-0.118 0.052	0.296 0.062	0.189 0.069	-0.011 0.076	0.122 0.082	0.029 0.088
1.205	$\pm$ 0.426 0.020	-0.034 0.039	-0.063 0.052	0.100 0.062	0.184 0.069	-0.093 0.077	0.081 0.082	0.145 0.088
1.245	$\pm$ 0.453 0.017	-0.025 0.035	-0.095 0.046	0.129 0.055	0.166 0.062	-0.147 0.069	0.053 0.077	0.074 0.080
1.285	$\pm$ 0.434 0.017	0.080 0.035	0.030 0.045	0.116 0.052	0.155 0.059	-0.225 0.066	-0.148 0.072	0.081 0.077
1.320	$\pm$ 0.466 0.019	0.071 0.042	0.190 0.052	0.108 0.062	0.063 0.068	-0.308 0.077	0.014 0.084	-0.121 0.090
1.355	$\pm$ 0.457 0.016	0.123 0.034	0.192 0.043	0.097 0.050	0.116 0.056	-0.286 0.061	-0.057 0.068	0.003 0.072

c)

BEAM MOMENTUM (GEV/C)	$C_0/A_0$	$C_1/A_0$	$C_2/A_0$	$C_3/A_0$	$C_4/A_0$	$C_5/A_0$	$C_6/A_0$	$C_7/A_0$
1.125	$\pm$ 0.0	-0.058 0.020	-0.001 0.015	0.003 0.012	0.011 0.011	0.001 0.010	0.011 0.009	0.007 0.008
1.165	$\pm$ 0.0	-0.061 0.016	-0.012 0.012	0.003 0.010	0.036 0.009	-0.001 0.008	0.004 0.007	0.005 0.006
1.205	$\pm$ 0.0	-0.047 0.015	-0.008 0.011	-0.021 0.009	0.039 0.008	0.003 0.007	-0.002 0.007	0.001 0.006
1.245	$\pm$ 0.0	-0.052 0.013	-0.035 0.010	-0.006 0.008	0.044 0.007	-0.013 0.007	0.009 0.006	-0.002 0.006
1.285	$\pm$ 0.0	-0.045 0.012	-0.014 0.010	-0.022 0.008	0.038 0.007	-0.023 0.006	0.003 0.006	-0.013 0.005
1.320	$\pm$ 0.0	-0.035 0.014	-0.025 0.011	-0.019 0.010	0.037 0.008	-0.034 0.008	-0.002 0.007	-0.011 0.006
1.355	$\pm$ 0.0	-0.024 0.011	-0.012 0.009	-0.013 0.008	0.036 0.007	-0.010 0.006	0.008 0.005	0.008 0.005

d)

BEAM MOMENTUM (GEV/C)	$D_0/A_0$	$D_1/A_0$	$D_2/A_0$	$D_3/A_0$	$D_4/A_0$	$D_5/A_0$	$D_6/A_0$	$D_7/A_0$
1.125	$\pm$ 0.0	0.0	-0.062 0.011	0.002 0.006	-0.019 0.004	-0.003 0.003	-0.003 0.002	0.002 0.002
1.165	$\pm$ 0.0	0.0	-0.034 0.009	0.010 0.005	-0.007 0.003	0.002 0.002	-0.002 0.002	0.002 0.001
1.205	$\pm$ 0.0	0.0	-0.027 0.008	0.019 0.004	-0.010 0.003	0.001 0.002	0.001 0.002	0.001 0.001
1.245	$\pm$ 0.0	0.0	-0.040 0.007	0.025 0.004	-0.004 0.003	0.001 0.002	-0.002 0.001	0.001 0.001
1.285	$\pm$ 0.0	0.0	-0.024 0.007	0.030 0.004	-0.008 0.002	0.005 0.002	-0.003 0.001	-0.002 0.001
1.320	$\pm$ 0.0	0.0	-0.027 0.007	0.023 0.004	-0.013 0.003	0.000 0.002	-0.003 0.002	-0.000 0.001
1.355	$\pm$ 0.0	0.0	-0.032 0.006	0.026 0.003	-0.015 0.002	0.002 0.002	-0.002 0.001	-0.001 0.001

Table (4.4)

 $\Lambda(1520)\pi$  Legendre Coefficients

a)

BEAM MOMENTUM (GEV/C)	$A_0$	$A_1/A_0$	$A_2/A_0$	$A_3/A_0$	$A_4/A_0$	$A_5/A_0$	$A_6/A_0$	$A_7/A_0$
0.960	0.075	-0.384	0.358	0.043	0.255	0.140	-0.005	-0.022
	$\pm$ 0.009	0.080	0.105	0.124	0.144	0.157	0.167	0.183
1.005	0.066	-0.293	0.304	-0.149	0.088	-0.105	-0.337	-0.067
	$\pm$ 0.008	0.095	0.122	0.139	0.160	0.173	0.188	0.200
1.045	0.054	0.031	0.210	0.275	0.144	-0.146	0.100	-0.017
	$\pm$ 0.006	0.086	0.112	0.132	0.151	0.164	0.178	0.190
1.085	0.036	0.133	0.060	0.058	-0.017	-0.239	-0.035	-0.159
	$\pm$ 0.004	0.106	0.137	0.161	0.179	0.197	0.213	0.233
1.125	0.036	0.290	0.291	0.217	-0.100	0.061	0.032	-0.173
	$\pm$ 0.004	0.108	0.136	0.162	0.180	0.205	0.221	0.238
1.165	0.033	0.302	0.107	0.190	0.184	0.299	-0.112	-0.171
	$\pm$ 0.004	0.100	0.134	0.155	0.176	0.195	0.211	0.222
1.205	0.027	0.335	0.325	0.037	-0.080	-0.209	-0.007	-0.101
	$\pm$ 0.002	0.116	0.146	0.175	0.201	0.224	0.245	0.268
1.245	0.026	0.249	0.297	0.010	-0.015	-0.179	0.137	0.150
	$\pm$ 0.002	0.105	0.133	0.161	0.178	0.200	0.217	0.229
1.285	0.034	0.156	0.467	0.027	0.307	-0.147	-0.235	-0.108
	$\pm$ 0.002	0.093	0.120	0.139	0.158	0.176	0.197	0.212
1.320	0.034	-0.053	0.624	-0.349	0.308	0.167	0.155	0.367
	$\pm$ 0.002	0.104	0.131	0.159	0.178	0.198	0.217	0.230
1.355	0.043	0.029	0.523	-0.169	0.101	-0.174	0.074	0.227
	$\pm$ 0.003	0.078	0.097	0.117	0.132	0.146	0.158	0.169

b)

BEAM MOMENTUM (GEV/C)	$B_0/A_0$	$B_1/A_0$	$B_2/A_0$	$B_3/A_0$	$B_4/A_0$	$B_5/A_0$	$B_6/A_0$	$B_7/A_0$
0.960	0.292 ± 0.024	-0.090 0.050	0.082 0.065	0.045 0.076	-0.045 0.089	-0.096 0.097	0.008 0.101	0.074 0.115
1.005	0.185 ± 0.029	-0.006 0.056	0.043 0.071	0.049 0.079	0.062 0.090	-0.138 0.101	-0.048 0.109	0.125 0.116
1.045	0.235 ± 0.027	-0.078 0.052	-0.050 0.067	0.037 0.081	-0.048 0.089	-0.064 0.098	0.054 0.107	0.002 0.115
1.085	0.113 ± 0.034	0.072 0.061	0.101 0.080	0.140 0.094	0.005 0.104	-0.119 0.114	-0.184 0.122	-0.063 0.139
1.125	0.139 ± 0.036	0.103 0.067	0.109 0.082	0.051 0.096	-0.119 0.104	0.167 0.119	0.017 0.130	-0.136 0.141
1.165	0.100 ± 0.033	0.026 0.060	0.117 0.078	0.077 0.091	-0.066 0.101	0.082 0.112	-0.084 0.119	-0.123 0.124
1.205	0.323 ± 0.034	0.059 0.072	0.066 0.091	-0.126 0.109	-0.240 0.123	-0.359 0.137	0.040 0.152	-0.162 0.166
1.245	0.283 ± 0.032	0.137 0.066	-0.052 0.084	-0.052 0.100	-0.064 0.110	0.037 0.127	-0.035 0.136	0.070 0.143
1.285	0.128 ± 0.029	0.143 0.056	-0.012 0.073	0.137 0.082	-0.103 0.092	-0.057 0.100	0.071 0.112	-0.061 0.122
1.320	0.167 ± 0.031	0.063 0.062	-0.029 0.079	0.077 0.094	-0.057 0.109	0.152 0.120	0.154 0.132	-0.071 0.142
1.355	0.221 ± 0.024	0.093 0.049	0.008 0.061	0.004 0.071	0.011 0.080	-0.048 0.090	-0.003 0.097	0.122 0.103

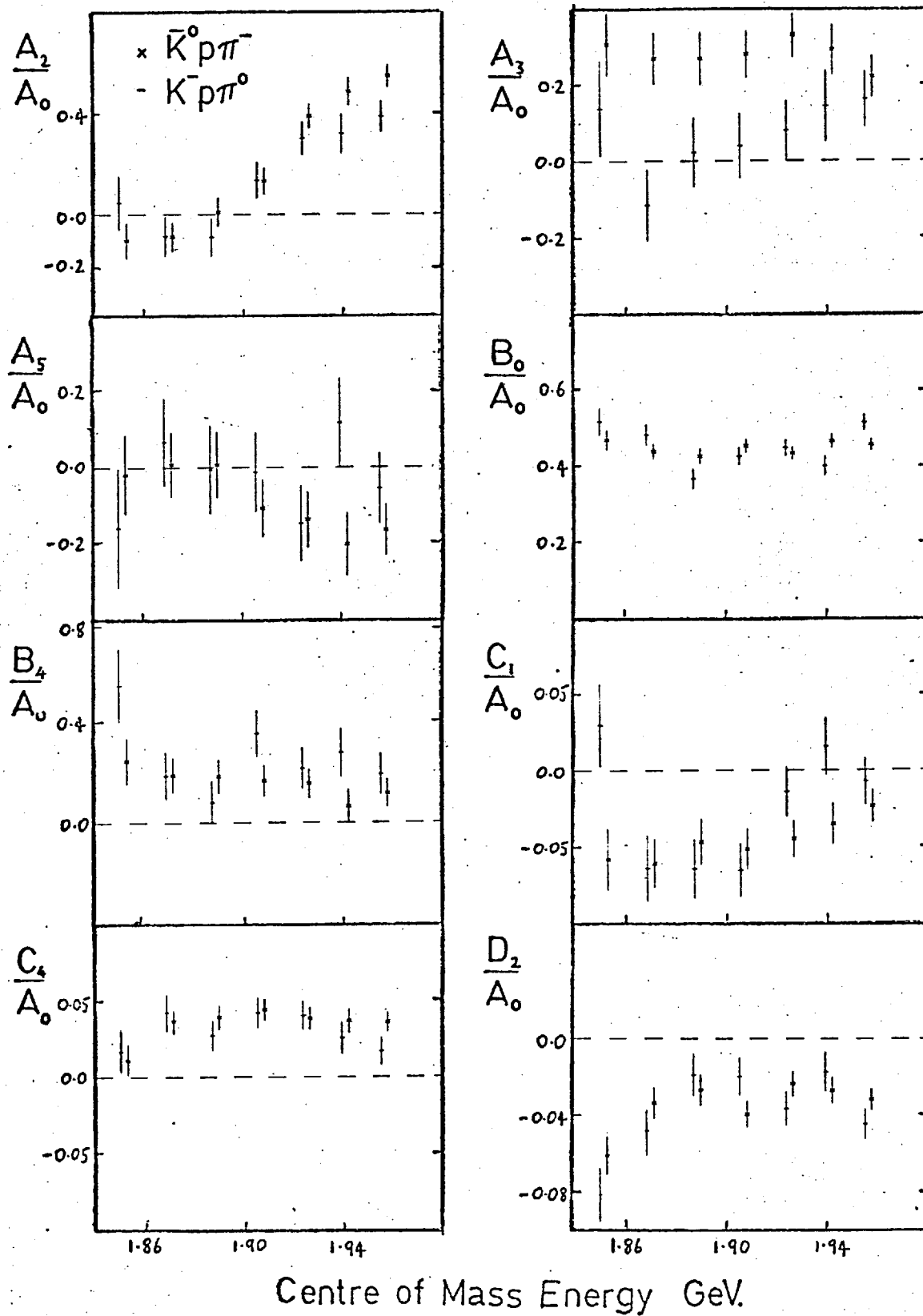
c)

BEAM MOMENTUM (GEV/C)	$c_0/A_0$	$c_1/A_0$	$c_2/A_0$	$c_3/A_0$	$c_4/A_0$	$c_5/A_0$	$c_6/A_0$	$c_7/A_0$
0.960	0.0	0.040	-0.074	-0.004	-0.036	-0.019	0.009	-0.021
	±	0.030	0.023	0.020	0.017	0.016	0.015	0.014
1.005	0.0	0.109	-0.065	0.060	-0.029	-0.013	-0.012	-0.017
	±	0.037	0.029	0.025	0.021	0.020	0.018	0.017
1.045	0.0	-0.001	-0.006	0.037	-0.026	0.005	0.011	-0.000
	±	0.032	0.025	0.021	0.018	0.017	0.016	0.014
1.085	0.0	0.024	-0.004	0.007	-0.036	0.018	0.012	-0.029
	±	0.045	0.035	0.029	0.025	0.023	0.021	0.019
1.125	0.0	0.055	0.037	-0.031	-0.016	0.001	0.007	-0.029
	±	0.041	0.032	0.026	0.024	0.021	0.020	0.019
1.165	0.0	0.068	-0.015	0.024	-0.007	0.008	0.033	-0.029
	±	0.042	0.030	0.025	0.022	0.020	0.018	0.018
1.205	0.0	-0.011	0.026	0.001	-0.000	-0.014	-0.004	-0.028
	±	0.043	0.034	0.029	0.024	0.021	0.020	0.018
1.245	0.0	0.030	0.008	-0.018	-0.046	0.002	-0.013	-0.004
	±	0.038	0.030	0.024	0.021	0.020	0.018	0.018
1.285	0.0	0.093	-0.006	0.012	-0.023	0.001	0.021	-0.013
	±	0.035	0.027	0.024	0.021	0.019	0.017	0.016
1.320	0.0	0.084	-0.065	0.013	-0.072	0.010	-0.012	0.009
	±	0.035	0.028	0.025	0.023	0.021	0.019	0.018
1.355	0.0	0.082	-0.007	0.038	-0.048	-0.001	-0.030	-0.006
	±	0.026	0.021	0.018	0.016	0.015	0.014	0.013

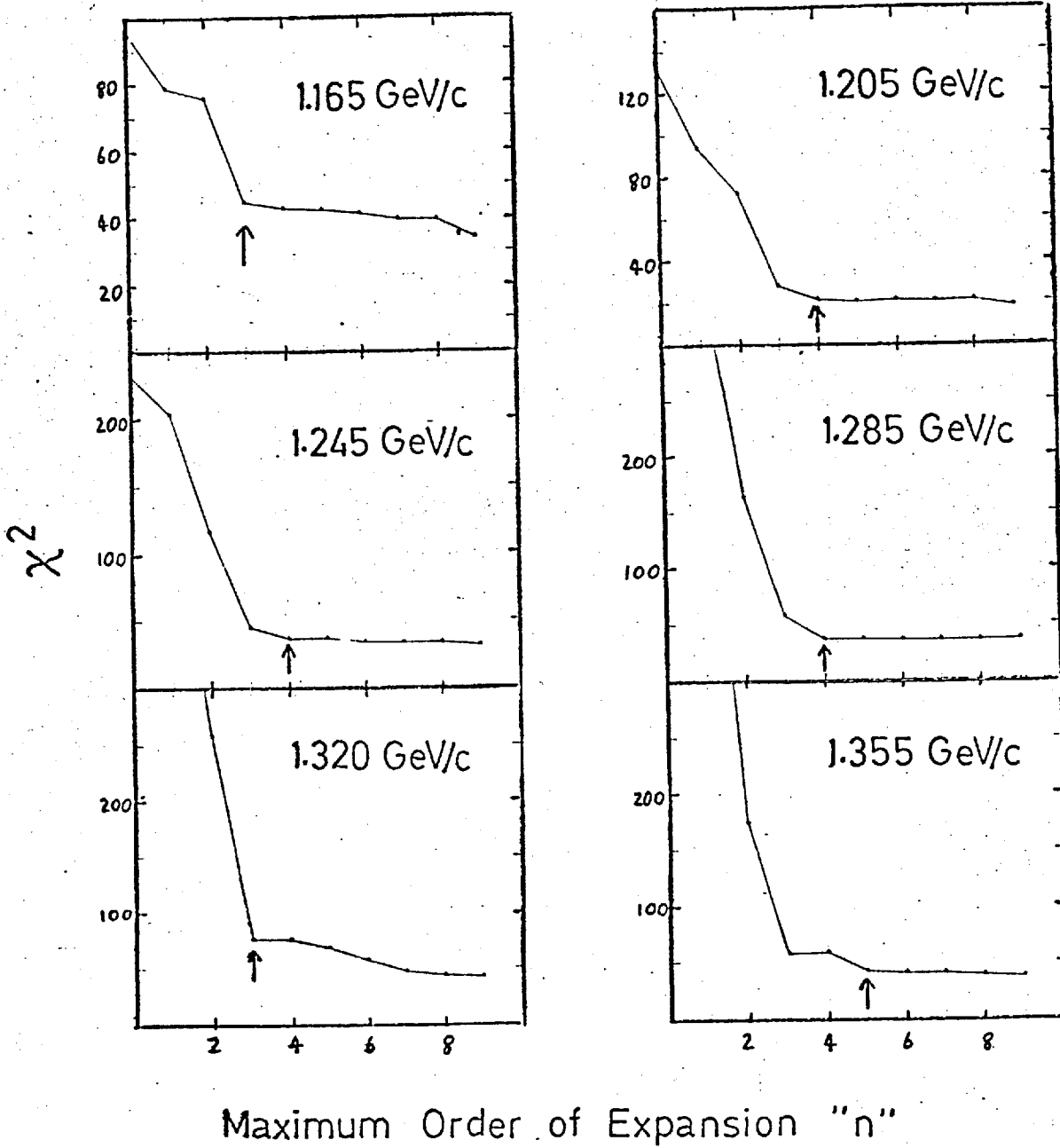
d)

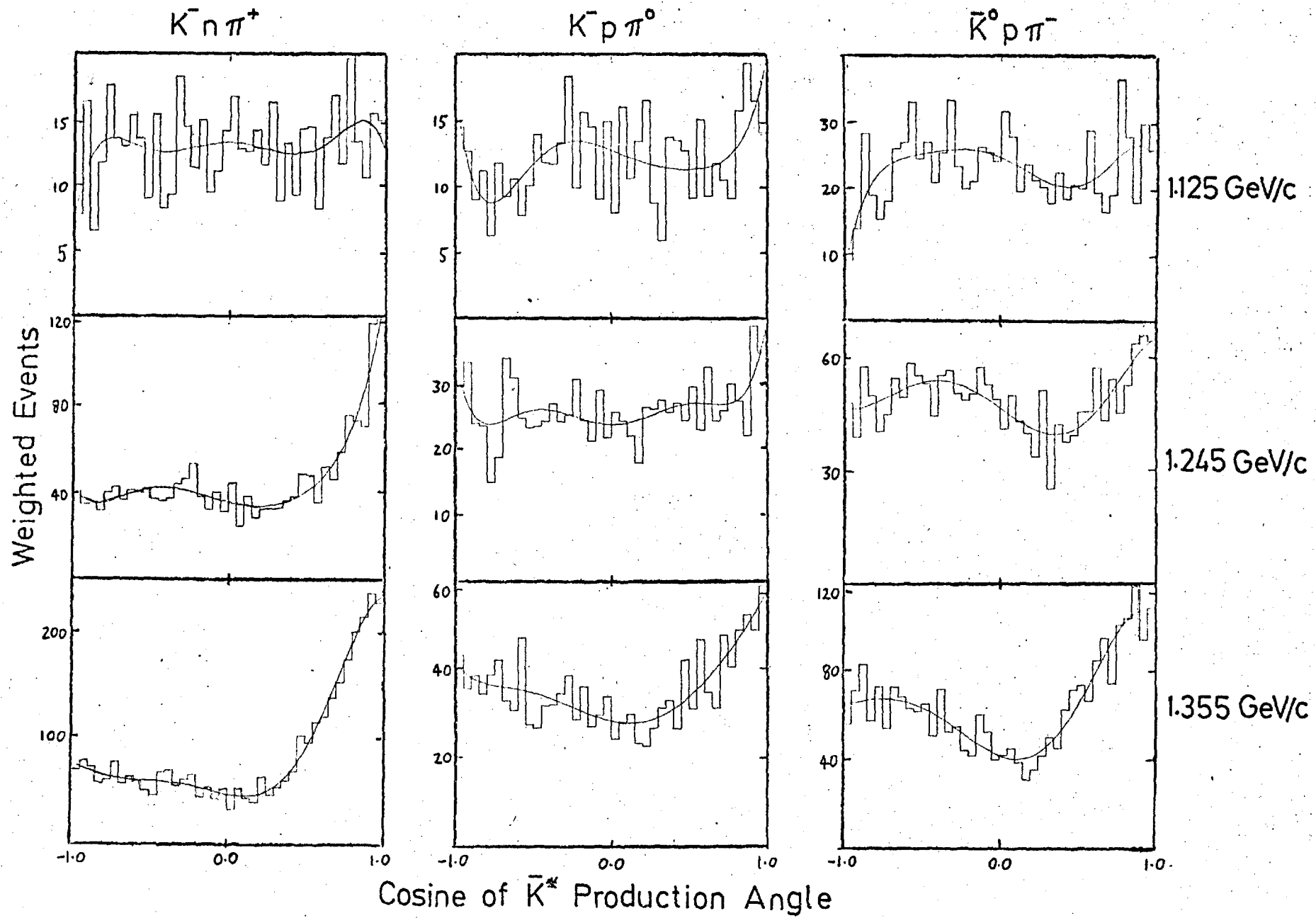
BEAM MOMENTUM (GEV/C)	$D_0 / A_0$	$D_1 / A_0$	$D_2 / A_0$	$D_3 / A_0$	$-D_4 / A_0$	$D_5 / A_0$	$D_6 / A_0$	$D_7 / A_0$
0.960	0.0	0.0	-0.044	0.011	-0.004	-0.000	-0.000	-0.003
	±		0.011	0.006	0.004	0.003	0.002	0.002
1.005	0.0	0.0	-0.026	-0.006	-0.008	0.001	0.002	-0.002
	±		0.013	0.008	0.005	0.004	0.003	0.002
1.045	0.0	0.0	-0.015	0.0	-0.008	-0.002	0.004	-0.001
	±		0.013	0.007	0.005	0.003	0.003	0.002
1.085	0.0	0.0	-0.009	-0.002	-0.017	-0.004	-0.002	-0.000
	±		0.016	0.008	0.006	0.004	0.003	0.003
1.125	0.0	0.0	-0.013	-0.009	0.001	0.008	0.002	0.0
	±		0.015	0.009	0.005	0.004	0.003	0.003
1.165	0.0	0.0	-0.003	0.0	0.003	0.006	0.008	0.002
	±		0.016	0.008	0.006	0.004	0.003	0.002
1.205	0.0	0.0	-0.025	-0.004	-0.006	-0.001	-0.002	-0.001
	±		0.016	0.009	0.006	0.004	0.004	0.003
1.245	0.0	0.0	-0.022	-0.006	-0.003	-0.002	0.004	-0.002
	±		0.015	0.008	0.006	0.004	0.003	0.002
1.285	0.0	0.0	-0.038	-0.002	-0.004	0.004	0.000	0.002
	±		0.013	0.007	0.005	0.004	0.003	0.002
1.320	0.0	0.0	-0.016	-0.002	-0.001	-0.002	0.000	0.002
	±		0.014	0.008	0.005	0.004	0.003	0.002
1.355	-0.0	0.0	-0.019	-0.002	-0.001	-0.002	-0.001	0.001
	±		0.011	0.006	0.004	0.003	0.002	0.002

## 4.2

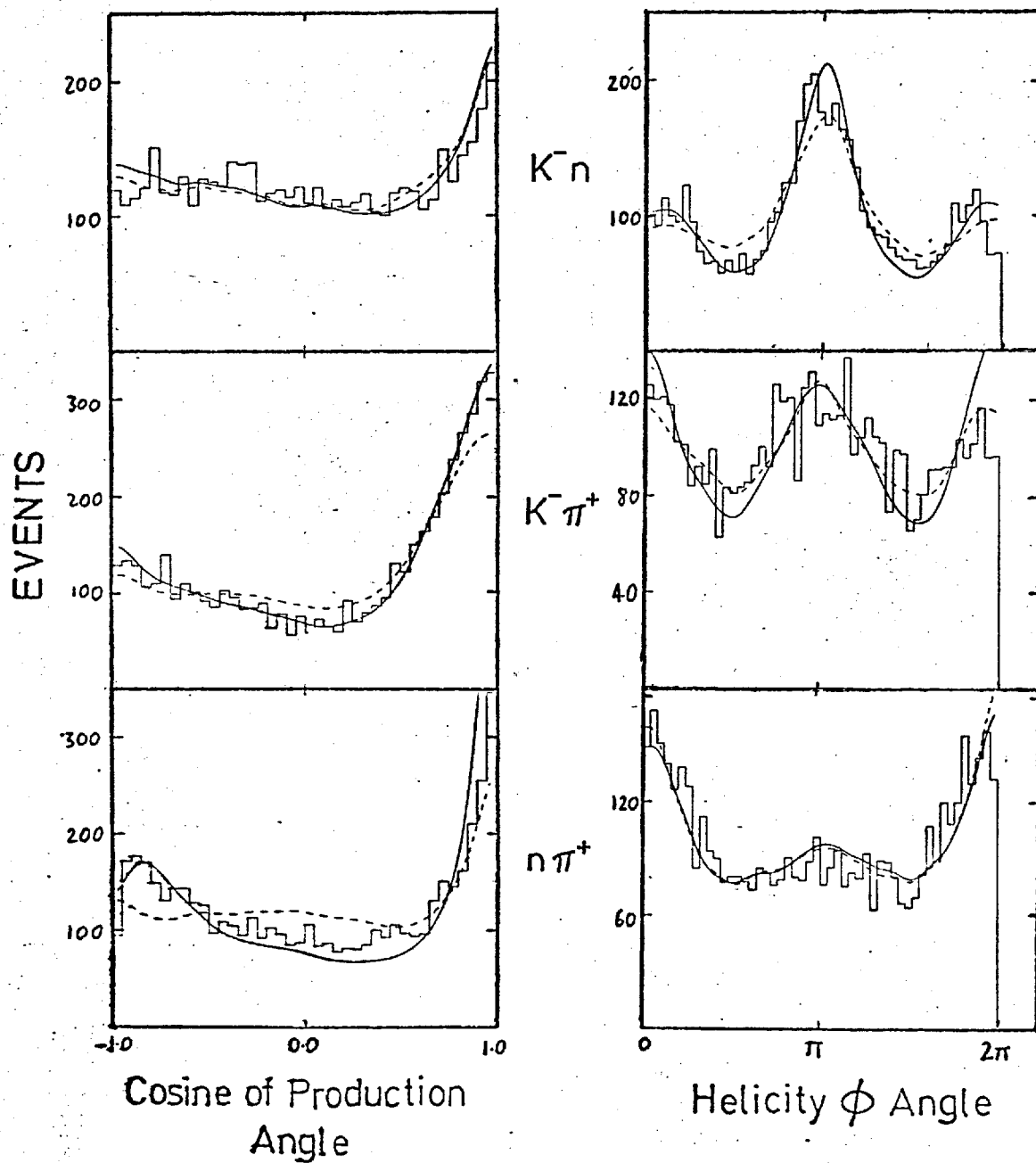


## 4.3





## 4.6



5.1 Introduction

Partial wave analysis is the study of structure in the direct or S-channel of a reaction in terms of the individual angular momenta or partial waves taking part in the reaction. Structure in the S-channel appears as a combination of resonant waves which can interfere with each other constructively or destructively, so as to reproduce the energy variations in the cross-section and differential cross-section, and hence the Legendre coefficients which describe them.

Two methods exist for partial wave analysis; the energy independent and energy dependent methods. In the former case, sufficient accurate data is required at each energy for a solution, or range of statistically acceptable solutions, to be found which gives possible values to the complex partial wave amplitudes at that energy. In a single channel analysis such as  $\pi N \rightarrow \pi N$ , the data takes the form of Legendre coefficients describing both the differential cross-section and polarization of the final state nucleon, of the reactions involving  $\pi^+ p$  and  $\pi^- p$  incident states, together with information from the total cross-sections. These coefficients can be related, via Clebsch-Gordan coefficients, to binomial combinations of partial wave amplitudes. As long as the number of data points exceeds the number of unknowns (the partial wave amplitudes) a solution can be found. Continuity is then imposed on the possible solutions at different energies and for each wave to select out the most likely solution at each energy, and finally an energy dependent study is made on the resulting partial wave amplitudes to determine the resonant effects present.

On applying the above method to the quasi two-body reaction  $K^- p \rightarrow \bar{K}^* N$ , we must determine whether the number of data points exceeds the number of unknowns. It will be shown later that about forty-four

partial waves exist for total angular momentum less than  $\frac{9}{2}$ . Thus a maximum of eighty-eight unknowns are present. Assuming structure in the differential cross-section and differential density matrix elements (in future referred to as  $\frac{d\sigma}{dn}$  and  $\rho \frac{d\sigma}{dn}$ ) require Legendre coefficients up to order six, then a maximum of twenty-five data points for each charge state of the  $\bar{K}^*N$  system are available. Thus the fit would be highly under-constrained and so no solution could be obtained. This fact alone prevents an energy independent analysis of the  $\bar{K}^*N$  system.

A possible alternative could be to use the complete three-body data in all four variables. The isobar model<sup>(26)</sup> is such an example. Here a relationship is set up between the partial wave amplitudes and the four variable density function, which is fitted to the data either in a number of mass bins spread over the Dalitz Plot<sup>(27)</sup> or by a maximum likelihood approach using all events simultaneously.<sup>(28)</sup> This method requires high statistics at each energy. In the SLAC-LBL analysis of  $\pi N \rightarrow \pi \pi N$ <sup>(29)</sup> large quantities of data were available for this method to be successfully carried out. A similar application has been made by the Birmingham group<sup>(30)</sup> to their  $K^-d \rightarrow \bar{K} \pi N(N)$  data, but it is generally felt that data is too limited in  $\bar{K}^*N$  experiments to validate its usefulness.

It is for the above reasons that an energy dependent analysis was undertaken in this study. In this case the energy dependence of the partial waves is already assumed, whether as Breit-Wigner functions for resonances, or simple functions of energy in the case of backgrounds. The eighty-eight or so unknowns can now be fitted with data from all energies simultaneously. In this chapter the formalism for the analysis is developed, with special emphasis on the  $\bar{K}^*N$  system. A description of the computer program used in the  $\bar{K}^*N$  analysis is also given. The

next chapter describes in detail the procedure taken in the analysis, together with a rudimentary partial wave analysis of the  $\Lambda(1520)\pi$  system.

## 5.2 The Formalism

The following is based on ref. (8) and uses the helicity formalism of Jacob and Wick<sup>(19)</sup> to express  $\frac{d\sigma}{d\Omega}$  and the  $\rho \frac{d\sigma}{d\Omega}$ 's in terms of a series of partial wave products and Legendre polynomials. In this way the partial waves are simply related to the experimental Legendre coefficients described in the previous chapter.

Consider a general two-body reaction in its centre of mass:-

$$a + b \rightarrow c + d \quad 5.1$$

with the particles having arbitrary spins  $S_a, S_b, S_c, S_d$ . The scattering amplitude  $f(\theta)$  is defined such that:-

$$\frac{d\sigma}{d\Omega} = |f(\theta)|^2 \quad \text{where } \hat{a} \cdot \hat{c} = \cos \theta \quad 5.2$$

$f(\theta)$  can be expressed in terms of a transition matrix summed over all helicity combinations of the four particles.

$$f(\theta) = \frac{1}{p\sqrt{(2S_a+1)(2S_b+1)}} \sum_{\text{all } \lambda} \langle \lambda_c \lambda_d | T(\cos \theta, E) | \lambda_a \lambda_b \rangle \quad 5.3$$

The term outside the summation is a phase space normalization factor, where  $p$  is the incoming centre of mass momentum, and  $E$  is the centre of mass energy. To expand the plane wave T matrix in terms of angular momentum eigenstates, we need to refer to the formalism based on the S-matrix, where the relevant expansion is:-<sup>(19)</sup>

$$\langle p' \theta' \phi' \lambda_c \lambda_d | S(E) | p \theta^0 \phi^0 \lambda_a \lambda_b \rangle = \sum_{j,m} \frac{2j+1}{4\pi} D_{m\lambda}^{j*}(\phi', \theta', 0) \langle \lambda_c \lambda_d | S^j(E) | \lambda_a \lambda_b \rangle D_{m\lambda}^j(\phi^0, \theta^0, 0) \quad 5.4$$

$$\text{where } \lambda = \lambda_a - \lambda_b \text{ and } \lambda' = \lambda_c - \lambda_d$$

$(\theta^0, \phi^0)$  are the polar and azimuthal angles of the incident beam direction in a given axis system and  $(\theta, \phi)$  are for the final beam direction.  $p$  and  $p'$  are the initial and final momenta.

Eqn. (5.4) can be simplified if the axis system is defined such that 'y' is normal to the production plane and 'z' is along the incident beam direction. In this case  $\theta^0 = \phi^0 = \psi = 0$ , and making use of the properties of the rotation D matrices:-

$$D_{m\lambda}^J(0,0,0) = d_{m\lambda}^J(0) = \delta_{m\lambda} \quad 5.5$$

where  $\delta$  is the Kronecker delta and:-

$$D_{\lambda\lambda'}^{J*}(0,\theta,0) = d_{\lambda\lambda'}^J(\theta) \quad 5.6$$

In this axis system, therefore, there is a unique value of m, the z component of J, such that  $m = \lambda_a - \lambda_b$  and its summation in eqn. (5.4) is suppressed. Furthermore, since the  $\phi$  dependence drops out, the normalization factor includes an extra  $2\pi$  and eqn. (5.4) becomes:-

$$\langle p'\theta 0 \lambda_c \lambda_d | S(E) | p 0 0 \lambda_a \lambda_b \rangle = \sum_J (J+\frac{1}{2}) \langle \lambda_c \lambda_d | S^J(E) | \lambda_a \lambda_b \rangle d_{\lambda\lambda'}^J(\theta) \quad 5.7$$

Using the relationship  $T(E) = -iS(E)$  for inelastic scattering eqn.(5.3) becomes:-

$$f(\theta) = \frac{1}{p\sqrt{(2S_a+1)(2S_b+1)}} \sum_{J,m,\lambda} (J+\frac{1}{2}) \langle \lambda_c \lambda_d | T^J(E) | \lambda_a \lambda_b \rangle d_{\lambda\lambda'}^J(\theta) \quad 5.8$$

For partial wave expansion the two particle helicity state  $|Jm\lambda_1\lambda_2\rangle$  must be expressed as a sum over a complete set of orbital angular momentum states  $|Jm\{s\rangle$ . The characteristic coefficient is:<sup>(19)</sup>

$$\langle Jm\{s | Jm\lambda_1\lambda_2 \rangle = \left(\frac{2\ell+1}{2J+1}\right)^{\frac{1}{2}} C(\ell 0 s \lambda | J \lambda) C(s, \lambda, s_2 - \lambda_2 | S, \lambda, -\lambda_2) \quad 5.9$$

where  $S = s_1 + s_2$ , the total spin, and C is a Clebsch-Gordan coefficient.

Thus:-

$$f(\theta) = \frac{1}{p\sqrt{(2S_a+1)(2S_b+1)}} \sum \sqrt{(\ell'+\frac{1}{2})(\ell+\frac{1}{2})} C(\ell' 0 s' \lambda' | J \lambda') C(s_c \lambda_c s_d - \lambda_d | S, \lambda_c - \lambda_d) \cdot C(\ell 0 s \lambda | J \lambda) C(s_a \lambda_a s_b - \lambda_b | S, \lambda_a - \lambda_b) \langle \ell' s' | T^J(E) | \ell s \rangle d_{\lambda\lambda'}^J(\theta) \quad 5.10$$

where the summation is over  $J \ell s \ell' s'$  and all helicities  $\lambda_a \lambda_b \lambda_c \lambda_d$ .

The differential cross-section is obtained by taking the modulus-squared of eqn.(5.10) and using the properties of d functions:-

$$d_{\lambda_a \lambda_c}^{J_1} d_{\lambda_b \lambda_d}^{J_2} = (-1)^{\lambda_c - \lambda_d} \sum_{\ell=|J_1-J_2|}^{J_1+J_2} C(J_1, \lambda_1, J_2, -\lambda_2 | \ell, \lambda_1 - \lambda_2) C(J_1, \lambda_1', J_2, -\lambda_2' | \ell, \lambda_1' - \lambda_2') d_{\lambda_1 - \lambda_2, \lambda_1' - \lambda_2'}^{\ell}(\theta) \quad 5.11$$

and  $d_{0m}^{\ell}(\theta) = (-1)^m d_{m0}^{\ell}(\theta) = \left[ \frac{(\ell-m)!}{(\ell+m)!} \right]^{\frac{1}{2}} P_{\ell}^m(\cos \theta)$   
to give:-

$$\frac{d\sigma}{d\Omega} = \frac{1}{p^2(2S_a+1)(2S_b+1)} \sum \sqrt{(\ell_1+\frac{1}{2})(\ell_1-\frac{1}{2})(\ell_2+\frac{1}{2})(\ell_2-\frac{1}{2})} (-1)^{\lambda_c - \lambda_d} \prod_{i=1}^{10} C_i \quad 5.12$$

$$\times \langle \ell_1' s_1' | T^{J_1}(E) | \ell_1 s_1 \rangle \langle \ell_2' s_2' | T^{J_2}(E) | \ell_2 s_2 \rangle^* P_{\ell}^m(\cos \theta)$$

where  $C_i$  are ten Clebsch-Gordan coefficients.

The summation extends over  $\ell$  where  $|J_1 - J_2| \leq \ell \leq J_1 + J_2$  and all values of  $J_1, J_2, \ell_1', \ell_2', s_1, s_1'$  and all helicities  $\lambda_a, \lambda_b, \lambda_c, \lambda_d$ , obeying the condition  $s_1 = s_2, s_1' = s_2', \lambda_1 = \lambda_2, \lambda_1' = \lambda_2'$  for no polarization of the target particle.

Furthermore, for no polarization, the imaginary part of eqn.(5.12) can be shown to vanish.

The joint density matrix element for particles c and d is defined as:-

$$\rho_{m_c m_c'}^{m_d m_d'}(x) = \frac{1}{p^2(2S_a+1)(2S_b+1)} \sum_{m_a m_b} \langle m_c m_d | T(x, E) | m_a m_b \rangle \langle m_c' m_d' | T(x, E) | m_a m_b \rangle^* \quad 5.13$$

$$\frac{1}{p^2(2S_a+1)(2S_b+1)} \sum_{\text{all } m} | \langle m_c m_d | T(x, E) | m_a m_b \rangle |^2$$

where  $x = \cos \theta$ , and the denominator is the differential cross-section, used for normalization. The expression is in terms of spin components rather than helicities. In the helicity representation eqn.(5.13) can be expressed as:-

$$\rho_{m_c m_c'}^{m_d m_d'}(x) \frac{d\sigma}{d\Omega} = \frac{1}{p^2(2S_a+1)(2S_b+1)} \sum_{\lambda_a \lambda_b} \langle m_c m_d | T(x, E) | \lambda_a \lambda_b \rangle \langle m_c' m_d' | T(x, E) | \lambda_a \lambda_b \rangle^* \quad 5.14$$

If  $m_c$  and  $m_d$  are evaluated in the helicity systems of c and d respectively, no rotation is involved when converting from spin component amplitudes to helicity amplitudes.

Then:-

$$\langle m_c m_d | T(x, E) | \lambda_a \lambda_b \rangle = (-1)^{s_d - \lambda_d} \langle \lambda_c \lambda_d | T(x, E) | \lambda_a \lambda_b \rangle \quad 5.15$$

where the phase factor  $(-1)^{s_d - \lambda_d}$  is introduced following the Jacob and Wick convention. (19) Inserting eqn. (5.15) into eqn. (5.14):-

$$\rho_{m_c m_c'}^{m_d m_d'}(x) \frac{d\sigma}{d\Omega} = \frac{1}{p^2(2s_a+1)(2s_b+1)} \sum_{\lambda_a \lambda_b} (-1)^{\lambda_d - \lambda_a} \langle \lambda_c \lambda_d | T(x, E) | \lambda_a \lambda_b \rangle \langle \lambda_c' \lambda_d' | T(x, E) | \lambda_a \lambda_b \rangle^* \quad 5.16$$

which can be decomposed into partial waves using the same technique as with the differential cross-section. Then:-

$$\rho_{m_c m_c'}^{m_d m_d'}(\cos \theta) \frac{d\sigma}{d\Omega} = \frac{1}{p^2(2s_a+1)(2s_b+1)} \sum (-1)^{\lambda_d - \lambda_a + \lambda_c - \lambda_c'} \prod_{i=1}^{10} C_i \sqrt{(l_1' + \frac{1}{2})(l_1 + \frac{1}{2})(l_2' + \frac{1}{2})(l_2 + \frac{1}{2})} \quad 5.17$$

$$\times \left[ \frac{l - (\lambda_c' - \lambda_c)}{l + (\lambda_c' - \lambda_c)} \right]^{\frac{1}{2}} \langle l_1' s_1' | T^{J_1}(E) | l_1 s_1 \rangle \langle l_2' s_2' | T^{J_2}(E) | l_2 s_2 \rangle^* P_l^{\lambda_c' - \lambda_c}(\cos \theta)$$

where  $C_i$  are the same ten Clebsch-Gordan coefficients as in eqn. (5.12).

The summation runs over  $J_1, J_2, l_1', l_1, l_2', l_2, l, s_1', s_2', s_1 (=s_2), \lambda_a, \lambda_b$ . For no polarization in the initial states  $s_1 = s_2$  and  $\lambda_1 = \lambda_2$ . Furthermore, since  $m_c$  and  $m_d$  are evaluated in their relevant helicity systems:-

$$m_d = \lambda_d, \quad m_d' = \lambda_d', \quad m_c = \lambda_c, \quad m_c' = \lambda_c'.$$

If we are interested in the decay of particle  $c$  only then  $\lambda_d = \lambda_d' = m_d = m_d'$  and a sum over  $m_d$  is included. Thus, finally, the density matrix element for particle  $c$  only is:-

$$\rho_{m_c m_c'}(\cos \theta) \frac{d\sigma}{d\Omega} = \frac{1}{p^2(2s_a+1)(2s_b+1)} \sum (-1)^{\lambda_c - \lambda_c'} \prod_{i=1}^{10} C_i \sqrt{(l_1' + \frac{1}{2})(l_1 + \frac{1}{2})(l_2' + \frac{1}{2})(l_2 + \frac{1}{2})} \quad 5.18$$

$$\times \left[ \frac{l - m_c + m_c'}{l + m_c - m_c'} \right]^{\frac{1}{2}} \langle l_1' s_1' | T^{J_1}(E) | l_1 s_1 \rangle \langle l_2' s_2' | T^{J_2}(E) | l_2 s_2 \rangle^* P_l^{m_c - m_c'}(\cos \theta)$$

summed over  $J_1, J_2, l_1', l_1, l_2', l_2, l, s_1', s_2', s_1 (=s_2), \lambda_a, \lambda_b, \lambda_d$

On comparing eqns. (5.12) and (5.18) with eqns. (4.3) of the previous chapter, it can be seen that the Legendre coefficients  $A_l, B_l, C_l, D_l$  may be expressed as linear sums of partial wave products:-

$$X_l = \sum_{\substack{l_1, l_1', s_1, s_1', J_1 \\ l_2, l_2', s_2, s_2', J_2}} a_l \langle l_1' s_1' | T^{J_1}(E) | l_1 s_1 \rangle \langle l_2' s_2' | T^{J_2}(E) | l_2 s_2 \rangle^* \quad 5.19$$

where  $a$  contains all the factors relevant to the partial waves

associated with it. It can be easily calculated for all products and

for each of  $A_i$ ,  $B_i$ ,  $C_i$  and  $D_i$  up to any arbitrary order of expansion, and tables of these values exist for several final spin-parity states. (31)

They are usually called Tripp coefficients, after the author who first tabulated them for  $J^P = 0^{-1+}$  final state, (32) and the convention will be used in this thesis in order to distinguish them from the Legendre coefficients. For this analysis the Tripp coefficients were calculated by computer using the above formulae.

### 5.3 Application to the $\bar{K}^* N$ system

To determine which partial waves exist in the  $K^- p \rightarrow \bar{K}^* N$  channel, it is best to consider the spin-parities of the system i.e.  $0^{-1+} \rightarrow 1^{-1+}$ . Parity conservation imposes the condition  $(-1)^{l+l'} = (-1)^{l+l'}$  for the incoming and outgoing orbital angular momenta, i.e.  $l$  and  $l'$  must be even or odd together. In the final state there are two total spin values  $\frac{1}{2}$  and  $\frac{3}{2}$ . For a given total angular momentum  $J$  there are two values of  $l = J \pm \frac{1}{2}$ . The partial waves can then be determined as follows:-

$$\begin{array}{ll}
 1. & l = J + \frac{1}{2} \quad \begin{array}{l} s = \frac{1}{2} \Rightarrow l' = J + \frac{1}{2} = l \\ s = \frac{3}{2} \Rightarrow l' = J + \frac{1}{2} = l \quad \text{or} \quad l' = J - \frac{3}{2} = l - 2 \end{array} & 5.20 \\
 2. & l = J - \frac{1}{2} \quad \begin{array}{l} s = \frac{1}{2} \Rightarrow l' = J - \frac{1}{2} = l \\ s = \frac{3}{2} \Rightarrow l' = J - \frac{1}{2} = l \quad \text{or} \quad l' = J + \frac{3}{2} = l + 2 \end{array}
 \end{array}$$

For example, for  $J = \frac{5}{2}$   $l = J + \frac{1}{2}$  gives FF51 FF53 FP53  
 $l = J - \frac{1}{2}$  gives DD51 DD53 DG53

The spectroscopic notation is used throughout for the partial waves such that FP53 corresponds to a wave with  $l = 3$   $l' = 1$   $J = \frac{5}{2}$  and  $S = \frac{3}{2}$ . It can be seen that there are three partial waves for each spin-parity state, except when  $J = \frac{1}{2}$  where only two exist. Furthermore, two possible isotopic spin values occur in the S-channel,  $I=0$  and  $1$ . Thus each partial wave amplitude can be expressed as a combination of  $I=0$  and  $I=1$  amplitudes with appropriate Clebsch-Gordan coefficients. The nomenclature to be used, therefore, is the following:- a resonant state will be denoted as

e.g. F05 for  $l=3$   $I=0$   $J=\frac{5}{2}$ , which consists of three partial waves; OFF51, OFF53, OFP53 where the prefix denotes  $I=0$ . Where the  $I$ -spin is obvious the prefix is dropped.

To estimate the number of partial waves to be considered, it is necessary to study the energy dependence of the experimental Legendre coefficients. From the discussion of the previous chapter, it appears that structure is seen up to the seventh order of expansion. Eqns.(5.12) and (5.18) therefore show that the maximum value of  $J$  to be considered is  $\frac{7}{2}$ . Thus a maximum of forty-four waves need to be taken into account from both  $I=0$  and  $l$  contributions. This profusion of partial waves makes for a very complex analysis unless steps are taken to reduce the complexity. A minimum structure assumption has been used in this analysis, where the data is fitted with the minimum number of resonances necessary, together with background amplitudes which are either constant in energy, or have some simple energy dependence. If all forty-four waves are used, the analysis still requires at least eighty-eight parameters, which means that several statistically acceptable solutions will be obtained. It will be shown that a sample of these possible solutions are very similar to each other and thus represent a statistical scatter around the true unique solution.

It is necessary to determine how each partial wave amplitude is expressed in terms of  $I=0$  and  $I=1$  amplitudes, and hence determine a similar expression for the partial wave products of eqns.(5.12) and (5.18).

Consider the two channels:-

$$K^-_p \rightarrow K^{*-}_p$$

$$K^-_p \rightarrow \bar{K}^{*0}_n$$

5.21

The amplitudes for these processes are combinations of  $I=0$  and  $I=1$  amplitudes given by the appropriate Clebsch-Gordan coefficients. The relationships are calculated as follows with the usual convention of

'baryon first':-

$$\begin{aligned} T(K^-p \rightarrow K^{*-}p) &= \langle pK^{*-} | T | pK^- \rangle = \langle \langle \frac{1}{2}, \frac{1}{2} | \langle \frac{1}{2}, -\frac{1}{2} | T | \frac{1}{2}, \frac{1}{2} \rangle | \frac{1}{2}, -\frac{1}{2} \rangle \rangle \quad 5.22 \\ &= \langle \langle 1, 0 | \frac{1}{\sqrt{2}} + \langle 0, 0 | \frac{1}{\sqrt{2}} | T | \frac{1}{\sqrt{2}} | 1, 0 \rangle + \frac{1}{\sqrt{2}} | 0, 0 \rangle \rangle \\ &= \frac{1}{2} T^1 + \frac{1}{2} T^0 \end{aligned}$$

$$\begin{aligned} T(K^-p \rightarrow \bar{K}^{*0}n) &= \langle n\bar{K}^{*0} | T | pK^- \rangle = \langle \langle \frac{1}{2}, -\frac{1}{2} | \langle \frac{1}{2}, \frac{1}{2} | T | \frac{1}{2}, \frac{1}{2} \rangle | \frac{1}{2}, -\frac{1}{2} \rangle \rangle \quad 5.23 \\ &= \langle \langle 1, 0 | \frac{1}{\sqrt{2}} - \langle 0, 0 | \frac{1}{\sqrt{2}} | T | \frac{1}{\sqrt{2}} | 1, 0 \rangle + \frac{1}{\sqrt{2}} | 0, 0 \rangle \rangle \\ &= \frac{1}{2} T^1 - \frac{1}{2} T^0 \end{aligned}$$

where the matrix elements have been expressed in terms of I-spin states, and  $T^0$  and  $T^1$  are the I=0 and I=1 amplitudes respectively.

For a particular partial wave amplitude:-

$$\begin{aligned} T_{\ell JS}(K^{*-}p) &= \frac{1}{2} (\text{Re } T'_{\ell JS} + i \text{Im } T'_{\ell JS}) + \frac{1}{2} (\text{Re } T^0_{\ell JS} + i \text{Im } T^0_{\ell JS}) \\ \text{i.e. } T_{\ell JS}(K^{*-}p) &= \frac{1}{2} (\text{Re } T'_{\ell JS} + \text{Re } T^0_{\ell JS}) + i \frac{1}{2} (\text{Im } T'_{\ell JS} + \text{Im } T^0_{\ell JS}) \quad 5.24 \end{aligned}$$

$$\text{Similarly } T_{\ell JS}(\bar{K}^{*0}n) = \frac{1}{2} (\text{Re } T'_{\ell JS} - \text{Re } T^0_{\ell JS}) + i \frac{1}{2} (\text{Im } T'_{\ell JS} - \text{Im } T^0_{\ell JS}) \quad 5.25$$

Thus:-

$$\begin{aligned} \text{Re} \left( \begin{array}{c} T_{\ell JS}^* \\ K^{*-}p \\ \bar{K}^{*0}n \end{array} T_{\ell' J' S'} \right) &= \frac{1}{4} (\text{Re } T'_{\ell JS} \pm \text{Re } T^0_{\ell JS}) (\text{Re } T'_{\ell' J' S'} \pm \text{Re } T^0_{\ell' J' S'}) \quad 5.26 \\ &\quad + \frac{1}{4} (\text{Im } T'_{\ell JS} \pm \text{Im } T^0_{\ell JS}) (\text{Im } T'_{\ell' J' S'} \pm \text{Im } T^0_{\ell' J' S'}) \end{aligned}$$

$$\begin{aligned} \text{i.e. } \text{Re} \left( \begin{array}{c} T_{\ell JS}^* \\ K^{*-}p \\ \bar{K}^{*0}n \end{array} T_{\ell' J' S'} \right) &= \frac{1}{4} (\text{Re } T^0_{\ell JS} \text{Re } T^0_{\ell' J' S'} + \text{Im } T^0_{\ell JS} \text{Im } T^0_{\ell' J' S'}) \quad 5.27 \\ &\quad \pm \frac{1}{4} (\text{Re } T^1_{\ell JS} \text{Re } T^0_{\ell' J' S'} + \text{Im } T^1_{\ell JS} \text{Im } T^0_{\ell' J' S'}) \\ &\quad \pm \frac{1}{4} (\text{Re } T^0_{\ell JS} \text{Re } T^1_{\ell' J' S'} + \text{Im } T^0_{\ell JS} \text{Im } T^1_{\ell' J' S'}) \\ &\quad + \frac{1}{4} (\text{Re } T^1_{\ell JS} \text{Re } T^1_{\ell' J' S'} + \text{Im } T^1_{\ell JS} \text{Im } T^1_{\ell' J' S'}) \end{aligned}$$

Thus, for a given set of  $\ell JS \ell' J' S'$  there are four terms, two of which involve interference between I=0 and I=1 amplitudes, and two of which involve interference between amplitudes of the same I-spin. As can be seen from eqn.(5.27), the interference terms involving the two I-spin states have opposite sign for the two channels. This means that structure in a Legendre coefficient due to interference between waves of the same I-spin will have the same sign in the two channels, whereas for opposite I-spins the relative sign will be negative. This important effect serves to fix the relative I-spin of interfering waves in the partial wave analysis.

#### 5.4 The Program

The program used for this analysis was the Rutherford Laboratory two-body partial wave analysis program "APPLE",<sup>(33)</sup> extensively modified for the reaction type  $0^{-1/2+} \rightarrow 1^{-1/2+}$  and run on the Laboratory's IBM 360/195 computer. The object of the program was to set up theoretical Legendre coefficients at each energy from a set of input partial wave amplitude parameters and the appropriate Tripp coefficients, and to fit the experimental Legendre coefficients by minimizing the overall chi-squared:-

$$\chi^2 = \sum_{\text{all } X_l} \left( \frac{X_l^{\text{expt}} - X_l^{\text{theo}}}{\Delta X_l^{\text{expt}}} \right)^2 \quad 5.28$$

where  $X_l$  is a coefficient,  $\Delta X_l$  is its error with respect to the parameters. Because of the large amount of computation required, the fast minimizing routine VA04A<sup>(34)</sup> was employed.

Each partial wave amplitude was given the following energy dependent form:-

$$T_{lJJI} = A e^{i\phi} \cdot B(l, E) + \sum_{i=1}^3 B W_i(E) \quad 5.29$$

which is the sum of a background term multiplied by an angular momentum barrier factor, and up to three optional Breit Wigner resonance amplitudes.

The amplitude,  $A$ , and relative phase,  $\phi$ , of the background were each given a Legendre polynomial dependence on the centre of mass energy:-

$$A = \sum_{n=0}^{n_{\text{max}}} a_n P_n^0(E') \quad \phi = \sum_{m=0}^{m_{\text{max}}} b_m P_m^0(E') \quad 5.30$$

$$\text{where } E' = \frac{2(E - E_{\text{bot}})}{E_{\text{top}} - E_{\text{bot}}} - 1$$

and  $E_{\text{top}}$ ,  $E_{\text{bot}}$  are the upper and lower limits respectively of the centre of mass energy region.  $a_n$  and  $b_m$  are parameters to be fitted.

$n_{\text{max}}$  and  $m_{\text{max}}$  are the maximum orders of expansion which were normally

taken as zero; that is the background was normally assumed constant in energy. In practise,  $n_{\max}$  and  $m_{\max}$  were never taken beyond 2.

The form of the background barrier factor,  $B(l,E)$  was given by:-

$$B(l,E) = \left[ \frac{B_{l_{in}} \times B_{l_{out}}}{B_{l_{in}}^{\max} \times B_{l_{out}}^{\max}} \right]^{\frac{1}{2}} \times \frac{E^{\max}}{E} \quad 5.31$$

where  $B_l$  is the Blatt and Weisskopf barrier factor<sup>(14)</sup> for orbital angular momentum  $l$ , multiplied by  $kr$  where  $k$  is the centre of mass momentum for that system and  $r$  is the effective radius of interaction - taken to be 1 fermi in this analysis.  $E$  is the centre of mass energy; "in" and "out" correspond to the incoming  $\bar{K}N$  system and outgoing  $\bar{K}^*N$  system respectively. For the latter case, values of centre of mass momenta were calculated at the  $\bar{K}^*$  peak mass. At a later stage of the analysis the outgoing barrier factor was integrated over the  $\bar{K}^*$  line shape to allow for the finite width of the resonance.

The expression  $\frac{k}{E}$  is included as a two body phase space factor. The subscript "max" corresponds to a calculation at the maximum centre of mass energy point of the region. The denominator of eqn.(5.31) is therefore a normalization factor which imposes a maximum value of unity on the background barrier factor.

The Breit-Wigner amplitude used was the standard non-relativistic form:-

$$BW(E) = \frac{\sqrt{\Gamma_e(E) \Gamma_r(E)}/2}{(E_R - E) - i\Gamma(E)/2} \times e^{i\psi} \quad 5.32$$

where  $E_R$  is the resonance peak mass;  $\Gamma(E)$  is the full width, and is energy dependent;  $\Gamma_e$  and  $\Gamma_r$  are the energy dependent partial widths for the formation of the resonance (assumed to be the "elastic" channel, "e") and its decay via the channel "r" - in this case  $\bar{K}^*N$ .  $\psi$  is a relative phase at resonance, which the  $SU(3)$  model predicts to be either

0 or  $\pi$ , corresponding to the  $\pm$  sign for the square root in the numerator.

The resonance full width  $\Gamma(E)$  can be expressed as a sum of energy dependent partial widths for the various possible decay channels  $i$  :-

$$\Gamma(E) = \sum_i \Gamma_i(E) \quad 5.33$$

The explicit energy dependence of each  $\Gamma_i(E)$  may be separated out by writing it as a product of an energy independent reduced width  $\gamma_i$ , and a function of energy (barrier factor etc.):-

$$\Gamma_i(E) = \gamma_i V_i(E) \quad 5.34$$

The branching ratio  $\alpha_i$  to channel  $i$  is of course energy independent, so it can be written as the ratio of the reduced width for channel  $i$ , to the reduced total-width  $\gamma$  (also energy independent):-

$$\alpha_i = \frac{\gamma_i}{\gamma} = \frac{\gamma_i V_i(E)}{\gamma V_i(E)} \quad 5.35$$

$$\text{Thus} \quad \gamma_i V_i(E) = \Gamma_i(E) = \gamma \alpha_i V_i(E) \quad 5.36$$

$$\text{i.e.} \quad \Gamma(E) = \gamma \sum_i \alpha_i V_i(E) \quad 5.37$$

An assumption is now made that the energy dependence of the total width is given only by the energy dependence of the elastic partial width  $\Gamma_e(E)$  i.e.:-

$$\Gamma(E) = \gamma \sum_i \alpha_i V_i(E) \approx \gamma V_e(E) \quad 5.38$$

This is the same as saying  $\alpha_e \gg \alpha_{i \neq e} (\approx 1)$

With this assumption eqn.(5.32) becomes:-

$$BW(E) = \frac{\frac{\gamma}{2} \sqrt{\alpha_e \alpha_r} [V_e(E) V_r(E)]^{\frac{1}{2}}}{(E_R - E) - i \frac{\gamma}{2} V_e(E)} \times e^{i\psi} \quad 5.39$$

The energy dependent functions are:-

$$V_e(E) = \frac{B_{\ell_{in}}}{B_{\ell_{in}}^R} \times \frac{E^R}{E} \quad V_r(E) = \frac{B_{\ell_{out}}}{B_{\ell_{out}}^R} \times \frac{E^R}{E} \quad 5.40$$

where the  $B_i$ 's are defined as on page (119). "R" denotes a calculation

at the resonance peak mass, such that the energy dependent functions are normalized to unity at this point. Again, the outgoing term is calculated at the peak mass of the  $\bar{K}^*$ , and at a later stage is integrated over the  $\bar{K}^*$  lineshape. For resonant masses below the  $\bar{K}^*$  threshold  $V_r(E)$  was set to unity since  $B^R$  would be imaginary.

Thus the amplitude at resonance is  $\sqrt{\alpha_e \alpha_r}$ ; the full width at resonance =  $\gamma$ ; and the resonance mass =  $E_R$ . Since  $\alpha_e + \alpha_r \leq 1$ , it is evident that the maximum value of the amplitude can never exceed  $\pm 0.5$ , thus imposing a unitarity bound. Furthermore, from scattering theory a partial wave is defined as:- (35)

$$T_l = \frac{\eta_l e^{2i\delta_l} - 1}{2i} \quad 5.41$$

for elastic scattering and:-

$$T_l = \frac{\eta_l' e^{2i\delta_l'}}{2i} \quad 5.42$$

for inelastic scattering,

where  $\eta$  and  $\delta$  are the absorption and phase-shift parameters. The value  $\eta = 1$  defines the unitarity bound on the amplitude. For the elastic case the bound describes a circle of radius 0.5 and centred at  $(0, \frac{i}{2})$  in the Argand plane. For the inelastic case the circle is centred at the origin and imposes the limiting value of 0.5 on the amplitude. To constrain the partial wave amplitudes within the unitarity bound, a penalty  $\chi^2$  was added if any amplitude exceeded 0.5 in a fit.

\*\*\*\*\*

## Chapter 6

## The Partial Wave Analysis (Experiment)

### 6.1 Introduction

This chapter describes a full partial wave analysis of the  $\bar{K}^* N$  system using the formalism of the previous chapter. The information gained from a preliminary solution of the dominant partial waves is fed back into the Dalitz Plot analysis in the form of production barrier factors applied to the  $\bar{K}^*$ , and better fits to the data are obtained. Improved values of the cross-section are then re-applied to the partial wave analysis. Data from the Birmingham  $K^- d \rightarrow \bar{K}^0 \pi^- n(p)$  analysis<sup>(36)</sup> is included to constrain the partial wave amplitudes, and three similar solutions are obtained from fits to the combined data. A very rudimentary qualitative partial wave analysis is also described for the  $\Lambda(1520)\pi$  system, using only data from the present experiment.

### 6.2 The Preliminary Solution

The basic set of resonances considered were those classed as "established" and "probable" as a result of the two-body partial wave analysis of this experiment.<sup>(37)</sup> A resonance was not considered if its peak mass lay more than one full width away from the lowest energy point of the region, i.e. 1850 MeV. The basic set are given in table (6.1.a). Due to the somewhat large errors in the Legendre coefficients, the masses and widths of these resonances were fixed at the values given in ref. (37), and shown in table (6.1.a), to reduce the number of parameters to be fitted. Each resonance was included in all partial waves pertaining to its  $J^{PI}$  state. At a later stage of the analysis the resonances classed as "possible" in ref.(37) and listed in table (6.1.b) were included one at a time to try and improve on the solution obtained.

For the majority of this preliminary analysis the Legendre coefficients of the first two energies of the CRS data were included.

They were later discarded because they were in conflict with the coefficients of the present experiment in the same energy region. It is for this reason that they are not given in tables (4.1) and (4.2).

For this preliminary analysis the Legendre coefficients were fitted up to orders  $A_6$ ,  $B_6$ ,  $C_4$  and  $D_4$  in both charge states. Later on, higher orders were included to constrain the amplitudes of the high spin waves.

For the first run all waves were included, with the background amplitudes constant in energy but as variable parameters of the fit. Their amplitude parameters were started close to zero with arbitrary starting values for their phases. All the resonances of table (6.1.a) were included with arbitrary amplitudes. The overall number of parameters to be fitted was 113 for 840 data points. After an hour of computer CPU time and 50 iterations, the  $\frac{\chi^2}{NDF}$  dropped to  $\frac{1071}{735} = 1.46$  with a final change in  $\chi^2$  ( $\delta\chi_{last}^2$ ) of 3.0. Several small contributions were set to zero and fixed, including the resonant amplitude OPF33(1900). The dominant resonant waves were S11(1955), OFP53(1822) and OGD73(2110). The latter confirmed the large value stated by Litchfield<sup>(38)</sup>. Because of the excessive amount of computer time required, no subsequent runs were taken to convergence - their quality being determined by  $\delta\chi_{last}^2$ .

To look for structure in the intermediate waves, each  $J^{\text{PI}}$  state in turn from D03 to F17 was tested in the following way. The background amplitude and phase of each contributing partial wave were assigned linear terms in their energy dependence, which were allowed to vary in the fit, but started close to zero. The zeroth order terms were shifted away from their previous values in order that the run should be started away from the present minimum. Each run was allowed twelve minutes. The result showed that the largest drop in  $\chi^2$  occurred for the D03 state. However, two of the three contributing waves were seen to perform a

clockwise rotation in the Argand plane, which is generally contrary to the direction taken for a resonant wave. Nevertheless, the linear terms were removed and a resonance inserted with variable mass and width, to see if the improvement in  $\chi^2$  could be reproduced. Although the resonance was inserted in all three waves, the three contributions were coupled to the same mass and width parameters which were to be fitted. This was a general feature of the analysis whenever variable mass and width were used. Arbitrary starting values of 1960 MeV and 120 MeV for mass and width respectively were used, with amplitudes of 0.05 for each wave. The result of the run was a  $\frac{\chi^2}{\text{NDF}}$  of  $\frac{1014}{730} = 1.39$  and  $\delta\chi^2_{\text{last}} = 2$ , with fitted mass and width values of 1890 and 227 MeV respectively. The fitted DS33 amplitude was 0.08, and much larger than the two DD amplitudes, which would be expected from barrier factor considerations. The drop in  $\chi^2$  of 57 units and the physical values of the fitted parameters are evidence for the existence of a possible resonance in this state. The obvious candidate for this resonance is a  $\Lambda(2010)$  mentioned in the Particle Data Group tables. (3)

To check the validity of this D03 resonance, it was removed from the solution. The solution was then reminimized, the resonance reinserted with different mass, width and amplitudes, and the solution again reminimized. The result was a  $\frac{\chi^2}{\text{NDF}}$  of  $\frac{997}{730} = 1.37$  and  $\delta\chi^2_{\text{last}} = 1$ , and fitted mass and width of 1885 MeV and 245 MeV respectively. The similarity of these values to the previous fitted values are further evidence for the existence of this D03 resonance. On studying the fit to the Legendre coefficients, however, no definite improvement could be observed in any one coefficient. This would be expected, though, because of the large width of the resonance.

To check that the resonance appeared in the D03 state and not the D13 state, the above procedure was repeated for the latter. The fitted

width was 1520 MeV, thus effectively throwing out the resonance. This result also confirmed that the "possible" D13(1920) did not couple to the  $\bar{K}^* N$  system.

A search was now made for the presence of the two remaining "possible" resonances in the energy region. The F05(2100) was inserted into the  $\frac{\chi^2}{\text{NDF}} = 1.46$  solution (i.e. without the D03 resonance), with variable mass and width. The fitted width was 500 MeV, i.e. effectively throwing out the resonance.

The S01(1825) was tested in a similar way. The result was a  $\frac{\chi^2}{\text{NDF}}$  of  $\frac{999}{731} = 1.37$  and  $\delta\chi^2_{\text{last}} = 2$ , i.e. a drop in  $\chi^2$  of 80 units. However, the fitted width was 100 MeV compared to the two-body analysis result of 230 MeV (used as a starting value). The fitted mass was 1863 MeV. Despite this small width the resonance parameters were inserted into the solution containing the D03 resonance. The final  $\frac{\chi^2}{\text{NDF}}$  was  $\frac{953}{726} = 1.31$  and  $\delta\chi^2_{\text{last}} = 2$ . The D03 parameters were reasonably stable but the S01 width dropped to 37 MeV. Various runs with different starting values of mass and width for the S01 showed a preference for the narrow width. Constraining these values to lie near the two-body analysis values (by imposing a penalty  $\chi^2$  if the parameters strayed too far) produced a much higher  $\chi^2$  than the above value. It was quite certain then, that the S01 structure was not the "possible" state seen in the two-body analysis, and was most probably the result of fitting a statistical fluctuation at the lowest two energy points. The resonance was, however, kept in the solution.

Several resonance contributions which had given consistently small amplitudes throughout the analysis were now removed from the solution. These were almost all sub-threshold resonances. In addition the two lowest CRS data points were removed and the OPF33(1900) contribution was reinserted for completeness. The final  $\frac{\chi^2}{\text{NDF}}$  was  $\frac{865}{652} = 1.33$  and

$\delta\chi^2_{\text{last}} = 2.8$  for 104 parameters. This was classed as the preliminary solution.

The variations of the resonance parameters through the analysis are shown in table (6.2), and are seen to be remarkably constant. The dominant amplitudes come from the G07(2110), F05(1822), P01(1853) and S11(1955), with a further large contribution from the D03 resonance. It must be stated, however, that this solution is one of many possible acceptable solutions to the data.

### 6.3 Refitting the Dalitz Plot

The above partial wave solution gives a total amplitude for each partial wave(resonance plus background) at each energy. It is therefore possible to calculate the cross-section for each partial wave at each energy, using the Tripp coefficients for  $A_0$ , for this particular solution. Hence the relative intensities of the outgoing orbital angular momentum,  $l_{\text{out}}$ , states at each energy can also be calculated. This information shows which  $l_{\text{out}}$  values are dominant at each energy, and an empirical barrier factor can thus be set up for the  $\bar{K}^*$  which reflects this. On applying this factor to the  $\bar{K}^*$  Breit-Wigner function in Chapter 3, the Dalitz Plot can be refitted without the use of the mass depression technique.

Table (6.3a) gives the partial wave amplitudes at each energy for this experiment from 1.125 GeV/c upwards for the dominant waves (i.e. amplitudes greater than 0.1 at that particular energy). It can be seen that only outgoing S and P waves are important, with D waves growing in importance with energy. This is obviously due to the vicinity of the  $\bar{K}^* N$  threshold.

Now the  $A_0$  Legendre coefficient can be shown to be related to the partial wave products by the relation:-

$$A_0 = \sum_{\substack{l'l' \\ s's}} (J+\frac{1}{2}) |T_{ll'}|^2 \quad 6.1$$

where the Tripp coefficient in this case is  $J + \frac{1}{2}$ .

For example, at 1.125 GeV/c the  $A_0$  contribution of the dominant waves is given by:-

$$\begin{aligned} A'_0 &= \frac{1}{4} ( 1 \times |15511|^2 + 1 \times |0PP13|^2 + 2 \times |0DS33|^2 + 3 \times |0FP53|^2 ) \quad 6.2 \\ &= \frac{1}{4} ( 0.025 + 0.055 + 0.036 + 0.127 ) \end{aligned}$$

using the amplitudes of table (6.3a) and the I-spin factor,  $\frac{1}{4}$ . The total S and P wave contributions are therefore in the ratio 1:3. Thus a combination of S and P wave barrier factors are required at 1.125 GeV/c for Dalitz Plot fitting purposes. Table (6.3b) shows the intensity ratios for S, P and D waves at the other energies. It can be seen that in all cases the P wave must be taken into account with a D wave effect appearing at the higher energies.

To implement the above result an empirical barrier factor of the form:-

$$a_0 + a_1 \left( \frac{p^2}{p^2 + X^2} \right) + a_2 \left( \frac{p^4}{9X^4 + 3X^2 p^2 + p^4} \right) \quad 6.3$$

where  $X = 200$  MeV/c;  $P =$  centre of mass momentum was applied to the  $\bar{K}^*$  Breit-Wigner function of eqn.(3.4). The  $a_0$ ,  $a_1$ , and  $a_2$  parameters were taken as the relative S:P:D wave intensity ratio. Because of normalization problems, however, these parameters became redundant, and the effective result was an S-wave barrier with some P and D wave admixture. The Dalitz Plot analysis of section (3.6) was then repeated, with the nominal mass of the  $\bar{K}^*$ , (3) for the present experiment only.

At almost every energy and in all three channels a dramatic improvement was seen for the fit to the  $\bar{K}^*$  with no mass depression necessary. Furthermore, the data below 1.125 GeV/c could also be fitted properly if the same barrier factor as at 1.125 GeV/c was assumed. The results of these fits are presented in table (6.4) and should be

compared with the results of table (3.3) in chapter 3. The partial cross-sections for the  $\bar{K}^*$  are seen to be consistently higher than before, since the fit is now able to extract that  $\bar{K}^*$  contribution which could previously only be classed as background. Typical fits to the  $(\bar{K}\pi)$  system are shown in figure (6.1). The solid curve is the result of the interference model together with the application of the  $\bar{K}^*$  barrier factor, and the dashed curve is for the interference model alone. Typical fits to the  $K^-p\pi^0$  channel below 1.125 GeV/c are shown in figure (6.2). The other two channels are not shown owing to lack of structure in this region.

The  $\bar{K}^*N$  and  $\Lambda(1520)\pi$  partial cross-sections of table (6.4) are the final values obtained. They are plotted in figure (6.3) together with the cross-sections from the CRS data obtained in chapter 3 using the interference model alone. They are seen to be in good agreement with other analyses in this energy region.

The errors on the cross-sections have been calculated in such a way as to reflect the spread of values for the three models considered, i.e. no interference, interference between  $\bar{K}^*$  and S-wave, and interference plus  $\bar{K}^*$  barrier factor. For each channel and at each energy from 1.125 GeV/c upwards, the mean and standard deviation from the three estimates were obtained with each value weighted by the inverse of the  $\frac{\chi^2}{NDF}$  of the fit for the respective model. The final error in the cross-section was a combination of the above standard deviation, the statistical error and the error in the microbarn equivalent. Below 1.125 GeV/c the errors were based on the percentage error at 1.125 GeV/c together with an estimate of the error in the fitted fraction.

It can be seen from table (6.4) that the ratio of the  $K^{*-}p$  cross-sections for the  $\bar{K}^0p\pi^-$  and  $K^-p\pi^0$  channels at each energy is consistently less than 2:1. Thus the change from the mass depression technique to the

inclusion of barrier factors did not improve on this. The conclusion to be gained from this result is that the  $\bar{K}^*$  cannot be cleanly separated from the other processes in the  $\bar{K}^- p \pi^0$  channel. This may be due in part to non-negligible interference between the resonant processes. Since interference between different two-body systems cannot be quantitatively calculated for the Dalitz Plot analysis described in chapter 3, as can be done for interference within the same system, the possibility of further interference has had to be ignored and is assumed to be negligible. Thus the cross-section ratio problem appears to be inherent in the models considered in this study and must be left unsolved.

The Legendre coefficients for the  $\bar{K}^* N$  system were calculated from these latest fits and were found to be essentially unchanged from the values obtained from the interference model alone. The only change made to the coefficients, therefore, was to update the  $A_0$ 's to account for the change in the cross-sections.

#### 6.4 Integrated barrier factors

In obtaining the preliminary solution for the  $\bar{K}^* N$  partial wave analysis, no account had been taken of the finite width of the  $\bar{K}^*$ , the outgoing barrier factor being calculated at the peak mass of the  $\bar{K}^*$  as if it were a stable particle. This technique is obviously incorrect at the  $\bar{K}^* N$  threshold ( $E^* = m_N + m_{\bar{K}^*}$ ) where the factor goes to zero, thus giving a zero cross-section. In fact, the finite width of the  $\bar{K}^*$  gives an appreciable cross-section even below the threshold centre of mass energy. Thus, rather than calculate a barrier factor at one unique  $\bar{K} N$  mass, an average should be taken at each energy over the lineshape of the  $\bar{K}^*$ , ideally over the entire mass range ( $-\infty < m < +\infty$ )

The outgoing barrier factors  $B_{\ell_{out}}$  in eqns.(5.31) and (5.40) were replaced by the expression:-

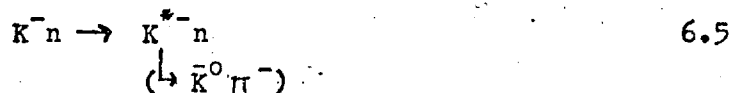
$$\frac{\int_{m_0-2\Gamma}^{m_0+2\Gamma} \theta W * B_{\ell_{out}} dm^2}{\int_{m_0-2\Gamma}^{m_0+2\Gamma} \theta W dm^2} \quad 6.4$$

where BW is the simple relativistic Breit-Wigner form:-  $\frac{1}{(m^2 - m_0^2)^2 + m_0^2 \Gamma^2}$   
 $m_0$  is the peak mass of the  $\bar{K}^*$ , and  $\Gamma$  is its width.

The integrals were carried out numerically by computer over the mass-squared region between  $(m_0 \pm 2\Gamma)^2$  with the barrier factor taken as zero outside the physical extent of the mass region allowed by phase space. The expression  $B_{l_{out}} / B_{l_{out}}^{max}$  (max = maximum centre of mass energy of the region) is plotted against centre of mass energy for all values of  $l_{out}$  up to 4 in fig.(6.4) for both the original (dashed curve) and integrated forms. It can be seen at the lowest energies that a large discrepancy occurs between the two forms as expected, since the non-integrated form goes to zero just below the energy region for all values of  $l_{out}$ . The result of this is that the energy independent partial wave amplitudes in the low energy region are actually smaller than the preliminary solution would suggest so as to cancel the increase in size of the barrier factor.

### 6.5 Incorporation of further data

In order to constrain the ratio between the  $I = 0$  and  $I = 1$  contributions resulting from the subsequent partial wave solutions, data from the Birmingham  $K^-d$  experiment<sup>(36)</sup> was included. The reaction:-



proceeds via pure  $I = 1$  states in the S-channel. Most of the Legendre coefficients presented in ref.(36) from threshold to 2170 MeV centre of mass energy were thus incorporated in the analysis. The  $A_0$ 's were, of course, the most important part of the data, since they gave directly the total  $I = 1$  cross-section.

On applying the preliminary solution to this data (with only the  $I = 1$  waves contributing) there was seen to be complete disagreement in the  $A_0$ 's, with the solution giving values two to three times that of the data throughout the energy region. After checking the validity of

the  $A_0$ 's, the only conclusion left was that the solution was wrong as regards the  $I = 1$  contribution.

It is interesting to consider where this error occurred. On looking at the high energy region of the  $A_0$ 's, the average values for the  $\bar{K}^{*0}n$  and  $K^{*-}p$  channels are almost equal at about 0.3. For the Birmingham  $A_0$ 's tabulated in table (6.5) the average in the high energy region is about 0.2. Denoting  $f_0$  and  $f_1$  as the total  $I = 0$  and  $I = 1$  amplitudes respectively, then using the I-spin factors of section (5.3) we obtain:-

$$\begin{aligned} K^{*-}p & \quad \frac{1}{4} |f_0|^2 + \frac{1}{4} |f_1|^2 + \frac{1}{2} \text{Re}(f_0 f_1^*) \simeq 0.3 & 1. & \quad 6.6 \\ \bar{K}^{*0}n & \quad \frac{1}{4} |f_0|^2 + \frac{1}{4} |f_1|^2 - \frac{1}{2} \text{Re}(f_0 f_1^*) \simeq 0.3 & 2. \\ K^{*-}n & \quad |f_1|^2 \simeq 0.2 & 3. \end{aligned}$$

The first two expressions show that the interference term is negligible, and with the third, uniquely determine the ratio  $\sigma_{I=0} : \sigma_{I=1} \simeq 5 : 1$ . This shows that the  $I = 0$  channel dominates the structure at the higher energies, which is not surprising since most of the resonant structure is in this channel.

Without expression (6.6.3), a second possibility is that the  $I = 0$  and  $I = 1$  cross-sections are almost equal and that the interference term just happens to go to zero. It appears as if the preliminary solution chose the latter case, and thus assigned a much larger cross-section to the  $I = 1$  channel than was in fact required. However, this cross-section could only be assigned to the background amplitudes which, in main, determine the trend in the  $A_0$ . Thus the resonant amplitudes are expected to be relatively stable in the high waves on inclusion of the constraining  $K^{*-}n$  data.

#### 6.6 Development of Solution A

For the remainder of this chapter, "constant" background means

that there are no energy dependent terms except the barrier factor, whereas a "fixed" background parameter is not allowed to vary in a fit.

Several runs were first made with constant background in all waves and no resonances. This was to find an average value for the  $\frac{\chi^2}{NDF}$  corresponding to zero structure. For each run, all amplitudes were started at the same value but with random phases. The average  $\frac{\chi^2}{NDF}$  was found to lie around  $\frac{2700}{887} = 3.0$ . All runs produced very similar fitted curves, but varied wildly in the fitted parameters. This was because no specific structure was being fitted, and so a large number of solutions could be found which reproduced the same average effect.

Furthermore, the  $J=\frac{1}{2}$  amplitudes were found in many cases to lie near the unitarity limit of 0.5, especially when the starting amplitudes were close to zero. A reason for this is that in these initial fits the parameters were fed into the minimizer (VAO4A) in the order of increasing  $J$ . Thus the initial calculations would be made by varying the  $J=\frac{1}{2}$  parameters. If the amplitudes were started close to zero, the minimizer would automatically take these waves to the unitarity limit to reduce the  $\chi^2$  by as much as possible over the whole energy region; these waves being the least inhibited by barrier factors. The remaining waves would then be biased by the large  $J=\frac{1}{2}$  waves. Two solutions to this problem would be to start the amplitudes around 0.25, and feed the parameters into the minimizer in the reverse order, i.e. from  $J=\frac{7}{2}$  downwards. In the former case, there would be little chance of a wave reaching 0.5 unless there was a good reason. In the latter case the  $J=\frac{7}{2}$  waves, being highly barrier suppressed at low energies, would be unable to contribute to the whole energy region and thus would never be expected to reach 0.5.

With the above considerations in mind, a run was carried out using the reverse order of parameter input and with all background

amplitudes starting at 0.25 with random signs and zero phases. In order to tie down the relative phases somewhat, the G07(2110) was included with arbitrary amplitudes. The final  $\frac{\chi^2}{NDF}$  was  $\frac{2355}{884} = 2.66$  with  $\delta\chi^2_{last} = 1$  and a very large GD amplitude (0.2) compared to GG, as normally expected from barrier considerations.

An established resonance was now needed at the low energy region, but overlapping the G07 to some extent, in order to fix the relative phase between the low and high energy regions. One possibility is the P03(1900), which was added with arbitrary amplitudes in all waves. The result was a  $\frac{\chi^2}{NDF}$  of  $\frac{2168}{881} = 2.46$  and  $\delta\chi^2_{last} = 11$ . Fitted amplitudes of less than 0.1 were assigned to the P03, but large improvements were seen in several coefficients. This is contrary to the result of the preliminary solution where little P03 was seen.

Structure in the  $A_4/A_0$  and  $B_4/A_0$  coefficients of the  $\bar{K}^{*0}$  channel at low energies appeared to be an interference effect, since it changed sign with respect to the average background beneath it at around 1910 MeV. The lack of structure in the  $K^{*0}$  channel, due possibly to bad statistics, prevented the relative I-spin of the interfering waves from being identified. However, the change of sign at 1910 MeV suggested that one of the interfering states was either the P03(1900) or the F15(1920) - the only established resonances with a mass in this area. The P03 can interfere only with F5 and F7 waves, and the F15 can interfere only with P3, F5 and F7. From the shape of the structure and the established resonances present, the only possible interferences were:- P03 x F05(1822), P03 x F17(2040), F15 x F05(1822) and F15 x F17(2040). The Tripp coefficients relevant for these interferences (see table (6.6)) seem to favour the P03 slightly more than the F15. The increase in the quality of the above fit on inclusion of the P03 further favours this resonance.

As a result of these considerations, and because the Birmingham solution assigned a large amplitude to it, the F17(2040) was inserted

in all F17 waves into the present solution with arbitrary amplitudes. The result was a  $\frac{\chi^2}{\text{NDF}}$  of  $\frac{2080}{878} = 2.37$  and  $\delta\chi^2_{\text{last}} = 1$ . Very little improvement was seen, and almost all in the  $A_4/A_0$  coefficient. The fitted FF73 amplitude dominated the three at about 0.07.

The F05(1822) was then inserted into this solution with amplitudes similar to the preliminary solution. At the same time the phases of several background amplitudes which were consistently smaller than 0.04 during the analysis were fixed. This was to reduce the total number of meaningful parameters to an acceptable level without removing important contributions. At several points in the subsequent analysis the phases of backgrounds were fixed or released according to this criterion. Thus, at this stage a total of 87 variable parameters were present.

The result of this run was a  $\frac{\chi^2}{\text{NDF}}$  of  $\frac{1682}{888} = 1.89$  and  $\delta\chi^2_{\text{last}} = 7$ , i.e. a drop of 400 units of  $\chi^2$ . The fitted F05 amplitudes showed that the FP53 wave dominated at 0.23 agreeing in magnitude and relative sign with the preliminary solution. The  $\bar{K}^{*0}$   $A_4/A_0$  and  $B_4/A_0$  coefficients were now fitted correctly, and an improvement was seen in the fit to the  $A_0$ 's for both this and the  $K^{*0}$  channel in the low energy region.

Although the F15(1920) was not expected to improve this fit, it was tested in the above solution, and its fitted amplitudes were found to be negligible.

For completeness, the S11(1955) and P01(1853) were included with amplitudes similar to those of the preliminary solution. The final  $\frac{\chi^2}{\text{NDF}}$  was  $\frac{1556}{886} = 1.76$  and  $\delta\chi^2_{\text{last}} = 3$ . The only large fitted amplitude was that of the PP13 wave (0.1). The large decrease in the S11(1955) amplitudes was probably due to the Birmingham data producing a constraint on the size of the  $I = 1$  amplitudes.

Despite the procedure taken to prevent a biasing of the  $J=\frac{1}{2}$  waves

towards large amplitudes, the S01 background amplitudes were still excessively large; the SD13 wave being close to the unitarity limit. To test for structure in this state, linear terms were introduced in both waves, with starting values taken in such a way as to reduce the overall amplitude to well below 0.5 at all energies. At the same time, linear terms were introduced into the ODS33 wave in order to test for the D03 structure seen in the preliminary solution. The resulting fit gave a  $\frac{\chi^2}{\text{NDF}}$  of  $\frac{1279}{880} = 1.45$  and  $\delta\chi^2_{\text{last}} = 1$ . The improvement was due almost entirely to the S01 structure, with very little structure in the ODS33 wave. The drop in  $\chi^2$  occurred mainly in the  $K^{*-}p$  channel where, for example, the drop was more than 100 in the  $A_0$ , due to an improvement to the fit at the lower energies.

At this point, higher order coefficients were included in the data to constrain the amplitudes of the high spin waves. These were the normalized  $A_7$ ,  $B_7$ ,  $C_5$ ,  $C_6$ ,  $D_5$  and  $D_6$  for  $\bar{K}^{*0}n$  and  $C_5$  for  $K^{*-}p$ . On running the above solution with this extra data a  $\frac{\chi^2}{\text{NDF}}$  of  $\frac{1413}{1005} = 1.41$  was obtained with  $\delta\chi^2_{\text{last}} = 1$  and little change in the resonance parameters.

With the preliminary solution in mind, the ODS33 linear background terms were replaced by a resonance in all three D03 waves with starting mass 1980 MeV and width 150 MeV and arbitrary amplitudes. The starting mass and width were taken from the result of a parallel solution which will be described later. The result was a  $\frac{\chi^2}{\text{NDF}} = \frac{1417}{1002} = 1.41$  and  $\delta\chi^2_{\text{last}} = 5$ . Thus no improvement in the solution was obtained. The fitted mass and width were 1986 and 256 MeV respectively, and the largest amplitude was the ODS33 wave (0.07). Despite the temptation to drop this resonance, it was kept in the solution so as to comply with the results of the parallel solution.

The linear background terms in the S01 state were now replaced by a resonance with starting mass 2040 MeV and width 190 MeV taken from the parallel solution, and arbitrary amplitudes. The result was a  $\frac{\chi^2}{\text{NDF}}$

of  $\frac{1366}{1001} = 1.37$  and  $\delta\chi^2_{last} = 6$ . The fitted mass stayed constant but the width increased to 350 MeV. Further, the DS33 amplitude of the D03 resonance increased to 0.16 and looked more resonant in shape on the Argand diagram. It was thus suspected that the S01 and D03 may be competing against each other, although the OSD13 amplitude of 0.31 seemed to insist on a large resonance in this wave. The stability of the solution to the width of the S01 was tested by fixing it at 230 MeV. The final  $\chi^2$  was unchanged, showing that the solution was insensitive to the width. It was henceforth fixed at 230 MeV.

The existence of this possible S01 resonance is unconfirmed by any previous analysis, but appears to have a large coupling via the SD wave to  $\bar{K}^*N$ . It will be shown to be required in the two further solutions to be described.

All other resonances in the energy region were tested with this solution, but none of them appeared to be required. Applying linear backgrounds to the other states besides S01 and D03 did not improve the  $\chi^2$ . Thus the above solution was taken to convergence with a  $\frac{\chi^2}{NDF}$  of  $\frac{1320}{1006} = 1.31$  and classed as solution "A". With the Birmingham data subtracted the final  $\frac{\chi^2}{NDF}$  was  $\frac{972}{787} = 1.24$  for 95 parameters. A summary of the development of this solution is given in table (6.7) together with the resonance amplitudes at each stage of the analysis.

### 6.7 Solution B

Several runs were attempted with constant background in all waves, and with a random set of amplitudes, and the set of basic "established" and "probable" resonances seen to be important in solution A, also with a random set of amplitudes. The solution with the lowest  $\chi^2$  was taken as the basic solution "B". This had a  $\frac{\chi^2}{NDF}$  of  $\frac{1364}{881} = 1.55$  and  $\delta\chi^2_{last} = 4$  (before the higher order coefficients were included). As can be seen from table (6.8) many of the amplitudes and relative signs of the

resonances were in close agreement with solution A. Further, the  $\frac{\chi^2}{\text{NDF}}$  was also very much lower.

Once again the S01 background amplitudes were seen to be large. Linear terms were thus applied and the solution was rerun to give a  $\frac{\chi^2}{\text{NDF}}$  of  $\frac{1314}{877} = 1.50$  and  $\delta\chi^2_{\text{last}} = 2$ . The fitted structure showed similar features to that at the same point in the development of solution A.

The ODS33 wave had a large fitted amplitude, and linear terms were also applied here. The result was a  $\frac{\chi^2}{\text{NDF}}$  of  $\frac{1232}{879} = 1.40$  and  $\delta\chi^2_{\text{last}} = 1$ . The fitted structure of this wave showed strong resonant-like features on the Argand diagram, to a much greater extent than solution A.

The higher order coefficients were then included in the data, and the above solution was rerun, giving a  $\frac{\chi^2}{\text{NDF}}$  of  $\frac{1376}{1005} = 1.37$  and  $\delta\chi^2_{\text{last}} = 2$ .

To test for the presence of a resonance in the D03 state, the linear terms in ODS33 were removed and a resonance with arbitrary mass and width of 1920 MeV and 120 MeV respectively was inserted in all three waves. The result was a  $\frac{\chi^2}{\text{NDF}}$  of  $\frac{1368}{1003} = 1.36$  and  $\delta\chi^2_{\text{last}} = 6$ , with fitted values of 1984 MeV for mass and 160 MeV for width, and the DS amplitude (0.13) much larger than the DD waves. Although the change in  $\chi^2$  was small, the fact that a resonance shape could reproduce the linear background structure supported the claim for a possible resonance in the D03 state.

It was obvious from the wide anti-clockwise circle on the Argand diagram of the OSD13 wave that the "possible" S01(1825) was not producing this structure. Nor, indeed, could the narrow effect at 1860 MeV seen in the preliminary solution produce such a wide circle. The linear background terms of this state in the above solution were thus replaced by a resonance of arbitrary mass 1950 MeV and width 150 MeV in both waves. The result was a  $\frac{\chi^2}{\text{NDF}}$  of  $\frac{1355}{1003} = 1.35$  and  $\delta\chi^2_{\text{last}} = 6$ . The fitted S01 mass and width were 2042 and 194 MeV respectively with a large amplitude (0.22) assigned to the OSD13 contribution. Although the change

in  $\chi^2$  was minimal, the OSD13 contribution reproduced exactly the linear background structure on the Argand diagram. However, the DO3 resonance width increased to 253 MeV, almost 100 MeV higher than before. This instability in the width was probably due to these two resonances competing against each other, due to the fact that both had similar masses and widths.

To test the importance of this S01 resonance, and at the same time to test its stability, it was completely removed from the solution leaving constant background in the S01 state. The resulting fit gave a  $\frac{\chi^2}{\text{NDF}}$  of  $\frac{1444}{1007} = 1.43$  and  $\delta\chi^2_{\text{last}} = 1$ , showing the need for structure in the S01 state. On replacing the resonance with starting values of 2000 MeV for mass and 150 MeV for width, the result was a  $\frac{\chi^2}{\text{NDF}}$  of  $\frac{1337}{1003} = 1.33$  and  $\delta\chi^2_{\text{last}} = 6$ , and fitted mass and width values of 2025 MeV and 202 MeV respectively. The solution was essentially unchanged compared with the  $\frac{\chi^2}{\text{NDF}} = 1.35$  fit, thus presenting good evidence for the existence of a possible resonance in the S01 state. No definite improvement in the fit to any one coefficient, however, could be seen: probably due to the large width of this resonance.

The above procedure was then applied to the DO3 resonance. On removal, the  $\frac{\chi^2}{\text{NDF}}$  became  $\frac{1477}{1008} = 1.47$  and  $\delta\chi^2_{\text{last}} = 6$ , i.e. an increase in  $\chi^2$  of 150. This was due mainly to the ODS33 background amplitude becoming large and contributing to a bad fit to the data at the higher energies. The resonance was then replaced with starting values of mass and width at 1950 MeV and 120 MeV respectively. The  $\frac{\chi^2}{\text{NDF}}$  dropped to  $\frac{1347}{1004} = 1.34$  and  $\delta\chi^2_{\text{last}} = 1$ , and the fitted mass and width values were 1987 MeV and 182 MeV respectively. This decreased width value should be compared with 270 MeV for the S01 resonance as a result of this fit. This is further possible evidence of the competition between the two resonances. However, it can be seen from the above that the existence of

both resonances is strongly supported.

Each of the remaining resonances of table (6.1) was inserted, in turn, into this solution but no further improvement in the fit was obtained. Each state in turn was then assigned linear background terms (except S01 and D03), but again no improvement was obtained. The solution was finally taken to convergence with a  $\frac{\chi^2}{NDF}$  of  $\frac{1303}{1006} = 1.29$  and classed as solution "B". With the Birmingham data subtracted, the  $\frac{\chi^2}{NDF}$  was  $\frac{963}{787} = 1.22$ . During the final minimization the D03 width was seen to fluctuate a great deal and ended up with a value of 312 MeV. The instability of this width is somewhat disquietening, but the fact that structure is present in the D03 state is good evidence in itself for the presence of a resonance with width about 250 MeV.

The resonance amplitudes at the main stages in the development of this solution are shown in table (6.8), and many of the final amplitudes are very similar to solution A. which is ambiguous to this extent.

### 6.8 Solution C

This solution is based on the Birmingham solution to their own data. This involved using their integrated barrier factors for the  $I = 1$  background waves in addition to a change of the normalization point for these factors from the maximum centre of mass energy of the region to the value 1.975 GeV.

The barrier factor thus used for the  $I = 1$  waves was:-

$$B(l, E) = \left[ \frac{B_{l_{in}} \times B_{l_{out}}}{B_{l_{in}}^0 \times B_{l_{out}}^0} \right]^{\frac{1}{2}} \times \frac{E^0}{E} \quad 6.7$$

where  $B_l = \left( \frac{p^2}{p^2 + \chi^2} \right)^l \cdot p$  and  $B_l^0$  is calculated at 1.975 GeV ( $=E^0$ ).  $p$  is the centre of mass momentum of the incoming or outgoing system. The term within the square root was integrated over the  $\vec{K}^*$  in the same way as described on page (129). The  $I = 1$  amplitudes were fixed at the values given in ref. (36).

Several runs were attempted using random  $I = 0$  background waves and the "established" and "probable" resonances of solutions A and B with arbitrary amplitudes. No acceptable fits were obtained, with the  $\frac{\chi^2}{\text{NDF}}$  averaging around  $\frac{2400}{922} = 2.6$ . With the inclusion of linear background terms in the S01 state, little improvement was seen.

The parameters of the  $I = 0$  waves were now allowed to vary. All waves fixed to zero in the Birmingham solution were also varied except the PF, DG and FH waves, and the F17(2040) width was taken from 137 MeV to the two-body analysis value of 190 MeV and fixed. The S01 linear background terms were also included, and one of the above solutions was rerun. The result was a  $\frac{\chi^2}{\text{NDF}}$  of  $\frac{1386}{878} = 1.58$  and  $\delta\chi^2_{\text{last}} = 5$ , i.e. a drop of 1000 in  $\chi^2$ . Several of the  $I = 1$  background amplitudes had changed by an appreciable amount, although the fit to the Birmingham data was only 32 units of  $\chi^2$  greater than the Birmingham solution itself. Thus it appeared as if a new, equally good solution to that data had been obtained, but which was also compatible with the data of the present experiment and the CRS data. The F17(2040) amplitudes were only slightly different from the  $\frac{\chi^2}{\text{NDF}} = 2.6$  solution, and the OSD13 structure was showing similar features to that seen in solutions A and B.

The S11(1955) was now added with arbitrary amplitudes, and linear background terms were applied to the ODS33 wave. The higher order coefficients were also included in the data. The result was a  $\frac{\chi^2}{\text{NDF}}$  of  $\frac{1410}{1000} = 1.41$  and  $\delta\chi^2_{\text{last}} = 4$ , with the ODS33 showing signs of structure.

The linear terms in the ODS33 background were replaced by a resonance in all three D03 waves with starting values of mass and width at 1980 MeV and 160 MeV respectively. The result was a  $\frac{\chi^2}{\text{NDF}}$  of  $\frac{1330}{1001} = 1.33$  and  $\delta\chi^2_{\text{last}} = 3$ ; with fitted mass and width values of 1958 MeV and 116 MeV respectively, and a ODS33 amplitude of 0.06. Although there was a reasonable improvement to the fit, the fitted width was inconsistent with the results of solutions A and B. The linear terms in the S01

background were replaced by a resonance with starting values of mass and width at 2040 MeV and 190 MeV respectively. The result was a  $\frac{\chi^2}{\text{NDF}}$  of  $\frac{1344}{998} = 1.35$  and  $\delta\chi^2_{\text{last}} = 1$ , with fitted mass and width values of 2025 MeV and 243 MeV respectively. Although the  $\chi^2$  had increased slightly, the solution was still consistent with the previous two solutions.

The D03 width was tested for stability by fixing its value at 230 MeV, minimizing the solution, releasing the parameter, and re-minimizing. The final fitted value was 130 MeV, showing that the solution preferred a narrow width.

After testing for the presence of any further structure, of which none was seen, the solution was taken to convergence with a  $\frac{\chi^2}{\text{NDF}}$  of  $\frac{1324}{1009} = 1.31$ . Before the final run, small background waves were removed for the  $I = 1$  states, and were assigned fixed phases in the  $I = 0$  case. The resonance amplitudes at the main stages of this solution are shown in table (6.9). Note that the D03 width increased to 219 MeV in the final run.

### 6.9 Discussion of the solutions

The three final solutions are presented in table (6.10) as sets of resonant amplitudes with a common overall sign. It can be seen that there is generally impressive agreement between the three solutions. Except for three amplitudes, at least two of the three solutions for each wave are in very close agreement, with all three having the same relative signs. The dominant resonances are the G07(2110), F05(1822), and P01(1853), with the new resonance in the S01 state also contributing a large amplitude. The stability of the parameters of this S01 state is quite remarkable considering the width of the state. A probable reason for this is that the large width of the resonance would tend to prevent the mass parameter from varying very far from its starting value.

The  $D_{03}$  resonance is not so stable, with large differences in the values of the width. However, the consistency in the relative signs of its amplitudes is convincing evidence for some form of resonance in this state. This is further confirmed by a very similar resonant state found in the  $K^-p \rightarrow \Lambda(1520)\pi$  analysis of the CRS collaboration.<sup>(39)</sup>

Because of the method of analysis, no errors can be assigned to the resonance parameters. With so many parameters fitted simultaneously, there is no reliable method of estimating errors anyway. The possibility of taking the average of the three solutions must also be discarded since they may be ambiguous solutions and not estimates of the same solution.

Solution C is shown as curves superimposed on the data in fig.(6.5), for the present experiment and CRS. It can be seen that the solution reproduces all the main features of the data, consistent with the assumption of minimum structure. The Argand diagrams are shown in fig. (6.6).

#### 6.10 Qualitative Partial Wave Analysis of the $\Lambda(1520)\pi$ system

The reaction  $K^-p \rightarrow \Lambda(1520)\pi$  takes place via pure  $I = 1$  in the S-channel. This means a much simpler S-channel structure is present, which could be analysed qualitatively to obtain the essential information. Furthermore, the presence of only one spin state in the  $\Lambda(1520)\pi$  system reduces the total number of partial waves to 14 for  $J$  less than  $\frac{9}{2}$ .

A selection of the Legendre coefficients for this channel and for the present experiment are plotted in fig.(6.7). The important features of the data are as follows:-

A large enhancement is seen at low energies in  $A_0$ . An increase is also present at the higher energies. Similar effects are seen in  $A_2/A_0$ . An enhancement is seen in the central region of  $A_1/A_0$ , which is also vaguely discernable in  $A_3/A_0$ . No further structure is seen in the higher  $A_L$  coefficients.

Apart from two bad data points, the trend in  $B_0/A_0$  is very similar

to  $A_0$ .  $C_1/A_0$  is consistently positive throughout the energy region, and  $C_2/A_0$  takes a negative dip at the lower energies.  $C_4/A_0$  shows a similar dip.

To explain the above structure in a qualitative manner it is best to start with the  $A_1$ 's. The large enhancement in  $A_0$  at low energies is, without doubt, the D15(1765), seen several times before in the  $\Lambda(1520)\pi$  system.<sup>(40)</sup> The Tripp coefficients predict a similar effect in  $A_2/A_0$  of the same sign. This is in fact seen. Litchfield et al.<sup>(17)</sup> have observed strong F17(2040) production in the  $\Lambda(1520)\pi$  analysis of the CRS data. It would thus appear as if this resonance should also contribute in the energy region of the present experiment. The increasing  $A_0$  at the higher energies seems to support this hypothesis. This is confirmed by a similar rise in  $A_2/A_0$  where the Tripp coefficients predict an enhancement of the same sign as in  $A_0$ .

The enhancement in  $A_1/A_0$  is due to an interference between states of opposite parity. It is tempting to identify these states with the D15(1765) and F17(2040). To attempt an identification, it is necessary to compare this structure with that in  $A_3/A_0$ . Here the structure is more difficult to resolve, but it can just about be seen that it is about half the magnitude of that in  $A_1/A_0$ . Assuming that the effect is due to interference between D15(1765) and something else, table (6.11a) lists the possible partial wave products with the Tripp coefficients for  $A_1$  and  $A_3$ . It can be seen that only two combinations have  $A_1$  and  $A_3$  Tripp coefficients of about the correct ratio and relative sign. These are DP5 x FD7 and DF5 x FG7, confirming the interference between D15(1765) and F17(2040). Furthermore, in the convention of "baryon  $\rightarrow$  baryon", the relative sign of the partial wave amplitudes contributing to the dominant interference term is negative.

Except for the presence of two bad data points, the  $B_0/A_0$  structure

is similar to  $A_0$ . This is also predicted by the Tripp coefficients if the D15 and F17 states dominate.

The similarity of the structure in  $C_2/A_0$  and  $C_4/A_0$  is possibly due to interference involving the D15(1765) at low energies. Table (6.11b) gives the Tripp coefficients for  $C_2$  and  $C_4$  for interference involving the D15 state. It can be seen that only two terms have coefficients which are consistent with the data. These are  $|DF5|^2$  and  $DP5 \times DF5$ . The first term has negative Tripp coefficients in both  $C_2$  and  $C_4$  contributing a negative definite value to the Legendre coefficients. The second term can contribute a negative value if the relative sign of the two amplitudes is negative. This is further evidence for the dominant D15(1765).

An estimate of the branching fraction of the D15(1765) to  $\Lambda(1520)\pi$  can be made by studying the  $A_0$  plot. Assuming the D15 to be the only resonant state in the low energy region, and assuming a constant background beneath it, then:-

$$\begin{aligned} & \text{magnitude of enhancement above background} && 6.8 \\ & = \alpha \alpha' \times (\text{Tripp coefficient}) \times (\text{branching fraction of } \Lambda(1520) \text{ to } K\bar{p}) \\ & \quad \times (\text{I-spin factor for } K\bar{p} \rightarrow D15(1765) \rightarrow \Lambda(1520)\pi) \\ & \approx 0.04 \pm 0.01 \end{aligned}$$

where  $\alpha$  and  $\alpha'$  are the D15(1765) branching fractions into  $\bar{K}N$  and  $\Lambda(1520)\pi$  respectively.

The Tripp coefficient is  $(J+\frac{1}{2}) = 3$ . The branching fraction of  $\Lambda(1520)$  to  $K\bar{p}$  is a combination of the experimental branching fraction to the  $\bar{K}N$  system which is currently taken as  $0.46^{(3)}$  and the Clebsch-Gordan coefficient for subsequent decay to  $K\bar{p}$ , which is  $\frac{1}{2}$ . The I-spin factor can also be seen to be  $\frac{1}{2}$ . A value of  $\alpha$  can be taken from ref.(37) as 0.41.

Substituting these values into eqn.(6.8) gives a value for the branching fraction of D15(1765) into  $\Lambda(1520)\pi$  of  $0.28 \pm 0.07$  which is

in rough agreement with the Particle Data Group<sup>(3)</sup> value of  $0.16 \pm 0.03$ .  
The discrepancy is obviously due to the fact that the D15(1765) cannot  
be cleanly distinguished from the background in the  $A_0$  plot.

\*\*\*\*\*

Table (6.1)

## a) "Established" and "Probable" Resonances Considered in the Analysis

Wave	Mass (MeV)	Width (MeV)	Elastic Branching Fraction	Class
S11	1955	170	$0.44 \pm 0.05$	Probable
P01	1853	166	$0.21 \pm 0.04$	Probable
P03	1900	72	$0.18 \pm 0.02$	Established
D15	1774	130	$0.41 \pm 0.03$	Established
F05	1822	81	$0.57 \pm 0.02$	Established
F15	1920	130	$0.05 \pm 0.03$	Established
F17	2040	190	$0.24 \pm 0.02$	Established
G07	2110	250	$0.30 \pm 0.03$	Established

## b) "Possible" Resonances

Wave	Mass (MeV)	Width (MeV)	Elastic Branching Fraction
S01	$1825 \pm 20$	$230 \pm 20$	$0.37 \pm 0.05$
D13	$1920 \pm 50$	$300 \pm 80$	-
F05	$2100 \pm 50$	$200 \pm 50$	$0.07 \pm 0.03$

Table (6.2)

## Resonance Amplitudes during the Preliminary Analysis.

Resonance	Partial Wave	All "Established" and "Probables" $\frac{\chi^2}{\text{NDF}} = 1.46$	Add D03 Resonance $\frac{\chi^2}{\text{NDF}} = 1.37$	Add S01 Resonance $\frac{\chi^2}{\text{NDF}} = 1.31$	Remove Small Contributions $\frac{\chi^2}{\text{NDF}} = 1.33$
S11(1955)	SS11	0.18	0.17	0.17	0.13
	SD13	-0.15	-0.18	-0.16	-0.12
P01(1853)	PP11	0.04	0.03	0.03	0.05
	PP13	0.22	0.22	0.22	0.19
P03(1900)	PP31	0.01	0.02	0.02	0.01
	PP33	0.01	-0.01	0.01	0.02
	PF33	-	-	-	-0.04
F05(1822)	FP53	0.25	0.25	0.26	0.22
F15(1920)	FF51	0.05	0.05	0.04	0.04
	FP53	0.01	0.02	0.02	0.02
	FF53	0.02	0.02	0.02	0.03
F17(2040)	FF71	0.04	0.06	0.05	0.06
	FF73	-0.04	-0.04	-0.04	-0.01
G07(2110)	GG71	-0.07	-0.03	-0.03	0.01
	GD73	0.27	0.28	0.28	0.29
	GG73	0.09	0.11	0.10	0.15
S01(1860)	SS11	-	-	0.05	0.07
	SD13	-	-	-0.03	-0.03
	Mass	-	-	1863 MeV	1863 MeV
	Width	-	-	37 MeV	33 MeV
D03(1890)	DS33	-	0.11	0.13	0.16
	DD33	-	0.03	0.03	0.05
	Mass	-	1888 MeV	1891 MeV	1892 MeV
	Width	-	245 MeV	266 MeV	293 MeV

Table (6.3)

## a) Dominant Partial Wave Amplitudes for the Preliminary Solution

Beam Momentum GeV/c	1.125	1.165	1.205	1.245	1.285	1.320	1.355
Partial Wave							
1SS11	0.13 + 0.09i	0.16 + 0.12i	0.18 + 0.15i	0.19 + 0.18i	0.18 + 0.21i	0.17 + 0.23i	0.15 + 0.24i
OSD13			0.11 - 0.03i	0.14 - 0.03i	0.16 - 0.03i	0.18 - 0.03i	0.19 - 0.03i
1SD13			-0.09 - 0.06i	-0.12 - 0.10i	-0.14 - 0.13i	-0.14 - 0.16i	-0.13 - 0.18i
1PP11			0.02 + 0.11i	0.02 + 0.12i	0.03 + 0.13i	0.03 + 0.14i	0.03 + 0.15i
OPP13	0.04 + 0.23i	0.03 + 0.24i	0.02 + 0.23i	0.01 + 0.22i	0.02 + 0.20i	0.02 + 0.19i	0.03 + 0.18i
1PP13		0.02 + 0.10i	0.02 + 0.12i	0.03 + 0.14i	0.03 + 0.16i	0.03 + 0.17i	0.03 + 0.18i
OPP31			-0.05 + 0.10i	-0.07 + 0.11i	-0.07 + 0.12i	-0.08 + 0.13i	-0.08 + 0.14i
1PP31				0.08 + 0.05i	0.09 + 0.06i	0.10 + 0.06i	0.11 + 0.06i
ODS33	0.10 + 0.09i	0.11 + 0.12i	0.10 + 0.13i	0.09 + 0.14i	0.07 + 0.14i	0.06 + 0.13i	0.06 + 0.12i
OFF53	-0.10 + 0.18i	-0.11 + 0.15i	-0.12 + 0.14i	-0.10 + 0.13i	-0.10 + 0.12i	-0.09 + 0.12i	-0.09 + 0.12i
OGD73						0.10 - 0.04i	0.12 - 0.03i

## b) Intensity Ratios for S, P and D Waves

Beam Momentum GeV/c	$\bar{K}^{*0}_n$	$K^{*-}_p$
1.125	S : P = 1 : 3.00	S : P = 1 : 3.00
1.165	S : P = 1 : 1.40	S : P = 1 : 2.40
1.205	S : P : D = 1 : 1.27 : 0.37	S : P = 1 : 2.30
1.245	S : P : D = 1 : 1.30 : 0.57	S : P : D = 1 : 2.30 : 0.13
1.285	S : P : D = 1 : 1.28 : 0.77	S : P : D = 1 : 2.33 : 0.22
1.320	S : P : D = 1 : 1.37 : 1.30	S : P : D = 1 : 2.42 : 0.67
1.355	S : P : D = 1 : 1.79 : 1.45	S : P : D = 1 : 2.36 : 1.12

Table (6.4)

Final Partial Cross-Sectionsa)  $\underline{K^- n \pi^+}$ 

Beam Momentum GeV/c	$\frac{\chi^2}{\text{NDF}}$	L	$\sigma_{\bar{K}^*}$ mb.	$\sigma_{\Delta}$ mb.	$\sigma_{\Sigma(1765)}$ mb.
0.960	2.30	-153	$0.107 \pm 0.060$	$0.142 \pm 0.015$	-
1.005	1.28	- 82	$0.160 \pm 0.080$	$0.079 \pm 0.008$	-
1.045	1.15	- 67	$0.312 \pm 0.060$	$0.154 \pm 0.016$	-
1.085	1.40	49	$0.400 \pm 0.060$	$0.125 \pm 0.013$	-
1.125	1.00	144	$0.562 \pm 0.046$	$0.193 \pm 0.021$	-
1.165	1.19	355	$0.701 \pm 0.035$	$0.098 \pm 0.014$	-
1.205	1.02	763	$0.819 \pm 0.036$	$0.033 \pm 0.068$	-
1.245	1.03	1451	$1.063 \pm 0.035$	$0.087 \pm 0.058$	$0.022 \pm 0.014$
1.285	1.47	1926	$1.153 \pm 0.036$	$0.113 \pm 0.050$	$0.050 \pm 0.014$
1.320	1.04	1992	$1.316 \pm 0.042$	$0.106 \pm 0.022$	$0.074 \pm 0.020$
1.355	1.10	3472	$1.488 \pm 0.040$	$0.073 \pm 0.028$	$0.137 \pm 0.034$

b)  $\bar{K}^0 p \pi^-$

Beam Momentum GeV/c	$\frac{\chi^2}{\text{NDF}}$	L	$\sigma_{\bar{K}}^*$ mb.	$\sigma_{\Delta}$ mb.
0.960	1.51	-170	$0.158 \pm 0.080$	$0.074 \pm 0.010$
1.005	1.21	-125	$0.285 \pm 0.085$	$0.104 \pm 0.010$
1.045	1.38	-120	$0.373 \pm 0.093$	$0.150 \pm 0.015$
1.085	1.54	- 59	$0.661 \pm 0.100$	$0.073 \pm 0.010$
1.125	1.44	11	$1.007 \pm 0.094$	$0.192 \pm 0.018$
1.165	1.21	370	$1.129 \pm 0.059$	$0.162 \pm 0.014$
1.205	1.19	714	$1.150 \pm 0.051$	$0.162 \pm 0.011$
1.245	1.53	1390	$1.148 \pm 0.039$	$0.153 \pm 0.023$
1.285	1.02	1788	$1.125 \pm 0.036$	$0.160 \pm 0.012$
1.320	1.36	1739	$1.036 \pm 0.035$	$0.191 \pm 0.024$
1.355	0.96	3092	$1.087 \pm 0.034$	$0.182 \pm 0.012$

c)  $\bar{K}^- p \pi^0$

Beam Momentum GeV/c	$\frac{\chi^2}{\text{NDF}}$	L	$\sigma_{\bar{K}^*}$ mb.	$\sigma_{\Delta}$ mb.	$\sigma_{\Sigma(1765)}$ mb.	$\sigma_{\Lambda(1520)}$ mb.	$\frac{\sigma_{\bar{K}^* \pi^0 p \pi^-}}{\sigma_{\bar{K}^* \pi^0}}$
0.960	1.05	-622	$0.067 \pm 0.047$	$0.041 \pm 0.010$	-	$0.706 \pm 0.080$	-
1.005	1.17	-370	$0.119 \pm 0.084$	$0.179 \pm 0.039$	-	$0.580 \pm 0.067$	-
1.045	0.89	-243	$0.203 \pm 0.100$	$0.113 \pm 0.024$	-	$0.450 \pm 0.050$	-
1.085	1.40	- 27	$0.328 \pm 0.066$	$0.197 \pm 0.042$	-	$0.285 \pm 0.033$	-
1.125	1.23	121	$0.515 \pm 0.047$	$0.235 \pm 0.055$	-	$0.267 \pm 0.030$	$1.96 \pm 0.26$
1.165	1.10	381	$0.608 \pm 0.035$	$0.309 \pm 0.045$	$0.062 \pm 0.010$	$0.227 \pm 0.025$	$1.86 \pm 0.14$
1.205	1.24	717	$0.651 \pm 0.037$	$0.255 \pm 0.038$	$0.109 \pm 0.010$	$0.179 \pm 0.011$	$1.77 \pm 0.13$
1.245	1.47	1254	$0.616 \pm 0.025$	$0.272 \pm 0.034$	$0.064 \pm 0.014$	$0.172 \pm 0.010$	$1.86 \pm 0.10$
1.285	1.15	1709	$0.659 \pm 0.025$	$0.327 \pm 0.016$	$0.120 \pm 0.010$	$0.215 \pm 0.011$	$1.71 \pm 0.08$
1.320	1.07	1518	$0.540 \pm 0.021$	$0.273 \pm 0.014$	$0.141 \pm 0.013$	$0.213 \pm 0.014$	$1.92 \pm 0.10$
1.355	0.96	2881	$0.604 \pm 0.021$	$0.342 \pm 0.031$	$0.189 \pm 0.017$	$0.259 \pm 0.015$	$1.80 \pm 0.08$

Table (6.5) Birmingham A<sub>o</sub>'s used in the Analysis

Centre of Mass Energy GeV	A <sub>o</sub>
1.855	0.012 ± 0.005
1.885	0.072 ± 0.014
1.915	0.072 ± 0.012
1.945	0.105 ± 0.017
1.975	0.109 ± 0.016
2.005	0.132 ± 0.018
2.035	0.164 ± 0.030
2.065	0.183 ± 0.023
2.095	0.142 ± 0.019
2.125	0.179 ± 0.019
2.155	0.180 ± 0.024

These values are taken from ref. (36).

Table (6.6)  $A_4$  and  $B_4$  Tripp Coefficients  
for  $\bar{K}N \rightarrow \bar{K}^*N$

Wave Product	$A_4$ Contribution	$B_4$ Contribution
PP31 FF51	10.30	3.43
PP31 FF71	5.71	1.91
PP33 FF53	-5.14	-3.07
PP33 FF73	-5.90	1.10
PP33 FH73	-4.62	-2.46
PF33 FP53	-8.40	-5.04
PF33 FF53	5.14	4.11
PF33 FF73	-4.43	-1.48
PF33 FH73	3.96	3.30
FF51 FF51	2.57	0.85
FF51 FF71	4.68	1.56
FP53 FF53	-6.30	-1.68
FP53 FF73	5.42	0.99
FP53 FH73	-1.54	-2.20
FF53 FF53	-1.29	0.69
FF53 FF73	3.62	-0.81
FF53 FH73	4.86	1.80

Table (6.7)

## Summary of Development of Solution "A"

Resonance	Partial Wave	Add G07(2110)	Add P03(1900)	Add F17(2040)	Add F05(1822)	Add S11(1955) +P01(1853)	Add Linear Terms to D03 and S01 Background	Resonances in D03 and S01 "Solution A"
		$\frac{\chi^2}{\text{NDF}} = 2.66$	$\frac{\chi^2}{\text{NDF}} = 2.46$	$\frac{\chi^2}{\text{NDF}} = 2.37$	$\frac{\chi^2}{\text{NDF}} = 1.89$	$\frac{\chi^2}{\text{NDF}} = 1.76$	$\frac{\chi^2}{\text{NDF}} = 1.45$	$\frac{\chi^2}{\text{NDF}} = 1.32$
S11(1955)	SS11					0.03	-0.02	-0.05
	SD13					-0.04	-0.12	-0.09
P01(1853)	PP11					-0.02	-	-0.06
	PP13					-0.10	-0.14	-0.20
P03(1900)	PP31		-0.05	-0.07	-0.10	-0.11	-0.08	-0.08
	PP33		0.09	0.10	0.10	0.11	0.11	0.12
	PF33		0.05	0.06	0.05	0.06	0.06	0.10
F05(1822)	FP53				-0.23	-0.26	-0.19	-0.19
F17(2040)	FF73			-0.07	-0.09	-0.10	-0.02	-0.06
G07(2110)	GG71	-0.03	-0.04	-0.03	-0.09	-0.12	-0.02	0.02
	GD73	-0.20	-0.22	-0.22	-0.24	-0.18	-0.18	-0.23
	GG73	-0.05	-0.10	-0.10	-0.15	-0.18	-0.10	0.06
D03(1980)	Mass							1978 MeV
	Width							246 MeV
	DD31							-0.07
	DS33							-0.20
S01(2030)	Mass							2025 MeV
	Width							230 MeV
	SS11							0.05
	SD13							-0.27

Table (6.8)

## Summary of Development of Solution "B"

Resonance	Partial Wave	Important Resonances of Soln. "A"	Add Linear Terms in S01	Add Linear Terms in ODS33	Include High Order Coefficients	Resonance in D03	Resonance in S01	Take to Convergence. Solution "B"
		$\frac{\chi^2}{\text{NDF}} = 1.55$	$\frac{\chi^2}{\text{NDF}} = 1.50$	$\frac{\chi^2}{\text{NDF}} = 1.40$	$\frac{\chi^2}{\text{NDF}} = 1.37$	$\frac{\chi^2}{\text{NDF}} = 1.36$	$\frac{\chi^2}{\text{NDF}} = 1.35$	$\frac{\chi^2}{\text{NDF}} = 1.29$
S11 (1955)	SS11	0.05	0.04	0.05	0.05	0.05	0.04	0.06
	SD13	-0.02	0.00	0.03	0.03	0.02	0.03	0.03
P01 (1853)	PP11	0.12	0.11	0.12	0.13	0.13	0.13	0.13
	PP13	0.25	0.25	0.23	0.23	0.25	0.27	0.27
P03 (1900)	PP31	0.02	0.02	0.04	0.05	0.03	0.03	0.03
	PP33	0.04	0.03	0.01	0.00	0.00	0.03	-
	PF33	-0.09	-0.09	-0.09	-0.09	-0.10	-0.09	-0.11
F05 (1822)	FP53	0.13	0.13	0.14	0.14	0.16	0.21	0.20
F17 (2040)	FF73	0.06	0.07	0.07	0.07	0.06	0.07	0.08
G07 (2110)	GG71	0.04	0.03	0.03	0.00	-0.02	0.00	0.07
	GD73	0.23	0.22	0.21	0.20	0.20	0.18	0.20
	GG73	0.13	0.14	0.12	0.00	0.01	-0.05	0.03
D03 (1980)	Mass					1984	1997	2003 MeV
	Width					159	253	312 MeV
	DD31					0.04	0.04	0.13
	DS33					0.13	0.19	0.23
	DD33					0.01	-0.01	-
S01 (2030)	Mass						2042	2020 MeV
	Width						194	246 MeV
	SS11						-0.04	-
	SD13						0.22	0.38

Table (6.9)

Summary of Development of Solution "C"

Resonance	Partial Wave	Release I=1 Waves Add Linear Terms in S01	Add S11(1955) + Linear Terms in ODS33	Resonance in D03	Resonance in S01 and take to Convergence. Solution "C"
		$\frac{\chi^2}{\text{NDF}} = 1.58$	$\frac{\chi^2}{\text{NDF}} = 1.41$	$\frac{\chi^2}{\text{NDF}} = 1.33$	$\frac{\chi^2}{\text{NDF}} = 1.31$
S11 (1955)	SS11		0.00	-0.01	-0.08
	SD13		-0.07	-0.08	-0.10
P01 (1853)	PP11	-0.04	-0.06	-0.08	-0.11
	PP13	-0.16	-0.16	-0.17	-0.23
P03 (1900)	PP31	-0.03	-0.05	-0.06	-0.05
	PP33	0.08	0.08	0.08	0.06
	PF33	0.07	0.08	0.08	0.11
F05 (1822)	FP53	-0.18	-0.17	-0.18	-0.21
F17 (2040)	FF73	-0.09	-0.09	-0.09	-0.07
G07 (2110)	GG71	-0.03	-0.04	-0.06	-0.12
	GD73	-0.24	-0.22	-0.22	-0.23
	GG73	-0.13	-0.10	-0.11	-0.16
D03 (1980)	Mass			1958	1978 MeV
	Width			116	219 MeV
	DD31			-0.04	-0.10
	DS33			-0.06	-0.11
	DD33			-0.02	-0.01
S01 (2030)	Mass				2023 MeV
	Width				263 MeV
	SS11				-
	SD13				-0.28

Table (6.10)

Comparison of Solutions "A", "B" and "C"

Resonance	Partial Wave	Solution "A"	Solution "B"	Solution "C"
		$\frac{\chi^2}{\text{NDF}} = \frac{1324}{1006} = 1.32$	$\frac{\chi^2}{\text{NDF}} = \frac{1303}{1006} = 1.29$	$\frac{\chi^2}{\text{NDF}} = \frac{1324}{1009} = 1.31$
S11 (1955)	SS11	0.05	0.06	0.08
	SD13	0.09	0.03	0.10
P01 (1853)	PP11	0.06	0.13	0.11
	PP13	0.20	0.27	0.23
P03 (1900)	PP31	0.08	0.03	0.05
	PP33	-0.12	-	-0.06
	PF33	-0.10	-0.11	-0.11
F05 (1822)	FP53	0.19	0.20	0.21
F17 (2040)	FF73	0.06	0.08	0.07
G07 (2110)	GG71	-0.02	0.07	0.12
	GD73	0.23	0.20	0.23
	GG73	-0.06	0.03	0.16
D03 (1980)	Mass	1978	2003	1978 MeV
	Width	246	312	219 MeV
	DD31	0.07	0.13	0.10
	DS33	0.20	0.23	0.11
	DD33	-	-	0.01
S01 (2030)	Mass	2025	2020	2023 MeV
	Width	230	246	263 MeV
	SS11	-0.05	-	-
	SD13	0.27	0.38	0.28

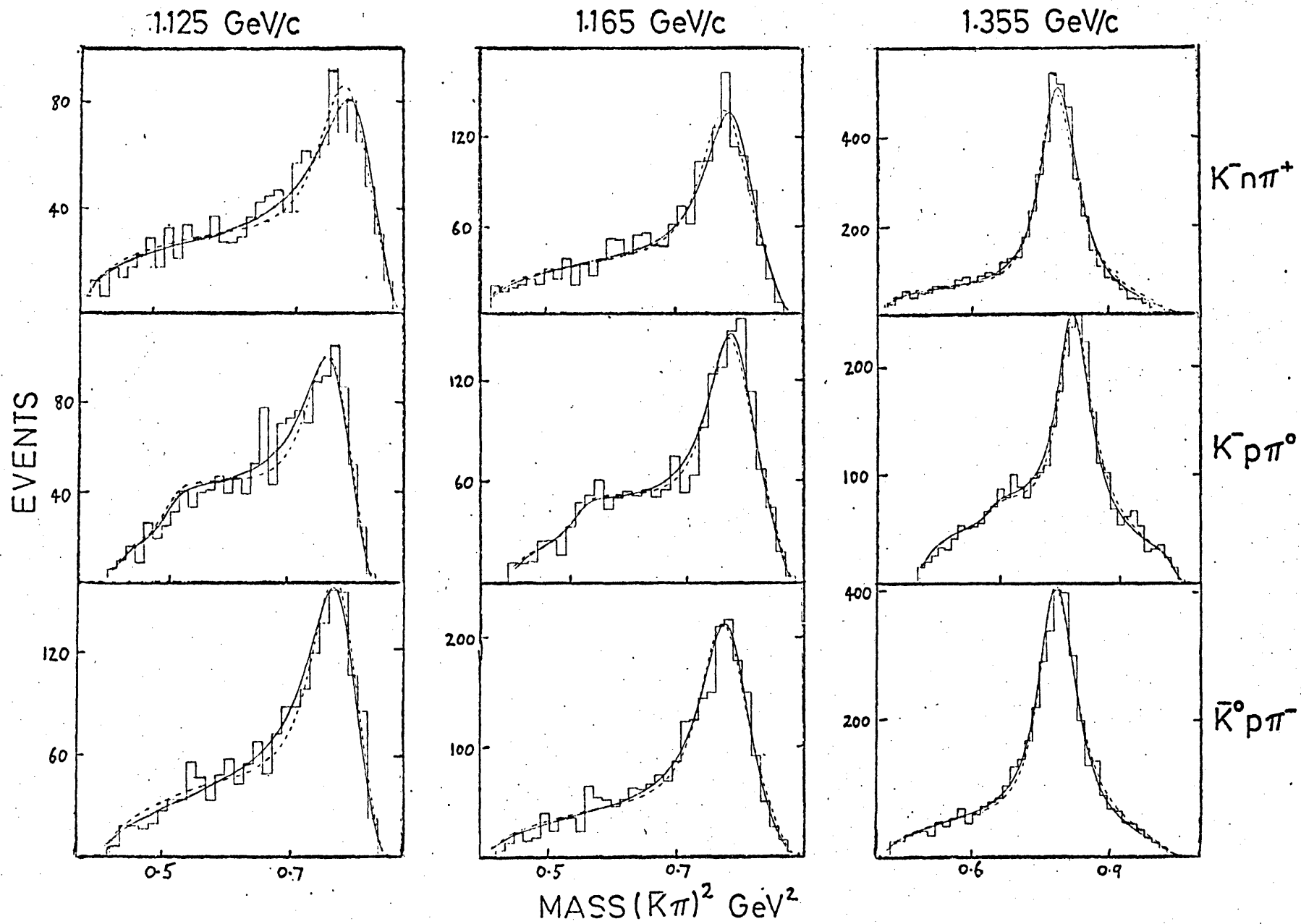
Table (6.11)

a)  $A_1$  and  $A_3$  Tripp Coefficients  
for  $KN \rightarrow \Lambda(1520)\pi$

Wave Product	$A_1$ Contribution	$A_3$ Contribution
DP5 PS3	6.57	0.00
DF5 PS3	0.00	-5.37
DP5 PD3	-1.31	-5.25
DF5 PD3	6.44	-1.07
DP5 FD5	1.05	4.21
DF5 FD5	0.98	3.25
DP5 FG5	0.00	-0.96
DF5 FG5	0.75	3.51
DP5 FD7	9.93	4.97
DF5 FD7	-0.87	-4.06
DP5 FG7	0.00	-3.70
DF5 FG7	9.72	3.02

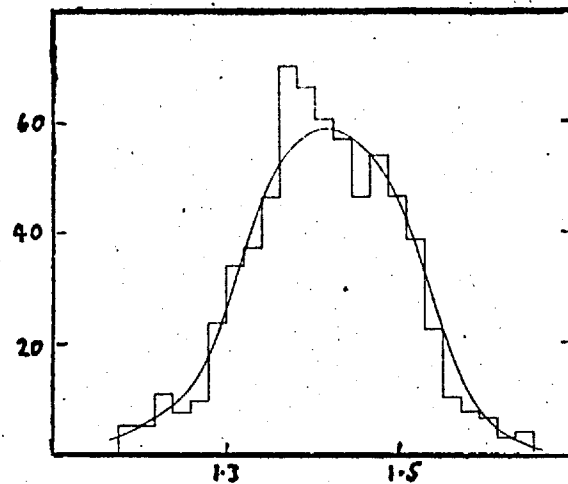
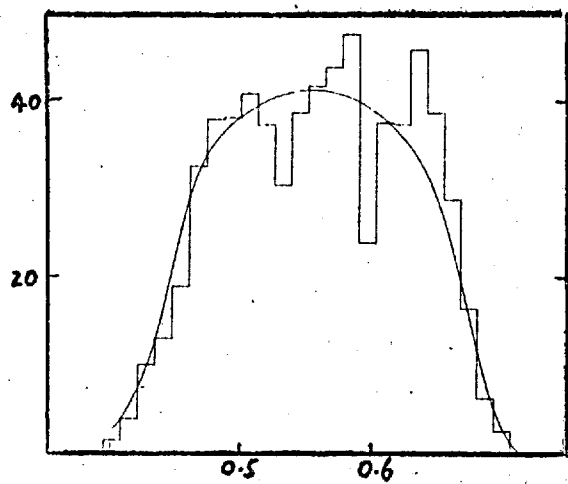
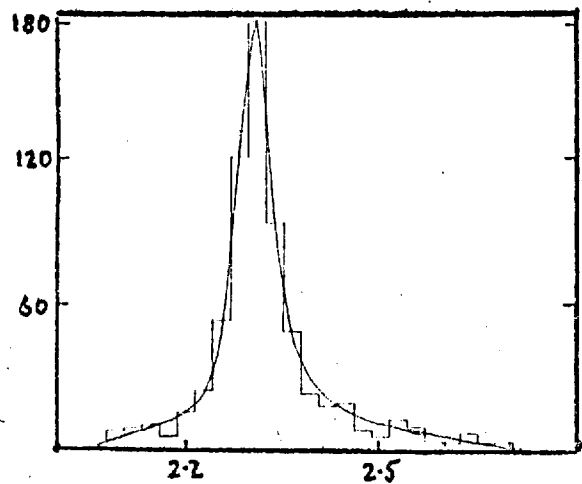
b)  $C_2$  and  $C_4$  Tripp Coefficients  
for  $KN \rightarrow \Lambda(1520)\pi$

Wave Product	$C_2$ Contribution	$C_4$ Contribution
DP5 DP3	-0.29	0.36
DF5 DP3	0.20	-0.11
DP5 DF3	-0.03	-0.18
DF5 DF3	0.15	-0.40
DP5 DP5	0.30	0.22
DP5 DF5	0.12	0.09
DF5 DF5	-0.30	-0.22
DP5 GF7	-0.22	-0.05
DF5 GF7	-0.01	-0.04

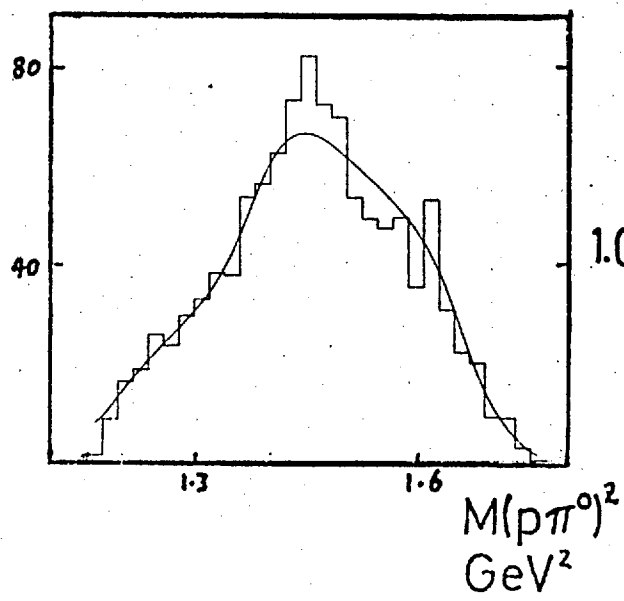
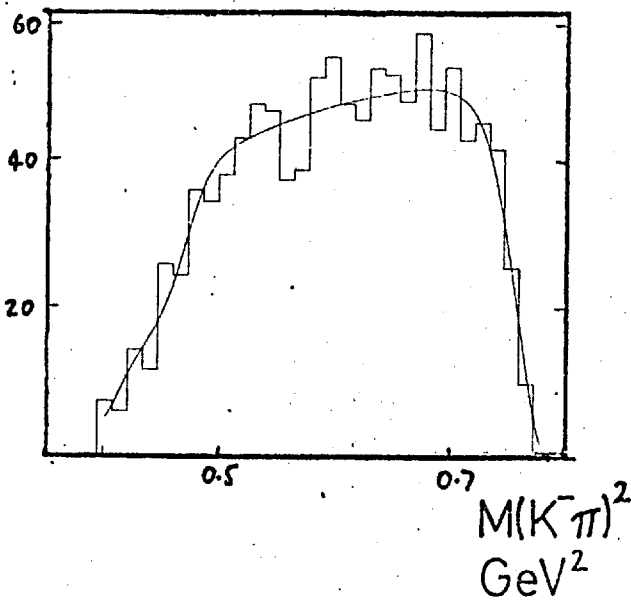
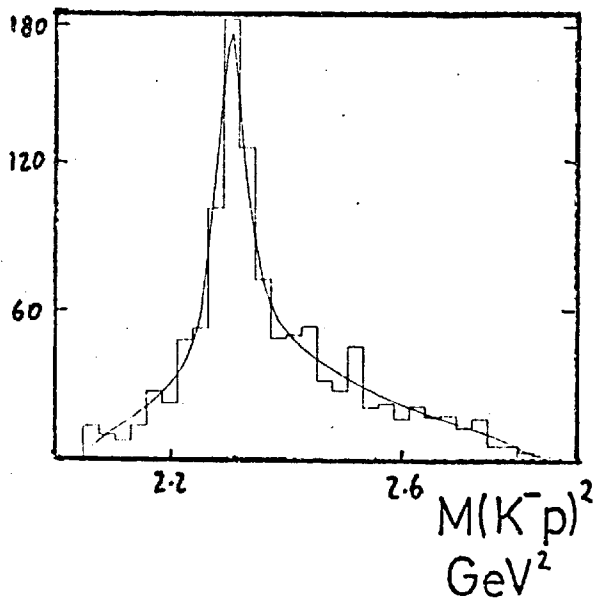


6.1

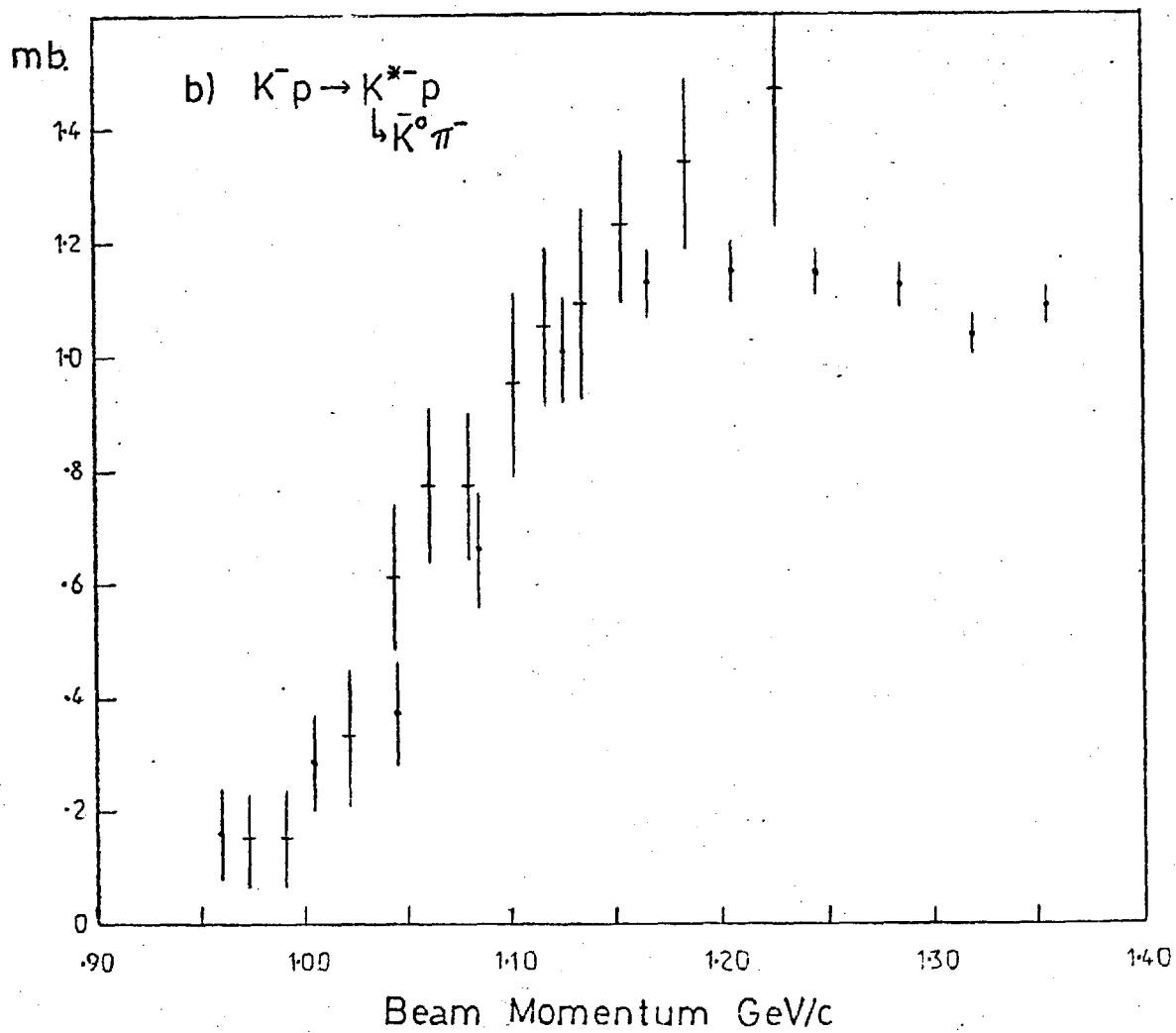
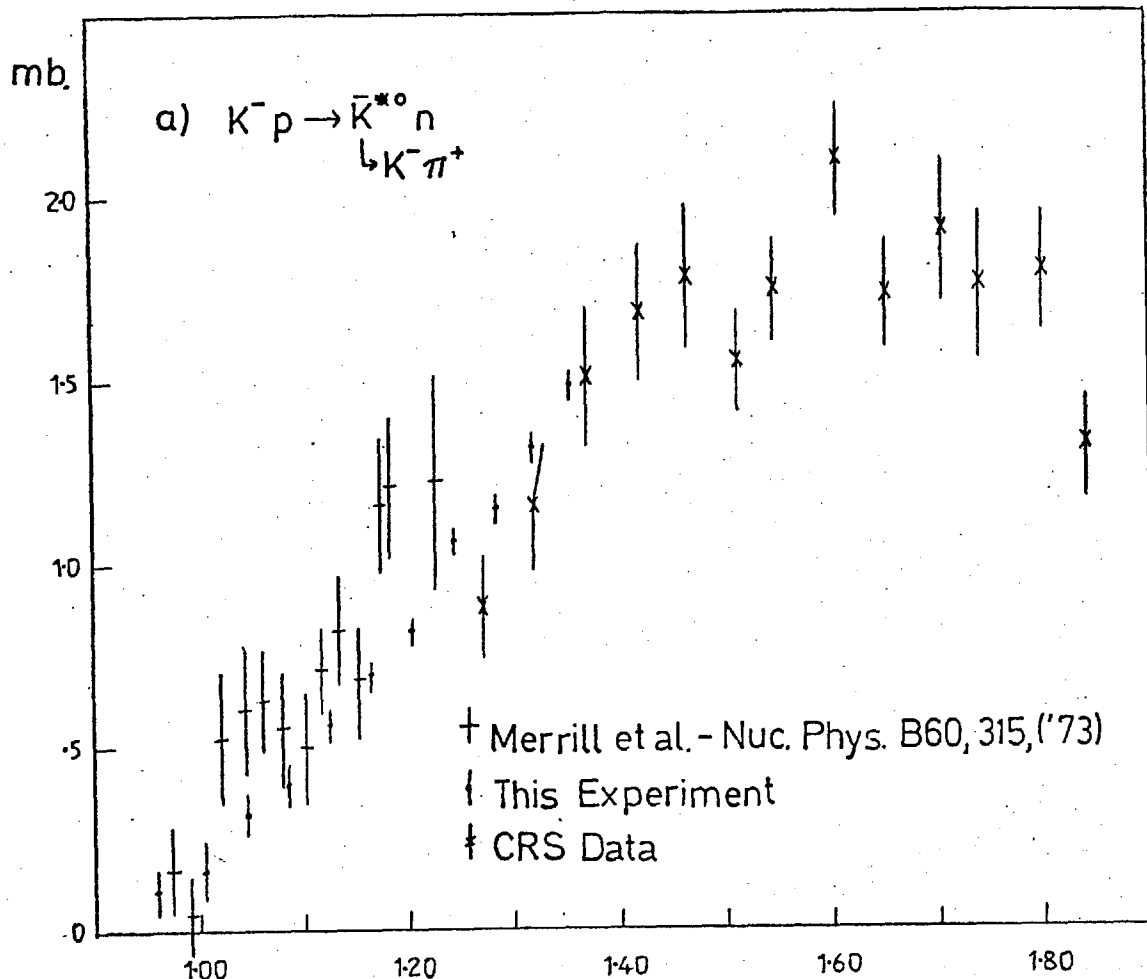
EVENTS

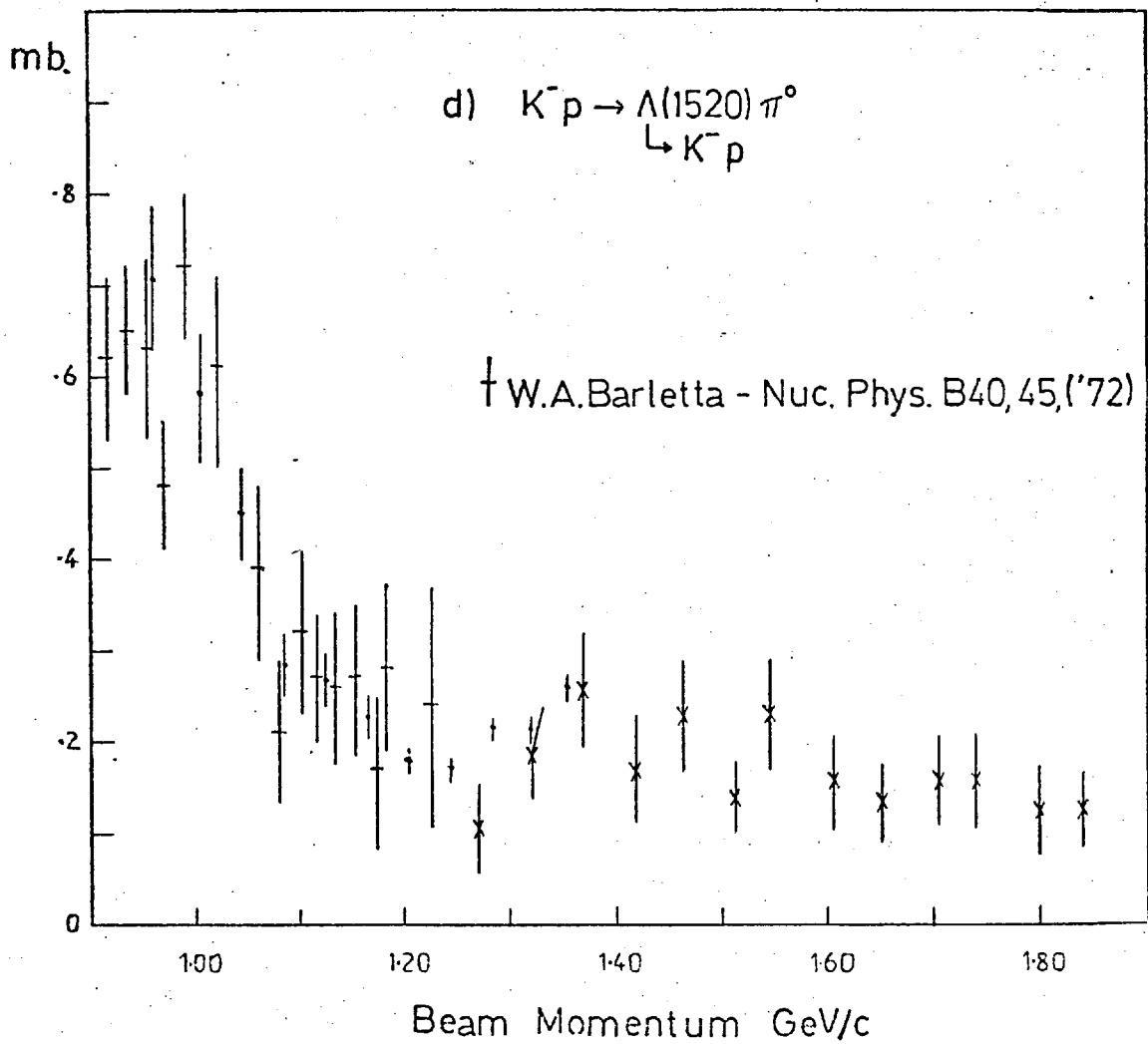
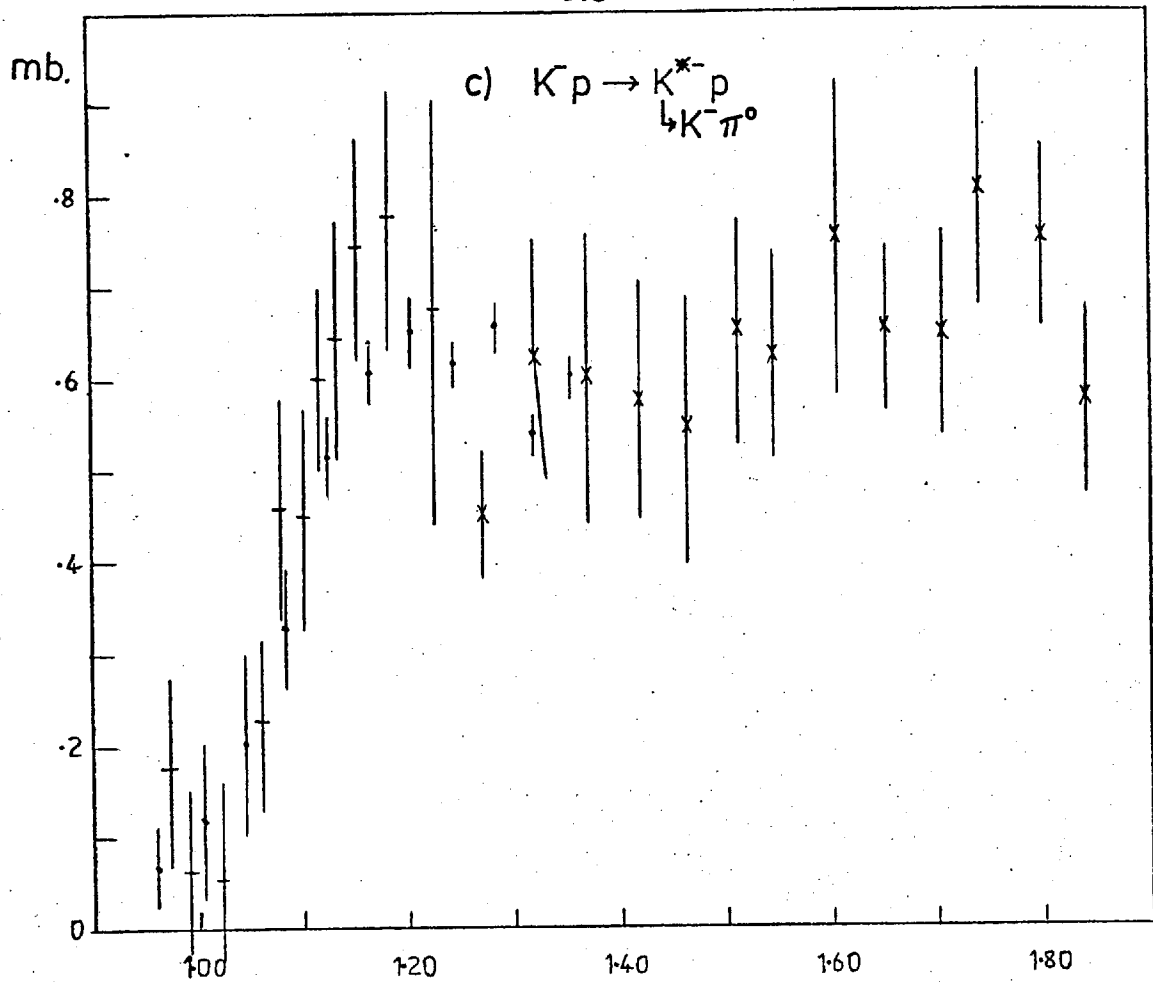


0.960 GeV/c

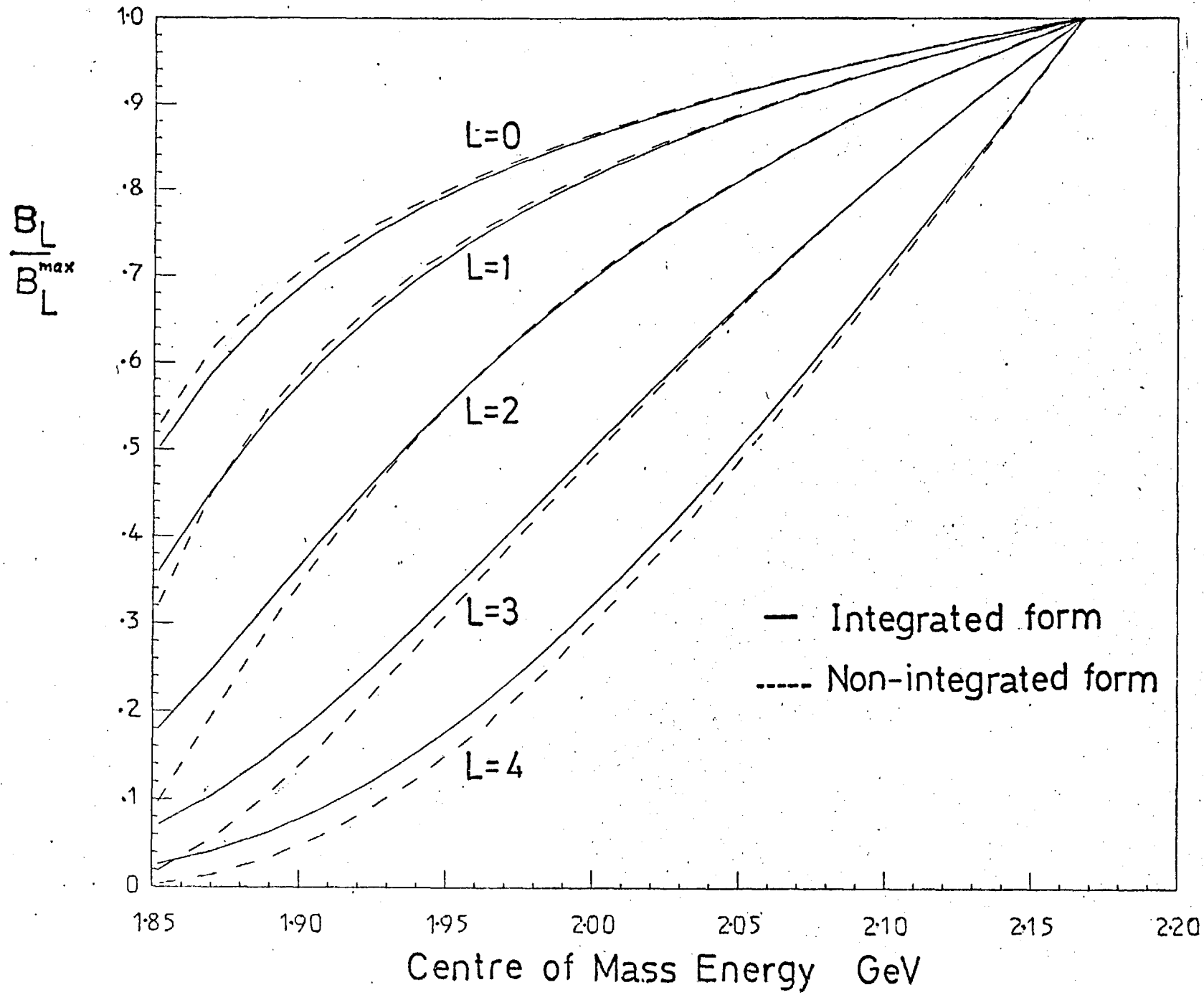


1.045 GeV/c

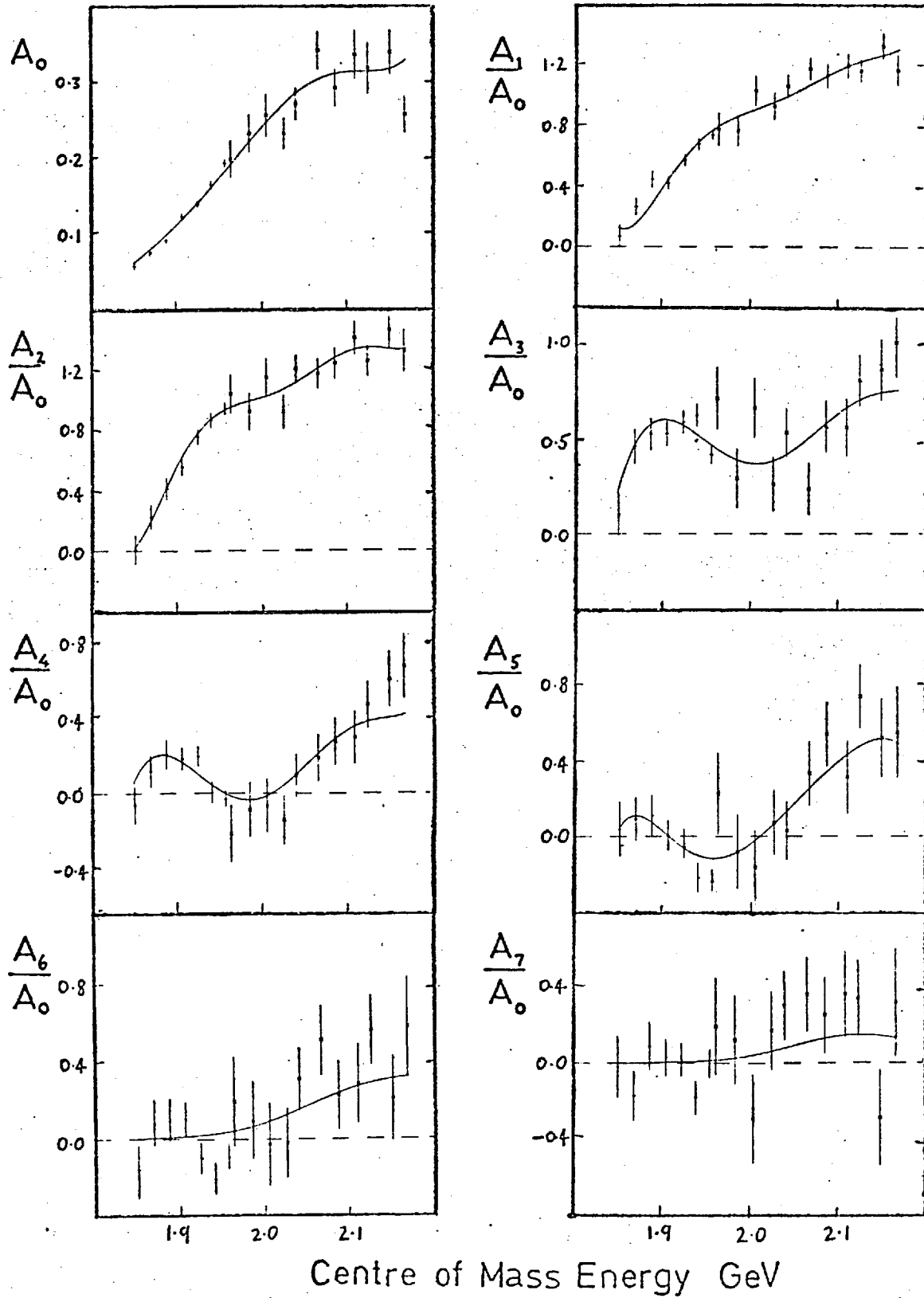




6.4

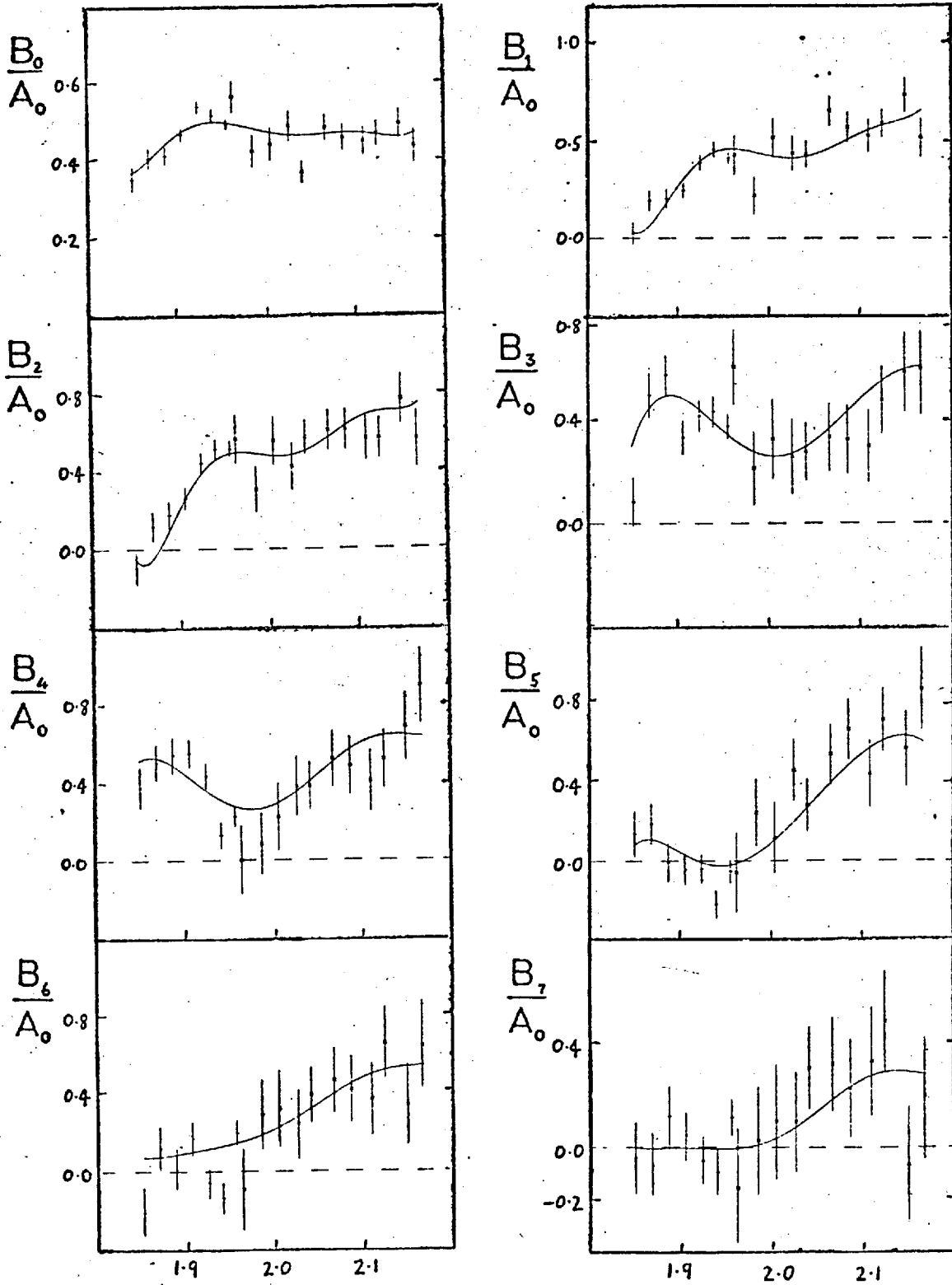


6.5 a)

 $\bar{K}^* n$ 

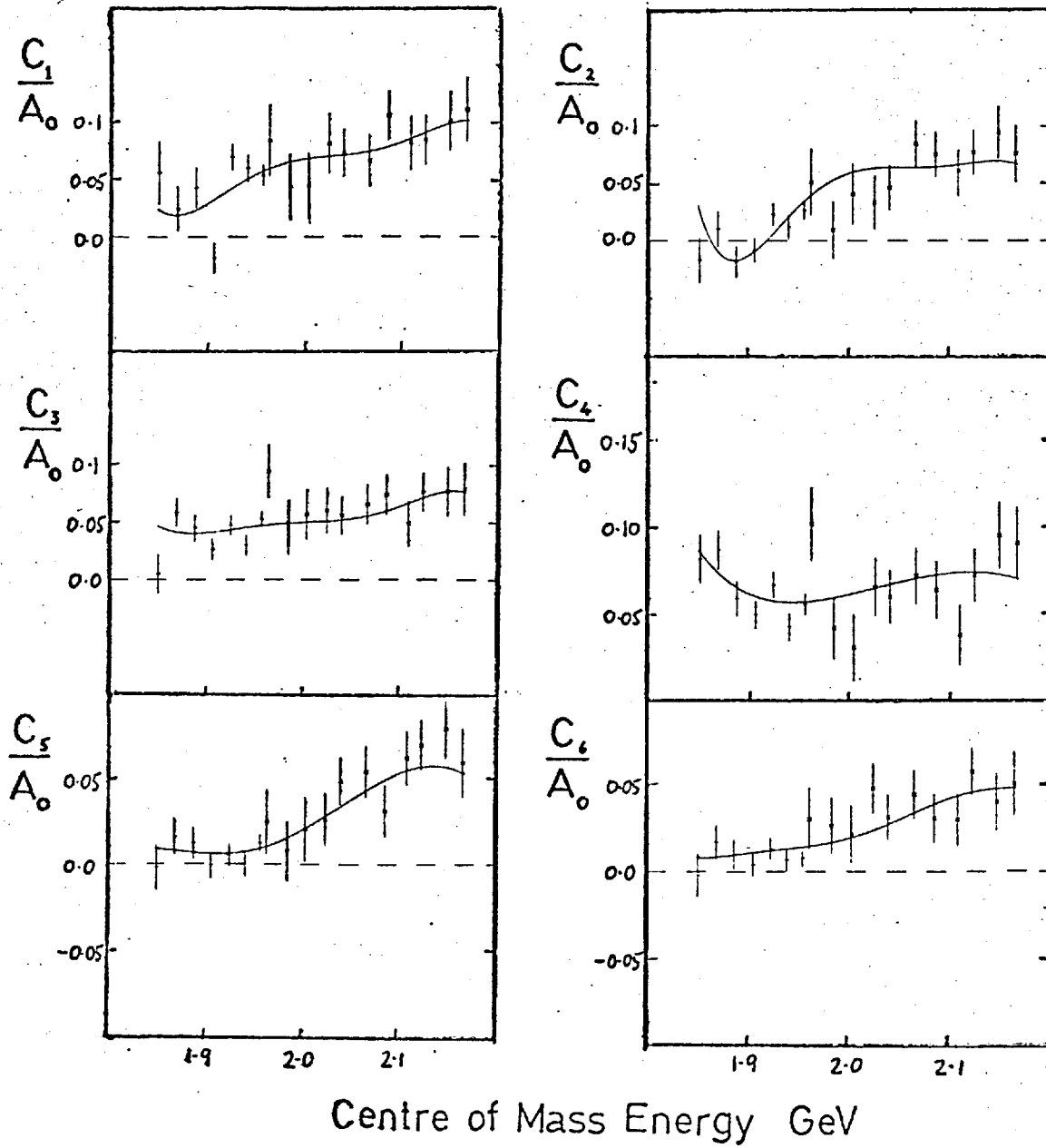
6.5 b)

$\bar{K}^{*0} n$

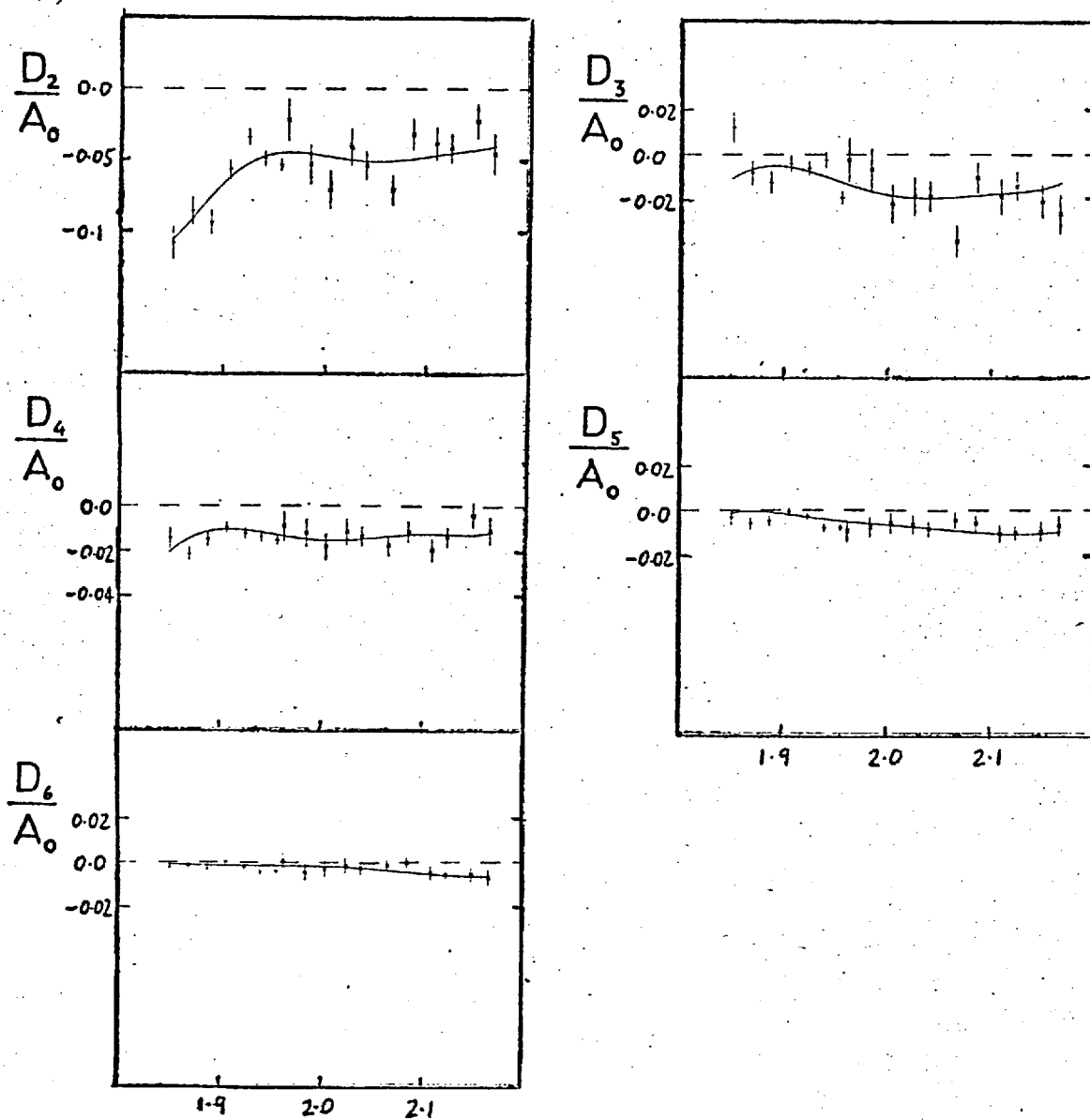


Centre of Mass Energy GeV

6.5 c)

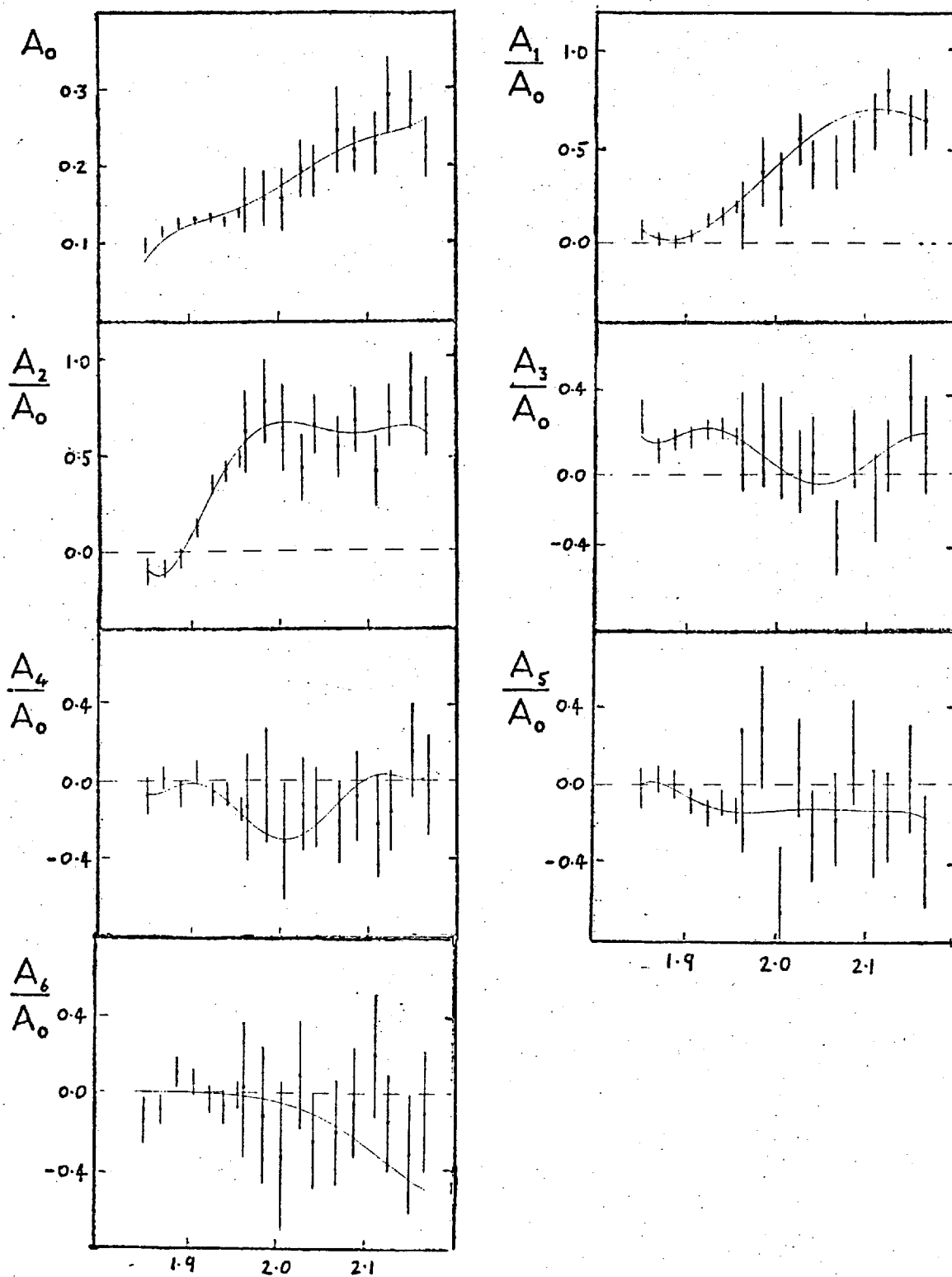
 $\bar{K}^{*0} n$ 

6.5 d)

 $\bar{K}^{*0} n$ 

Centre of Mass Energy GeV

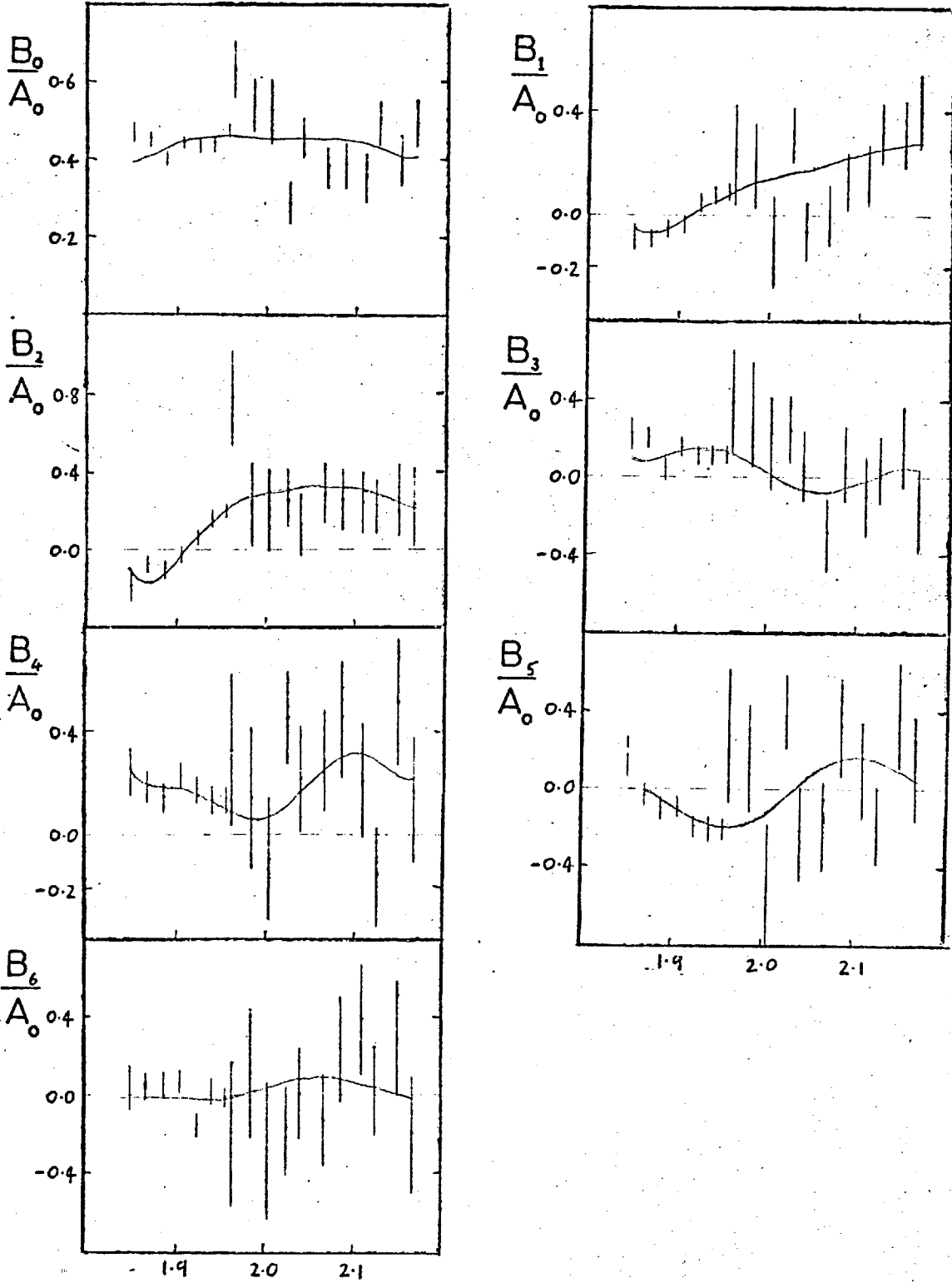
6.5 e)

 $K^{*-} p$ 

Centre of Mass Energy GeV

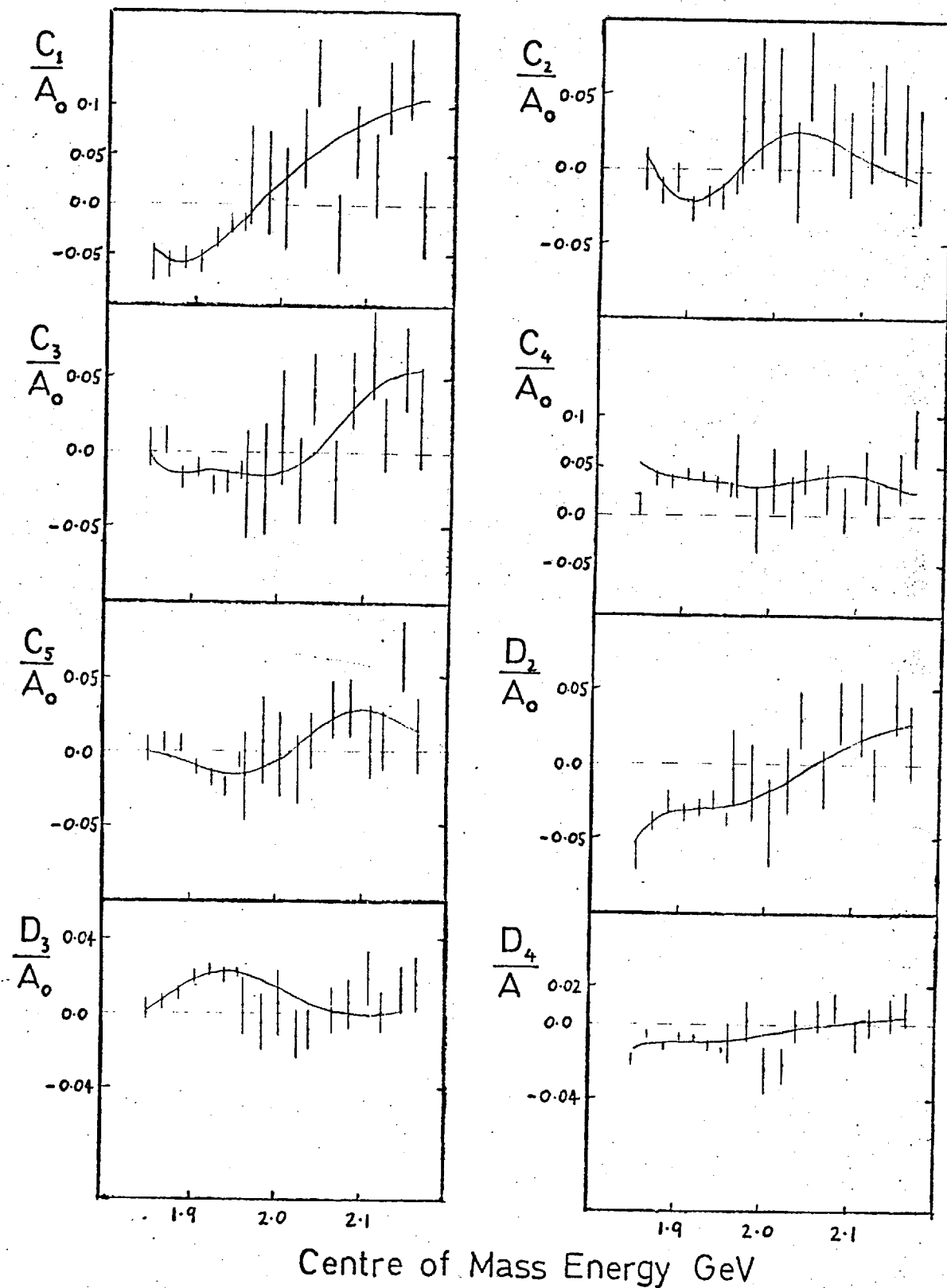
6.5 f)

$K^{*-} p$

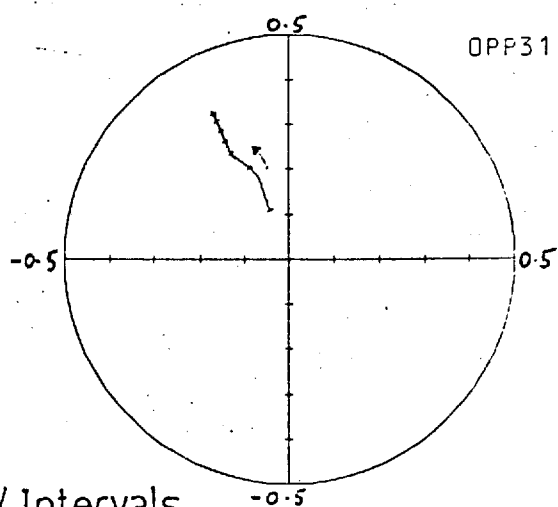
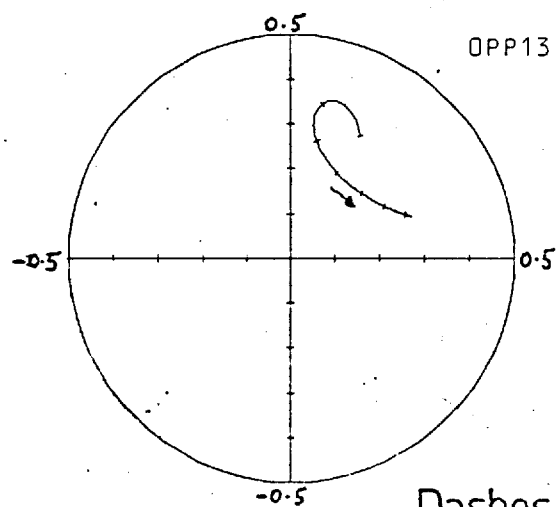
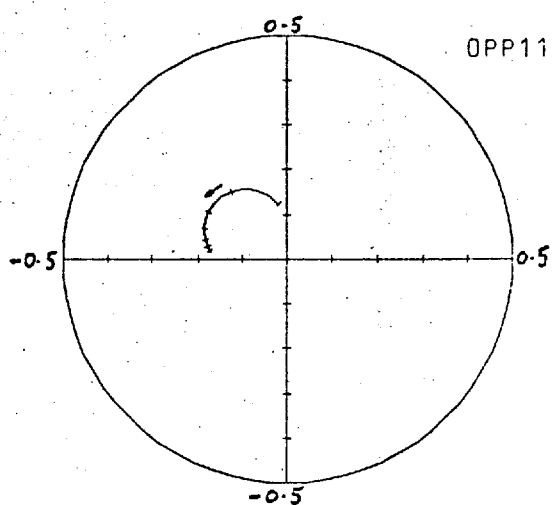
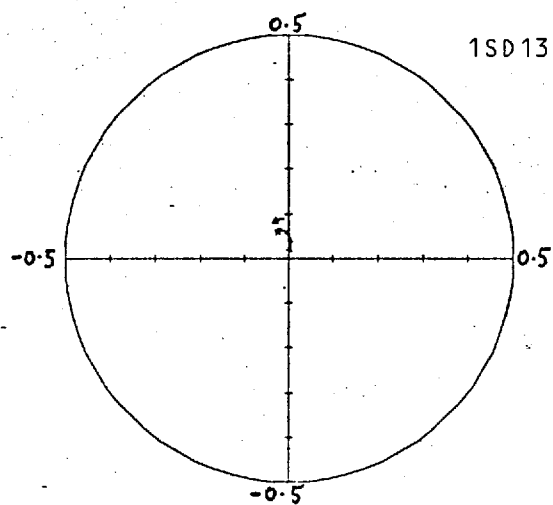
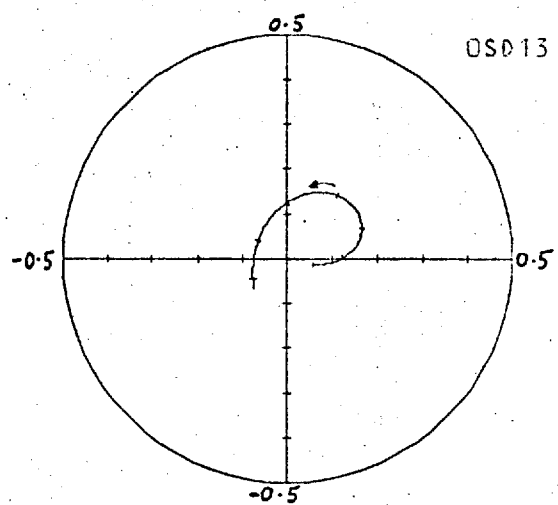
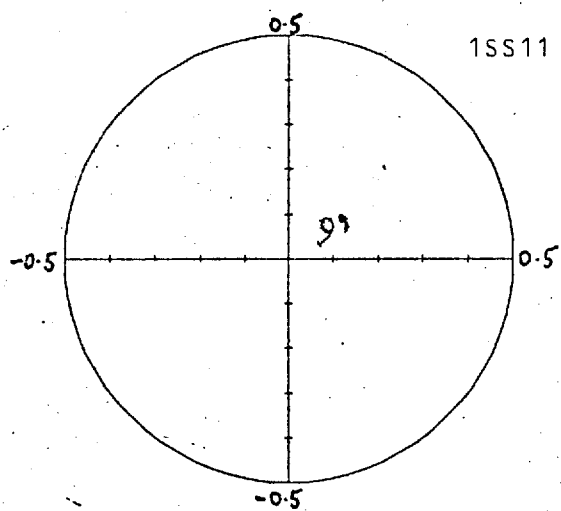


Centre of Mass Energy GeV

6.5 g)

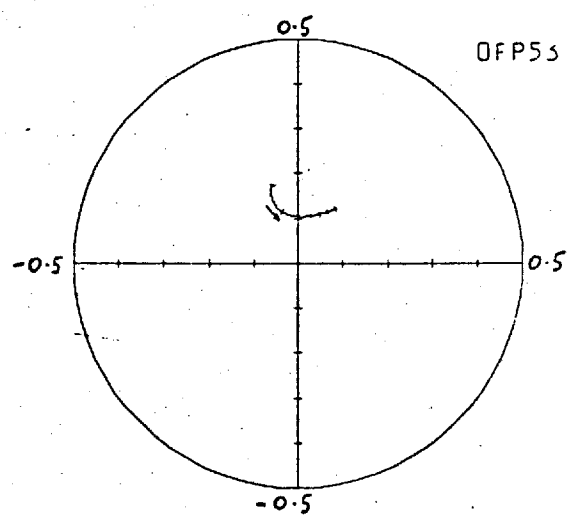
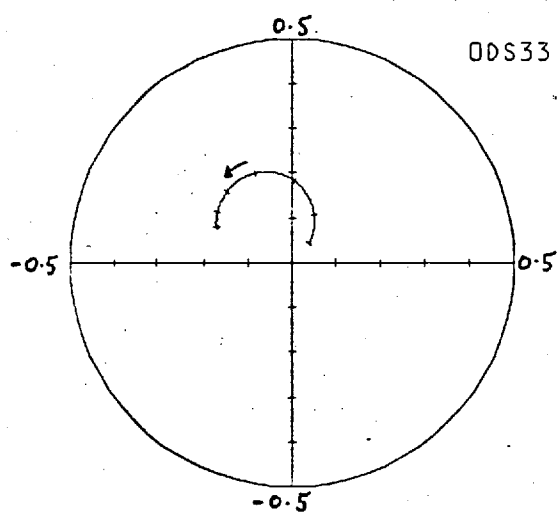
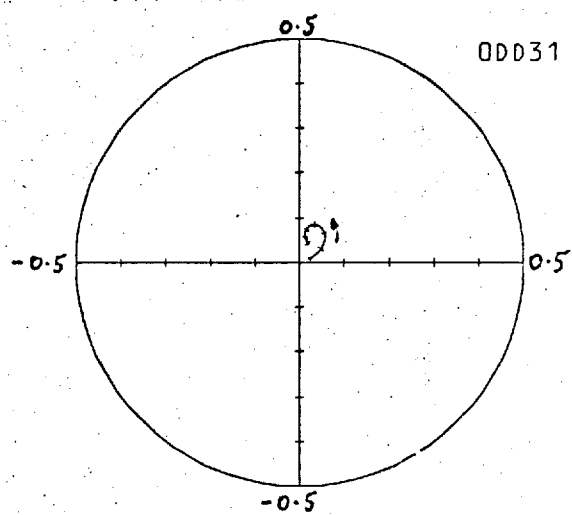
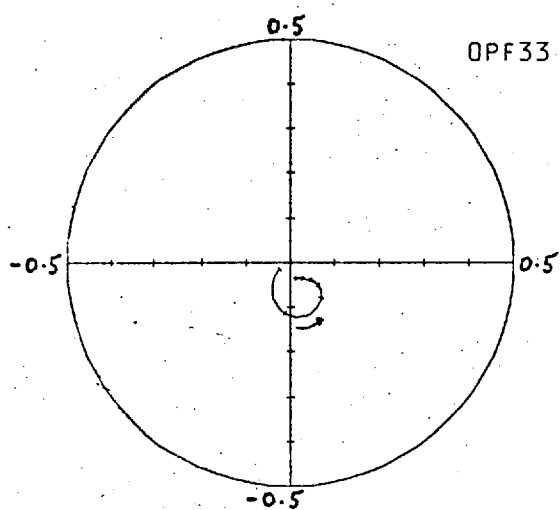
 $K^{\pi^-} p$ 

## 6.6 a)

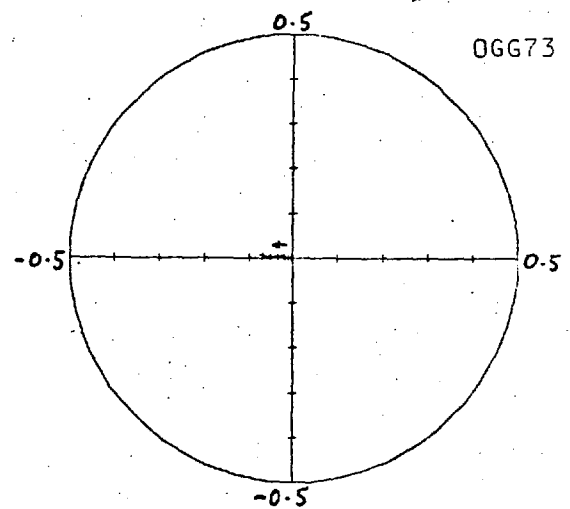
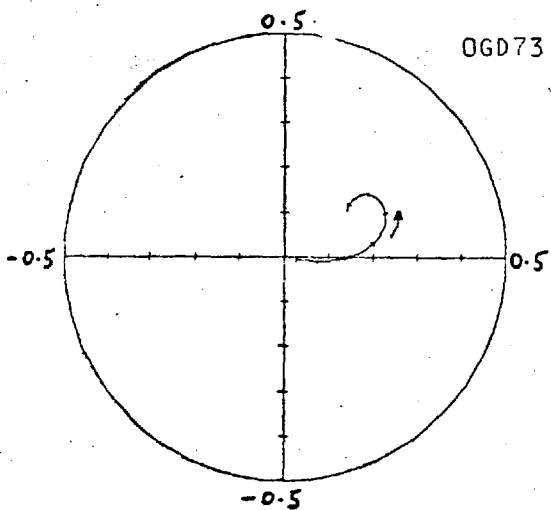
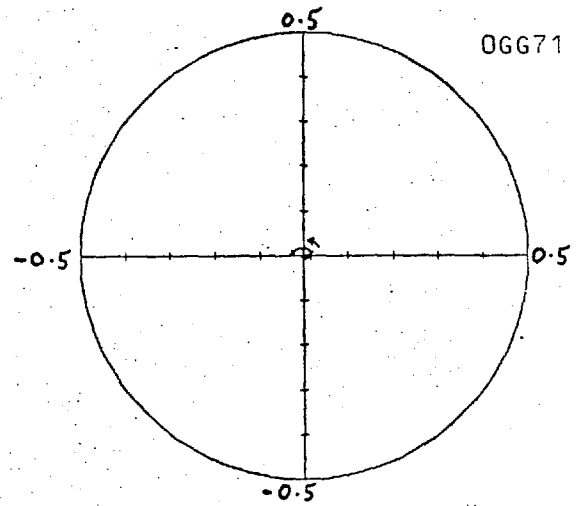
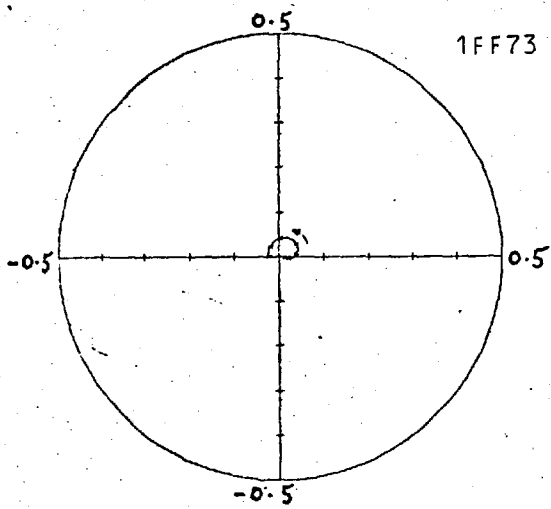


Dashes at 50MeV Intervals

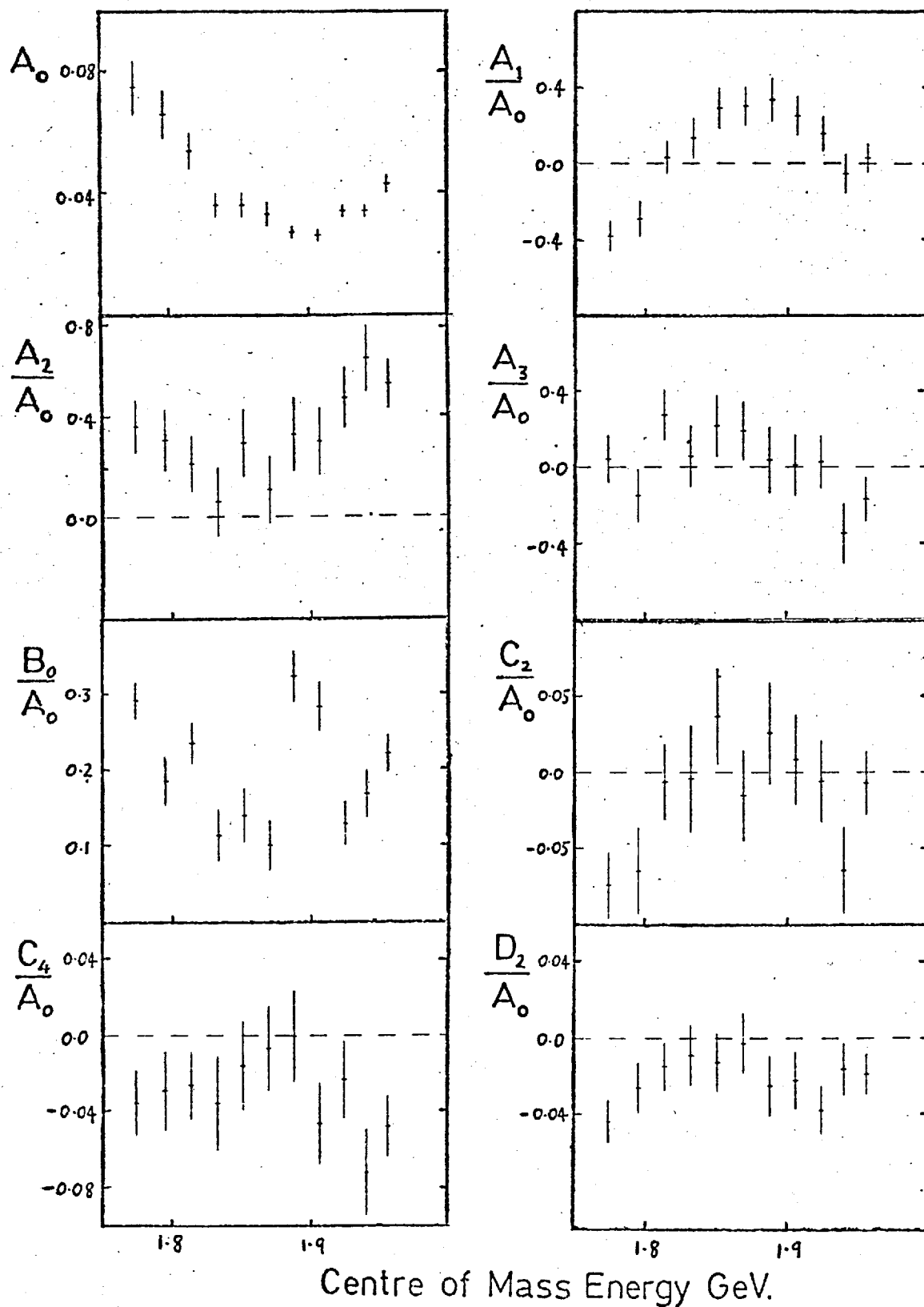
## 6.6 b)



6.6 c)



6.7

 $\Lambda(1520)\pi$ 

7.1 Introduction

In this chapter the results of the partial wave analysis of the reaction  $K^- p \rightarrow \bar{K}^* N$  are compared with a model based on the  $SU(6)_w$  symmetry. A short historical development of the model is first given, beginning with  $SU(3)$  and culminating in the Melosh transformation. The model to be used is motivated by this transformation and a brief description of it is given. The predictions of the model are obtained from fits to the experimental decay rates of the  $N^*$ 's to  $N\rho$  described in the literature. The  $\bar{K}^* N$  data is then included in an overall fit to determine the consistency of the model. A short discussion is also given in which the  $SU(6)_w$  symmetry is used to try and classify the new states discovered in the analysis.

7.2 Historical Development

$SU(3)$  symmetry<sup>(41)</sup> has been found to be a very successful "approximate" symmetry of the strong interactions. A broken form of the symmetry has been used to classify the known hadrons into multiplet representations of  $SU(3)$  - the so called decuplets, octets and singlets - with masses split within each multiplet according to the Gell-Mann — Okubo formula.

The lack of firm experimental evidence for hadrons belonging to other  $SU(3)$  representations such as  $10^*$  or  $27$  is evidence for the existence of a set of three fundamental quarks<sup>(42)</sup> which constitute the basic triplet representation of  $SU(3)$ . In the quark model the baryons are made up of three quarks, and the mesons of a quark-antiquark pair. It is closely connected with  $SU(3)$  but gives some extra predictions.

Within  $SU(3)$  the two-body decays of hadrons within one multiplet can generally be expressed in terms of a single coupling constant. In the

case of the decay of an octet member to two other octet members, however, there are two coupling constants of opposite symmetry with respect to the interchange of the final two particles. These constants are unrelated within the symmetry.

Several successful fits to the known decay rates have been made<sup>(43)</sup> within the SU(3) symmetry, and the coupling constants, have been obtained for several multiplets, together with the so-called mixing angles. These angles result from the intermultiplet mixing of pure SU(3) states with the same quantum numbers to form the physical states.

The suspicion that the particle spectrum obeyed a higher symmetry than SU(3) led to SU(6),<sup>(44)</sup> in which the quark spin (assumed to be  $\frac{1}{2}$ ) was incorporated into a six-dimensional quark representation. To cover resonances with spin greater than  $\frac{3}{2}$ , orbital angular momentum was introduced between the quarks and combined vectorially with the quark spin to produce the total angular momentum of the system. This symmetry was called SU(6) x O(3). The resulting three quark baryon multiplets are the 56, 70 and 20 representations. The main features of the baryon spectrum can be reproduced with (56, 0<sup>+</sup>), (70, 1<sup>-</sup>) and (56, 2<sup>+</sup>) multiplets of increasing mass. These are defined by (m, L<sup>P</sup>) where m is the SU(6) representation, L is the quark orbital angular momentum and P is the parity of the system which always appears to be of the form  $P = (-1)^L$ . The SU(3) decomposition of the baryon multiplets are as follows:-

$$(56, 0^+) = {}^4 10_{\frac{1}{2}} + {}^2 8_{\frac{1}{2}} \quad 7.1$$

$$(70, 1^-) = {}^2 8_{\frac{1}{2}} + {}^2 8_{\frac{3}{2}} + {}^4 8_{\frac{1}{2}} + {}^4 8_{\frac{3}{2}} + {}^4 8_{\frac{5}{2}} + {}^2 10_{\frac{1}{2}} + {}^2 10_{\frac{3}{2}}$$

$$(56, 2^+) = {}^2 8_{\frac{3}{2}} + {}^2 8_{\frac{5}{2}} + {}^4 10_{\frac{1}{2}} + {}^4 10_{\frac{3}{2}} + {}^4 10_{\frac{5}{2}} + {}^4 10_{\frac{7}{2}}$$

defined by  ${}^{2S+1}R_J$  where S is the total quark spin, R is the SU(3)

representation and J is the total angular momentum. In the case of mesons the common pseudoscalar and vector mesons are incorporated in a 35, L = 0

multiplet made up as follows:-

$$(35, 0^-) = {}^3 8 + {}^1 8 + {}^3 1$$

Higher baryon and meson multiplets with larger values of L and correspondingly increasing average mass are currently being filled with the new resonances discovered over the past few years.

Besides orbital excitation it is also possible to have radial excitation between the quarks.<sup>(45)</sup> The Roper resonance then becomes a member of the first radial excitation of the ground state  $(56, 0^+)$  with radial quantum number  $n = 2$ . The model predicts a vast spectrum of multiplets with various values of  $n$ . As yet, very few resonances can be assigned to these higher multiplets.

As defined,  $SU(6) \times O(3)$  is appropriate for classifying particle states. However, being a "rest symmetry" it is expected to be invalid for processes such as decays involving moving states. In fact the symmetry forbids the known decays  $\Delta \rightarrow N\pi$  and  $\rho \rightarrow \pi\pi$ . The concept of W-spin was therefore set up by Lipkin and Meshkov<sup>(46)</sup>, defined by the generators:-

$$W_x = P_{int} S_x \quad W_y = P_{int} S_y \quad W_z = S_z \quad 7.2$$

for a particle of intrinsic parity  $P_{int}$  and spin  $S$  moving along the z-axis. Applied to free quarks these W-spin generators commute with the generators of the Lorentz boost in the z-direction and would thus appear to be appropriate for moving systems. The new symmetry was called  $SU(6)_w \times O(3)$ .

However, it has been suggested that  $SU(6)_w \times O(3)$  is too strong a symmetry for the decay of resonances with L greater than zero. This is because the symmetry requires  $\Delta L_z = 0$ , whereas the transverse recoil momentum of the quarks in a decay process can give rise to  $\Delta L_z = \pm 1$  transitions as well. The problem occurs when a decay can proceed via

two final orbital angular momenta,  $l$ . The amplitudes for different  $l$  are related by the symmetry in a manner known to be incompatible with experiment. If  $\Delta L_z = \pm 1$  transitions are allowed then this link is broken. Thus a weaker version of  $SU(6)_w \times O(3)$  is required. Several independent approaches have been made. (47)

In the " $l$ -broken  $SU(6)_w$ " model, all decay processes via one outgoing  $l$  wave remain interrelated as in the unbroken symmetry. Only those  $SU(6)_w$  relations that link two different outgoing  $l$  waves are relaxed. Fainman et al. (48) have carried out fits to decay rates using this model and a reasonable degree of success has been had.

In the "Quark Pair Creation" model, an additional quark-antiquark pair is created from the vacuum in a decay process, and has the quantum numbers of the vacuum, i.e.  ${}^3P_0$ . The model is almost identical with the " $l$ -broken" model.

Models working with explicit quark wave functions have been studied, with transition operators describing pion emission used to connect initial and final states. The result is very similar to the above two models, but also relates decays involving different  $SU(6)$  multiplets.

### 7.3 The Melosh Approach

Quarks are considered the fundamental constituents of hadrons, and  $SU(6)_w$  symmetry is used to classify single particle states at rest or in motion. This version of  $SU(6)_w$  has been called  $SU(6)_w$ , constituents with corresponding "constituent" quarks.

The current algebra of Gell-Mann and Dashen postulates that measurable current operators transform simply under an  $SU(6)_w$  derived from measurable charges. This algebra is called  $SU(6)_w$ , currents. (49)

The specific matrix element for a transition between two hadrons is of the form  $\langle \text{hadron}' | Q_5^\alpha | \text{hadron} \rangle$  where  $Q_5^\alpha$  is one of the sixteen vector and axial vector charges,  $Q^\alpha$  and  $Q_5^\alpha$ , which make up a subalgebra of

$SU(6)_w$ , currents. ( $Q_5$  is used since it is related by the PCAC hypothesis to the pion field).  $Q_5^\alpha$  transforms simply under  $SU(6)_w$ , currents, but if the equality  $SU(6)_w$ , constituents =  $SU(6)_w$ , currents was made, serious contradictions with experiment would occur. Gell-Mann suggested that the two were connected by a unitary transformation  $V$ .

$$\text{i.e. } |\text{hadron}\rangle = |\text{I.R. constituents}\rangle = V |\text{I.R. currents}\rangle$$

(I.R. = irreducible representation)

The matrix element then becomes:-

$$\begin{aligned} \langle \text{hadron}' | Q_5^\alpha | \text{hadron} \rangle &= \langle \text{I.R. currents}' | V^{-1} Q_5^\alpha V | \text{I.R. currents} \rangle \\ &= \langle \text{I.R. currents}' | \tilde{Q}_5^\alpha | \text{I.R. currents} \rangle \end{aligned}$$

Melosh suggested a simple form for  $V^{(50)}$  in which the transformed axial charges  $\tilde{Q}_5^\alpha$  maintain their former  $\Delta L_z = 0$  term, but acquire new  $\Delta L_z = \pm 1$  contributions, which turn out to behave exactly as that in the quark pair creation model for pion emission. The transformation is known as the Melosh transformation.

#### 7.4 The Model

##### a) Pseudoscalar meson decays

Hey, Litchfield and Cashmore (in future referred to as HLC) have used an  $SU(6)_w$  model motivated by the Melosh transformation to relate together the decays of members of the  $(70, 1^-)$  multiplet and of members of the  $(56, 2^+)$  multiplet involving the emission of a pseudoscalar meson. The decay matrix element for pion emission is related to that of the axial charge, using PCAC, by:-

$$\langle B\pi | A \rangle \sim (M_B^2 - M_A^2) \langle B | Q_5^\alpha | A \rangle$$

In the HLC model<sup>(51)</sup>, the helicity amplitude for the process:-

$$A(J^A \lambda L S^A) \longrightarrow B(S^B \lambda) + \pi$$

where B is in the  $(56, 0^+)$

has the structure:-

$$g_\lambda = (M_B^2 - M_A^2) \tilde{g}_\lambda \quad 7.3$$

$$\text{where } \tilde{g}_\lambda = \sum_{L_z} C(L L_z S^A (\lambda - L_z) | J^A \lambda) C(S^B \lambda 1 - L_z | S^A (\lambda - L_z)) \quad 7.4$$

LS coupling W-spin

$$\times \left\{ \begin{array}{cc|c} 56 & 35 & M^A \\ (N^B, 2S^B+1) & (8,3) & (N^A, 2S^A+1) \end{array} \right\} \left\{ \begin{array}{c|c} N^B & 8 \\ B & \pi \end{array} \middle| \begin{array}{c} N^A \\ A \end{array} \right\}_\alpha t^{L_z}$$

SU(6) factor SU(3) factor

The  $t^{L_z}$ 's are independent reduced matrix elements.  $M^A N^A S^A$  ( $M^B N^B S^B$ ) denote the SU(6), SU(3) and SU(2) representations of state A(B).  $\alpha$  denotes a sum over F and D type couplings in the case of octets.

For massless pions, PCAC gives a decay rate:-

$$\Gamma = \frac{P}{8\pi M_A^2} \frac{1}{2J^A+1} \sum_\lambda |g_\lambda|^2 = \frac{P}{8\pi M_A^2} \frac{1}{2J^A+1} \sum_\ell |g_\ell|^2 \quad 7.5$$

where P is the centre of mass momentum for decay and  $M_A$  is the mass of state A. For convenience, the partial wave amplitude  $g_\ell$  is also defined and related to  $g_\lambda$  by a set of Clebsch-Gordan coefficients.

For the  $(70, 1^-)$  and  $(56, 2^+)$  transitions, linear combinations of the  $t^{L_z}$ 's are defined for each transition:-

$$\begin{array}{ll} \text{For the } (70, 1^-) & t^0 = -\frac{1}{3}(S+2D) \quad t^1 = \frac{1}{3}(S-D) \\ \text{For the } (56, 2^+) & t^0 = -\frac{1}{5}(2P+3F) \quad t^1 = \frac{\sqrt{3}}{5}(P-F) \end{array}$$

S, D, P and F are the reduced partial wave amplitudes, and their relationship with the  $g_\ell$ 's are tabulated in ref.(51).

Since pions have mass, PCAC is only approximate in the real world. HLC have instead used an angular momentum barrier factor for each partial wave:-

$$\Gamma_\ell = \frac{P M_N}{M_A} B_\ell(P, r) \frac{1}{2J^A+1} |g_\ell|^2 \quad 7.6$$

where  $M_N$  is the nucleon mass

The form  $P^{2\ell}$  was used as the barrier factor,  $B_\ell$ , in their final fits.

Two and three-way mixing were used for the  $N^*$ 's and  $Y^*$ 's to form the physical state. The possible mixing within the  $(70, 1^-)$  and  $(56, 2^+)$  are shown in fig.(7.1). Their mathematical forms are given in ref.(51).  $\frac{\mathcal{E}_F}{\mathcal{E}_D}$  ratios for octet decays are predicted from the  $SU(6)_w$  symmetry and were used in their fits.

$$\text{For the } (70, 1^-) \quad 2_8 \Rightarrow \frac{F}{D} = \frac{5}{3} \quad 4_8 \Rightarrow \frac{F}{D} = -\frac{1}{3}$$

$$\text{For the } (56, 2^+) \quad 2_8 \Rightarrow \frac{F}{D} = \frac{2}{3}$$

$$\text{where } \frac{F}{D} = \sqrt{\frac{5}{3}} \frac{\mathcal{E}_F}{\mathcal{E}_D}$$

To extend the model to  $\bar{K}$  decays, HLC have divided out the  $SU(3)$  factor for  $N\bar{K}$  decays from the amplitudes and replaced them with the relevant factors for  $Y^*$  decays to  $N\bar{K}$ .

Their latest fits to the experimental data on  $\pi$  and  $\bar{K}$  decays are reported in ref.(52) where reasonable success has been achieved and fitted values for S, D, P and F are presented together with the fitted mixing angles.

#### b) Photoproduction and $\rho$ decays

The Melosh transformed transverse components of the dipole operator can be expressed in terms of four reduced amplitudes A, B, C and D such that:- (53)

$$\begin{aligned} \tilde{D}_1 \sim & A (w=0 \quad w_2=0 \quad \Delta L_2 = \pm 1) \\ & + B (w=1 \quad w_2 = \pm 1 \quad \Delta L_2 = 0) \\ & + C (w=1 \quad w_2 = 0 \quad \Delta L_2 = \pm 1) \\ & + D (w=1 \quad w_2 = \mp 1 \quad \Delta L_2 = \pm 2) \end{aligned} \quad 7.7$$

Decays via photon emission are related to the transverse components of the electromagnetic current, which are in turn related to those of the dipole operator. The relation is given in ref.(53). HLC have fitted the measured photoproduction rates for members of the  $(70, 1^-)$  and

(56, 2<sup>+</sup>) and extracted values for A, B, C and D for each multiplet.

In the Melosh approach  $\pi$  and  $\rho$  decays are not simply related since they involve different current operators. Other models do relate the decays. The only possibility within this model is to relate  $\rho$  decays to the matrix elements of the electromagnetic current. HLC have taken the isovector portion of the algebraic structure for photon transitions ( $\lambda = \pm 1$ ) and have extrapolated from  $q^2 = 0$  to  $q^2 = m_\rho$  and assumed that this approximates the  $SU(6)_W$  structure of transverse  $\rho$  decays. This has also been carried out for the  $\lambda = 0$  part of the electromagnetic current which is assumed to transform as a sum of a  $\Delta L_z = 0$  term with  $W=0$  ( $a_0$ ) and  $\Delta L_z = \pm 1$  with  $W=1$  ( $a_1$ ). The Clebsch-Gordan coefficients between the helicity amplitudes and the reduced amplitudes for the isovector part of the electromagnetic current are given in ref.(54) for  $N\rho$  transitions of the (70, 1<sup>-</sup>) and (56, 2<sup>+</sup>). The relations between helicity amplitudes and partial wave amplitudes are also given.

Due to lack of sufficient data and the large number of parameters, ( $A_\rho, B_\rho, C_\rho, a_0, a_1$  for (70, 1<sup>-</sup>);  $A'_\rho, B'_\rho, C'_\rho, D'_\rho, a'_0, a'_1$  for (56, 2<sup>+</sup>)), HLC have used a naive vector dominance model to assume that the ratios of A, B, C and D are unchanged in going from photoproduction to transverse  $\rho$  amplitudes i.e.  $A_\rho = r_{70} A$ , etc. for (70, 1<sup>-</sup>), and  $A'_\rho = r_{56} A$  for (56, 2<sup>+</sup>) with A, B, C and D determined from photoproduction analysis. Furthermore, VDM predicts  $r = r_{70} = r_{56} \sim 1.3$ . The parameters used were therefore  $r, a_0, a_1, a'_0, a'_1$ . The mixing angles were taken from the fits to the pseudoscalar meson decays.

Their fits to the  $N\rho$  decays were carried out by setting up a partial wave amplitude as:-

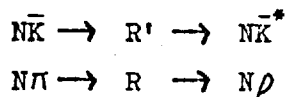
$$T_{454}^J = \frac{M_N}{M_A} \frac{1}{2J^2+1} \frac{1}{\Gamma} \sqrt{\rho B_L(\rho) q B_L(q)} g_L^{(\pi N)} g_{L5}^{J(\rho N)} \quad 7.8$$

with the  $N\rho$  barrier factor integrated over the  $\rho$  lineshape. Their final results are given in ref.(52).

### 7.5 Application to $\bar{K}^* N$ decays

In the analysis of the previous chapter the amplitudes for the decay to  $\bar{K}^* N$  of several well established resonances have been extracted. In particular, the P03(1900), F05(1822) and F17(2040) have been assigned to the  $(56, 2^+)$  multiplet and it would appear that their relative amplitude signs could be predicted from the fitted parameters of  $\rho$  decays given in ref.(52). Furthermore, the lack of mixing for these states means that their amplitudes are determined purely by these parameters. The S11(1955) has been assigned to the  $(70, 1^-)$  and its amplitudes can also be predicted using the mixing angles given in ref.(52).

We therefore wish to convert the reduced amplitudes for  $N\rho$  decays of ref.(54) to those for  $N\bar{K}^*$  decays; i.e. we wish to relate the reactions:-



where R and R' belong to the same SU(3) multiplet.

Consider first the  $N\bar{K}$  and  $N\pi$  couplings. If R and R' belong to an octet, the SU(3) factors of the reduced amplitude are:-

$$\begin{aligned} \text{For } N^* &\longrightarrow N\pi &: & \frac{3\sqrt{5}}{10} g_D + \frac{1}{2} g_F \\ \Lambda &\longrightarrow N\bar{K} &: & \frac{\sqrt{10}}{10} g_D + \frac{\sqrt{2}}{2} g_F \\ \Sigma &\longrightarrow N\bar{K} &: & -\frac{\sqrt{30}}{10} g_D + \frac{\sqrt{6}}{6} g_F \end{aligned} \quad 7.9$$

where the  $\frac{g_F}{g_D}$  ratios are given on page (181). If R and R' belong to a decuplet, then the SU(3) factors are:-

$$\begin{aligned} \text{For } \Delta &\longrightarrow N\pi &: & -\frac{\sqrt{2}}{2} g_{10} \\ \Sigma &\longrightarrow N\bar{K} &: & -\frac{\sqrt{6}}{6} g_{10} \end{aligned} \quad 7.10$$

Thus to convert from  $N\pi$  couplings to  $N\bar{K}$  couplings, the relevant factors are substituted into the following expressions which are then multiplied to the reduced amplitudes.

$$\frac{\Sigma \rightarrow N\bar{K}}{\Delta \rightarrow N\pi} \quad \left( = \frac{1}{\sqrt{3}} \right) \quad \text{for decuplets}$$

$$\frac{Y^* \rightarrow N\bar{K}}{N^* \rightarrow N\pi} \quad \text{for octets}$$

For  $N\rho$  and  $N\bar{K}^*$  couplings the same  $SU(3)$  factors are used since  $\pi \equiv \rho$  and  $\bar{K} \equiv \bar{K}^*$  under  $SU(3)$ . For  $\frac{\epsilon_F}{\epsilon_D}$  ratios, however, it is necessary to distinguish between the  $W=0$  and  $W=1$  parts of the current. The  $W=1$  parts correspond to the B, C, D and  $a_1$  terms, and here the  $\frac{\epsilon_F}{\epsilon_D}$  ratios are the same as for  $N\pi$  and  $N\bar{K}$  couplings. The  $W=0$  parts correspond to the A and  $a_0$  terms, and here  $SU(6)_W$  predicts:-

$$\begin{aligned} \text{For } (70, 1^-) : 4_8 \Rightarrow \epsilon_F = \epsilon_D = 0; \quad 2_8 \Rightarrow \frac{\epsilon_F}{\epsilon_D} &= \frac{1}{\sqrt{5}} \\ (56, 2^+) : 2_8 \Rightarrow \epsilon_D &= 0 \end{aligned} \quad 7.11$$

The final physical amplitudes for the unmixed states are calculated using eqn.(7.8) applied to  $N\bar{K}$  and  $N\bar{K}^*$  couplings. In the case of the S11(1955), the mixing angles of ref.(52) are used to obtain the physical state from the three pure  $SU(6)$  states, i.e.:-

$$S11(1955) = -0.75 \quad 4_8 - 0.30 \quad 2_8 + 0.59 \quad 2_{10}$$

The outgoing barrier factor is integrated over the  $K^*$  lineshape.

## 7.6 Results and Conclusions

Appendix table (A.1) gives the three modified partial wave solutions resulting from a four variable Dalitz Plot analysis of the same data. Table (7.1) gives the mean amplitudes for the four resonances under study taken from the three solutions, with intuitive errors required for  $SU(6)_W$  fitting purposes. The  $N\rho$  amplitudes used by HLC are also given.

The parameters of the best fit by HLC to the  $N\rho$  decays (given in ref.(52)) have been used to predict the amplitudes for  $N\bar{K}^*$  decays. The results are given in table (7.1), and it is immediately seen that two amplitudes exceed the unitarity bound of 0.5. This means that, assuming

the model is approximately correct, either the widths of the  $P03(1900)$  and  $F05(1822)$  have been underestimated, or the fitted values of the parameters are wrong. Assuming the latter case, a fit was made to the combined data for  $N\rho$  and  $N\bar{K}^*$  decays (excluding the  $S11(1955)$ ) using the HLC parameter values as starting values. The results are shown in table (7.1).

The three crucial amplitudes,  $OPF33(1900)$ ,  $OPF53(1822)$  and  $1FF73(2040)$  agree in sign and magnitude with the results of the fit, although the  $N\rho$  fit quality has decreased. However, the remaining  $P03$  amplitudes bear no relation to the fitted values. Furthermore, the  $S11$  amplitudes are also in disagreement with the predictions of the fit. The fitted "r" parameter is seen to be reasonably unchanged.

Apart from the  $PP3$  amplitudes, the fit to the three crucial amplitudes ("crucial" since they form the interference effect mentioned on page (133) ) is impressive, and by themselves would appear to offer good evidence for the consistency of the model. The  $S11$  discrepancy can be traced to the mixing angles which HLC have obtained from very meagre data. It would appear as if the values are clearly wrong.

The  $PP3$  amplitudes cannot be explained away so easily. One possibility is that the experimental amplitudes deduced in Chapter 6 are wrong. In order to check the possibility that the  $PP3$  amplitudes should be much larger, the results of the  $SU(6)_w$  fit for the two amplitudes were inserted into one of the three partial wave solutions and fixed. The solution was minimized for several iterations, the two amplitudes were then released, and the solution reminimized. The result showed a preference for the original experimental amplitude values.

It would thus appear that it is the  $SU(6)_w$  model itself that is wrong to some extent. A possible reason may be due to the barrier factor. PCAC requires the same factor for the two possible  $\{out$  values, whereas the factor actually used has quite different values for the two cases.

The ideal factor may be somewhere between the two. Thus the basic Melosh motivated  $SU(6)_W$  model may in itself be a reasonable approximation, after all, for the decays to vector meson - nucleon.

### 7.7 Classification of the Remaining Resonances.

The G07(2110) has been assigned as a singlet state to the  $(70, 3^-)$  multiplet. This is the simplest location for a  $\frac{7}{2}^-$  resonance. The lack of  $SU(6)_W$  reduced amplitudes for this multiplet means that no predictions can be made for its  $\bar{K}^* N$  decay mode.

As mentioned earlier, the possibility of radial excitation between the quarks allows for a whole spectrum of  $SU(6)$  multiplets based upon the radial excitation quantum number "n". The P01(1853) could be assigned to either the  $(70, 0^+)_2$  or  $(56, 0^+)_4$ , where the subscript denotes the n value.

The D03 state with mass  $\sim 1980$  MeV which appears to have been discovered in this analysis, might have originally been assigned to the  ${}^4_8\frac{3}{2}$  member of the  $(70, 1^-)$  multiplet. However, the recent discovery of another D03 state by Hansen et al. <sup>(55)</sup> with amplitudes in good agreement with predictions, means that the state at 1980 MeV belongs to a higher multiplet. Again, the simplest location would be in the  ${}^4_8\frac{3}{2}$  member of the  $(70, 3^-)$  multiplet.

The S01 state with mass 2030 MeV cannot be located in the usual multiplets. It would therefore have to be assigned to a radial excitation state, preferably of the  $(70, 1^-)$ . The Harmonic Oscillator Quark model of Dalitz and Horgan <sup>(56)</sup> predicts a linear relationship between "n" and mass-squared. Figure (7.2) shows that this is in fact the case for the common multiplets. Furthermore, it can be seen where the radially excited  $(70, 1^-)$  state with n=3 is situated. A prediction can now be made for the mass of the S01 using the mass of the Roper resonance situated in the  $(56, 0^+)_2$  multiplet, and the mass of the nucleon. Then:-

$$m_{Roper}^2 - m_N^2 = m_{S01(n=3)}^2 - m_{S01(n=1)}^2$$

Taking  $m_{\text{Roper}} = 1430 \text{ MeV}$ , and using the  $\text{S01}(1670)$  member of the  $(70, 1^-)_1$  multiplet, the prediction for the equivalent  $\text{S01}$  state in the radially excited  $(70, 1^-)$  is:-

$$m_{\text{S01}(n=3)} = 2000 \text{ MeV}$$

which is in excellent agreement with the result of the partial wave analysis. It would thus appear that the new  $\text{S01}$  resonance is a radial excitation of the  $\text{S01}(1670)$ . There is, however, no explanation of the fact that the outgoing  $D$  wave dominates the decay.

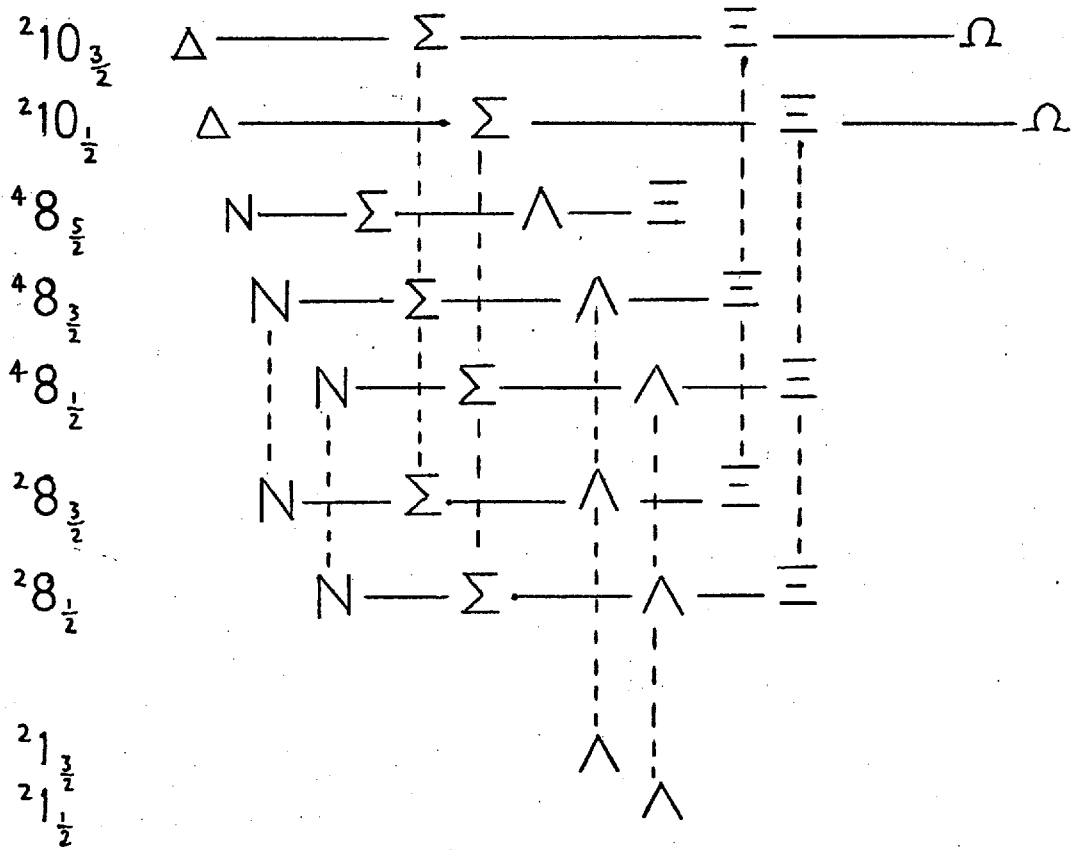
\* \* \* \* \*

Table(7.1)      Results of the SU(6) Fits

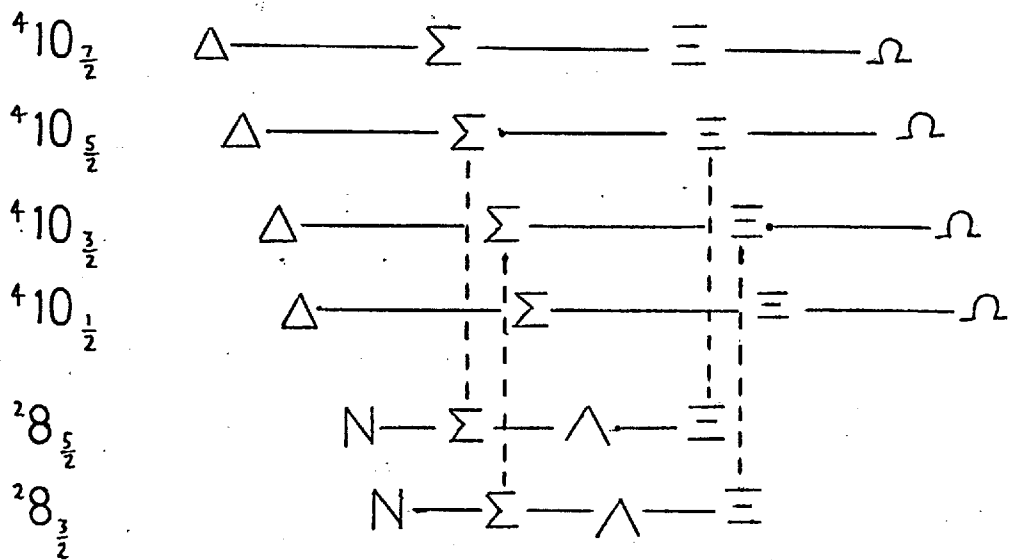
Resonance	Partial Wave	Experimental Amplitude	Fit to $N_p$ decays only (HLC solution)	Fit to $N_p$ and $N\bar{K}^*$ decays
$N^*$				
<u>(70,1<sup>-</sup>)</u>				
S11(1510)	SS11	-0.12 ± 0.08	-0.12	-0.11
S11(1660)	SD13	+0.29 ± 0.10	+0.26	+0.13
D13(1520)	DS33	-0.32 ± 0.10	-0.32	-0.31
D15(1670)	DD53	-0.15 ± 0.10	-0.05	-0.03
<u>(56,2<sup>+</sup>)</u>				
P13(1730)	PP31	+0.35 ± 0.10	+0.25	+0.11
F15(1680)	FP53	-0.27 ± 0.10	-0.35	-0.08
	FF53	-0.15 ± 0.10	-0.21	-0.13
F35(1860)	FP53	+0.28 ± 0.08	0.00	-0.02
$Y^*$				
<u>(70,1<sup>-</sup>)</u>				
S11(1955)	SS11	-0.03 ± 0.05	+0.24	+0.21
	SD13	-0.05 ± 0.10	-0.19	-0.10
<u>(56,2<sup>+</sup>)</u>				
P03(1900)	PP31	-0.05 ± 0.10	+0.82	+0.32
	PP33	+0.10 ± 0.10	-0.31	-0.11
	PF33	+0.12 ± 0.02	+0.17	+0.06
F05(1822)	FP53	-0.13 ± 0.03	-0.54	-0.15
F17(2040)	FF73	-0.07 ± 0.02	-0.11	-0.06
Parameters				
r			3.59	2.00
$a_0(70,1^-)$			-44.50	-20.80
$a_1(70,1^-)$			4.80	1.27
$a_0(56,2^+)$			-1.69	9.43
$a_1(56,2^+)$			-20.50	-13.10
$\chi^2/\text{NDF}$			11.1/3	50.7/8

7.1

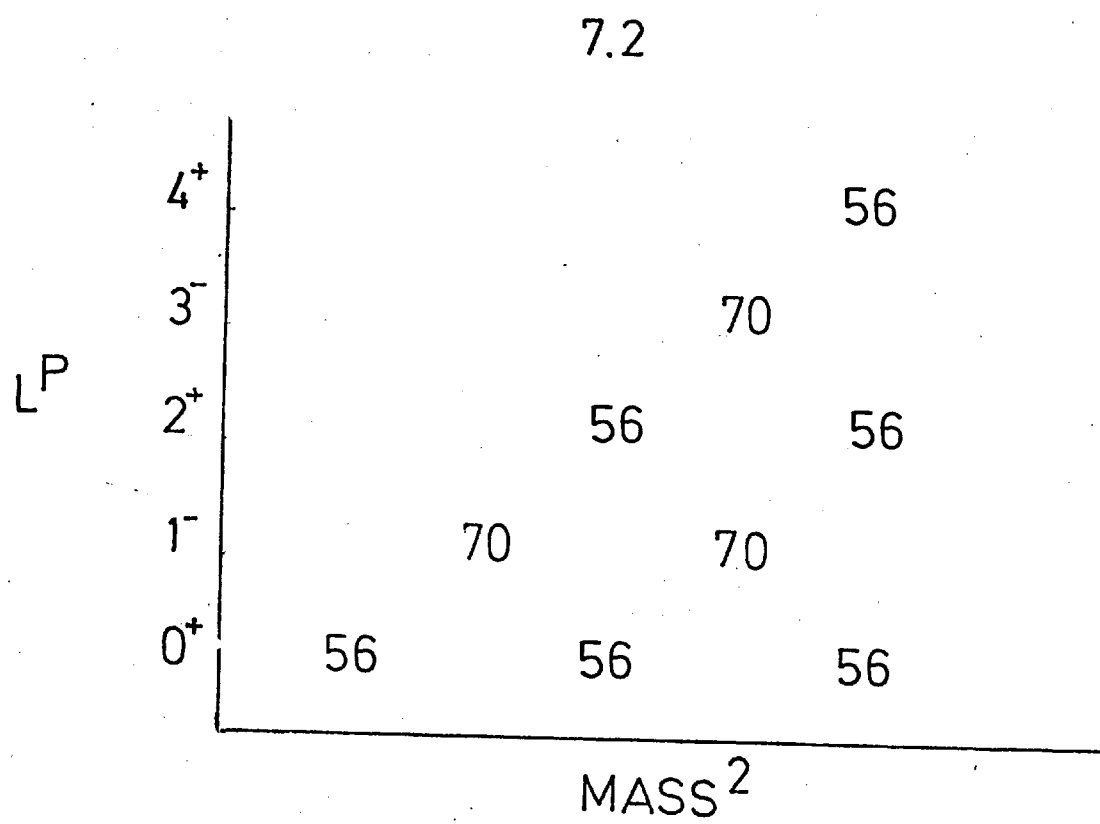
(70, 1<sup>-</sup>)



(56, 2<sup>+</sup>)



! Mixing Possibilities



AppendixA Refinement of the Partial Wave Solutions

At the end of Chapter 4 it was mentioned that the  $\bar{K}N\pi$  data was currently being reanalysed using a four-variable approach. A refined set of Legendre coefficients for the reaction  $K^- p \rightarrow \bar{K}^* N$  have now been obtained without the problem of the background removing part of the structure. In this way coefficients have been obtained for the first four energies as well, but only data from the fourth energy (1.085 GeV/c) has been included in the partial wave analysis, together with the first two energies of the CRS data.

It was mentioned in Chapter 5 that the outgoing barrier factor was not applied to the F05(1822) during the whole of the partial wave analysis. The integrated form has now been applied and is now calculated in all cases by an integral over the region  $m_{\bar{K}^*} \pm 8\Gamma$  where  $m_{\bar{K}^*}$  is the peak mass of the  $\bar{K}^*$  and  $\Gamma$  is its full width.

All three solutions were run with the refined coefficients as data. The results are shown in table (A.1), where it is seen that little change has occurred in the partial wave amplitudes except the F05(1822). Table (A.1) represents the final results of this analysis.

\* \* \* \* \*

Table (A.1)

Comparison of Solutions "A", "B", and "C" for the new data

Resonance	Partial Wave	Solution "A"	Solution "B"	Solution "C"
		$\frac{\chi^2}{\text{NDF}} = \frac{1464}{1152} = 1.27$	$\frac{\chi^2}{\text{NDF}} = \frac{1463}{1153} = 1.27$	$\frac{\chi^2}{\text{NDF}} = \frac{1476}{1156} = 1.28$
S11(1955)	SS11	0.02	0.02	0.06
	SD13	0.09	0.00	0.08
P01(1853)	PP11	0.01	0.12	0.08
	PP13	0.19	0.27	0.26
P03(1900)	PP31	0.08	0.04	0.05
	PP33	-0.13	-	-0.10
	PF33	-0.11	-0.11	-0.13
F05(1822)	FP53	0.15	0.12	0.12
F17(2040)	FF73	0.07	0.07	0.07
G07(2100)	GG71	0.05	0.10	0.11
	GD73	0.23	0.20	0.21
	GG73	0.05	0.06	0.09
D03(1980)	Mass	1986	1984	1975 MeV
	Width	162	169	180 MeV
	DD31	0.07	0.09	0.09
	DS33	0.17	0.17	0.12
	DD33	-	-	-0.02
S01(2030)	Mass	2025	2011	2040 MeV
	Width	137	124	265 MeV
	SS11	-0.07	-	-
	SD13	0.19	0.23	0.29

References

- 1) a) Geometry program manual, Rutherford Laboratory (1968).  
b) Kinematics program manual, Rutherford Laboratory (1968).
- 2) JUDGE program manual, Rutherford Laboratory (1970).
- 3) Particle Data Group; Review of Particle Properties; Reviews of Modern Physics, Vol. 48, No.2, Part 2, (1976).
- 4) D.H. Saxon;  $\bar{K}N\pi$  Ambiguities in Survey 2; Rutherford Laboratory Bubble Chamber Group Physics Note 78 (1974), (unpublished).
- 5) G.P. Gopal; Elastic Scattering in  $K^-p$  Survey 2; Rutherford Laboratory Bubble Chamber Group Physics Note 65 (1973), (unpublished).
- 6) a) J. Goldberg et al.; Phys. Lett. 30B, 434, ('69).  
b) K. Buchner et al.; Nucl. Phys. B45, 333, ('72).
- 7) J.D. Jackson; Nuo. Cim. 34, 1644, ('64).
- 8) S.M. Deen; Generalised Partial Wave Analysis; Rutherford Laboratory preprint RPP/H/68, (unpublished).
- 9) For example:- G.T. Jones; Proceedings of 1974 School for Young High Energy Physicists; Rutherford Laboratory publication RL-75-009.
- 10) J. Daboul; Nucl. Phys. B4, 180, ('67).
- 11) G.P. Gopal; On Determination of Spin Density Matrix Elements; Rutherford Laboratory Bubble Chamber Group Physics Note 47 (unpublished) and G.P. Gopal; private communication.
- 12) CERN TC Program Library; MINUIT writeup.
- 13) a) R.W. Bland et al.; Nucl. Phys. B13, 595, ('69).  
b) A. Berthon et al.; Nucl. Phys. B63, 54, ('73).
- 14) J.M. Blatt and V.F. Weisskopf; Theoretical Nuclear Physics ; (Wiley, 1952), page 361.
- 15) A. Berthon et al.; Nuo. Cim. 21, 146, ('74)

- 16) P.J. Litchfield; private communication.
- 17) P.J. Litchfield et al.; Nucl. Phys. B74, 12,19,39 , ('74).
- 18) A. Kotanski and K. Zalewski; Nucl. Phys. B22, 317, ('70).
- 19) M. Jacob and G.C. Wick; Annals of Physics 7, 404, ('59).
- 20) N.A. McCubbin and L. Lyons; Nucl. Phys. B86, 13, ('75).
- 21) P.S. Jones; Thesis - University College, London 1971, (unpublished).
- 22) For example:- P.J. Litchfield et al.; Nucl. Phys. B74, 39, ('74).
- 23) A. Kernan et al.; contribution to Purdue Baryon Conference (1973).
- 24) Y. Gell et al.; Nucl. Phys. B33, 379, ('71).
- 25) CERN TC Program Library; FOWL writeup.
- 26) R.J. Cashmore; The Isobar Model; Scottish Universities Summer School, (1973).
- 27) M. De Beer et al.; Nucl. Phys. B12, 599,617, ('69).
- 28) D.J. Herndon et al.; LBL-1065 / SLAC-PUB-1108 ('72) publications.
- 29) A review of the analyses of this reaction is given by R.J. Cashmore; contribution to Purdue Baryon Conference (1973).
- 30) M.J. Corden et al.; Nucl. Phys. B92, 365, ('75).
- 31) For the reaction type  $0^{-} \frac{1}{2}^{+} \longrightarrow 1^{-} \frac{1}{2}^{+}$  see A. Brandstetter et al.; Rutherford Laboratory report RHEL/R.224 (1971).
- 32) R.D. Tripp; Baryon Resonances; CERN report 65-7 (1965).
- 33) A.J. Van Horn; APPLE program user's guide; Rutherford Laboratory Bubble Chamber Group Physics Note 83 (1974) (unpublished).
- 34) Harwell Subroutine Library; VA04A writeup.
- 35) For example:- W.S.C. Williams; An Introduction to Elementary Particles; (Academic Press, 2nd edition, 1971), page 125.
- 36) M.J. Corden et al.; Data and Partial Wave Analysis for Reaction  $K^{-} n \longrightarrow K^{*}(890)^{-} n$ ; submitted to Oxford Baryon Conference (1976).
- 37) Rutherford Laboratory - Imperial College Collaboration; Partial Wave Analysis of  $\bar{K}N$  Two-Body Reactions Between 1480 and 2170 MeV; Rutherford Laboratory preprint RL-75-182.

- 38) P.J. Litchfield;  $S \leq -1$  Baryon Spectroscopy; Proceedings of Aix Conference C1-227.
- 39) A. Brandstetter et al.; Nucl. Phys. B39, 13, ('72).
- 40) For example:- W.A. Barletta; Nucl. Phys. B40, 45, ('72).
- 41) M. Gell-Mann and Y. Ne'eman; The Eightfold Way; (Benjamin, New York, 1964).
- 42) M. Gell-Mann; Phys. Lett. 8, 214, ('64).
- 43) a) D.E. Plane et al.; Nucl. Phys. B22, 93, ('70).  
b) A. Barbaro-Galtieri; Proceedings of XVI International Conference on High Energy Physics; Vol 1, page 159, (1972).
- 44) F. Gürsey and L. Radicati; Phys. Rev. Lett. 13, 173, ('64).
- 45) O.W. Greenberg; Phys. Rev. Lett. 13, 598, ('64).
- 46) H.J. Lipkin and S. Meshkov; Phys. Rev. Lett. 14, 670, ('65).
- 47) A review of these approaches is given by J.L. Rosner; Physics Reports; Vol 11, No. 4.
- 48) D. Faiman and D.E. Plane; Nucl. Phys. B50, 379, ('72).
- 49) R. Dashen and M. Gell-Mann; Phys. Lett. 17, 142, ('65).
- 50) H.J. Melosh; Phys. Rev. D9, 1095, ('74).
- 51) A.J.G. Hey, P.J. Litchfield and R.J. Cashmore; Nucl. Phys. B95, 516, ('75).
- 52) P.J. Litchfield, R.J. Cashmore and A.J.G. Hey; Rutherford Laboratory preprint RL-76-111 (1976).
- 53) A.J.G. Hey and J. Weyers; Phys. Lett. 48B, 69, ('74).
- 54) R.J. Cashmore, A.J.G. Hey and P.J. Litchfield; Nucl. Phys. B98, 237, ('75).
- 55) P.N. Hansen, J. Moss and G.C. Oades; contribution to Oxford Baryon Conference (1976).
- 56) R. Horgan and R.H. Dalitz; Nucl. Phys. B66, 135, ('73).

### Acknowledgements

On joining an experiment at the data analysis stage it becomes very difficult to acknowledge the work of any individual involved in the data taking and data reduction stages. I would therefore like to thank as a whole all the people involved, from the accelerator crews at CERN to the scanning, measuring and book-keeping staff at Imperial College.

I am indebted to my supervisor, Professor I. Butterworth, for his help and guidance during the course. Thanks are due to Dr. T. C. Bacon for his invaluable assistance. I would also like to thank my colleagues in the Bubble Chamber Group of the Rutherford Laboratory and especially Dr. G. P. Gopal for all their help and advice.

Dr. R. J. Cashmore has been of invaluable help in the analysis of the final chapter. I would also like to thank him for allowing me the use of his  $SU(6)_w$  fitting program.

The vast majority of the diagrams in this thesis have been produced using the SMOG system on the IBM 360 computer at the Rutherford Laboratory. I would like to thank all the people involved in setting up this system. I would also like to thank my sister, Dena, for her excellent typing of this thesis.

Final thanks are due to the Science Research Council for their financial support during the course.

\* \* \* \* \*